

Boston University College of Engineering

Ronald A. Roy, Professor and Chair
Department of Mechanical Engineering
110 Cummington Street
Boston, Massachusetts 02215
Tel: 617-353-4846
Fax: 617-353-5866
Email: ronroy@bu.edu

BOSTON
UNIVERSITY

4 November 2009

Robert Manning
Office of Naval Research
ONR Code 32
875 North Randolph Street
Arlington, VA 22203-1995

Subject: Final Report

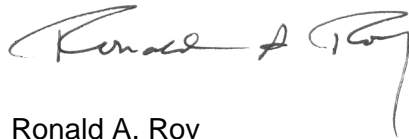
Reference: Contract N00014-08-1-0148

Dear Dr. Manning:

Boston University is pleased to submit our Final Report entitled "Supplemental Student Support: Detection and Identification of Buried Targets Using Time Reversal Acoustics."

Technical questions concerning this report should be addressed to me at 617-353-4846 or ronroy@bu.edu.

Sincerely,



Ronald A. Roy

Professor and Chairman

Cc: Eric Garfield, Office of Naval Research (electronic)

Director, Naval Research Lab
Attn: Code 5596
4555 Overlook Avenue, SW
Washington, DC 20375-5320

Defense Technical Information Center
8725 John J. Kingman Road, STE 0944
Ft. Belvoir, VA 22060-6218

FINAL REPORT
TO THE OFFICE OF NAVAL RESEARCH

Grant No. N00014-08-1-0148

**SUPPLIMENTAL STUDENT SUPPORT:
DETECTION AND IDENTIFICATION OF BURIED
TARGETS USING TIME REVERSAL ACOUSTICS**

by

Ronald A. Roy and Zachary, J. Waters

Boston University
Department of Mechanical Engineering
110 Cummington Street
Boston, MA 02215

November 4, 2009

The Following Final Report for ONR Grant N00014-08-1-0148 was submitted by Zachary J. Waters to the Boston University College of Engineering in partial fulfillment of the requirements for the Degree of Doctor of Philosophy. The Grant provided supplement student support for work on ONR Grant No. N00014-06-1-0044, entitled "Detection and Identification of Buried Targets using Time Reversal Acoustics".

The degree was conferred in May of 2009.

Ronald A. Roy
Principal Investigator
November 4, 2009

BOSTON UNIVERSITY
COLLEGE OF ENGINEERING

Dissertation

**SENSING RESONANT OBJECTS IN THE PRESENCE OF NOISE AND
CLUTTER USING ITERATIVE, SINGLE-CHANNEL ACOUSTIC
TIME REVERSAL**

by

ZACHARY JOHN WATERS

B.S., Boston University, 2004
M.S., Boston University, 2008

Submitted in partial fulfillment of the
requirements for the degree of
Doctor of Philosophy

2009

**SENSING RESONANT OBJECTS IN THE PRESENCE OF NOISE AND
CLUTTER USING ITERATIVE, SINGLE-CHANNEL ACOUSTIC
TIME REVERSAL**

(Order No.)

ZACHARY JOHN WATERS

Boston University, College of Engineering, 2009
Major Professor: Ronald A. Roy, Ph.D., Professor of Mechanical Engineering

ABSTRACT

The presence of noise and coherent returns from clutter often confounds efforts to acoustically detect and identify target objects buried in inhomogeneous media. Using iterative time reversal with a single channel transducer, returns from resonant targets are enhanced, yielding convergence to a narrowband waveform characteristic of the dominant mode in a target's elastic scattering response. The procedure consists of exciting the target with a broadband acoustic pulse, sampling the return using a finite time window, reversing the signal in time, and using this reversed signal as the source waveform for the next interrogation. Scaled laboratory experiments (0.4-2 MHz) are performed employing a piston transducer and spherical targets suspended in the free field and buried in a sediment phantom. In conjunction with numerical simulations, these experiments provide an inexpensive and highly controlled means with which to examine the efficacy of the technique. Signal-to-noise enhancement of target echoes is demonstrated. The methodology reported provides a means to extract both time and frequency information for surface waves that propagate on an elastic target. Methods developed in the laboratory are then applied in medium scale (20-200 kHz) pond experiments for the detection of a steel shell buried in sandy sediment.

Contents

List of Tables	ix
List of Figures	x
1 Introduction	1
2 Theory of Acoustic Time Reversal and Resonance Scattering	11
2.1 Theory of Single-Channel Acoustic Time Reversal	12
2.1.1 Single-channel, Iterative Time Reversal (ITR)	12
2.1.2 Time Reversal in the Presence of Noise	17
2.2 Review of Acoustic Scattering Theory	20
2.2.1 Acoustic Scattering from Spheres	21
2.2.2 Resonance Identification	40
3 Methodology	60
3.1 Experimental Setup	61
3.2 System Calibration	67
3.3 Transducer Characteristics	74
3.3.1 Range Dependence	74
3.3.2 Angle Dependence	79
3.4 Target Characterization	83
3.5 Sediment Phantom Characterization	92
4 Free Field Results	103
4.1 Resonant Target Echo Enhancement	104
4.2 Time Reversal in the Presence of Stochastic Noise	107
4.3 Isolation of Surface Elastic Waves and Scattering Resonances	117
4.4 Time Reversal with Multiple Targets Present	134

5 Buried Target Results.....	139
5.1 Sediment Loaded Target Response.....	140
5.2 Buried Target Echo Enhancement	147
5.3 Sliding Window Study	149
5.4 Convergence with Target Depth	152
5.5 Multiple Resonance Isolation	156
5.6 Comprehensive Parameter Investigations.....	160
5.6.1 Overview – Sensitivity to Incident Angle.....	160
5.6.2 Normal Incidence Angle	165
5.6.3 10-Degree Incidence Angle	168
5.6.4 20-Degree Incidence Angle	174
5.6.5 Summary of Parameter Investigation.....	178
5.7 Target Selectivity	180
6 Pond Experiments.....	186
6.1 Experimental Setup and Methodology.....	187
6.2 Target Response.....	193
6.3 Free Field Results	197
6.4 Buried Target Results	200
7 Summary and Conclusions	206
A Additional Scattering and Wave Propagation Theory	216
A.1 Acoustic Scattering from an Elastic Sphere.....	216
A.2 Resonance Scattering Theory - Solid Stainless Steel Sphere	222
A.3 Scattering from an Elastic Cylindrical Shell Filled with an Elastic Medium .	228
A.4 Lamb Waves.....	238
B Why Time Reverse?	243

List of Tables

2.1	Material properties used in the analytical prediction of the aluminum spherical shell's monostatic farfield form function.	38
2.2	List of resonance ka locations (center frequency of resonance) for each partial wave of the a_{0-} , a_{0+} , and s_0 Lamb type wave resonances in the purely elastic response of the standard shell target.	54
2.3	Comparison of predicted and measured echo delays, with respect to the specular echo, of symmetric, s_0 , and an antisymmetric, a_{0-} , Lamb waves propagating on the standard spherical shell target. Predicted values assume a frequency of 0.8 MHz. 59	
3.1	Material properties used in the analytical prediction of the monostatic farfield form function of the aluminium spherical shell target.....	85
4.1	Wave types and their center frequencies, measured arrival times, and predicted arrival times for the $5\mu s$ duration time reversal window shifting experiment.....	125
4.2	Comparison of echo delays of a_{0-} antisymmetric Lamb waves measured using the single-channel time reversal technique to those predicted by resonance scattering theory. The values in this table are determined from waveforms at the relative window times highlighted in Figures 4.15c to 4.15h. The normalized root mean square error between the measured and predicted echo delay is presented in the last column of the table.....	133
5.1	Comparison of convergence frequencies observed for different target burial depths in experiments and through application of the buried target scattering simulation....	153
6.1	Summary of field experiments conducted at the Naval Surface Warfare Center – Panama City Division. The date and a summary of each experiment are provided.	186
6.2	Material properties used in form function calculations for the stainless steel shell target employed in field experiments.....	194

List of Figures

1.1	Schematic of array based time reversal, part I. A point source emits a pulse of acoustic energy that travels through the propagation medium and is received by each element of a time reversal mirror (array).	3
1.2	Schematic of array based time reversal, part II. Signals received at the array are time reversed and retransmitted resulting in a focusing of energy back on the location of the point source.	4
2.1	Schematic of the iterative, single-channel time reversal procedure	16
2.2	Schematic of the geometry for the scattering of a plane acoustic wave by a fluid-filled elastic spherical shell submerged in an infinite fluid medium.	25
2.3	Magnitude of the monostatic farfield acoustic form function for a rigid sphere plotted versus the dimensionless Helmholtz number, ka , the number of wavelengths that fit around the circumference of the sphere; (a.) $0 \leq ka \leq 1$ (b.) $0 \leq ka \leq 30$	35
2.4	Scattered pressure fields from a rigid sphere (real part) under steady state driving with (a.) $ka = 1$, (b.) $ka = 20$. The horizontal and vertical axes are normalized and presented in units of the sphere's radius, a . The sphere's location is depicted by the black circle at the center of the image. The intensity value of the pixels in the images represents the pressure amplitude at that location, normalized to the maximum pressure amplitude in the image. The plane wave insonifying the sphere approaches from the left side of each figure.	36
2.5	Magnitude of the monostatic farfield acoustic form function for a 6.35 mm outer diameter hollow aluminum spherical shell plotted versus frequency, assuming a vacuum filled interior (solid line) and an air-filled interior (dashed line).	37
2.6	Form function of the aluminum spherical shell target between 550-650 kHz where the density of the fluid external to the sphere is varied $\pm 5\%$ from its nominal value.	39
2.7	Form function of the aluminum spherical shell target between 550-650 kHz where the sound speed of the fluid external to the sphere is varied $\pm 5\%$ from its nominal value.	39

2.8	Theoretical time trace, normalized amplitude versus time, of a backscattered waveform from the standard hollow aluminum shell target, given a 2 cycle 1 MHz sine wave interrogation pulse. A specular return and three surface elastic wave (SEW) returns are identified with arrows.	41
2.9	Schematic depicting the types of waves scattered from an elastic spherical shell excited by a plane wave of infinite extent.	41
2.10	Magnitude of the far-field monostatic form function for a solid stainless steel sphere plotted versus the dimensionless parameter ka	42
2.11	Far-field acoustic form function of the standard aluminum spherical shell target decomposed into the individual components of its partial wave series solution. (a.) Magnitude of the far-field acoustic form function versus frequency. (b.)-(l.) Partial waves $n = 0$ to $n = 10$, magnitude versus frequency. The vertical axis is normalized and presented on the same scale for all figure panels. The gray shaded region depicts the frequency range of interest for the current work. At the right of panels b-l is plotted the angular dependence of each partial wave.....	51
2.12	Far-field acoustic form function of a rigid sphere decomposed into the individual components of its partial wave series solution. (a.) Magnitude of the far-field acoustic form function versus frequency. (b.)-(l.) Partial waves $n = 0$ to $n = 10$, magnitude versus frequency. The vertical axis is normalized and presented on the same scale for all figure panels. The gray shaded region depicts the frequency range of interest for the current work. At the right of panels b-l is plotted the angular dependence of each partial wave.	52
2.13	Far-field acoustic form function of the standard aluminum spherical shell target decomposed into the individual components of its partial wave series solution after subtraction of the partial waves from a rigid sphere. (a.) Magnitude of the far-field acoustic form function versus frequency. (b.)-(l.) Partial waves $n = 0$ to $n = 10$, magnitude versus frequency, after background subtraction. The vertical axis is normalized and presented on the same scale for all figure panels. The gray shaded region depicts the frequency range of interest for the current work. At the right of panels b-l is plotted the angular dependence of each partial wave. In (f.) resonance types are identified with arrows.....	53
2.14	Dispersion curves of symmetric, s_0 , and asymmetric, a_{0+} , Lamb waves that propagate on a plate and on the standard spherical shell target. The waves' phase velocity is normalized by the sound speed of water, $c = 1479$ m/s, and plotted versus ka . Dispersion curves for plate waves are presented as solid lines and their	

- types are labeled accordingly. Phase velocities of symmetric and asymmetric Lamb waves on the spherical shell are shown as squares and circles, respectively. 55
- 2.15 Plot depicting the displacement (from equilibrium) of the standard spherical shell's inner and outer surfaces at $ka = 2.6083$. The $n = 4$ term in the partial wave series solution of the target's response under steady state forcing is shown. The infinite plane wave exciting the target approaches from the left. The arrows are vectors showing the displacement of each surface of the shell from their un-deformed positions. The solid lines indicate the position of the shell's surfaces at the maximum deflection amplitude. The shell's displacement is scaled so that it is clearly visible for demonstrational purposes. 56
- 2.16 Plot depicting the displacement (from equilibrium) of the standard spherical shell's inner and outer surface at $ka = 39.3559$. The $n = 10$ term in the partial wave series solution of the target's response under steady state forcing is shown. The infinite plane wave exciting the target approaches from the left. The arrows are vectors showing the displacement of each surface of the shell from their un-deformed positions. The solid lines indicate the position of the shell's surfaces at the maximum deflection amplitude. The shell's displacement is scaled so that it is clearly visible for demonstrational purposes. 57
- 2.17 Phase and group velocities of symmetric, s_0 , and antisymmetric, a_{0-} , Lamb waves that propagate on the standard spherical shell target. The wave velocities are normalized by the sound speed of water, $c = 1479$ m/s, and plotted versus frequency over a range relevant to the current work. Phase velocities of symmetric and antisymmetric Lamb waves on the spherical shell are shown as squares and circles, respectively. The phase velocity results are interpolated with a solid line. 58
- 2.18 Echo delay with respect to the specular return versus frequency, of symmetric (s_0 , square) and antisymmetric (a_{0-} , circles) Lamb waves that circumnavigate the spherical shell target. The delays for both the first and second circumnavigations of the a_{0-} wave are shown. 59
- 3.1 Picture of experimental setup. In the foreground is the steel test tank in which time reversal experiments are carried out. The tank is surrounded by an aluminum frame to which positioning equipment is mounted. In the background, behind the tank, is the electronic instrumentation rack and computer workstation controlling the experimental system. 64
- 3.2 Picture of the aluminum spherical shell target suspended in the free field, at the center of the test tank. The target is positively buoyant and is held in place by a

- layer of $\sim 0.5\mu\text{m}$ Scotch 3170 polypropylene packing tape that spans the width of the tank. The tape is clamped in place with manually fashioned acrylic holders.... 65
- 3.3 Picture of the standard aluminum spherical shell target free-standing (to the right) and wrapped in a thin layer of nylon netting that is secured using a piece of monofilament line. 65
- 3.4 Diagram of experimental instrumentation used in time reversal experiments. Experiments are performed both with targets suspended in the free field beneath a layer of transparent tape and buried in a container filled with a sediment phantom. This illustration depicts the configuration used for buried target experiments. 66
- 3.5 System diagram for generation of the calibration filter used in scattering and time reversal experiments. 71
- 3.6 Waveforms and associated spectra from tests of the normalization procedure for the Panametrics V-303 unfocussed broadband, $Q\sim 2$, piston transducer nominally centered at 1 MHz. (a.) Linear chirp driving voltage sent to the transducer in which the transmitted pulse is directed normally at the pressure release water surface. (b.) Magnitude spectrum of (a). (c.) Transducer voltage for the first reflection from the pressure release tank surface. (d.) Solid line is the magnitude spectrum of (c) and the dashed line is the magnitude response of the inverse filter used in the transducer calibration procedure. (e.) Waveform (c) after application of the inverse filter. (f.) Magnitude spectrum of (e). The amplitude in all subplots is normalized to the maximum value and plotted on a linear scale. 72
- 3.7 Response of the system calibration filter used in time reversal experiments plotted versus frequency. (a.) The thin dashed line is the magnitude response of the Weiner filter. The thick solid line is the magnitude response of the final calibration filter designed using the Yule Walker method. (b.) Same as (a) but the phase response of the Yule Walker filter is plotted over the same frequency range. (c.) The phase delay and group delay of the Yule Walker filter. The solid gray box in both subplots shows the full bandwidth of interest. 73
- 3.8 Magnitude of the pressure field radiated from a circular baffled piston for a driving frequency of 1.6 MHz. The piston is 6.35 mm in radius, the same radius as the Panametrics V-303 transducer used in time reversal experiments. (a.) Magnitude of the pressure field as a function of axial and radial distance from the center of the piston. Thin black lines represent contours of constant pressure magnitude, marking relative values of 0.5, 0.25, and 0.125. Vertical white lines intersect the on-axis location of the nearfield distance, the standing distance used in experiments, and the Rayleigh distance of the piston; the positions of these lines all scale linearly with frequency (see equation (3.76)). (b.) The solid black line represents the magnitude of the pressure distribution along the central axis of the piston. Circles represent

measured values, normalized to the mean value of the predicted pressure at the same axial standing distance. The piston is positioned at the left side of each figure. Predicted values in both plots are normalized to their respective maximum value.. 78

- 3.9 Magnitude spectra of waveforms backscattered from the free water surface given a linear chirp spanning 0.4-1.6 MHz, the useable bandwidth of the calibrated transducer. The standing distance between the transducer's face and the free water surface is varied in steps of 0.5 cm between 8 cm and 12 cm. 79
- 3.10 Magnitude spectra of waveforms backscattered from the free water surface given a linear chirp spanning 0.4-1.6 MHz, the useable bandwidth of the calibrated transducer. The transducer is positioned at a standing distance of 10 cm and angles of incidence range from 0-20 degrees..... 81
- 3.11 Transducer directivity factor as a function of angle for frequencies of 0.4, 1, and 1.5 MHz. 82
- 3.12 Magnitude spectra of waveforms backscattered from the glass bead simulated sediment surface given a linear chirp spanning 0.4-1.6 MHz, the useable bandwidth of the calibrated transducer. The transducer is positioned at a standing distance of 10 cm and angles of incidence range from 0-20 degrees..... 82
- 3.13 Waveforms and associated spectra from the target characterization experiment. (a.) Magnitude of the calculated monostatic far-field form function for the aluminum spherical shell target used in time reversal experiments versus ka . (b.) The dashed line is the magnitude spectrum of the return from the target in which a linear chirp spanning 0.5 to 2 MHz is used for interrogation. The solid line is the magnitude spectrum of the response of the target generated from a numerical simulation. Both spectra are normalized to their respective values at 800 kHz. (c.) The dashed and solid lines are the time domain waveforms associated with the spectra in (b) of experiment and simulation, respectively. Both waveforms are normalized to their maximum value..... 88
- 3.14 Additional time traces from the target characterization experiment. Measured results are shown as dashed lines while those generated from numerical simulation are presented as a solid line. (a.) Return from the standard spherical shell target given a 2 cycle, 1 MHz sine wave incident waveform. (b.) Return from the target given a 23 μs duration linear frequency modulated (LFM) chirp spanning 0.4-1.6 MHz used as an incident waveform. (c.) Return from the target given a 45 μs duration LFM chirp spanning 0.4-1.6 MHz used as an incident waveform. 89
- 3.15 Normalized mean squared error between a measurement and simulation of the target response over the 650-1650 kHz frequency range. The density of aluminum 3003

used in the simulation is varied within its measured uncertainty. The vertical dashed line marks the density value reported by the supplier of the target.	90
3.16 Normalized mean squared error between a measurement and simulation of the target response over the 650-1650 kHz frequency range. The elastic modulus of aluminum 3003 used in the simulation is varied $\pm 5\%$ from its nominal value, which is marked by the vertical dashed line.....	91
3.17 Picture of the setup used in sediment phantom characterization experiments. Two Panametrics V-305 unfocussed piston transducers are press-fit into steel baffles. They are aligned axially at normal incidence on either side of a sample of the sediment phantom described in section 3.1. The separation distance between the two baffles can be varied precisely, for one is mounted with sleeve bearings to rods that run the length of the rig.....	97
3.18 Diagram of experimental instrumentation used to characterize the acoustic properties of the sediment phantom used in time reversal experiments.	98
3.19 Sound speed in distilled water as a function of frequency. The solid line is the speed predicted from a measurement of the water temperature. Small dots depict values estimated through time of flight measurements. The normalized root mean square error between the predicted and measured results is reported on the figure.....	99
3.20 Magnitude of the pressure field radiated from a circular baffled piston submerged in water as a function of axial and radial position. The piston is 19.05 mm in diameter, the same diameter as the Panametrics V-305 transducers used in sediment characterization experiments. Thin black lines represent contours of constant pressure magnitude and mark relative values of 0.5, 0.25, and 0.125. The thick vertical black lines in each figure represent the aperture over which pressure is numerically integrated to generate the correction factor used in attenuation measurements. The piston is positioned at the left side of each figure. Predicted values in both plots are normalized to their respective maximum value.....	100
3.21 Magnitude ratio of pressure averaged over a receiving aperture placed 10 cm away from a radiating piston, divided by the pressure magnitude at 8 cm. The solid line represents the result predicted from numerical simulations. The small dots represent measured values. The normalized root mean square error between the predicted and measured results is reported on the figure.	101
3.22 Dilatational wave speed in the sediment phantom as a function of frequency. Small dots depict values estimated through time of flight measurements.	102
3.23 Attenuation of dilatational waves in the sediment phantom as a function of frequency. Small dots depict values estimated via through-transmission	

measurements. The solid lines represent error bounds generated from uncertainty over multiple measurements, in the estimation of the diffraction correction, and in the separation distance.	102
4.1 Backscattered returns from the spherical shell target suspended in the free field through multiple iterations of the time reversal procedure. Vertical lines in (a)-(c) depict the position of a $20\mu s$ long time reversal window. (a.) The first backscattered return, iteration 0, where a 2 cycle 1 MHz sine waveform is used for interrogation. (b.) Backscattered return at iteration 10 of the time reversal procedure. (c.) Backscattered return at iteration 35 of the time reversal procedure. (d.) Waterfall plot of magnitude spectra of signals within the time reversal window for iterations 0 through 50 normalized to the maximum spectral magnitude at the final iteration. The spectra from (a)-(c) are highlighted with color lines.	106
4.2 Target returns given a $20\text{-}\mu s$ duration linear frequency modulated chirp interrogation waveform. Returns are generated in the presence of varying levels of additive Gaussian white noise. Panels (a.)-(d.) are time domain returns for signal to noise ratios of infinity, 15 dB, 12 dB, and 6 dB, respectively. The vertical dashed lines in each figure panel denote the position of a $20\text{ }\mu s$ receive window. The horizontal white dashed lines indicate the root-mean-square amplitude of the noise. Panels (e.)-(h.) present the magnitude spectrum of signals within the receive window in (a)-(d). The vertical dashed lines in these figure panels indicate the half-power bandwidth of the dominant target resonance present.....	112
4.3 Target returns after 50 iterations of time reversal given a $20\text{-}\mu s$ duration linear frequency modulated chirp interrogation waveform used for the initial interrogation. Returns are generated in the presence of varying levels of additive Gaussian white noise. Panels (a.)-(d.) are time domain returns for signal to noise ratios of infinity, 15 dB, 12 dB, and 6 dB, respectively. The vertical dashed lines in each figure panel denote the position of a $20\text{ }\mu s$ receive window. The horizontal white dashed lines indicate the root-mean-square amplitude of the noise. Panels (e.)-(h.) present the magnitude spectrum of signals within the receive window in (a)-(d). The vertical dashed lines in these figure panels indicate the half-power bandwidth of the dominant target resonance present.....	113
4.4 Magnitude spectrum of the numerically generated noise used in simulations of target scattering.	114
4.5 Selected performance curves comparing the efficacy of a single linear frequency modulated (LFM) chirp waveform, 10 iterations of time reversal, and 10 averages of returns from using a LFM chirp interrogation. The percentage of correct dominant target resonance identifications out of 300 trials is presented for signal-to-noise	

ratios ranging from 0-36 dB. The thick solid black lines near the bottom of the figure indicate the number of correct calls without a target in place.....	114
4.6 Performance curves for the single-channel time reversal technique utilizing 0-19 iterations. The percentage of correct dominant target resonance identifications out of 300 trials is presented for signal-to-noise ratios ranging from 0-36 dB. The thick solid black lines near the bottom of the figure indicate the number of correct calls without a target in place.....	115
4.7 Performance curves for the technique where 0-19 coherent averages are performed on target returns given a 20- μ s duration linear frequency modulated chirp. The percentage of correct dominant target resonance identifications out of 300 trials is presented for signal-to-noise ratios ranging from 0-36 dB. The thick solid black lines near the bottom of the figure indicate the number of correct calls without a target in place.....	115
4.8 Performance surface generated by subtracting the percentage of correct calls via the averaging technique from the percent correct calls observed through time reversal. Contours are drawn along values of -10%, 1%, 10% and 20%.	116
4.9 Schematic of how the relative window time, t_r , is defined in time reversal experiments. $\tau_{trigger}$ is the time at which a trigger event occurs. τ_{window} is the duration of the time reversal window. τ_{target} is the time at which a transmitted wave will interact with the target. (a.) A 3 cycle sine wave is transmitted at a scattering target and the echo is received. (b.) Returns from arbitrarily shaped transmissions appear to be centered within the time reversal window.....	118
4.10 Echo spectral magnitude versus frequency and time from a numerical experiment where the center of a 5 μ s duration time reversal window is shifted in steps of 0.5 μ s from relative window times, t_r , of -30 μ s to 60 μ s. Spectra from iteration 0 and iteration 50 are shown in (a) and (b), respectively. The intensities in each are normalized to the maximum value in (b). Wave packets are labeled according to their type. Incident waves approach the target from the left side of the figure.	122
4.11 The black solid line represents the maximum spectral magnitude recorded at each relative window time in Figure 4.10b, iteration 50. The solid gray line presents the same results for Figure 4.10a, iteration 0. Both results are normalized to the maximum value at iteration 50. Vertical dashed lines highlight the time locations of local maxima. The relative time between maxima is also presented.	123

- 4.12 Waveforms from iteration 50 of time reversal appearing at relative window times, t_r , marked by vertical dashed lines in Figure 4.11. The vertical dashed lines in (a)-(f) outline the location of a $5\mu\text{s}$ duration time reversal window. Panels (g)-(l) present the magnitude spectra of signals within the time reversal window in (a)-(f). Vertical dashed lines in these figure panels mark the location of the peak spectral magnitude. The vertical axes in time and frequency domain waveforms are presented in arbitrary units on the same scale. 124
- 4.13 Echo spectral magnitude versus frequency and time from a laboratory tank experiment where the center of a $5\mu\text{s}$ duration time reversal window is shifted in steps of $0.5\mu\text{s}$ from relative window times, t_r , of $-30\mu\text{s}$ to $60\mu\text{s}$. Spectra from iteration 0 and iteration 50 are shown in (a) and (b), respectively. Wave packets are labeled according to their type. Incident waves approach the target from the left side of the figure. 125
- 4.14 Echo spectral magnitude versus frequency and time where the center of the time reversal window is shifted in steps of $0.5\mu\text{s}$ from relative window times, t_r , of $-30\mu\text{s}$ to $60\mu\text{s}$. Panels (a)-(h) present results for window sizes ranging from $5-40\mu\text{s}$. Data is normalized to the maximum value within each figure panel. Incident waves approach the target from the left side of the figure. 130
- 4.15 The maximum spectral magnitudes recorded at each relative window time in corresponding panels from Figure 4.14. Vertical dashed lines highlight the time locations of local maxima of interest. Results are normalized to the maximum value within each figure panel. The letters superimposed on the dashed lines in (d) are associated with the corresponding panels in Figure 4.16. 131
- 4.16 Waveforms from iteration 50 of time reversal appearing at relative window times, t_r , marked by vertical dashed lines in Figure 4.15d. The vertical dashed lines in (a)-(f) outline the location of a $5\mu\text{s}$ duration time reversal window. Panels (g)-(l) present the magnitude spectra of signals within the time reversal window in (a)-(f). Vertical dashed lines in these figure panels mark the location of the peak spectral magnitude. The vertical axes in the time and frequency domain waveforms are presented in arbitrary units on the same scale. 132
- 4.17 Schematic of the physical setup for time reversal experiments with multiple targets present. The schematic is not drawn to scale. 137
- 4.18 (a) Magnitude of the calculated monostatic far-field form function for the aluminum spherical shell target used in time reversal experiments versus frequency. (b) Magnitude of form function of the solid stainless steel sphere plotted versus frequency. 137

- 4.19 Echo spectral magnitude versus frequency and time, where the center of the time reversal window is shifted in steps of $0.5\mu s$ from relative window times, t_r , of $-30\mu s$ to $60\mu s$. Panels (a)-(d) present results at iteration 0 for window sizes ranging from $5-20\mu s$ with both the aluminum shell target and solid sphere targets both in place. Panels (e)-(h) are the same as (a)-(d) but show iteration 50. Panels (i)-(l) present results at iteration 50 with only the solid stainless steel target in place. Data is normalized to the maximum value within each panel except (a)-(d) which are normalized to the maximum values in (e)-(h), respectively. 138
- 5.1 (a.) Magnitude of the calculated monostatic far-field form function for the aluminum spherical shell target used in time reversal experiments versus frequency. (b.) Magnitude of calculated form function of the aluminum shell target when loaded with the properties of the glass bead sediment. The shaded gray region highlights the frequency bandwidth of the time reversal system..... 144
- 5.2 Schematic of the assumed configuration of for buried target transient scattering simulations. The schematic is not drawn to scale. 145
- 5.3 Experimentally generated waveform received after interrogating the 2 cm deep buried aluminum shell target with a 2 cycle 1 MHz sine wave. Arrows highlight various types of returns. The return from the sediment surface is clipped so that target returns are clearly visible. 146
- 5.4 Waveform generated from the buried target numerical scattering simulation by interrogating the 2 cm deep buried aluminum shell target with a 2 cycle 1 MHz sine wave. Arrows highlight various types of returns. The return from the sediment surface is clipped so that target returns are clearly visible. 146
- 5.5 Convergence plot for the standard shell target buried 2 cm beneath the surface of the sediment through successive iterations of the time reversal procedure. The transducer is at normal incidence to the surface of the sediment. Vertical lines in (a)-(c) depict the position of a $20\mu s$ long time reversal window. (a.) The first backscattered return, iteration 0, where white noise $20\mu s$ in duration is used for interrogation. (b.) Backscattered return at iteration 10 of the time reversal procedure. (c.) Backscattered return at iteration 35 of the time reversal procedure. (d.) Waterfall plot of magnitude spectra of signals within the time reversal window for iterations 0 through 50 normalized to the maximum spectral magnitude at the final iteration. The spectra from (a)-(c) are highlighted. 148
- 5.6 Signal to noise ratio of returns within a $20\mu s$ long time reversal window as a function of relative window time, t_r , where white noise $20\mu s$ in duration is used to

- initiate the process. The black solid and blue dashed lines, representing iteration 0 and iteration 50, respectively, are computed over a frequency band of 0 to 2 MHz, encompassing the full bandwidth of the transducer used. The solid red line is computed from iteration 50 over a frequency band of 0.75 MHz to 1.2 MHz within which lies the dominant resonant wave mode of the buried target..... 151
- 5.7 Experimentally generated returns from iteration 50 of the time reversal procedure with the target buried at different depths in the glass bead sediment. The vertical dashed lines depict the position of a $20\mu s$ long time reversal window. (a) – (d) Time domain returns with center of the target buried at 1.5 cm, 2 cm, 2.5 cm, and 4 cm depths, respectively. (e) Return at iteration 50 with no target in place. Time domain waveforms are normalized to the peak amplitude in (d) and are all presented on the same scale. (f) – (j) Fourier transforms of signals within the time reversal window from (a) – (e). Frequency domain results are normalized to the peak spectral magnitude in (f) and are all presented on the same scale. 154
- 5.8 Numerically generated returns from iteration 50 of the time reversal procedure with the target buried at different depths in the glass bead sediment. The vertical dashed lines depict the position of a $20\mu s$ long time reversal window. (a) – (d) Time domain returns with center of the target buried at 1.5 cm, 2 cm, 2.5 cm, and 4 cm depths, respectively. (e) Return at iteration 50 with no target in place. Time domain waveforms are normalized to the peak amplitude in (d) and are all presented on the same scale. (f) – (j) Fourier transforms of signals within the time reversal window from (a) – (e). Frequency domain results are normalized to the peak spectral magnitude in (f) and are all presented on the same scale. 155
- 5.9 Results from an experiment where the center of the time reversal window is shifted in steps of $1\mu s$ from relative window times, t_r , of $-30\mu s$ to $60\mu s$ over the standard shell target buried at 2 cm depth. The intensity along the vertical axis represents the magnitude spectrum of the signal within the time reversal window. (a)-(d) present results at iteration 0 for window sizes of 8, 14, 20, and $26\mu s$. (e)-(h) present the same results but for iteration 50. Data is normalized to the maximum value for $t_r > 25\mu s$ within each row. The transducer is aligned at normal incidence to the surface of the sediment and incident waves approach the target from the left side of the figure. 159
- 5.10 Physical setup for time reversal experiments where the angle of incidence is varied. (a.) Picture of the physical setup showing the transducer aligned over the sediment, within which the standard shell target is buried. (b.) Schematic showing the cross-section of the sediment and target. The schematic is not drawn to scale..... 163
- 5.11 Time traces and spectra at iteration 50 of time reversal for incident angles of 0, 10, and 20 degrees. Vertical lines in the time traces highlight the location of the time

reversal window. Spectra are computed from the signal within the window and are normalized to the maximum value in (b).....	164
5.12 Magnitude spectra of reflections from the surface of the sediment for incident angles of 0, 10, and 20 degrees. A long linear chirp spanning the full system bandwidth is as the transmitted waveform in each case.....	164
5.13 SNR plot summarizing the results of a window parameter study conducted with the transducer at normal incidence. In the first two rows, the intensity of pixels is proportional to the square root of the energy within the time reversal window over the specified frequency band specified at the top of each column. The bottom row the pixel intensity is proportional to the signal-to-noise ratio observed. The vertical axis in each figure panel corresponds to the window size. The horizontal axes correspond to the relative window time.....	167
5.14 Results from an experiment where the center of the time reversal window is shifted in steps of $1\mu s$ from relative window times, t_r , of $-30\mu s$ to $60\mu s$ over the standard shell target buried at 2 cm depth. The intensity along the vertical axis represents the magnitude spectrum of the signal within the time reversal window. (a)-(d) present results at iteration 0 for window sizes of 8, 14, 20, and $26\mu s$. (e)-(h) present the same results but for iteration 50. Data is normalized to the maximum value for $t_r > 25\mu s$ within each row. The transducer is aligned at 10 degree incidence to the surface of the sediment and incident waves approach the target from the left side of the figure.	171
5.15 SNR plot summarizing the results of a window parameter study conducted with the transducer at 10 degree incidence. In the first two rows, the intensity of pixels is proportional to the square root of the energy within the time reversal window over the specified frequency band specified at the top of each column. The bottom row the pixel intensity is proportional to the signal-to-noise ratio observed. The vertical axis in each figure panel corresponds to the window size. The horizontal axes correspond to the relative window time.....	172
5.16 Convergence plot for the standard shell target buried 2 cm beneath the surface of the sediment through successive iterations of the time reversal procedure. The transducer is at 10 degree incidence to the surface of the sediment. Vertical lines in (a)-(c) depict the position of a $20\mu s$ long time reversal window. (a.) The first backscattered return, iteration 0, where white noise $20\mu s$ in duration is used for interrogation. (b.) Backscattered return at iteration 10 of the time reversal procedure. (c.) Backscattered return at iteration 35 of the time reversal procedure. (d.) Waterfall plot of magnitude spectra of signals within the time reversal window for iterations 0 through 50 normalized to the maximum spectral magnitude at the final iteration. The spectra from (a)-(c) are highlighted with solid black lines.	173

- 5.17 Results from an experiment where the center of the time reversal window is shifted in steps of $1\mu s$ from relative window times, t_r , of $-30\mu s$ to $60\mu s$ over the standard shell target buried at 2 cm depth. The intensity along the vertical axis represents the magnitude spectrum of the signal within the time reversal window. (a)-(d) present results at iteration 0 for window sizes of 8, 14, 20, and $26\mu s$. (e)-(h) present the same results but for iteration 50. Data is normalized to the maximum value for $t_r > 25\mu s$ within each row. The transducer is aligned at 20 degree incidence to the surface of the sediment and incident waves approach the target from the left side of the figure. 175
- 5.18 Convergence plot for the standard shell target buried 2 cm beneath the surface of the sediment through successive iterations of the time reversal procedure. The transducer is at 20 degree incidence to the surface of the sediment. Vertical lines in (a)-(c) depict the position of a $20\mu s$ long time reversal window. (a.) The first backscattered return, iteration 0, where white noise $20\mu s$ in duration is used for interrogation. (b.) Backscattered return at iteration 10 of the time reversal procedure. (c.) Backscattered return at iteration 35 of the time reversal procedure. (d.) Waterfall plot of magnitude spectra of signals within the time reversal window for iterations 0 through 50 normalized to the maximum spectral magnitude at the final iteration. The spectra from (a)-(c) are highlighted with solid black lines. 176
- 5.19 SNR plot summarizing the results of a window parameter study conducted with the transducer at 20 degree incidence. In the first two rows, the intensity of pixels is proportional to the square root of the energy within the time reversal window over the specified frequency band specified at the top of each column. The bottom row the pixel intensity is proportional to the signal-to-noise ratio observed. The vertical axis in each figure panel corresponds to the window size. The horizontal axes correspond to the relative window time..... 177
- 5.20 Plot summarizing the results of a window parameter studies for all angles of incidence investigated. The pixel intensity in all figures is proportional to the signal-to-noise ratio observed. 179
- 5.21 Wave mode images generated from raster scanning the transducer at normal incidence over an area of sediment containing an aluminum spherical shell (located at $[x, y] = [15, 30]$ mm) as well as a solid stainless steel sphere of the same diameter (located at $[x, y] = [30, 15]$ mm). Pixels in the images represent the energy within the time reversal window, at a specified transducer position, over a band-limited frequency range. Figures (a)-(d) are generated from the backscattered returns at iteration 0 over the full system bandwidth, shifting the time reversal window in $2\mu s$ steps from $23\mu s$ to $29\mu s$ relative to the specular return from the sediment

surface. Figures (e)-(h) are generated from backscattered returns after 50 iterations of the time reversal procedure, at the same relative window times as in Figures (a)-(d). Figures (i)-(l) and (m)-(p) are the same as in (e)-(h), but are defined over a band limited frequency range of 500-600 kHz and 750-1200 kHz, respectively. The energies displayed in all images are normalized to the maximum value in (n) and are presented on the same linear scale where white represents values greater than or equal to the maximum and black represents zero.	184
5.22 Wave mode images at iteration 50, generated from the same conditions as in Figure 8n, but with only the aluminum spherical shell target in place. The energy in (a) is band-limited to a frequency range of 750-950 kHz and (b) encompasses the 750-1200 kHz frequency range.	185
5.23 Energy spectra from data obtained along slices taken from the x-axis of Figure 9b at a transducer position of 22 mm for iteration 0 (Figure 10a) and iteration 50 (Figure 10b). The intensities in each image are normalized to their respective maximum values. In the images, white represents the maximum value and black represents the minimum value.	185
6.1 Schematic of the electronic instrumentation and configuration used in field experiments. The target is positioned on the axis of the projector and hydrophone with the weights on either side of the target as shown. Separate transmit and receive paths are shown with solid and dashed lines, respectively.	190
6.2 Picture of the experimental apparatus employed in field experiments. (a.) Sawhorse shaped stand on which the projector and hydrophone are mounted. The test pond is visible in the background. (b.) Stainless steel spherical shell target used in experiments. Weights are clamped to eyehooks located at the poles of the sphere.	191
6.3 Waveforms and associated spectra from tests of the calibration procedure for the system employed in field experiments. (a.) Linear chirp driving voltage sent to the projector in which the transmitted pulse is directed normally at the sediment surface and is received at mid-path by the hydrophone. (b.) Magnitude spectrum of (a). (c.) Voltage of the received waveform (d.) Magnitude spectrum of (c). (e.) Waveform in (c) after application of the calibration filter. (f.) Magnitude spectrum of (e). The amplitude/magnitude in all subplots is in arbitrary units.....	192
6.4 Scattering responses of the spherical shell of the same size and composition as the target used in field experiments (a.) Magnitude of the calculated monostatic far-field form function for the target loaded with water. (b.) Magnitude of calculated form function of the steel shell when loaded with the properties of water saturated medium grained sand, treated as a fluid. Both form functions are shown over the frequency bandwidth of the calibrated system used in experiments.....	195

6.5	Echo delay with respect to the specular return versus frequency, of symmetric, s_0 , Lamb waves that circumnavigate the spherical shell. The delays for both the first and second circumnavigations of the waves are shown. The solid lines and dashed lines correspond to cases where the target is loaded with water and sediment, respectively.	196
6.6	Convergence plot for the shell target in the free field through successive iterations of the time reversal procedure. The window is located at the expected position of the first s_0 Lamb wave circumnavigation. Vertical lines in (a)-(c) depict the position of a $60\mu s$ long time reversal window. (a.) The first backscattered return, iteration 0. (b.) Backscattered return at iteration 4 of time reversal. (c.) Backscattered return at iteration 14 of the time reversal procedure. (d.) Waterfall plot of magnitude spectra of signals within the time reversal window for iterations 0 through 14 normalized to the maximum spectral magnitude at the final iteration. The spectra from (a)-(c) are highlighted with lines of the same shading.....	198
6.7	Convergence plot for the shell target in the free field through successive iterations of the time reversal procedure. The window is located at the expected position of the second s_0 Lamb wave circumnavigation. Vertical lines in (a)-(c) depict the position of a $60\mu s$ long time reversal window. (a.) The first backscattered return, iteration 0. (b.) Backscattered return at iteration 4 of time reversal. (c.) Backscattered return at iteration 11 of the time reversal procedure. (d.) Waterfall plot of magnitude spectra of signals within the time reversal window for iterations 0 through 11 normalized to the maximum spectral magnitude at the final iteration. The spectra from (a)-(c) are highlighted with lines of the same shading.....	199
6.8	Convergence plots without and with the shell target buried at 6 inches. The window is located at the expected position of the first s_0 Lamb wave circumnavigation. Vertical lines in (a-c) & (e-g) depict the position of a $60\mu s$ long time reversal window. (a,e.) The first backscattered return, iteration 0. (b,f.) Backscattered return at iteration 4 of time reversal. (c,g.) Backscattered return at iteration 18 of the time reversal procedure. (d,h.) Waterfall plot of magnitude spectra of signals within the time reversal window for iterations 0 through 18 normalized to the maximum spectral magnitude at the final iteration. The spectra from (a-c) & (e-g) are highlighted with lines of the same shading.....	202
6.9	Magnitude and phase response of the high pass filter applied to returns in select buried target field experiments.	203
6.10	Convergence plots without and with the shell target buried at 6 inches with application of the high pass filter. The window is located at the expected position of	

	the first s_0 Lamb wave circumnavigation. Vertical lines in (a-c) & (e-g) depict the position of a $60\mu s$ long time reversal window. (a,e.) The first backscattered return, iteration 0. (b,f.) Backscattered return at iteration 4 of time reversal. (c,g.) Backscattered return at iteration 18 of the time reversal procedure. (d,h.) Waterfall plot of magnitude spectra of signals within the time reversal window for iterations 0 through 18 normalized to the maximum spectral magnitude at the final iteration. The spectra from (a-c) & (e-g) are highlighted with lines of the same shading.	204
6.11	Plots showing time traces at the final iteration for buried target time reversal experiments where the high pass filter is employed. (a.)-(c.) Results generated without a target in place. (d.)-(f.) Results generated with the target buried at 6 inch depth. In each row, the position of the time reversal window is highlighted with a solid gray box. From the top row to the bottom row, window positions correspond to the expected time location of the specular return, the first s_0 Lamb wave circumnavigation, and the second s_0 Lamb wave circumnavigation. Convergence frequencies are given in each plot.....	205
A.1	Schematic of the geometry for the scattering of a plane acoustic wave by an elastic sphere submerged in an infinite fluid medium.	217
A.2	Far-field acoustic form function of the solid stainless steel target decomposed into the individual components of its partial wave series solution after subtraction of the partial waves from a rigid sphere. (a.) Magnitude of the far-field acoustic form function versus frequency. (b.)-(l.) Partial waves $n = 0$ to $n = 10$, magnitude versus frequency, after background subtraction. The vertical axis is normalized and presented on the same scale for all subfigures. The gray shaded region depicts the frequency range of interest for the current work. Within subfigures b-l is plotted the angular dependence of each partial wave. In (d.) resonance types are identified with arrows.....	224
A.3	Phase and group velocities of Rayleigh ($l=1$) and whispering gallery ($l=2$) waves that propagate on a solid stainless steel target. The wave velocities are normalized by the sound speed of water, $c = 1476$ m/s, and plotted versus frequency over a range relevant to the current work. Phase velocities of the Rayleigh wave and the first whispering gallery wave are shown as circles and squares, respectively. The phase velocity results are interpolated with a solid line.	226
A.4	Echo delay with respect to the specular return versus frequency, of the first circumnavigation of Rayleigh ($l=1$) and whispering gallery ($l=2$) waves that circumnavigate the solid stainless steel target.	227

A.5	Schematic of the geometry for the scattering of a plane acoustic wave by an elastic sphere submerged in an infinite fluid medium.	228
A.6	Schematic depicting a flat plate <i>in vacuo</i> relevant to the calculation of Lamb wave dispersion curves.....	238
A.7	Dispersion curves for the phase velocity of Lamb waves on a plate. Symmetric Lamb waves are presented as solid lines whereas asymmetric Lamb waves are presented as dashed line. The phase velocity is normalize to that of water with $c = 1479$ m/s and plotted versus the dimensionless parameter kh	242
B.1	Schematic of a thought experiment where a windowed target echo is retransmitted with and without performing a time reversal operation. (a.) A short pulse centered at a delay equal to one half the length of the receive window is transmitted. The receive window is positioned with the echo at the rightmost side of the window. (b.) Retransmission of the windowed echo without time reversal. (c.) Retransmission of the echo after a time reversal operation has been performed.....	245
B.2	Results of a window shifting simulation with and without performing a time reversal operation. The receive window is shifted from relative window times of $-30\mu s$ to $60\mu s$. The average power within the time reversal window is computed at iteration 50. The numerical experiment is repeated for receive window sizes ranging from $4\mu s$ to $60\mu s$. (a.) Results generated from application of a time reversal operation. (b.) Results generated without performing a time reversal operation. The intensity within each subfigure is scaled to the maximum value recorded in (b).....	246

Chapter 1

Introduction

“Nothing has such power to broaden the mind as the ability to investigate systematically and truly all that comes under thy observation in life.”

Marcus Aurelius Antoninus, Meditations

It is well known that resonance frequencies of oscillation are observed in many natural and manmade systems. Perhaps the earliest recorded discussion of a resonant system is that of Galileo Galilei who, in 1602, wrote a letter within which he hypothesized the isochronous motion of a pendulum [1]. When a mechanical system is driven at resonance, the energy stored within the system dissipates slowly over time. This results in the system responding with maximal amplitudes of oscillation, a phenomenon that is exploited in many fields of science and engineering. A number of examples within the realm of acoustics are especially noteworthy. For example, in ultrasonic sensing and imaging applications, bubbles driven at or near resonance can be used to enhance the scattering contrast of tissue [2]. Acoustically exciting the resonance response of landmines, and the layer of soil beneath which they are buried, can significantly improve

the probability of detection [3]. In the realm of underwater acoustics, if the resonance response of a structure is excited using SONAR (Sound Navigation and Ranging) signals, it can lead to a marked effect on the scattered field, making it easier to identify the structure. This is true for target objects in the free field [4] and also for those buried in sediment at the ocean bottom [5-7], the latter of which are especially difficult to characterize.

In shallow water coastal regions (< 60 meters depth), the turbulent nature of waves and tidal currents can lead to the burial of targets resting on the seafloor. Using current technology, these buried targets are especially difficult to detect and identify due to strong returns from the water-sediment interface, attenuation of sonar signals in the sediment, and the presence of coherent returns from clutter in the ocean bottom [8]. Therefore, novel techniques are needed to extend the maximum detection depth and improve target identification. Recent advances in the field of time reversal acoustics show promise as a possible solution.

Time reversal in acoustics has its foundation based on the principle of reciprocity, described by Lord Rayleigh in the second volume of his *The Theory of Sound*. If sound waves are excited at a point A, the resulting velocity potential at a second point B is the same both in magnitude and phase, as it would have been at A, had B been the source of sound [9]. The wave equation is a second order partial differential equation in both space and time, and thus its solution is valid for positive and negative values of the time variable. The most common example of acoustic time reversal, depicted schematically in Figures 1.1 and 1.2, is based on an extension of these two principles. A point source and

an array of transducers, also called a “phase conjugate array” or “time reversal mirror”, are located some distance apart in the free-field, which can consist of either a homogeneous or inhomogeneous medium. A two-step process ensues. First, the point source emits a wave that travels through the medium and is received by the array, as in Figure 1.1. The temporal order of the signal received by each element of the array is then reversed and re-transmitted. The re-transmitted waves then travel through the medium, interfere constructively and destructively, and converge upon the location of the point source, as in Figure 1.2. If the point source were to be replaced with a small scattering object, time reversal and retransmission of received signals scattered from the object will result in a similar focusing effect. This can lead to significant improvements in the signal-to-noise ratio of scattered returns.

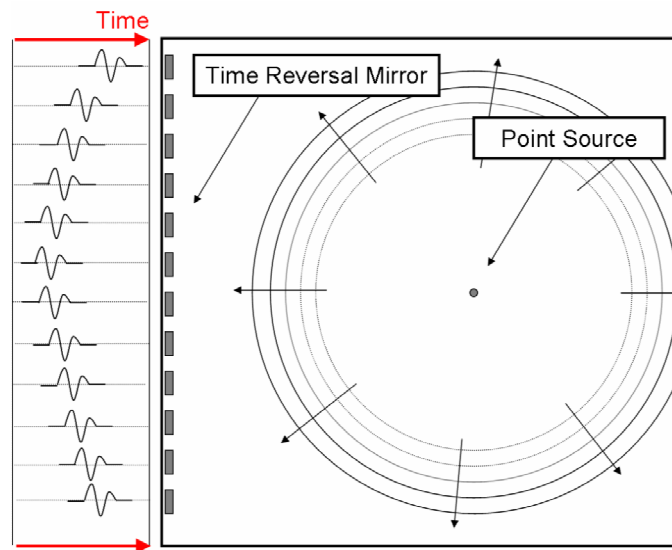


Figure 1.1: Schematic depiction of array based time reversal, Step I. A point source emits a pulse of acoustic energy that travels through the propagation medium and is received by each element of a time reversal mirror (array).

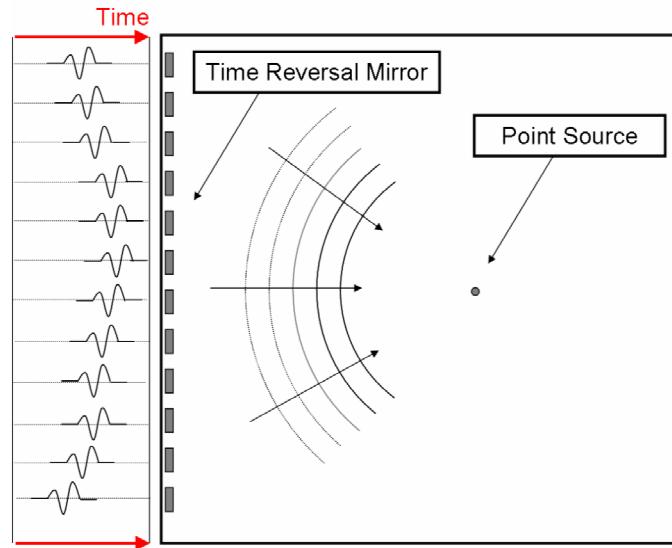


Figure 1.2: Schematic depiction of array based time reversal, Step II. Signals received at the array are time reversed and retransmitted resulting in a focusing of energy back on the location of the point source.

The first application of time reversal in acoustics is credited to Antares Parvulescu [10], who performed pioneering work in the mid 1960's and developed the matched signal (MESS) processing technique. Through correlation measurements Parvulescu attempted to distinguish between changes in the ocean's time varying response due to environmental fluctuations and those resulting from instability in measurement platforms due to drift, pitch, roll, and yaw. The advantage of Parvulescu's matched signal technique over numerical methods was that the cross-correlation of the ocean's impulse response at two different times could be measured directly from a hydrophone. Evaluating the cross-correlation between two signals would have, at the time, required days of computation.

Parvulescu's technique consisted of the following steps. The impulsive excitation of a source resulted in transmission of a waveform through the ocean. The impulse

response $h_1(t)$ was then recorded at the location of a receiver. The temporal order of the received impulse was reversed to produce what Parvulescu refers to as the matched signal $h_1(-t)$. The matched signal was sent from the source at some later time and propagated through the ocean which would then have an impulse response $h_2(t)$. The second received signal, $r(\tau)$, is a convolution of the matched signal with the new impulse response of the oceanic propagation path,

$$r(t) = \int h_1(-t)h_2(\tau - t)dt \quad (1.1)$$

This signal is equivalent to the cross-correlation of $h_1(t)$ with $h_2(t)$ and is obtained directly as a signal output from a hydrophone. If the ocean environment is stationary, the receiver would measure the autocorrelation of $h_1(t)$. Measuring the cross-correlation of impulses sent between a source and receiver at different times yielded a method of tracking changes in the ocean's impulse response. Out of a necessity to perform correlation measurements quickly, Parvulescu employed acoustic time reversal for the first time.

Widespread application of time reversal was first observed in the field of optics where phase-conjugate mirrors redirect a beam of light diverging from a point source to form a wave that retraces the path of the incident wave and converges upon the exact location of the source [11]. The details of optical phase conjugation are beyond the scope of this investigation and the reader is referred to reviews presented in Refs. [11] and [12] for further information. What is important to note is that acousticians realized great potential for the application of phase conjugation and sought to apply the technique in their own field of study.

In 1991, Jackson and Dowling [13] discussed the potential application of time reversal mirrors in underwater acoustics and provided an examination of the theory involved, focusing mainly on continuous “arrays”. In the same year Prada, Wu, and Fink [14] reported further theoretical work on time reversal mirrors along with three fascinating experimental results. Using a time reversal mirror consisting of 64 transducer elements in concave alignment, they demonstrated that time reversing and re-transmitting signals emitted by a hydrophone, located a distance away from the array, resulted in in-phase focusing at the location of the hydrophone; this effect is equivalent to that described in Figures 1.1 and 1.2. A second experiment demonstrated that iteratively time reversing signals backscattered by two thin wire targets resulted in spatial focusing on the larger and more reflective of the two. Their final experiment showed that focusing is achieved through time reversal, even in the presence of an aberrating layer positioned between the array and hydrophone. These three experiments demonstrated the potential of time reversal to achieve spatial focusing, selectively illuminate targets, and increase signal-to-noise in transmissions through an inhomogeneous environment. Many subsequent time reversal experiments consist of extended applications of these three canonical examples. A further discussion of the general principles of time reversal is presented by Fink *et al.* in a set of papers [15, 16] and in a review letter [17].

Iterative time reversal has been extensively studied by Prada who began with an investigation of its property to focus on the most reflective scatterer in a multiple target environment [18]. She then developed the DORT method, which stands for “Decomposition of the Time Reversal Operator.” For a scattering field with multiple

targets present, the DORT method can selectively focus on any specified target, not only the most reflective one as with iterative time reversal [19]. The method is based on a matrix formulation of the inter-element response between transducers in the time reversal mirror when subject to the scattering environment. The matrix is diagonalized and eigenvectors corresponding to non-zero eigenvalues can be used to focus on different targets in the scattering medium. Since the development of the DORT method, it has been applied to characterize Lamb waves in a cylindrical shell suspended in water [20], to selectively focus on targets in a waveguide [21, 22], and to characterize sub-wavelength scatterers [23, 24]. A disadvantage of the DORT method is due to the time consuming experimental procedure for determining the inter-element response of the array. Other investigations have presented alternative methods to achieve selective focusing. These methods use techniques to eliminate the response of stronger scatterers once they have been characterized [25-27]. The most recent advance in iterative time reversal schemes is through the application of Krylov methods to achieve convergence and the isolation of multiple targets much quicker than methods employing power iterations [28].

In addition to investigations in biomedical acoustics such as the tracking of kidney stones [17, 29] and for the focusing of acoustic waves inside the human skull [30], time reversal has been applied extensively in underwater acoustics. In 1998, Kuperman *et al.* implemented a time reversal mirror in the oceanic waveguide and obtained spatial focusing between a source and an array separated by a distance of over 6 kilometers [31]. In a second set of experiments, they were able to achieve spatial focusing over a distance

of 30 km and showed, by successfully refocusing old probe pulses to their original location, that time reversal invariance of the waveguide existed for as long as 1 week [32]. Since these groundbreaking experiments, further developments have been made, especially in the field of underwater acoustic communications [33-36].

Regarding the application of time reversal for the detection and identification of targets submerged in the oceanic waveguide, several investigations have been carried out using array based techniques. Carin *et al.* demonstrated a wideband time reversal technique used to image targets resting on the ocean bottom [37]. This imaging technique requires an accurate forward propagation model of the waveguide. A subsequent set of experiments were conducted by Gaumond *et al.* [38] where the DORT method was used to focus on and estimate the location of an echo-repeater suspended in shallow water during the TREX-04 experiments. Experiments utilizing the DORT technique have also been conducted by Prada *et al.* to isolate submerged targets [39] and to characterize elastic targets in a laboratory scale waveguide [40]. Finally, time reversal has also been shown to enhance the detection of proud (resting on the sediment surface) and partially buried targets through a passive implementation used to generate reflectivity maps of the ocean bottom [41].

In the current investigation, echo enhancement for buried targets is investigated using iterative time reversal with only a single channel time reversal mirror. Previous investigations of single-channel time reversal include the focusing of energy in elastic solids [42] and in cavities [43, 44] as well as in acoustic communications [45]. In the current work, the iterative single-channel time reversal technique consists of exciting a

target with a broadband pulse, digitizing the time-gated return, reversing the signal in time, and using this reversed signal as the source waveform for the next interrogation pulse. As will be seen, the technique automatically generates a matched filter for the spectral response of a buried resonant object and does not rely on spatial focusing to generate an enhancement in return levels. In an experimental study utilizing this technique, Pautet et al. [46] demonstrated enhancement of the spectral response of returns from elastic targets suspended in the free field.

The current work, motivated in part by the work of Pierson [47], is primarily concerned with the efficacy of the single channel time reversal technique for the detection and identification of deeply buried targets, *i.e.* greater than flush buried. Previously, Ref. [47] predicted an increase in the signal-to-noise ratio of returns from a buried target through iterative retransmission of its echo. This work, however, did not consider echo enhancement in the context of resonance scattering. Resonance in acoustic scattering occurs when the harmonic oscillation of a target yields an enhancement in the amplitude of the received echo. In this work, resonance enhancement is reported for a spherical target object located in the free field and fully buried in a sediment phantom consisting of water saturated glass beads. The methodology presented offers a straightforward and inexpensive alternative to array based schemes for isolation of the dominant resonance in the response of a target-object.

In Chapter 2, the theory of acoustic time reversal and resonance scattering is reviewed. Results of system characterization are then presented in Chapter 3; this includes a discussion of methods for transducer calibration, confirmation of the scattering

response of the target employed, and characterization of the acoustic properties of the sediment phantom within which targets are buried. With an understanding of the types of waves that propagate on the targets of interest and a well-characterized system, it is then possible to embark on a comprehensive investigation of the time reversal technique. Chapter 4 presents results from numerical simulations and experiments where time reversal is applied to enhance the scattering response of targets suspended in the free field. Chapter 5 presents results for targets buried in a sediment phantom. Finally, in Chapter 6, results from field experiments are reviewed, where the insight gained in laboratory experiments is applied to detect a stainless steel shell buried in sandy sediment between frequencies of 20-200 kHz. Conclusions are drawn in Chapter 7, which also provides suggestions for future study.

Chapter 2

Theory of Acoustic Time Reversal and Resonance Scattering

“Happy the man who could search out the causes of things.”

Virgil, Georgics

In the first section of this chapter, the theory behind iterative, single-channel time reversal is presented. The time reversal technique is shown to automatically select the appropriate driving frequency with which to excite the dominant resonance in the scattering response of a target object. This section is concluded with a comparison of the time reversal technique and an autocorrelation technique in the presence of stochastic noise. Section 2.2 of this chapter is devoted to a review of relevant acoustic scattering theory; no new theory is presented in this Section. The scattering response of a fluid-filled spherical shell is derived; this is the type of target primarily used in this work. Resonance scattering theory is then used to identify various features in a target's

scattering response and to identify the types of resonances on which the time reversal technique operates.

2.1 Theory of Single-Channel Acoustic Time Reversal

2.1.1 Single-channel, Iterative Time Reversal (ITR)

In this section, a description of the iterative, single-channel time reversal technique is presented in the context of buried object identification. Shown in the first panel of Figure 2.1 is a schematic of an unfocussed piston transducer positioned normally incident to an inhomogeneous medium, within which is buried a scattering target. For the purpose of demonstration, here it is assumed that the location of the target relative to the medium's surface is known *a priori*. The procedure is initiated by interrogating the target with a broadband pulse and waiting for the arrival of a backscattered return. The backscattered waveform consists of a return from the surface of the inhomogeneous medium and a return from the scattering target, as shown schematically in the second panel of Figure 2.1. The portion of the return associated with the scattering target is then selected with a shaded time-gate window and filtered in order to normalize the frequency response of the transducer. The temporal order of this windowed signal is then reversed. As shown in panel 3 of Figure 2.1, this new time-reversed signal is then transmitted where the output signal amplitude is set to a predefined maximum value. Repeating this process iteratively results in convergence of the output waveform to a monotonic signal, characteristic of the dominant resonance in the target's scattering response. Here, the general procedure is summarized with the following steps:

- 1) Interrogate the target with a broadband pulse.
- 2) Sample a portion of the returned signal using a time-domain window.
- 3) Filter the returned signal to account for the frequency response of the system,
which is determined separately via a calibration procedure.
- 4) Reverse the temporal order of the windowed and filtered signal.
- 5) Transmit the new, time-reversed signal, where the transmit signal amplitude is
normalized to a predefined maximum value.
- 6) Repeat steps 2-5 iteratively.

During this procedure, the time reversal window is maintained at the same space-time position as successive iterations are carried out. In order to search for a target whose location is unknown, an additional window-shifting procedure is carried out. This process consists of adjusting the time delay of the time reversal window in discrete steps with respect to a trigger event. At each step, with the window's position stationary, several iterations of the time reversal procedure are carried out. If the target's location is known, this same window-shifting procedure can also be used to selectively enhance different parts of its echo.

The convergence to a single resonance can be understood by the following simplified analysis carried out in the frequency domain for a target in the free field. Assuming that the system under investigation is linear and time invariant, the output waveform at the receiver (i.e. backscattered returns from the target) can be calculated from the product of the input waveform and the system's frequency response (here the target's scattering response). In the following analysis, the transmit-receive response of

the transducer used and the bandwidth limitation of the finite window size are neglected.

Under these assumptions, the first backscattered return from the target is,

$$R_1(\omega) = G(\omega) E(\omega) \quad (2.1)$$

where ω is the angular frequency, $G(\omega)$ is the target's scattering response, and $E(\omega)$ is the waveform initially used to interrogate the target. Subsequently, the first backscattered return will be referred to as iteration zero of the time reversal procedure. A time reversal operation, i.e. reversing the temporal order of a signal, is equivalent to phase conjugation in the frequency domain, and thus,

$$TR\{r_1(t)\} \Rightarrow R_1^*(\omega) = G^*(\omega) E^*(\omega) \quad (2.2)$$

Upon transmission of this time reversed signal, the second backscattered return is,

$$R_2(\omega) = G(\omega) R_1^*(\omega) = [G(\omega) G^*(\omega)] E^*(\omega). \quad (2.3)$$

One notes here that if the interrogation waveform, $E(\omega)$, is de-convolved from the result, the second return is equivalent to an autocorrelation of the target's response. Third and fourth returns will be of the form,

$$R_3(\omega) = G(\omega) [G(\omega) G^*(\omega)] E(\omega) \quad (2.4)$$

and

$$R_4(\omega) = [G(\omega) G^*(\omega)]^2 E^*(\omega), \quad (2.5)$$

respectively. Finally, the results can be generalized as

$$R_{2n-1}(\omega) = G(\omega) [G(\omega) G^*(\omega)]^{n-1} E(\omega) \quad (2.6)$$

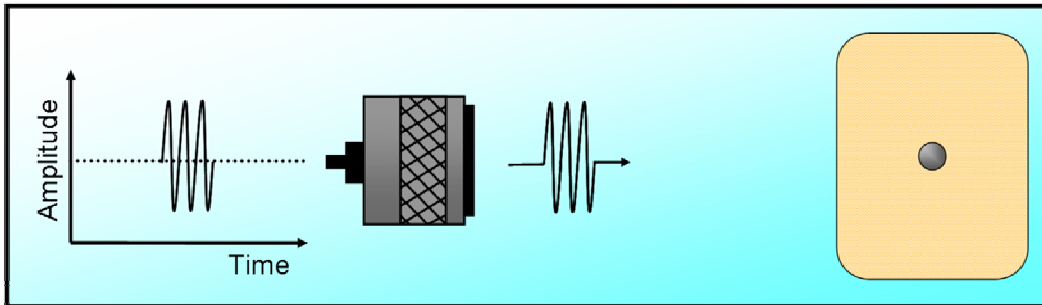
for odd numbered returns and

$$R_{2n}(\omega) = [G(\omega)G^*(\omega)]^n E^*(\omega) \quad (2.7)$$

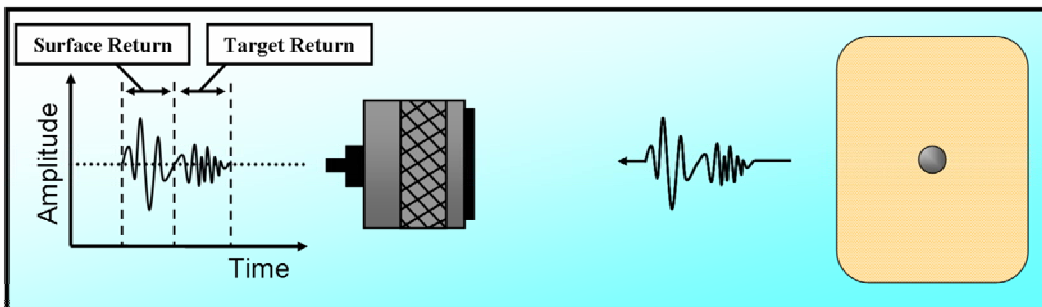
for even numbered returns where $n = 1, 2, \dots, N$. As evident in equations (2.6) and (2.7), successive iteration of the time reversal procedure raises the target's spectral response to a value proportional to the iteration number. This process results in convergence to a narrowband waveform that is characteristic of the dominant resonance in the backscattering response of the target [46-48]. For a discussion of the importance of the time reversal operation, the curious reader is referred to Appendix B.

This approach is best at sensing targets possessing a well-delineated resonance response. For the technique to successfully isolate a target of interest, the dominant spectral peak in its response must be greater in amplitude than those generated by interfaces, clutter, or other false targets in its vicinity. Practically speaking, many commonly encountered manmade objects possess geometrical symmetries that lead to resonances in their scattering response [5-7, 49]. Other objects that do not possess these symmetries will likely have a more broad spectral response. Thus, the time reversal technique will serve to automatically tailor waveforms that preferentially excite manmade targets of interest.

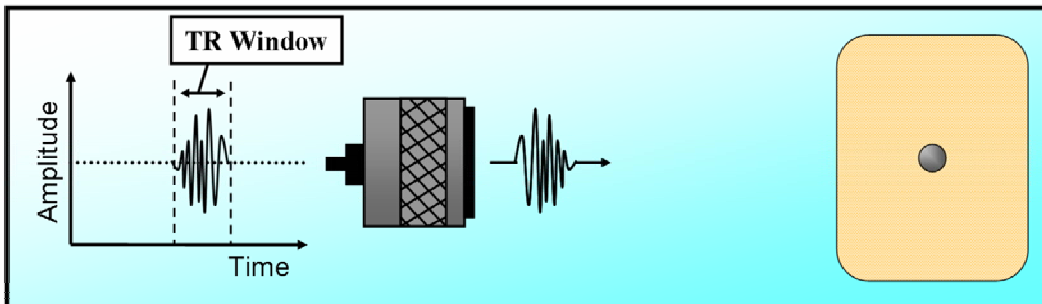
1.) Interrogate target with a broadband pulse



2. & 3.) Sample, window, & calibrate return signal



4. & 5.) Time Reverse, normalize, and transmit windowed signal



6.) Repeat steps 2 - 5 iteratively

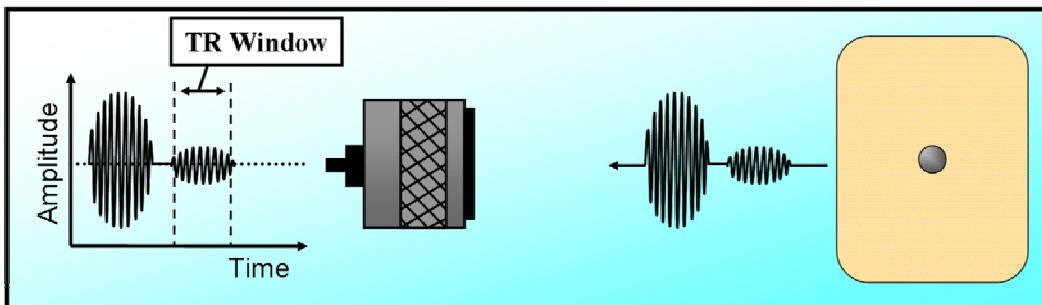


Figure 2.1: Schematic of the iterative, single-channel time reversal procedure

2.1.2 Time Reversal in the Presence of Noise

At this point, one might remark that iterative (active) retransmission of signals is unnecessary. One can simply transmit a single waveform, wait for the arrival of a backscattered return, de-convolve the outgoing waveform from the return, and multiply the result with a phase conjugated version of itself. This process is equivalent to computing the autocorrelation of the target's response,

$$A(\omega) = G(\omega) G^*(\omega). \quad (2.8)$$

Subsequently raising equation (2.8) to a power proportional to the number of time reversal iterations would provide a comparable result to that achieved in equations (2.6) and (2.7), via application the time reversal procedure,

$$R_n(\omega) \propto [A(\omega)]^n = [G(\omega) G^*(\omega)]^n. \quad (2.9)$$

Thus, only a single transmission is required to obtain the same information gained via application of the time reversal technique. However, while this is indeed true under ideal operating conditions, it will not necessarily be the case in the presence of noise.

Given the same operating conditions as in Section 2.1.1, but now with noise added at the output of the system, the first received signal, given an initial outgoing pulse $E(\omega)$, will be of the form

$$R_1(\omega) = G(\omega) E(\omega) + N_1(\omega). \quad (2.10)$$

$G(\omega)$ is the frequency response of the environment, $E(\omega)$ is an arbitrary waveform used for interrogation, and $N_1(\omega)$ is a term used to model additive noise. Here, the noise

is assumed to be stochastic in nature, that is, it is nondeterministic and uncorrelated with the response of the environment. Coherent noise sources are assumed to be a part of the system's frequency response, $G(\omega)$. The passive autocorrelation procedure described at the end of Section 2.1.1 is then applied to equation (2.10) without de-convolution of the input waveform, resulting in the following:

$$A(\omega) = R_1(\omega) R_1^*(\omega) = |G(\omega) E(\omega)|^2 + 2 \operatorname{Re}\{G(\omega) E(\omega) N_1^*(\omega)\} + |N_1(\omega)|^2. \quad (2.11)$$

If instead, a time reversal operation (phase conjugation) is carried out on equation (2.10), it results in a new time reversed waveform,

$$R_1^*(\omega) = G^*(\omega) E^*(\omega) + N_1^*(\omega). \quad (2.12)$$

This is used as the source waveform for a second interrogation. The second return will be of the following form:

$$\begin{aligned} R_2(\omega) &= G(\omega) R_1^*(\omega) + N_2(\omega) \\ &= G(\omega) G^*(\omega) E^*(\omega) + G(\omega) N_1^*(\omega) + N_2(\omega). \end{aligned} \quad (2.13)$$

Subsequent time reversal and retransmission results in a third return,

$$\begin{aligned} R_3(\omega) &= G(\omega) R_2^*(\omega) + N_3(\omega) \\ &= G(\omega) [G(\omega) G^*(\omega)] E(\omega) + G(\omega) G^*(\omega) N_1(\omega) + G(\omega) N_2^*(\omega) + N_3(\omega), \end{aligned} \quad (2.14)$$

and finally a fourth return,

$$\begin{aligned} R_4(\omega) &= G(\omega) R_3^*(\omega) + N_4(\omega) \\ &= [G(\omega) G^*(\omega)]^2 E^*(\omega) + [G(\omega) G^*(\omega)] G(\omega) N_1^*(\omega) + \dots \\ &\quad \dots + [G(\omega) G^*(\omega)] N_2(\omega) + G(\omega) N_3^*(\omega) + N_4(\omega) \end{aligned} \quad (2.15)$$

Through induction, the results can be generalized as follows, for even returns,

$$R_{2n}(\omega) = \left[G(\omega) G^*(\omega) \right]^n E^*(\omega) + \sum_{m=0}^{n-1} \left\{ \left[G(\omega) G^*(\omega) \right]^m G(\omega) N_{2(n-m)-1}(\omega) + \dots \right. \\ \left. \dots + \left[G(\omega) G^*(\omega) \right]^m N_{2(n-m)}(\omega) \right\}; n = 1, 2, \dots, N \quad (2.16)$$

and for odd returns,

$$R_{2n-1}(\omega) = \left[G(\omega) G^*(\omega) \right]^{n-1} G(\omega) E(\omega) + \sum_{m=0}^{n-1} \left\{ \left[G(\omega) G^*(\omega) \right]^m N_{2(n-m)-1}(\omega) + \dots \right. \\ \left. \dots + \left[G(\omega) G^*(\omega) \right]^m G(\omega) H(n-m-2) N_{2(n-m)}(\omega) \right\} \quad (2.17)$$

where m is an index, $n = 1, 2, \dots, N$ is proportional to the iteration number, and $H(x)$ is the Heaviside step function defined as

$$H(x) = \begin{cases} 0, & x < 0 \\ 1, & x \geq 0 \end{cases} \quad (2.18)$$

It is now possible to compare the waveforms generated via the autocorrelation technique and the time reversal technique. If the result of the autocorrelation procedure, equation (2.11), is subsequently raised to the power n , it results in an expression containing the product of the noise term with itself. The procedure amplifies the level of the noise at a similar rate as it amplifies the level of the target's response. Thus, *the dominant target response frequency will only be selected if it is above the level of the noise on the first transmission*. In contrast, with the time reversal procedure of equations (2.16) and (2.17), the terms including noise are incoherent and, as they are combined, will not be amplified as rapidly as the coherent target response. Therefore, for some range of operating conditions, the active time reversal technique should be more robust than the autocorrelation technique at increasing the ratio between the level of the target's

spectrum and the noise. This hypothesis will be investigated subsequently through the use of numerical simulations.

2.2 Review of Acoustic Scattering Theory

The study of sound propagation in the ocean and scattering from submerged objects is a rich field that burgeoned during World War II, when submarines became a prominent force in naval operations [50]. Manmade targets of interest in the ocean typically consist of a shell encasing some other medium, for example, an air filled cavity as in the case of a submarine, or a solid as in the case of a naval mine. Shell targets are known to exhibit distinctive resonance signatures that can be exploited in detection and identification efforts [5-7, 49]. In this work, an air-filled aluminum spherical shell is used as the primary target for scattering experiments. The choice of this target is based on the strong resonant nature of its elastic scattering response over the operational frequency range of scaled laboratory experiments. The types of resonances present in this target are relevant to ongoing efforts in the development of sonar systems and identification schemes. As will be seen, using iterative time reversal with a single-channel transducer, features in the time domain echo return that are associated with specific resonances can be isolated and enhanced to improve efforts in target identification. In this section, the scattering response of a spherical shell target is derived. Resonance scattering theory is then applied to determine the origin of wave mode resonances of the target on which the time reversal technique operates.

2.2.1 Acoustic Scattering from Spheres

The scattering of plane waves from spherical objects has been extensively studied, mainly due to analytical tractability and the insight it lends to more complicated problems. The curious reader is referred to Ref. [51] for a historical survey of early studies. The first treatment of *sound* scattering from a sphere was presented by Lord Rayleigh in 1872 in a paper [52] and subsequently in the second volume of *The Theory of Sound* [52]. Rayleigh considered the interaction of a plane acoustic wave with a rigid immovable sphere at low frequencies, where the wavelength of the incident wave is much larger than the size of the sphere. Scattering from spheres in this regime is now commonly referred to as Rayleigh scattering. Following World War II, a number of papers began to appear in the literature regarding the scattering of sound from penetrable objects, that is, objects that allow the incident sound wave to propagate/couple into their interior. For most practical objects of interest in the ocean, this consideration is especially important, for an incident sound wave can excite the vibratory response of the object, leading to a marked effect on the scattered field. In 1950, Anderson first detailed an exact solution for sound scattering from a fluid sphere, valid for all frequencies [53, 54]. Subsequently, in 1951, Faran took shear into account and determined systems of equations describing the field scattered from solid elastic spheres and cylinders [55]. These early papers are followed by a rich body of literature consisting of theoretical and experimental studies of additional complexity. A partial summary of subsequent investigations includes detailed studies of sound scattering from solid elastic spheres [56-

60] and cylinders [61-64], evacuated (hollow) or fluid-filled shells [65-71], and from suspensions of scatterers [72, 73].

The following analysis considers the scattering of a plane acoustic wave from a fluid-filled elastic spherical shell submerged in an infinite fluid medium. It follows the works of both Gaunard and Uberall [58] and Faran [55]. The elastic wave equation,

$$\rho \left(\frac{\partial^2 \underline{u}}{\partial t^2} \right) = (\lambda + 2\mu) \nabla (\nabla \cdot \underline{u}) - \mu \nabla \times (\nabla \times \underline{u}), \quad (2.19)$$

where ρ is density and \underline{u} is the displacement, governs the propagation of waves within this medium. The constants λ and μ are Lamé's coefficients that describe the elastic properties of the medium, under the assumption that stress is linearly proportional to strain. Taking the divergence of both sides of (2.19) results in the following equation,

$$\frac{\partial^2}{\partial t^2} (\nabla \cdot \underline{u}) = \frac{\lambda + 2\mu}{\rho} \nabla^2 (\nabla \cdot \underline{u}), \quad (2.20)$$

which describes the motion of waves that are irrotational and referred to as longitudinal, dilatational, or P waves [74]. These waves propagate with a speed,

$$c_d = \sqrt{\frac{\lambda + 2\mu}{\rho}}, \quad (2.21)$$

and are characterized by particle displacement in the direction of a wave's propagation.

In contrast, taking the curl of both sides of equation (2.19), results in the following equation,

$$\frac{\partial^2}{\partial t^2} (\nabla \times \underline{u}) = \frac{\mu}{\rho} \nabla^2 (\nabla \times \underline{u}), \quad (2.22)$$

which describes the motion of waves that are referred to as shear, transverse or S waves [74]. These waves propagate with a speed,

$$c_s = \sqrt{\frac{\mu}{\rho}}, \quad (2.23)$$

and are characterized by particle displacement that is perpendicular to a wave's direction of propagation. Solutions of equation (2.19) are found by assuming that the displacement in the medium can be expressed in terms of scalar and vector potential functions φ and Ψ , respectively, such that

$$\underline{u} = \underline{\nabla} \varphi + \underline{\nabla} \times \underline{\Psi}. \quad (2.24)$$

Substituting this expression into equations (2.20) and assuming an $e^{-i\omega t}$ time harmonic convention (where ω is angular frequency and t is time) demonstrates that the scalar potential satisfies the Helmholtz equation,

$$\nabla^2 \varphi + k_d^2 \varphi = 0 \quad (2.25)$$

where $k_d = \omega / c_d$ is the wave number for dilatational waves. This relationship will be subsequently useful in resolving the relevant components of stress in the system.

In spherical coordinates, the gradient and curl operators are as follows:

$$\underline{\nabla} \varphi = \frac{\partial \varphi}{\partial r} \hat{e}_r + \frac{1}{r} \frac{\partial \varphi}{\partial \theta} \hat{e}_\theta + \frac{1}{r \sin \theta} \frac{\partial \varphi}{\partial \phi} \hat{e}_\phi \quad (2.26)$$

$$\begin{aligned} \underline{\nabla} \times \underline{\Psi} = & \frac{1}{r \sin \theta} \left\{ \frac{\partial}{\partial \theta} (\psi_\phi \sin \theta) - \frac{\partial \psi_\theta}{\partial \phi} \right\} \hat{e}_r + \dots \\ & \dots + \left\{ \frac{1}{r \sin \theta} \frac{\partial \psi_r}{\partial \phi} - \frac{1}{r} \frac{\partial}{\partial r} (r \psi_\phi) \right\} \hat{e}_\theta + \frac{1}{r} \left\{ \frac{\partial}{\partial r} (r \psi_\theta) - \frac{\partial \psi_r}{\partial \theta} \right\} \hat{e}_\phi. \end{aligned} \quad (2.27)$$

Here, one notes that for scattering from a sphere there will be no dependence on ϕ and only one of the shear potential's components contributes, $\underline{\Psi} = (0, 0, \psi_\phi)$. Substituting equations (2.26) and (2.27) into equation (2.24) yields the components of displacement in spherical coordinates,

$$u_r = \frac{\partial \varphi}{\partial r} + \frac{\cot \theta}{r} \psi_\phi + \frac{1}{r} \frac{\partial \psi_\phi}{\partial \theta} \quad (2.28)$$

$$u_\theta = \frac{1}{r} \frac{\partial \varphi}{\partial \theta} - \frac{\psi_\phi}{r} - \frac{\partial \psi_\phi}{\partial r} \quad (2.29)$$

$$u_\phi = 0. \quad (2.30)$$

The constitutive relation, between the component of radial stress and displacement, can be expanded as [55]

$$\begin{aligned} \tau_{rr} &= \lambda (\underline{\nabla} \cdot \underline{u}) + 2\mu \left\{ \frac{\partial u_r}{\partial r} \right\} \\ &= -\lambda k_d^2 \varphi + 2\mu \left\{ \frac{\partial^2 \varphi}{\partial r^2} + \frac{\cot \theta}{r} \frac{\partial \psi_\phi}{\partial r} - \frac{\cot \theta}{r^2} \psi_\phi + \frac{1}{r} \frac{\partial^2 \psi_\phi}{\partial r \partial \theta} - \frac{1}{r^2} \frac{\partial \psi_\phi}{\partial \theta} \right\}. \end{aligned} \quad (2.31)$$

where, making use of the identity $\underline{\nabla} \cdot \underline{u} = \underline{\nabla} \cdot \underline{\nabla} \varphi = \nabla^2 \varphi$, equation (2.25) is substituted for the divergence term. The component of stress tangential to the sphere's surface is

$$\begin{aligned} \tau_{r\theta} &= \mu \left\{ \frac{\partial u_\theta}{\partial r} - \frac{u_\theta}{r} + \frac{1}{r} \frac{\partial u_r}{\partial \theta} \right\} \\ &= \mu \left\{ 2 \frac{\partial}{\partial r} \left[\frac{1}{r} \frac{\partial}{\partial \theta} \left(\varphi + \frac{\partial}{\partial r} (r\psi) \right) \right] + k_s^2 \frac{\partial^2 \psi}{\partial \theta^2} \right\} \end{aligned} \quad (2.32)$$

where $k_s = \omega / c_s$ is the wave number for shear waves. With the displacements and constitutive relations defined, it is now possible to proceed with solution of the boundary value problem of interest.

A spherical shell, of outer radius a and inner radius b , is located at the origin of an infinite space consisting of a fluid medium of density ρ_1 and dilatational wave speed c_{d1} . A schematic is presented in Figure 2.2. The shell, filled with a fluid of density ρ_3 and dilatational wave speed c_{d3} , consists of an elastic solid with density ρ_2 , dilatation wave speed c_{d2} , and shear wave speed c_{s2} . An infinite plane acoustic wave is incident upon the shell and approaches from the negative \hat{e}_z direction.

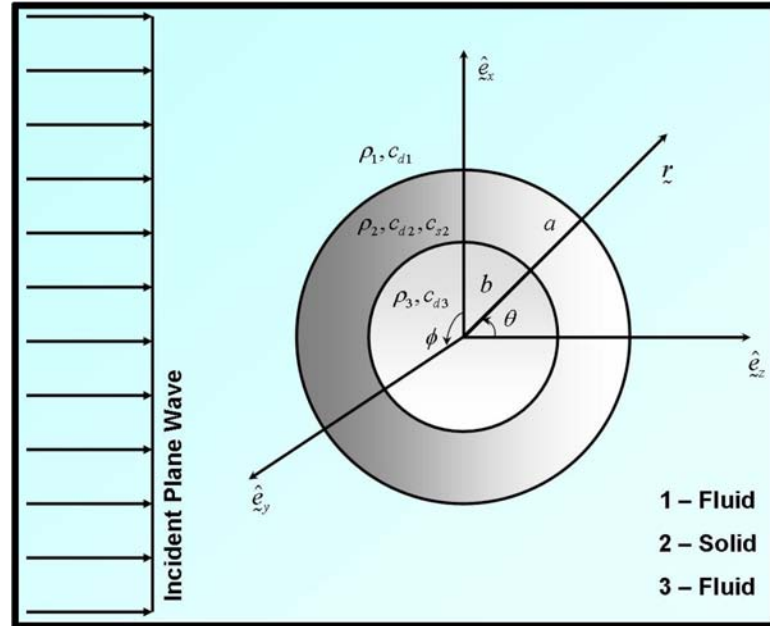


Figure 2.2: Schematic of the geometry for the scattering of a plane acoustic wave by a fluid-filled elastic spherical shell submerged in an infinite fluid medium.

It is then necessary to express the pressure of the incident plane wave as a sum of spherical harmonic functions [75]. Assuming an $e^{-i\omega t}$ time harmonic convention, the pressure of the incident wave, p_i , can be written

$$p_i = p_0 e^{i(-\omega t + k_1 r \cos \theta)} = p_0 \sum_{n=0}^{\infty} \alpha_n j_n(k_1 r) P_n(\cos \theta) e^{-i\omega t} \quad (2.33)$$

where p_0 is the pressure amplitude, $k_1 = \omega / c_{d1}$ is the wave number in the medium external to the sphere, $j_n(k_1 r)$ is a spherical Bessel function, $P_n(\cos \theta)$ is a Legendre polynomial, and the α_n are unknown coefficients. A Neumann function is not included in (2.33) to ensure that the solution remains bounded at the origin; the value of Neumann functions approaches infinity as their argument approaches zero. In order to determine the α_n coefficients, one notes the orthogonality property of Legendre polynomials [76],

$$\int_{-1}^1 P_n(\mu) P_m(\mu) d\mu = \begin{cases} 0 & n \neq m \\ \frac{2}{2n+1} & n = m. \end{cases} \quad (2.34)$$

Both sides of (2.33) are multiplied by $P_m(\cos \theta)$ and are then integrated,

$$\int_{-1}^1 e^{ik_1 r \cos \theta} P_m(\cos \theta) d \cos \theta = \int_{-1}^1 \alpha_n j_n(k_1 r) P_n(\cos \theta) P_m(\cos \theta) d \cos \theta. \quad (2.35)$$

Making use of (2.34), the solution is non-trivial only when $n = m$ and thus,

$$\int_{-1}^1 e^{ik_1 r \cos \theta} P_n(\cos \theta) d \cos \theta = \frac{2\alpha_n}{2n+1} j_n(k_1 r). \quad (2.36)$$

The Bessel function in (2.36) is substituted with the identity [77],

$$\begin{aligned}
j_n(k_1 r) &= \frac{(-i)^n}{2} \int_0^\pi e^{ik_1 r \cos \theta} P_n(\cos \theta) \sin \theta d\theta \\
&= \frac{(-i)^n}{2} \int_{-1}^1 e^{ik_1 r \cos \theta} P_n(\cos \theta) d \cos \theta,
\end{aligned} \tag{2.37}$$

resulting in the relationship,

$$\int_{-1}^1 e^{ik_1 r \cos \theta} P_n(\cos \theta) d \cos \theta = \frac{(-i)^n}{2n+1} \alpha_n \int_{-1}^1 e^{ik_1 r \cos \theta} P_n(\cos \theta) d \cos \theta. \tag{2.38}$$

After simplification, the solution for the α_n coefficients is

$$\alpha_n = i^n (2n+1). \tag{2.39}$$

Therefore, the expression for the incident plane wave expanded in terms of spherical harmonics is

$$p_i = p_0 e^{-i\alpha} \sum_{n=0}^{\infty} i^n (2n+1) j_n(k_1 r) P_n(\cos \theta). \tag{2.40}$$

The pressure scattered from the sphere, p_s , can be expressed as

$$p_s = p_0 e^{-i\alpha} \sum_{n=0}^{\infty} i^n (2n+1) a_n h_n^{(1)}(k_1 r) P_n(\cos \theta) \tag{2.41}$$

where $h_n^{(1)}(k_1 r)$ is a spherical Hankel function of the first kind. The $p_0 i^n (2n+1)$ term is included for convenience and it is assumed that the a_n coefficients absorb the appropriate factors to account for this substitution. The total pressure in the fluid external to the sphere is equal to the sum of the incident and scattered pressures,

$$p_1 = p_i + p_s = p_0 e^{-i\alpha} \sum_{n=0}^{\infty} i^n (2n+1) \left[j_n(k_1 r) + a_n h_n^{(1)}(k_1 r) \right] P_n(\cos \theta). \tag{2.42}$$

It is also necessary to determine the radial displacement, $u_{r,1}$, in the fluid external to the sphere. This is accomplished through use of the linearized momentum equation [78] where

$$u_{r,1} = \frac{1}{\rho_1 \omega^2} \frac{\partial p_1}{\partial r} = \frac{p_0}{\rho_1 \omega^2} e^{-i\omega t} \sum_{n=0}^{\infty} i^n (2n+1) \left[k_1 j_n'(k_1 r) + a_n k_1 h_n^{(1)'}(k_1 r) \right] P_n(\cos \theta). \quad (2.43)$$

Expressions for the potential functions in the shell material are

$$\varphi_2(r, \theta, t) = p_0 e^{-i\omega t} \sum_{n=0}^{\infty} i^n (2n+1) \left[b_n j_n(k_{d2} r) + c_n n_n(k_{d2} r) \right] P_n(\cos \theta), \quad (2.44)$$

$$\psi_2(r, \theta, t) = p_0 e^{-i\omega t} \sum_{n=0}^{\infty} i^n (2n+1) \left[d_n j_n(k_{s2} r) + e_n n_n(k_{s2} r) \right] \frac{d}{d\theta} [P_n(\cos \theta)]. \quad (2.45)$$

The potential functions in the filler fluid are

$$\varphi_3(r, \theta, t) = p_0 e^{-i\omega t} \sum_{n=0}^{\infty} i^n (2n+1) \left[f_n j_n(k_{d3} r) \right] P_n(\cos \theta) \quad (2.46)$$

$$\psi_3(r, \theta, t) = 0 \quad (2.47)$$

where the Neumann function in equation (2.46) is excluded to ensure that the solution remains bounded at the origin of the coordinate system, located at the sphere's interior.

The six unknown coefficients, a_n, b_n, c_n, d_n, e_n , and f_n are determined by matching the boundary conditions for displacement, normal stress, and transverse stress at the internal and external surfaces of the sphere. On the sphere's external surface, $r = a$,

$$p_1 = -\tau_{rr,2} \quad (2.48)$$

$$u_{r,1} = u_{r,2} \quad (2.49)$$

$$\tau_{r\theta,2} = 0 \quad (2.50)$$

and on the internal surface, at $r = b$,

$$\tau_{rr,2} = \tau_{rr,3} \quad (2.51)$$

$$u_{r,2} = u_{r,3} \quad (2.52)$$

$$\tau_{r\theta,2} = 0. \quad (2.53)$$

Application of the boundary conditions results in a set of linear equations that are presented here in matrix form as,

$$\begin{bmatrix} d_{11} & d_{12} & d_{13} & d_{14} & d_{15} & d_{16} \\ d_{21} & d_{22} & d_{23} & d_{24} & d_{25} & d_{26} \\ d_{31} & d_{32} & d_{33} & d_{34} & d_{35} & d_{36} \\ d_{41} & d_{42} & d_{43} & d_{44} & d_{45} & d_{46} \\ d_{51} & d_{52} & d_{53} & d_{54} & d_{55} & d_{56} \\ d_{61} & d_{62} & d_{63} & d_{64} & d_{65} & d_{66} \end{bmatrix} \begin{Bmatrix} a_n \\ b_n \\ c_n \\ d_n \\ e_n \\ f_n \end{Bmatrix} = \begin{bmatrix} A_1 \\ A_2 \\ A_3 \\ A_4 \\ A_5 \\ A_6 \end{bmatrix} \quad (2.54)$$

where,

$$d_{11} = a^2 h_n^{(1)}(k_1 a)$$

$$d_{12} = \left[-(\lambda_2 + 2\mu_2)(k_{d2}a)^2 + 2\mu_2 n(n+1) \right] j_n(k_{d2}a) - 4\mu_2 [k_{d2}a] j_n'(k_{d2}a)$$

$$d_{13} = \left[-(\lambda_2 + 2\mu_2)(k_{d2}a)^2 + 2\mu_2 n(n+1) \right] n_n(k_{d2}a) - 4\mu_2 [k_{d2}a] n_n'(k_{d2}a)$$

$$d_{14} = 2\mu_2 [n(n+1)] j_n(k_{s2}a) - 2\mu_2 [n(n+1)k_{s2}a] j_n'(k_{s2}a)$$

$$d_{15} = 2\mu_2 [n(n+1)] n_n(k_{s2}a) - 2\mu_2 [n(n+1)k_{s2}a] n_n'(k_{s2}a)$$

$$d_{16} = 0$$

$$A_1 = -a^2 j_n(k_1 a)$$

$$d_{21} = \frac{-k_1 a}{\rho_1 \omega^2} h_n^{(1)'}(k_1 a)$$

$$d_{22} = [k_{d2} a] j_n'(k_{d2} a)$$

$$d_{23} = [k_{d2} a] n_n'(k_{d2} a)$$

$$d_{24} = [-n(n+1)] j_n(k_{s2} a)$$

$$d_{25} = [-n(n+1)] n_n(k_{s2} a)$$

$$d_{26} = 0$$

$$A_2 = \frac{k_1 a}{\rho_1 \omega^2} j_n'(k_1 a)$$

$$d_{31} = 0$$

$$d_{32} = -2 j_n(k_{d2} a) + 2 [k_{d2} a] j_n'(k_{d2} a)$$

$$d_{33} = -2 n_n(k_{d2} a) + 2 [k_{d2} a] n_n'(k_{d2} a)$$

$$d_{34} = \left[2 - 2n(n+1) + (k_{s2} a)^2 \right] j_n(k_{s2} a) + 2 k_{s2} a j_n'(k_{s2} a)$$

$$d_{35} = \left[2 - 2n(n+1) + (k_{s2} a)^2 \right] n_n(k_{s2} a) + 2 k_{s2} a n_n'(k_{s2} a)$$

$$d_{36} = 0$$

$$A_3 = 0$$

$$d_{41} = 0$$

$$d_{42} = \left[-(\lambda_2 + 2\mu_2)(k_{d2} b)^2 + 2\mu_2 n(n+1) \right] j_n(k_{d2} b) - 4\mu_2 [k_{d2} b] j_n'(k_{d2} b)$$

$$d_{43} = \left[-(\lambda_2 + 2\mu_2)(k_{d2} b)^2 + 2\mu_2 n(n+1) \right] n_n(k_{d2} b) - 4\mu_2 [k_{d2} b] n_n'(k_{d2} b)$$

$$d_{44} = 2\mu_2 \left[n(n+1) \right] j_n(k_{s_2}b) - 2\mu_2 \left[n(n+1)k_{s_2}b \right] j_n'(k_{s_2}b)$$

$$d_{45} = 2\mu_2 \left[n(n+1) \right] n_n(k_{s_2}b) - 2\mu_2 \left[n(n+1)k_{s_2}b \right] n_n'(k_{s_2}b)$$

$$d_{46} = \lambda_3 \left[k_{d_3}^2 b^2 \right] j_n(k_{d_3}b)$$

$$A_4 = 0$$

$$d_{51} = 0$$

$$d_{52} = \left[k_{d_2}b \right] j_n'(k_{d_2}b)$$

$$d_{53} = \left[k_{d_2}b \right] n_n'(k_{d_2}b)$$

$$d_{54} = \left[-n(n+1) \right] j_n(k_{s_2}b)$$

$$d_{55} = \left[-n(n+1) \right] n_n(k_{s_2}b)$$

$$d_{56} = k_{d_3}b j_n'(k_{d_3}b)$$

$$A_5 = 0$$

$$d_{61} = 0$$

$$d_{62} = -2j_n(k_{d_2}b) + 2k_{d_2}b j_n'(k_{d_2}b)$$

$$d_{63} = -2n_n(k_{d_2}b) + 2k_{d_2}b n_n'(k_{d_2}b)$$

$$d_{64} = \left[2 - 2n(n+1) + k_{s_2}^2 b^2 \right] j_n(k_{s_2}b) + 2k_{s_2}b j_n'(k_{s_2}b)$$

$$d_{65} = \left[2 - 2n(n+1) + k_{s_2}^2 b^2 \right] n_n(k_{s_2}b) + 2k_{s_2}b n_n'(k_{s_2}b)$$

$$d_{66} = 0$$

$$A_6 = 0.$$

Note that only first order derivatives of the spherical Bessel functions are present in the above coefficients. Bessel's equation in spherical coordinates [77]

$$z^2 w'' + 2zw' + [z^2 - n(n+1)]w = 0 \quad (2.55)$$

is used to determine expressions for the second derivatives of spherical Bessel functions in terms of first derivatives only, as

$$w'' = -\frac{2}{z} w' + \left[\frac{n(n+1)}{z^2} - 1 \right] w \quad (2.56)$$

where w is a spherical Bessel function of the first, second, or third kind and z is the Bessel function's argument. In addition, Legendre's equation,

$$\frac{d^2 P_n}{d\theta^2} = -\cot \theta \frac{dP_n}{d\theta} - n(n+1) P_n \quad (2.57)$$

is used to expand the second derivatives of Legendre polynomials, which arise in stress terms that include a shear potential.

To determine the coefficients of the scattered field, the system of equations (2.54) is solved for a_n through the method of Gaussian elimination [79]. The computer program used for this calculation is written in MATLAB[®]. Spherical Bessel functions, solved numerically, are calculated from their ordinary counterparts according to the following relationships [78]:

$$\begin{aligned}
j_n(z) &= \left(\frac{\pi}{2z}\right)^{\frac{1}{2}} J_{n+1/2}(z) \\
n_n(z) &= \left(\frac{\pi}{2z}\right)^{\frac{1}{2}} N_{n+1/2}(z) \\
h_n(z) &= j_n(z) + in_n(z).
\end{aligned} \tag{2.58}$$

A Bessel function's first derivative is calculated through the following identity [76]:

$$\frac{d}{dz} j_n(z) = \frac{1}{2n+1} [nj_{n-1}(z) - (n+1)j_{n+1}(z)]. \tag{2.59}$$

For distances far away from the sphere (usually taken as > 10 sphere diameters), the Hankel function in equation (2.41) takes on an asymptotic form [56],

$$\lim_{k_1 r \rightarrow \infty} h_n(k_1 r) \rightarrow i^{-(n+1)} \frac{e^{ik_1 r}}{k_1 r}. \tag{2.60}$$

Equation (2.41) for the scattered field can then be reduced to the following expression,

$$p_s = p_0 \frac{a}{2r} \left\{ \frac{2}{ik_1 a} \sum_{n=0}^{\infty} (2n+1) b_n P_n(\cos \theta) \right\} e^{i(k_1 r - \alpha r)}. \tag{2.61}$$

The quantity inside the brackets, is referred to as the bistatic far-field acoustic form function, f_{∞} . The factor of 2 is included so that the form function for a rigid sphere asymptotically approaches unity for large values of ka . The target's form function in the monostatic, $\theta = 180^\circ$, backscattered direction is

$$f_{\infty} = \sum_{n=0}^{\infty} f_n(k_1 a) = \frac{2}{ik_1 a} \sum_{n=0}^{\infty} (-1)^n (2n+1) b_n. \tag{2.62}$$

A target's form function is a standard means of depicting its scattering response as a function of frequency. The analytical solution above will be used subsequently to

identify resonances in targets of interest. Appendix A includes additional derivations used to determine the field scattered from fluid and solid spheres and cylinders.

2.2.1.1 Rigid Sphere

The monostatic form function for a rigid sphere is depicted in Figure 2.3. The response is plotted against the dimensionless quantity $ka = 2\pi a / \lambda$, the number of wavelengths that fit around the circumference of the sphere. This result is calculated by setting the density of the shell material in equations (2.54) to be many orders of magnitude greater than the external fluid density, allowing the sphere to be moveable. A similar calculation can also be performed by setting the velocity at the sphere's surface identically equal to zero, resulting in the response of a rigid immovable sphere.

For a rigid sphere, the range where ka approaches zero, is referred to as the Rayleigh scattering region [53] where the wavelength of the incident acoustic wave is much larger than the radius of the sphere. In this regime, shown approximately in the left-most part of Figure 2.3a, the form function is proportional to $(ka)^2$. In optics, this type of scattering is primarily responsible for the daytime color of the sky being blue; particles in the air preferentially scatter light at the higher frequency (shortest wavelength) end of the visible spectrum. This phenomenon was famously postulated by Lord Rayleigh in 1899 [80] and later confirmed experimentally in 1913 by Jean Cabannes [81]. In the rigid target's response, as ka increases past unity, the form function begins to oscillate and eventually asymptotes to a value of one. In the limit of high frequency, the sphere acts as a plane specular reflector. The fluctuations in the mid-

frequency region are associated with waves that circumnavigate the sphere and interfere either constructively or destructively with the specular portion of the scattered field. These types of waves, referred to as creeping or Franz waves [82], are purely diffractive and travel slower than the ambient sound speed. So that the reader may obtain a qualitative idea of the scattered field for incident waves of both low and high frequency, plots of the pressure field scattered by a rigid sphere for $ka = 1$ and $ka = 20$ are presented in Figure 2.4a and Figure 2.4b, respectively.

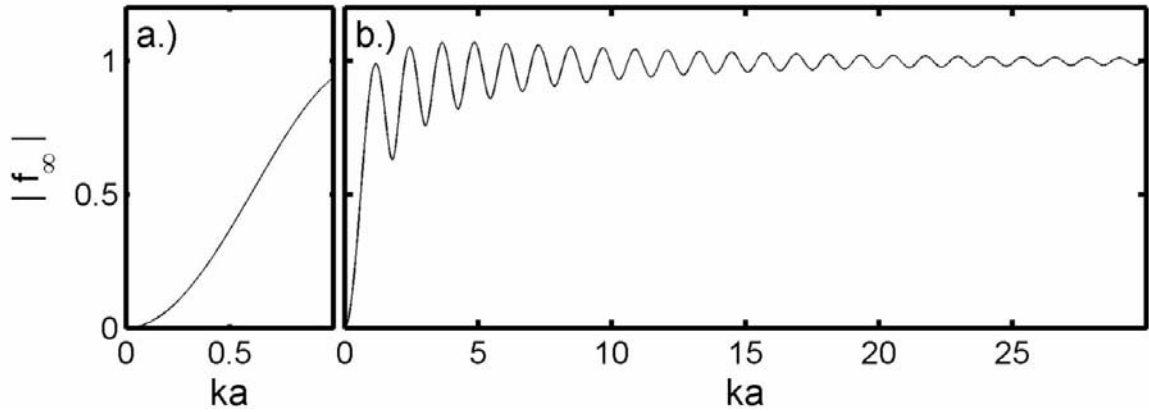


Figure 2.3: Magnitude of the monostatic farfield acoustic form function for a rigid sphere plotted versus the dimensionless Helmholtz number, ka , the number of wavelengths that fit around the circumference of the sphere; (a.) $0 \leq ka \leq 1$ (b.) $0 \leq ka \leq 30$.

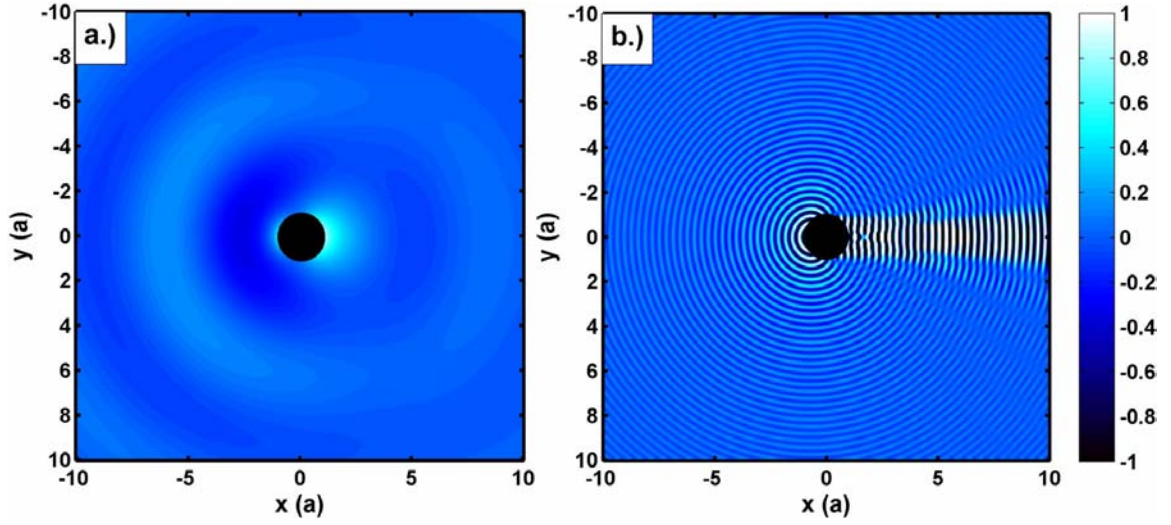


Figure 2.4: Scattered pressure fields from a rigid sphere (real part) under steady state driving with (a.) $ka = 1$, (b.) $ka = 20$. The horizontal and vertical axes are normalized and presented in units of the sphere's radius, a . The sphere's location is depicted by the black circle at the center of the image. The intensity value of the pixels in the images represents the pressure amplitude at that location, normalized to the maximum pressure amplitude in the image. The plane wave insonifying the sphere approaches from the left side of each figure.

2.2.1.2 Spherical Shell Target

The target primarily used in this work, and subsequently referred to as the ‘standard spherical shell target’, is a 6.35 mm outer diameter air-filled spherical shell made of aluminium 3003 with a nominal ratio of inner radius to outer radius of 0.91. The monostatic form function for this target is calculated from the solution presented in Section 2.2.1, using the properties shown in Table 2.1. The result is depicted by the dashed line in Figure 2.5. The target's response exhibits a number of resonance peaks associated with different wave modes in the target's scattering response; the origin of these peaks will be discussed subsequently in Section 2.2.2.

The circles in Figure 2.6 are generated from a solution that assumes the shell is filled with a fluid, more specifically air. However, originally in this work a classic solution for the scattered pressure, developed by Goodman and Stern [65] and reformulated by Hickling [66], was used to calculate the form function of the standard shell target. This solution assumes a vacuum filled interior for the shell. It was of interest as to whether this solution is also valid for the standard shell target. Superimposed on Figure 2.5, as a solid line, is the form function calculated from the solution assuming a vacuum filled interior. Clearly there is no discernable difference between the air-filled interior and evacuated interior solutions. Thus, the vacuum interior solution accurately predicts the behaviour of the scattered field. This formulation requires the solution of fewer boundary conditions and can be used in cases where computation time is of importance. The solution obtained by assuming a fluid-filled shell is however more general, and will be valid in cases where the shell's impedance is not sufficiently high relative to the interior fluid's impedance.

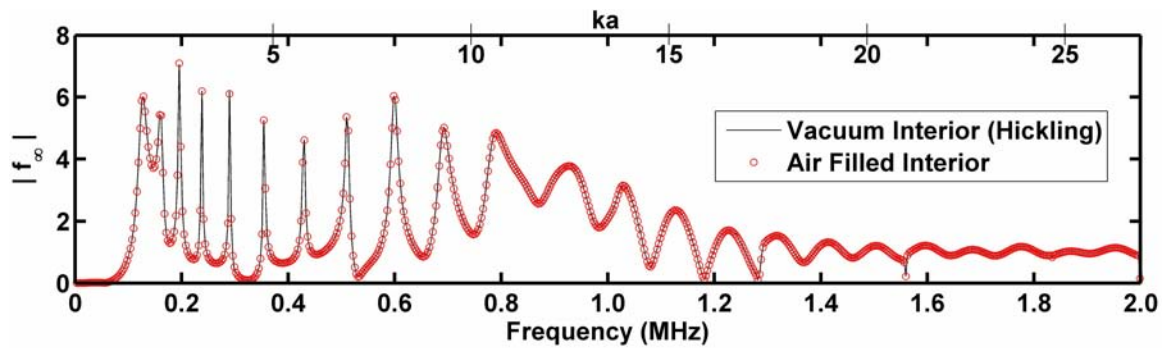


Figure 2.5: Magnitude of the monostatic farfield acoustic form function for a 6.35 mm outer diameter hollow aluminum spherical shell plotted versus frequency, assuming a vacuum filled interior (solid line) and an air-filled interior (dashed line).

Table 2.1: Material properties used in the analytical prediction of the aluminum spherical shell's monostatic farfield form function.

Shell outer radius	3.182 mm
Shell inner radius	2.892 mm
External fluid density, water	998 kg/m ³
External fluid sound speed, water	1483.8 m/s
Density, aluminum 3003	2680 kg/m ³
Dilatational wave speed, aluminum 3003	6171.8 m/s
Shear wave speed, aluminum 3003	3108.9 m/s

2.2.1.3 Effect of External Loading

The physical properties in the medium external to the sphere also affect the target's scattering response. Shown in Figure 2.6 is the form function for the aluminium shell target, zoomed on the resonance peak centered at 600 kHz. Within this figure, the density of the fluid external to the shell is varied $\pm 5\%$ from its nominal value. Increasing the density of the fluid results in a shift in the center of the resonance from higher to lower frequency. In contrast, increasing the sound speed in the external medium results in an upward shift in the resonance frequency, as observed in Figure 2.7 where the sound speed is varied $\pm 5\%$ from its original value. This simple analysis demonstrates that it is not always obvious how the resonance frequencies will change as the external medium is switched to one possessing a higher density and higher sound speed.

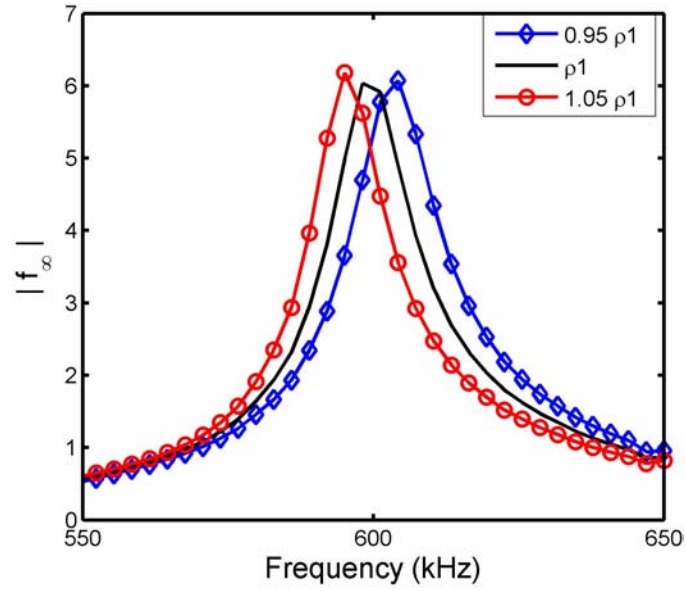


Figure 2.6: Form function of the aluminum spherical shell target between 550-650 kHz where the density of the fluid external to the sphere is varied $\pm 5\%$ from its nominal value.

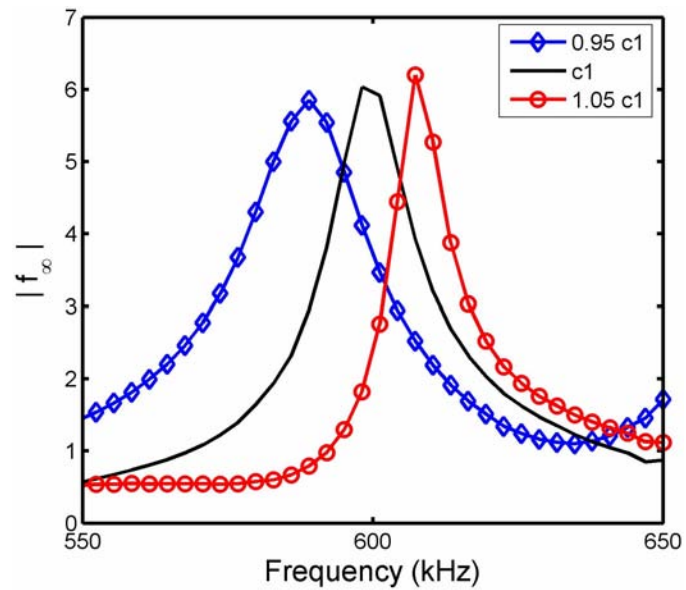


Figure 2.7: Form function of the aluminum spherical shell target between 550-650 kHz where the sound speed of the fluid external to the sphere is varied $\pm 5\%$ from its nominal value.

2.2.2 Resonance Identification

The form function of the standard spherical shell target, described in Section 2.2.1.2 and depicted in Figure 2.5, consists of a number of resonance peaks that are characteristic of different wave modes in the target's scattering response. Depicted in Figure 2.8 is the theoretical time trace of a typical backscattered return from this target, given a short broadband (here a 2-cycle, 1-MHz sine wave) incident waveform. The return consists of four consecutive wave packets, located between 150-175 μs . The first wave packet, whose center is located at 153 μs , is associated with a specular return from the proximal face of the target. A target's specular return does not exhibit resonance behavior and, for short pulses, the waveform shape is typically a replica of the incident pulse shape (i.e. the pressure of the incident acoustic wave and not the transmitted voltage). Following the specular return, at times of approximately 157 μs , 163 μs and 174 μs , are wave packets associated with 'surface elastic waves'. As depicted schematically in Figure 2.9, surface elastic waves circumnavigate the shell on its surface and are radiated into the external medium as they propagate. The objective of this section is to identify the resonances appearing in the standard spherical shell target's scattering response through the use of resonance scattering theory and analysis drawn from papers by Kargl and Marston [83] and Sammelmann *et al.* [84]. This is done in order to determine the types of waves upon which the time reversal procedure operates.

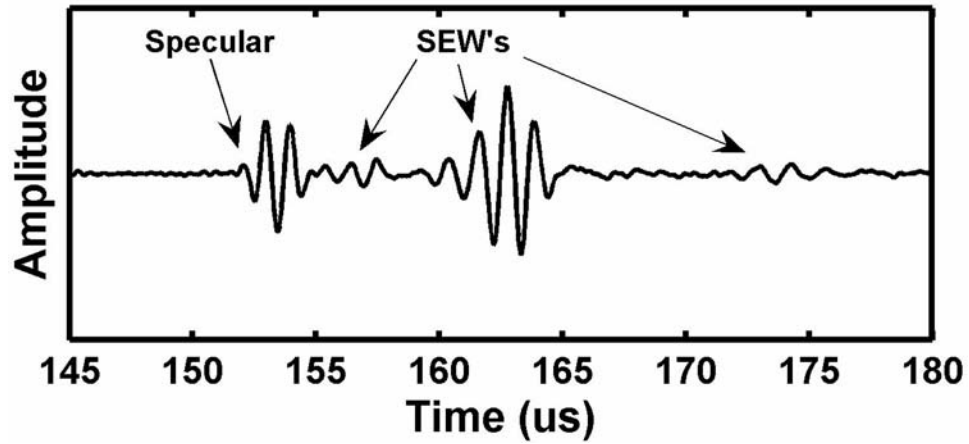


Figure 2.8: Theoretical time trace, normalized amplitude versus time, of a backscattered waveform from the standard hollow aluminum shell target, given a 2 cycle 1 MHz sine wave interrogation pulse. A specular return and three surface elastic wave (SEW) returns are identified with arrows.

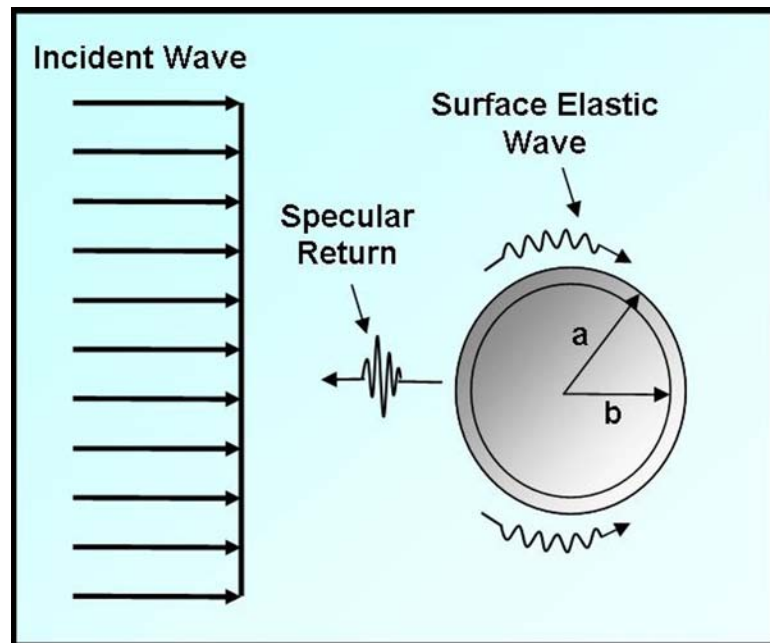


Figure 2.9: Schematic depicting the types of waves scattered from an elastic spherical shell excited by a plane wave of infinite extent.

Resonance scattering theory (RST) is a method through which the elastic components of a target's scattering response can be isolated and subsequently identified. The general technique has its origin in investigations of nuclear scattering [85, 86] and was first applied to acoustic scattering problems in 1978 [87]. Extensive reviews of the theory are found in Refs. [88] and [89]. In this work, the technique is employed to isolate resonances in the standard shell target's response.

The fundamental principle of RST is that the scattering response of a target can be decomposed into a purely elastic response and a background response. For example, Figure 2.10 presents the form function of a solid stainless steel sphere submerged in water. In the region $0 < ka < 5$, the target's response is identical to that of a rigid sphere; see Figure 2.3. However, for higher ka values, a number of peaks, valleys, and sharp dips in the response are apparent. These characteristics are attributed to eigenmodes (resonances) of vibration of the target, when driven by an incident acoustic wave. These resonances appear to be superimposed on top of a rigid 'background' response that is attributed to purely diffractive scattering phenomena.

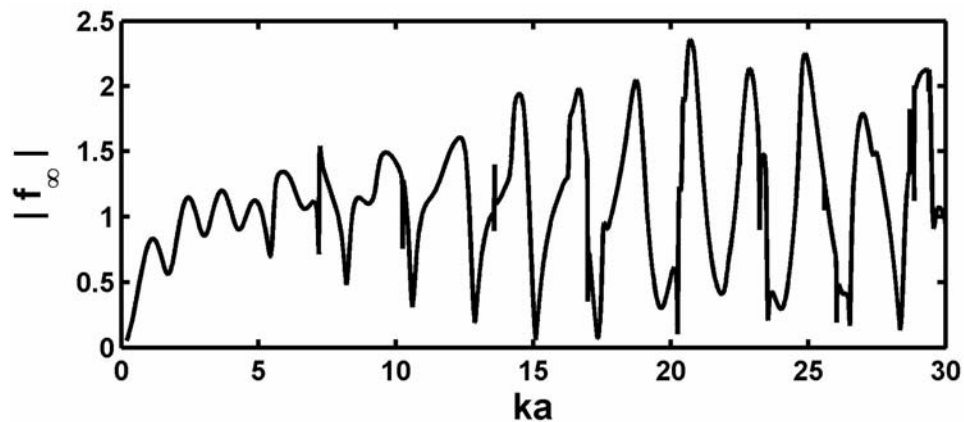


Figure 2.10: Magnitude of the far-field monostatic form function for a solid stainless steel sphere plotted versus the dimensionless parameter ka .

In RST, either a rigid or soft (pressure release) background is subtracted from an elastic target's response to isolate its *purely* elastic response. A rigid background is appropriate for solid targets and shell targets with a wall thickness normalized to the outer radius $t = (a - b) / a \geq 0.01$. A soft background is appropriate for shell thicknesses $t \leq 0.001$ [89]. For shells of wall thickness lying between these two limits, it was originally proposed that it would be appropriate to subtract an intermediate background [90]. However, subsequent investigations showed that there is no way to determine an appropriate intermediate background *a priori* and that a rigid background is suitable for most metallic shells of practical interest [89].

Presented in Figure 2.11 is the monostatic far-field acoustic form function for the standard spherical shell target decomposed into the individual terms in its partial wave series solution; see equation (2.62). In Figure 2.11a is shown the magnitude of the complete form function, normalized and plotted versus frequency, identical to Figure 2.5. The shaded gray region depicts the frequency range of interest for the current work. In Figure 2.11b to Figure 2.11l, partial waves $n = 0$ to $n = 10$ are shown individually, normalized to the same scale as Figure 2.11a. Also shown at the right of each figure panel is the angular dependence of each partial wave. In Figure 2.12, equivalent results are presented for a rigid sphere submerged in water.

It is clear from Figure 2.12 that each partial wave of the rigid sphere's response consists of a number of broad peaks that are uniformly distributed across frequency. These peaks are attributed to purely diffractive scattering effects where the waves may circumnavigate the sphere but do not penetrate its interior. These peaks, associated with

diffraction, are also seen in the standard spherical shell's partial waves in Figure 13. Of greater interest however, are the sharp peaks and dips superimposed on these. They are attributed to the elastic nature of the target, where the incident wave field penetrates the shell material and excites its vibratory response. To isolate the elastic modes of the standard spherical shell target, the rigid sphere's response is subtracted from the shell's elastic response. The results of this procedure are presented in Figure 2.13b to Figure 2.13l. The peaks in each of these sub-figures represent wave resonances attributed to the spherical shell's purely elastic scattering response. For reference, the total far-field form function of the target is repeated in Figure 2.13a, without background subtraction.

It is clear from Figure 2.13b that the monopole ($n = 0$) mode of the standard shell target does not contribute significantly to the scattered field, as its magnitude is relatively small in comparison with the other partial waves. As one examines higher partial wave numbers, three distinct resonance peaks become visible. This is especially evident in Figure 2.13f, where each peak is pointed out with an arrow and labeled according to its type. As will be seen, these resonances correspond to symmetric, s_0 , and antisymmetric, a_0 , 'Lamb-type' surface elastic waves. The peak labeled 'spurious' was found not to correspond directly to any physical wave type and is likely an artifact of the numerical computation. The reader should note that the location of a particular type of resonance peak appears to shift from low to high frequency with increasing partial wave number.

A number of investigations [59, 84] have shown that the phase velocity of the n^{th} surface elastic wave resonance, c_n , normalized by the ambient fluid sound speed is

$$\frac{c_n}{c} = \frac{(ka)_n}{\sqrt{n(n+1)}} \quad (2.63)$$

where $(ka)_n$ is the location of a particular resonance, n is the partial wave mode number.

By manually searching in the purely elastic target's response for the center frequency of resonance peaks up to $ka = 80$, the phase velocity of a particular wave type is determined through equation (2.63). The ka locations of resonance peaks for each of the three wave types present in Figure 2.13 are given in Table 2.2 for each partial wave number.

It is now useful to compare the phase velocity of wave modes in the standard spherical shell target to those of a flat plate possessing the same thickness and material properties. In a classic paper [91], Horace Lamb demonstrated that two different types of waves propagate on a flat elastic plate *in vacuo*. These waves are referred to as symmetric and asymmetric Lamb waves. The name of each wave type is representative of the displacement of the plate about the center of its cross-section. Symmetric Lamb waves on a flat plate are typically characterized by motion that is symmetric about the center of the plate's thickness and are dilatational in nature, whereas asymmetric Lamb waves are characterized by flexural type displacements that are asymmetric about the plate's center. A derivation of the dispersion relation for each of these wave types is reviewed in Appendix A.

Dispersion curves for the lowest order Lamb wave modes on a flat plate are plotted as solid lines in Figure 2.14. The shell thickness and material properties of the standard spherical shell target are used to produce this result. For flat plates, a wave's

phase velocity is typically plotted against the product kh , where k is the wave number and h is the plate's thickness. Here, this quantity is scaled as [83]

$$ka = kh \frac{c_n}{c} \left[1 - \left(\frac{b}{a} \right) \right]^{-1} \quad (2.64)$$

so that the dispersion curves can be compared with the wave modes of the standard spherical shell target. Superimposed in Figure 2.14 are the phase velocities of two wave modes of the spherical shell target, calculated from equation (2.63) using resonance locations listed in the first and second columns of Table 2.2. The s_0 mode is depicted with squares and the a_{0+} mode is depicted with circles. The agreement between the flat plate and spherical shell's dispersion curves indicates that the shell waves are indeed analogs to Lamb waves that propagate on a flat plate. Thus, it is reasonable to assume that the waves are confined to the sphere's surface and that their phase velocity can be approximated with equation (2.63). From this point on, the spherical shell equivalent to the asymmetric Lamb wave will be referred to as an antisymmetric Lamb wave, in accordance with the nomenclature typically found in the literature.

The wave mode listed in the third column of Table 2.2, is similar in nature to the a_{0+} antisymmetric Lamb wave and is typically referred to either as an a_{0-} antisymmetric Lamb wave [84], an A wave, or a Scholte-Stoneley wave [92]. It arises from a bifurcation of the spherical shell's a_0 Lamb wave mode when the shell is loaded with fluid [5, 84, 93] (the shell's a_0 wave equivalent splits into distinct a_{0+} and a_{0-} waves). For manmade targets of interest that become buried in the ocean, at standard operational frequencies (2-20 kHz) this wave typically provides the strongest contribution to the

scattered field[5]. In the current work, the frequencies and target size have been scaled approximately to this range. Extensive research has been carried out investigating the a_{0-} wave type and the reader is referred to Refs. [5, 84, 92-94] for further information regarding its properties and relevance.

To further confirm the nature of a particular resonance type, the displacement at the internal and external surfaces of the spherical shell is calculated. Equations (2.28) and (2.29) are expanded to determine exact expressions for the displacement of the shell material in the radial and tangential directions, respectively, where the sphere is excited at steady state by an infinite plane acoustic wave. The radial displacement is of the form,

$$\begin{aligned}
 u_{r,2}(r, \theta, t) = p_0 e^{-i\omega t} & \left\{ \sum_{n=0}^{\infty} i^n (2n+1) P_n(\cos \theta) [b_n k_{d2} j_n'(k_{d2} r) + c_n k_{d2} n_n'(k_{d2} r)] + \dots \right. \\
 & \dots + \frac{\cot \theta}{r} \sum_{n=0}^{\infty} i^n (2n+1) \frac{\partial P_n(\cos \theta)}{\partial \theta} [d_n j_n(k_{s2} r) + e_n n_n(k_{s2} r)] + \dots \\
 & \left. \dots + \frac{1}{r} \sum_{n=0}^{\infty} i^n (2n+1) \frac{\partial^2 P_n(\cos \theta)}{\partial \theta^2} [d_n j_n(k_{s2} r) + e_n n_n(k_{s2} r)] \right\} \quad (2.65)
 \end{aligned}$$

and displacement in the tangential direction is

$$\begin{aligned}
 u_{\theta,2}(r, \theta, t) = p_0 e^{-i\omega t} & \left\{ \frac{1}{r} \sum_{n=0}^{\infty} i^n (2n+1) \frac{\partial P_n(\cos \theta)}{\partial \theta} [b_n j_n(k_{d2} r) + c_n n_n(k_{d2} r)] + \dots \right. \\
 & \dots - \frac{1}{r} \sum_{n=0}^{\infty} i^n (2n+1) \frac{\partial P_n(\cos \theta)}{\partial \theta} [d_n j_n(k_{s2} r) + e_n n_n(k_{s2} r)] + \dots \\
 & \left. \dots - \sum_{n=0}^{\infty} i^n (2n+1) \frac{\partial P_n(\cos \theta)}{\partial \theta} [d_n k_{s2} j_n'(k_{s2} r) + e_n k_{s2} n_n'(k_{s2} r)] \right\}. \quad (2.66)
 \end{aligned}$$

First order derivatives of Legendre polynomials are determined through numerical differentiation and the second order derivatives are determined through equation (2.57).

The displacement at the external ($r = a$) and internal ($r = b$) surfaces of the sphere is calculated as a function of θ for a specific partial wave index, n , and ka value. Figure 2.15 depicts these results for a cross section of the spherical shell target given a partial wave index of $n = 4$ and $ka = 2.6083$; these are parameters for the location of an antisymmetric Lamb wave resonance (see Table 2.2). The solid line shows the location of the internal and external surfaces of the shell at their maximum displacement amplitude. The arrows are displacement vectors that depict the deformation of the shell from its at-rest equilibrium state. The displacement amplitudes have been scaled by a large linear factor to make the sphere's deformation visible. One can clearly see from the figure that the displacements at the internal and external surfaces of the sphere are in phase with one another and that the deformation of the shell is indeed flexural in nature. This is the behavior one would expect for an antisymmetric Lamb wave resonance. Figure 2.16 presents similar results but for $n = 10$ and $ka = 39.3559$, the expected location of a symmetric Lamb wave resonance. The results in this Figure indicate that the internal and external surfaces of the shell are moving out of phase with one another and that the displacement is 'dilatational' in nature, as expected from Lamb wave theory.

The remainder of this work focuses only on the spherical shell's s_0 and a_{0-} waves because the a_{0+} wave does not contribute significantly to the scattered field over the frequency range of interest. In Figure 2.17, the phase velocity of s_0 and a_{0-} waves are plotted as squares and circles, respectively, fit with a solid line. Also plotted is the group velocity of these waves; that is, the speed at which the envelope of a wave packet

travels. The group velocity is determined from the phase velocity using the following expression [83]:

$$\frac{c_{gn}}{c_n} = 1 - \frac{1}{ka} \left[ka - \frac{c_n}{(dc_n/d(ka))} \right]^{-1}. \quad (2.67)$$

Finally, from the group velocity, the delay between the specular echo and the $(m+1)$ circumnavigation ($m = 0, 1, 2, \dots$) of a Lamb wave around the shell, as it would appear in a scattered signal's time trace, is [83]

$$\Delta t = 2a \left[c^{-1} (1 - \cos \vartheta_n) + c_{gn}^{-1} (\pi - \vartheta_n + m\pi) \right] \quad (2.68)$$

where

$$\vartheta_n = \sin^{-1} \left(\frac{c}{c_n} \right). \quad (2.69)$$

The ϑ_n term is the angle at which the incident acoustic wave couples into the shell material – note that this angle has a value of zero at $\theta = 180^\circ$. Equation (2.69) is a trace velocity matching condition, which assumes that the surface wave phase velocity is greater than the ambient fluid sound speed, $c_n > c$. This is not always the case and for surface wave phase velocities slower than the ambient sound speed, where $c_n < c$, equation (2.69) yields a non-real result. Under this circumstance, the coupling angle is approximated to be $\theta_n = 90^\circ$. Calculated echo delays for the spherical shell's symmetric and antisymmetric Lamb waves are plotted versus frequency in Figure 2.18.

The time trace presented in Figure 2.8 is now re-examined in order to compare the echo delay of wave packets in the experimentally measured return to the predicted Lamb

wave propagation times. In the second column of Table 2.3 are listed the expected echo delays for the first circumnavigation of an s_0 Lamb wave and the first two circumnavigations of an a_{0-} Lamb wave for wave frequencies of 0.8 MHz. Although the incident waveform has a center frequency of 1 MHz, as the surface waves circumnavigate the shell, a downshift in the wave's frequency is typically observed. This is due to radiation damping, where higher frequencies are radiated more strongly into the surrounding fluid than lower frequencies. The 0.8 MHz frequency is selected based upon spectral analysis of the first antisymmetric Lamb wave echo. Measured echo delays listed in the third column of Table 2.3 correspond to the three wave packets following the specular return in Figure 2.8. These results clearly show reasonable agreement with the predicted Lamb wave arrival times. Having confidently identified the dominant resonances in the standard spherical shell's response, similar analysis can be used subsequently to determine the types of waves on which the time reversal technique operates.

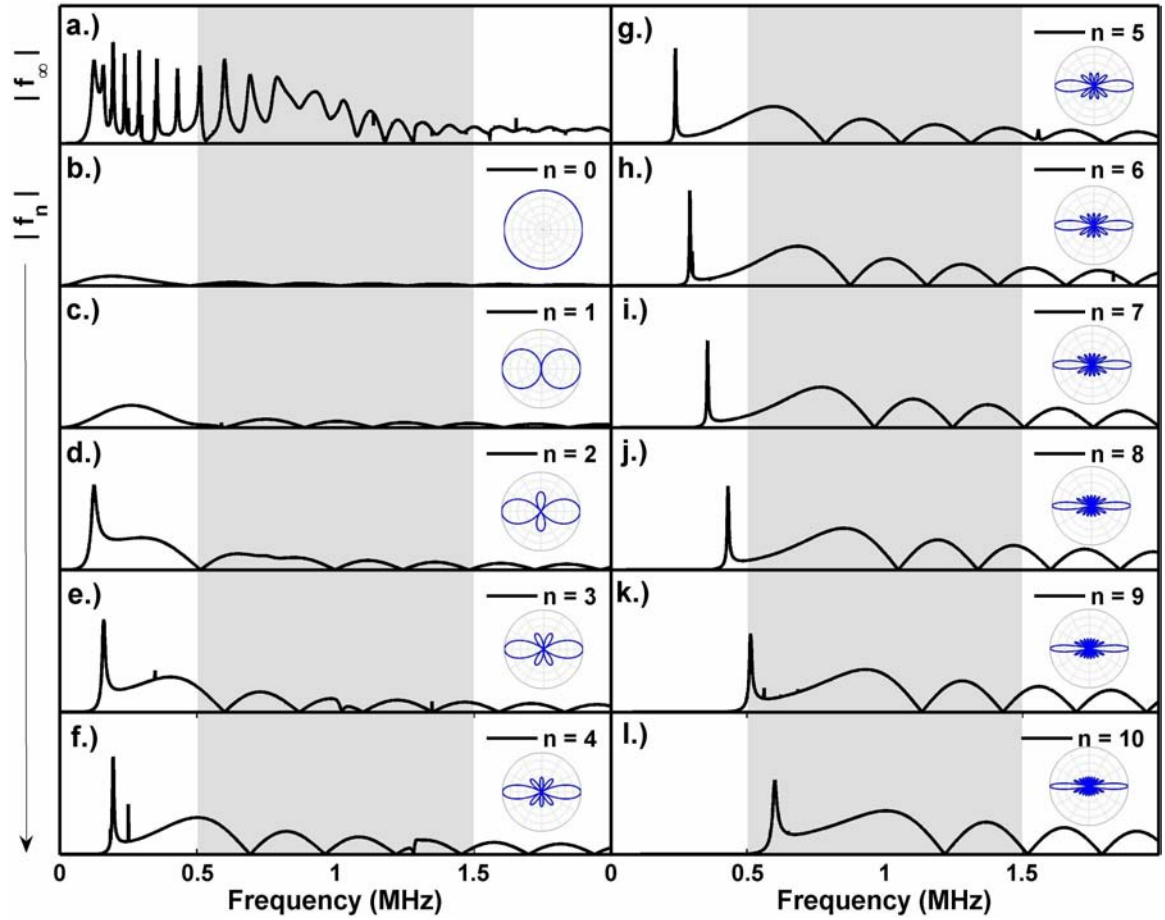


Figure 2.11: Far-field acoustic form function of the standard aluminum spherical shell target decomposed into the individual components of its partial wave series solution. (a.) Magnitude of the far-field acoustic form function versus frequency. (b.)-(l.) Partial waves $n = 0$ to $n = 10$, magnitude versus frequency. The vertical axis is normalized and presented on the same scale for all figure panels. The gray shaded region depicts the frequency range of interest for the current work. At the right of panels b-l is plotted the angular dependence of each partial wave.

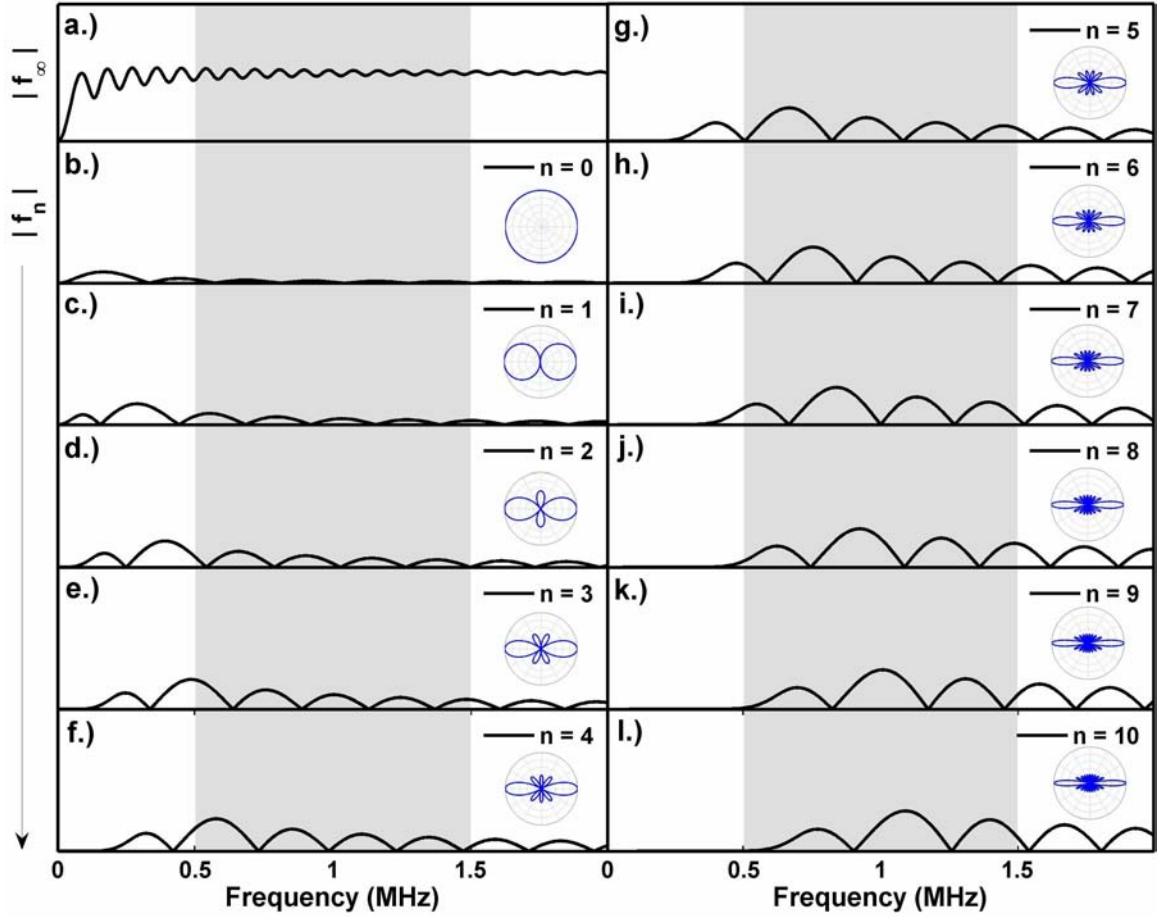


Figure 2.12: Far-field acoustic form function of a rigid sphere decomposed into the individual components of its partial wave series solution. (a.) Magnitude of the far-field acoustic form function versus frequency. (b.)-(l.) Partial waves $n = 0$ to $n = 10$, magnitude versus frequency. The vertical axis is normalized and presented on the same scale for all figure panels. The gray shaded region depicts the frequency range of interest for the current work. At the right of panels b-l is plotted the angular dependence of each partial wave.

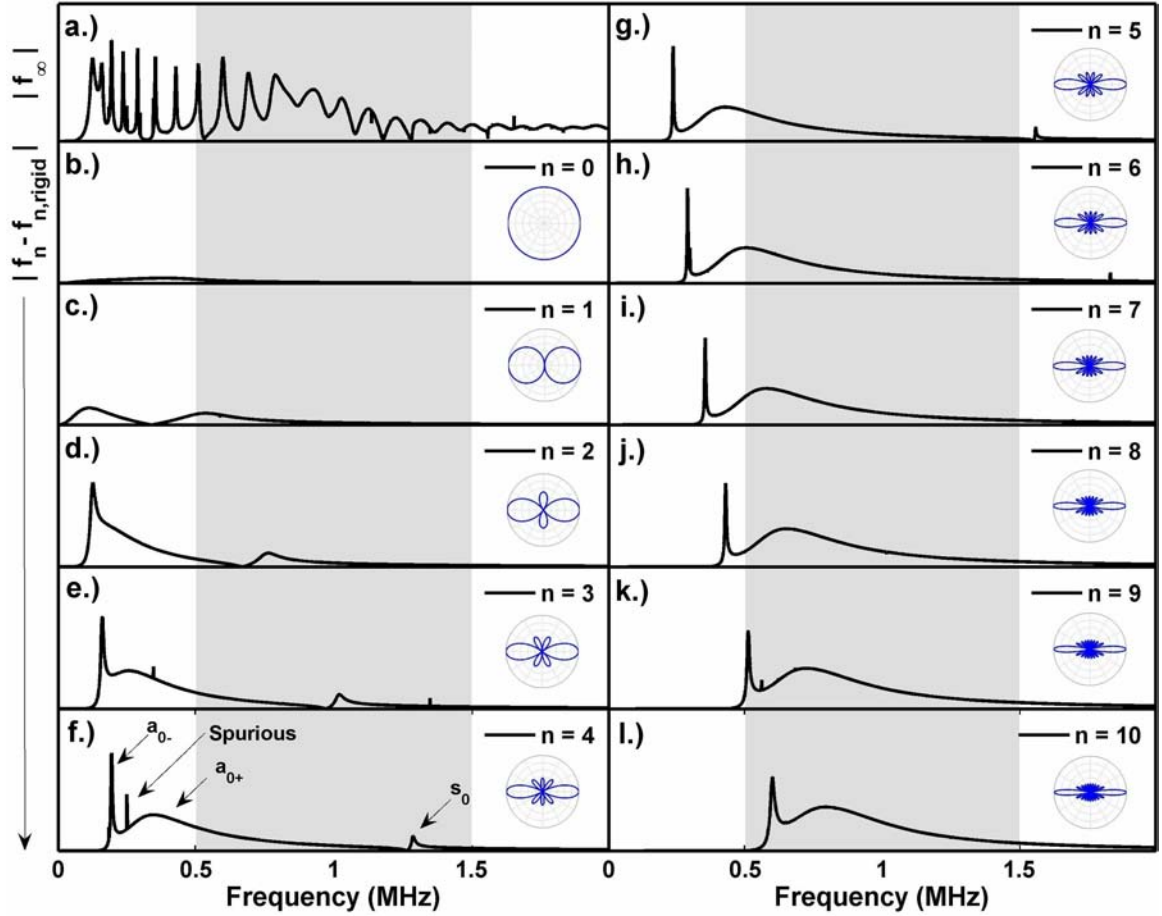


Figure 2.13: Far-field acoustic form function of the standard aluminum spherical shell target decomposed into the individual components of its partial wave series solution after subtraction of the partial waves from a rigid sphere. (a.) Magnitude of the far-field acoustic form function versus frequency. (b.)-(l.) Partial waves $n = 0$ to $n = 10$, magnitude versus frequency, after background subtraction. The vertical axis is normalized and presented on the same scale for all figure panels. The gray shaded region depicts the frequency range of interest for the current work. At the right of panels b-l is plotted the angular dependence of each partial wave. In (f.) resonance types are identified with arrows.

Table 2.2: List of resonance ka locations (center frequency of resonance) for each partial wave of the a_{0-} , a_{0+} , and s_0 Lamb type wave resonances in the purely elastic response of the standard shell target.

n	Resonance ka Location		
	s_0	a_{0+}	a_{0-}
1	-----	-----	-----
2	10.2810	-----	1.6882
3	13.7534	-----	2.1442
4	17.3697	-----	2.6083
5	21.0341	-----	3.1683
6	24.7145	-----	3.8804
7	28.3948	-----	4.7485
8	32.0672	-----	5.7526
9	35.7196	-----	6.8647
10	39.3559	-----	8.0568
11	42.9643	-----	9.3129
12	46.5407	-----	10.6091
13	50.0850	-----	11.9772
14	53.5814	-----	13.4573
15	57.0297	-----	14.8655
16	60.4300	20.1460	16.1376
17	63.7624	22.5303	17.3057
18	67.0227	24.6585	18.4178
19	70.2070	26.8187	19.4739
20	73.3113	29.0029	20.5141
21	76.3036	31.2031	21.5462
22	-----	33.3553	22.5463
23	-----	35.5396	23.5544
24	-----	37.7318	24.5545
25	-----	39.9400	25.5546
26	-----	42.1402	26.5547
27	-----	44.3484	27.5468
28	-----	46.5727	28.5389
29	-----	48.7809	29.5310
30	-----	50.9971	30.5231
31	-----	53.2213	31.5232
32	-----	55.4375	32.5073
33	-----	57.6618	33.4993
34	-----	59.8780	34.4914
35	-----	61.9262	35.4835
36	-----	64.3184	36.4836
37	-----	66.5347	37.4677
38	-----	68.7589	38.4598
39	-----	70.9671	39.4519
40	-----	73.1833	40.4440
41	-----	75.3115	41.4361
42	-----	77.5998	42.4282
43	-----	-----	43.4203
44	-----	-----	44.4124

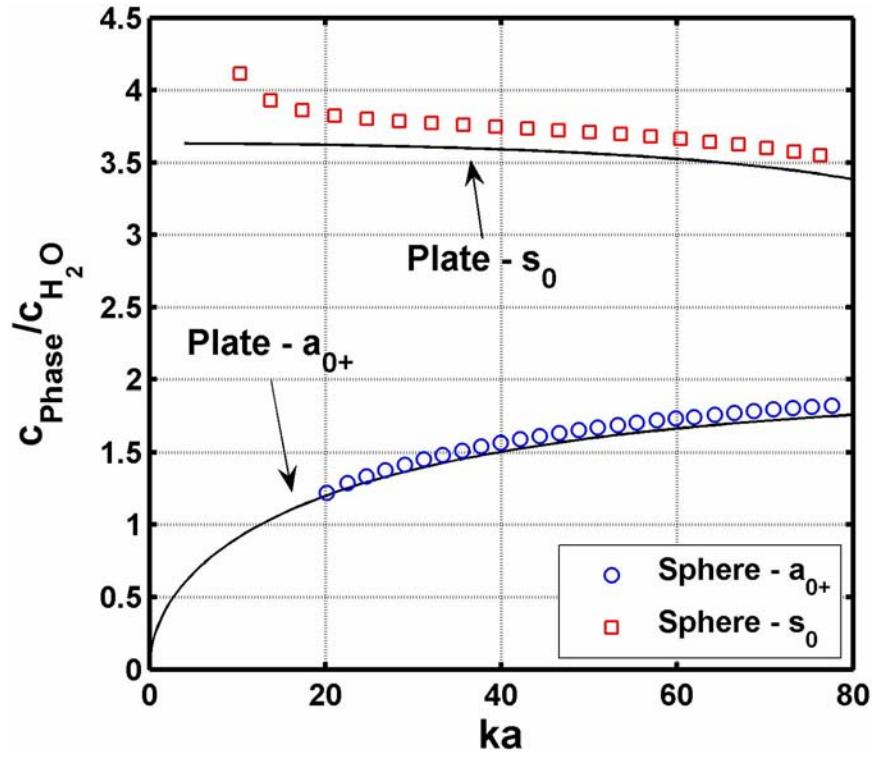


Figure 2.14: Dispersion curves of symmetric, s_0 , and asymmetric, a_{0+} , Lamb waves that propagate on a plate and on the standard spherical shell target. The waves' phase velocity is normalized by the sound speed of water, $c = 1479$ m/s, and plotted versus ka . Dispersion curves for plate waves are presented as solid lines and their types are labeled accordingly. Phase velocities of symmetric and asymmetric Lamb waves on the spherical shell are shown as squares and circles, respectively.

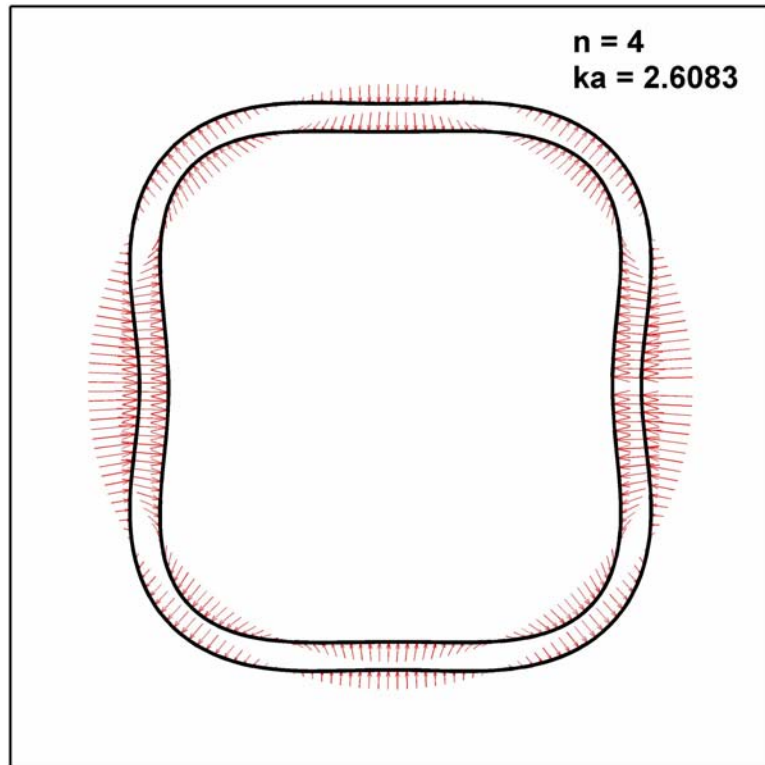


Figure 2.15: Plot depicting the displacement (from equilibrium) of the standard spherical shell's inner and outer surfaces at $ka = 2.6083$. The $n = 4$ term in the partial wave series solution of the target's response under steady state forcing is shown. The infinite plane wave exciting the target approaches from the left. The arrows are vectors showing the displacement of each surface of the shell from their un-deformed positions. The solid lines indicate the position of the shell's surfaces at the maximum deflection amplitude. The shell's displacement is scaled so that it is clearly visible for demonstrational purposes.

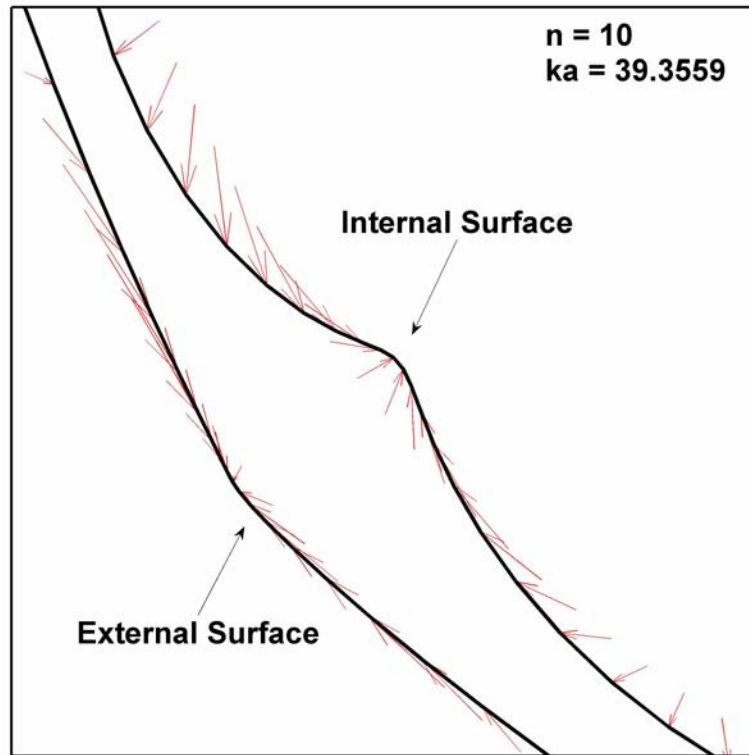


Figure 2.16: Plot depicting the displacement (from equilibrium) of the standard spherical shell's inner and outer surface at $ka = 39.3559$. The $n = 10$ term in the partial wave series solution of the target's response under steady state forcing is shown. The infinite plane wave exciting the target approaches from the left. The arrows are vectors showing the displacement of each surface of the shell from their un-deformed positions. The solid lines indicate the position of the shell's surfaces at the maximum deflection amplitude. The shell's displacement is scaled so that it is clearly visible for demonstrational purposes.

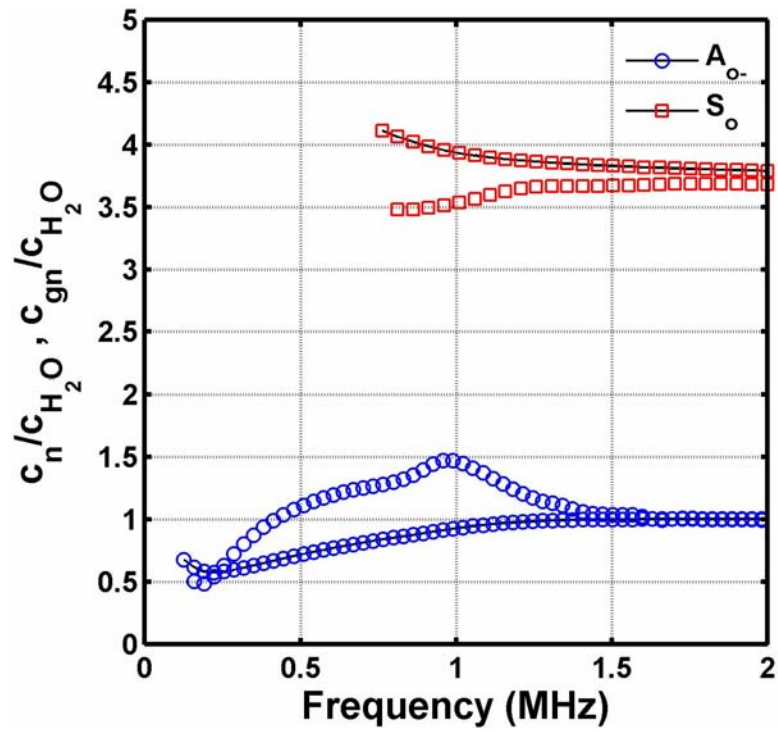


Figure 2.17: Phase and group velocities of symmetric, s_0 , and antisymmetric, a_{0-} , Lamb waves that propagate on the standard spherical shell target. The wave velocities are normalized by the sound speed of water, $c = 1479$ m/s, and plotted versus frequency over a range relevant to the current work. Phase velocities of symmetric and antisymmetric Lamb waves on the spherical shell are shown as squares and circles, respectively. The phase velocity results are interpolated with a solid line.

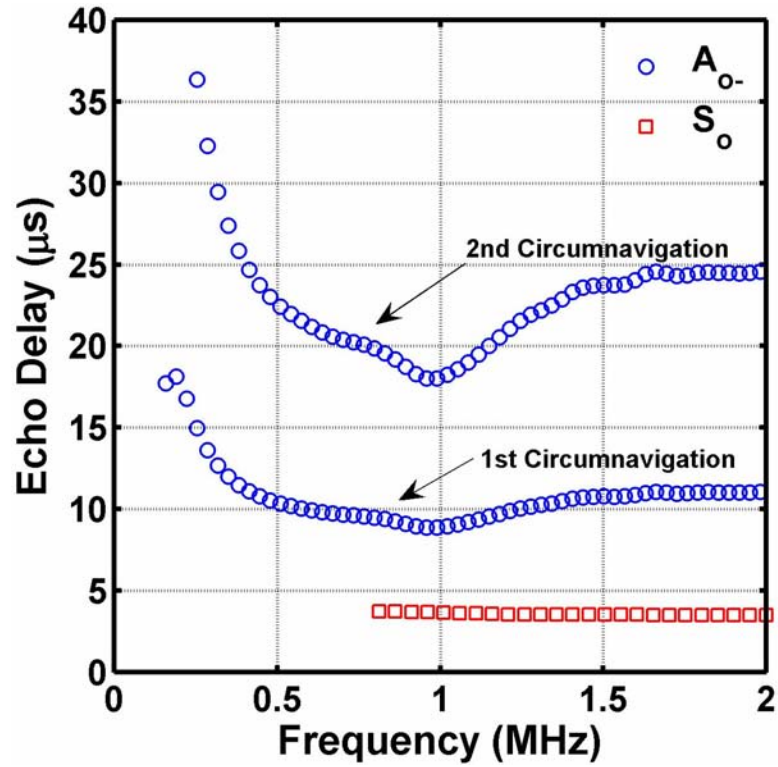


Figure 2.18: Echo delay with respect to the specular return versus frequency, of symmetric (s_0 , square) and antisymmetric (a_{0-} , circles) Lamb waves that circumnavigate the spherical shell target. The delays for both the first and second circumnavigations of the a_{0-} wave are shown.

Table 2.3. Comparison of predicted and measured echo delays, with respect to the specular echo, of symmetric, s_0 , and an antisymmetric, a_{0-} , Lamb waves propagating on the standard spherical shell target. Predicted values assume a frequency of 0.8 MHz.

Wave Type	Predicted Delay (μs)	Measured Delay (μs)
s_0 - 1 st circumnavigation	3.7	4
a_{0-} - 1 st circumnavigation	9.5	10
a_{0-} - 2 nd circumnavigation	19.9	21

Chapter 3

Methodology

“It doesn’t matter how beautiful your theory is, it doesn’t matter
how smart you are. If it doesn’t agree with experiment, it’s wrong.”

Richard P. Feynman

This chapter is devoted to a detailed description of the system employed in scaled laboratory experiments. In Section 3.1, an overview of the experimental setup is provided, detailing the physical setup as well as the electronic instrumentation. In order to ensure that the time reversal procedure is free to isolate resonances in the backscattering response of a target, any resonances present in response characteristics of the transducer or electronics employed must be equalized. A filter designed to account for the resonant response of the transducer and the electronics is described in Section 3.2. The sensitivity of this calibration filter to range and angle of incidence is investigated in Section 3.3. The response of the standard spherical shell target is measured experimentally in Section 3.4. The results of this measurement are compared to a

simulated result generated from the partial wave series model described in Chapter 2. Finally, the acoustic properties of the sediment phantom are characterized in Section 3.5.

3.1 Experimental Setup

Scaled time reversal experiments are conducted in a water-filled test tank located in the Underwater Sound Laboratory at Boston University. Monostatic pulse-echo experiments are conducted, in which the same transducer is used for the transmission and reception of acoustic energy. The transducer used is a 12.7 mm diameter Panametrics V-303 unfocussed broadband piston transducer. It possesses a nominal center frequency of 1 MHz with a quality factor of approximately 2. The transducer is mounted at the center of a 7 x 7 cm square acrylic baffle that is 12.7 mm thick. Metallic spheres and spherical shells are used as scattering targets and are either suspended in the free field, at the center of the tank, or buried within a sediment phantom, described below. A picture of the experimental setup is shown in Figure 3.1. The test tank is made of galvanized steel and has internal dimensions 0.75 m wide x 2.40 m long x 0.57 m deep. The tank is surrounded by a custom built aluminum frame to which a 3-axis positioning system is affixed. The positioning system affords control of the transducer's location in the vertical, and two orthogonally aligned horizontal directions. Both manually controlled micrometers and computer controlled Zaber T-LA Series linear actuators are used interchangeably for position control, depending on whether automated positioning is necessary for a particular experiment. The tank's water is filtered and degassed nightly using a particulate filter and pinhole degasser [95].

The primary target used in all experiments, the ‘standard spherical shell target’, is a 6.35-mm outer diameter air-filled spherical shell made of aluminium 3003. Several of these spheres were procured from the McMaster-Carr supply company. The target possesses a nominal inner to outer radius ratio of 0.91. It is positively buoyant and, for free field experiments, is suspended beneath a horizontal strip of $\sim 0.5 \mu\text{m}$ thick Scotch 3170 polypropylene packing tape, which spans the width of the tank. The tape is determined to be acoustically transparent through pulse-echo measurements. A photograph of this target configuration is presented in Figure 3.2. Targets are positioned at a distance of 10 cm from the transducer’s face; justification for this standing distance is discussed subsequently in Section 3.3.

For buried target experiments, the sphere is wrapped in a thin layer of nylon netting and secured using a piece of monofilament line to the bottom of a cubic acrylic container, 10 cm on a side with a wall thickness of 2 mm. A close up photograph of the target with and without the nylon netting is depicted in Figure 3.3. The container is filled with a sediment phantom consisting of a consolidation of spherical soda lime glass beads, such that the target’s center is buried at a depth varying from 1 cm to 4 cm. Samples of oceanic sediment with grain sizes a fraction of the smallest wavelength of interest were not readily available and thus, the glass bead consolidation is used as a substitute. In this document it is referred to as a glass bead sediment phantom or more simply a sediment phantom. A sieve analysis performed on a 250 mL sample of the beads revealed sizes ranging from 75 to 200 μm in diameter, with a mean diameter of 128 μm ; the mean grain size corresponds to approximately 1/10 of the smallest wavelength in the frequency range

of interest. The sediment phantom is initially prepared by slowly pouring the glass beads into degassed water and allowing the sample to sit, submerged within the test tank, for an extended period of time before scattering experiments are conducted. Subsequent observations show that the test tank and sediment sample are sufficiently gas free to eliminate any detectable echo returns from trapped gas pockets.

The transducer is positioned normally incident to the surface of the sediment at a standing distance of 10 cm. Scattering experiments from the sediment without a target in place indicate that reflections from the sides of the container are not present in backscattered returns and that the container is deep enough to allow time gate rejection of reflections from its bottom. To align the transducer, the spherical shell is unburied and the amplitude of the specular echo from the target is maximized. The target is then carefully reburied in the same position and the surface of the sediment is scraped flat.

A schematic of the experimental system in its buried target configuration is depicted in Figure 3.4. The thick solid line connecting instruments shows the path through which signals are transmitted. Software is used to generate all outgoing waveforms and is interfaced with a GAGE CompuGen 4300 D/A board. Once a waveform is loaded to the D/A board it is passed through an AR Model 25A250 power amplifier, routed through a Ritec RDX-6 passive diplexer, and sent to the transducer. The diplexer also contains a diode clamp, which prevents high amplitude signals from entering the preamplifier in transmit mode, and a diode expander, which limits interference from noise generated at the power amplifier in receive mode. The thick dashed line in Figure 3.4 displays the path through which received signals are routed.

Received signals are low pass filtered below 2 MHz using an active Krohn Hite 3905B filter/preamplifier, monitored in real time using a Tektronix 2465 analog oscilloscope, and acquired with a GAGE Compuscope 14200 A/D board with 14 bit dynamic range. The dotted line in Figure 3.4 displays paths over which signals are sent to control the timing of electronic instrumentation. A function generator is used to trigger both the D/A and A/D boards at a pulse repetition frequency of 100 Hz. The A/D board is operated at a sampling rate of 25 MHz and supplies a clock signal at the same frequency to the D/A board.

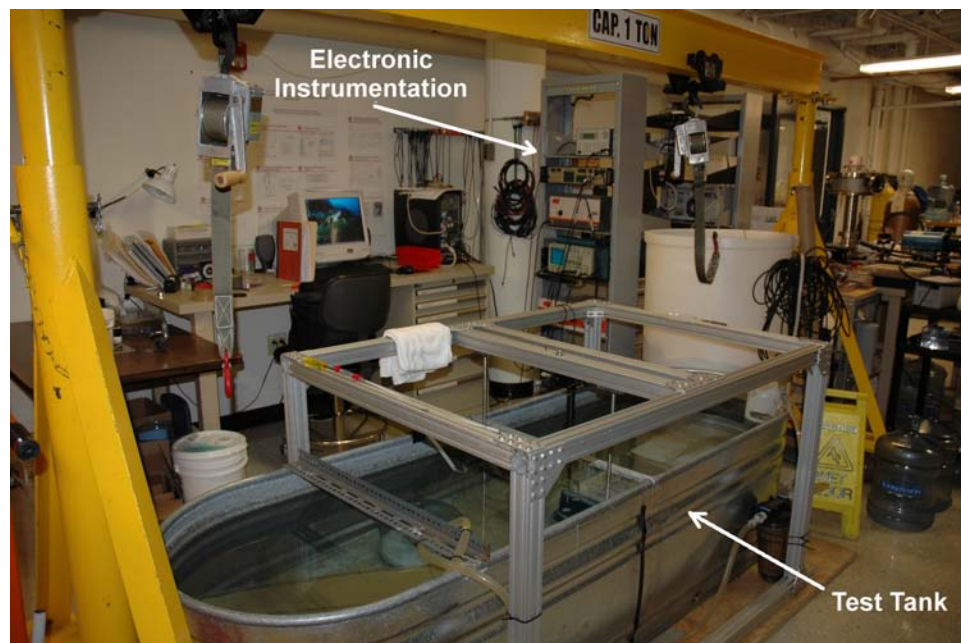


Figure 3.1: Picture of experimental setup. In the foreground is the steel test tank in which time reversal experiments are carried out. The tank is surrounded by an aluminum frame to which positioning equipment is mounted. In the background, behind the tank, is the electronic instrumentation rack and computer workstation controlling the experimental system.

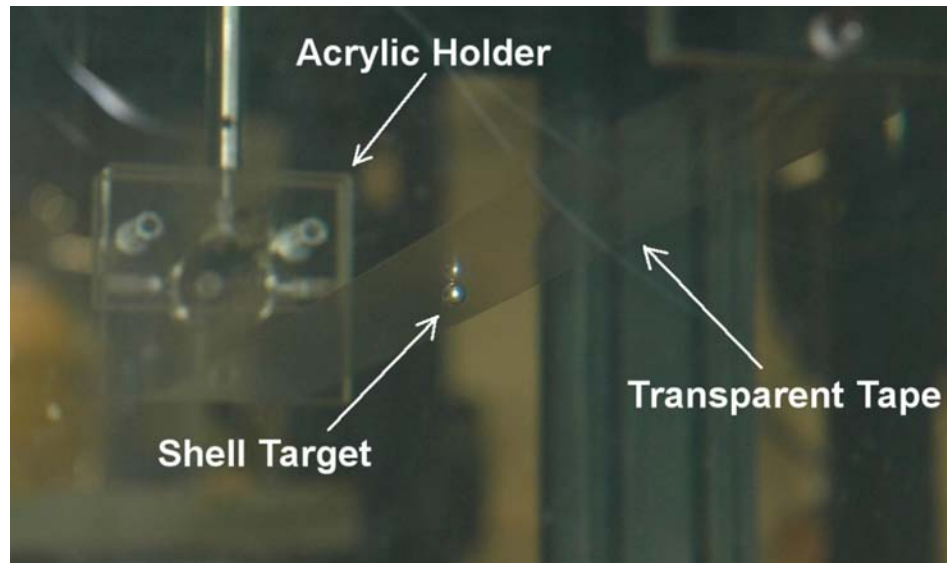


Figure 3.2: Picture of the aluminum spherical shell target suspended in the free field, at the center of the test tank. The target is positively buoyant and is held in place by a layer of $\sim 0.5\mu\text{m}$ Scotch 3170 polypropylene packing tape that spans the width of the tank. The tape is clamped in place with manually fashioned acrylic holders.

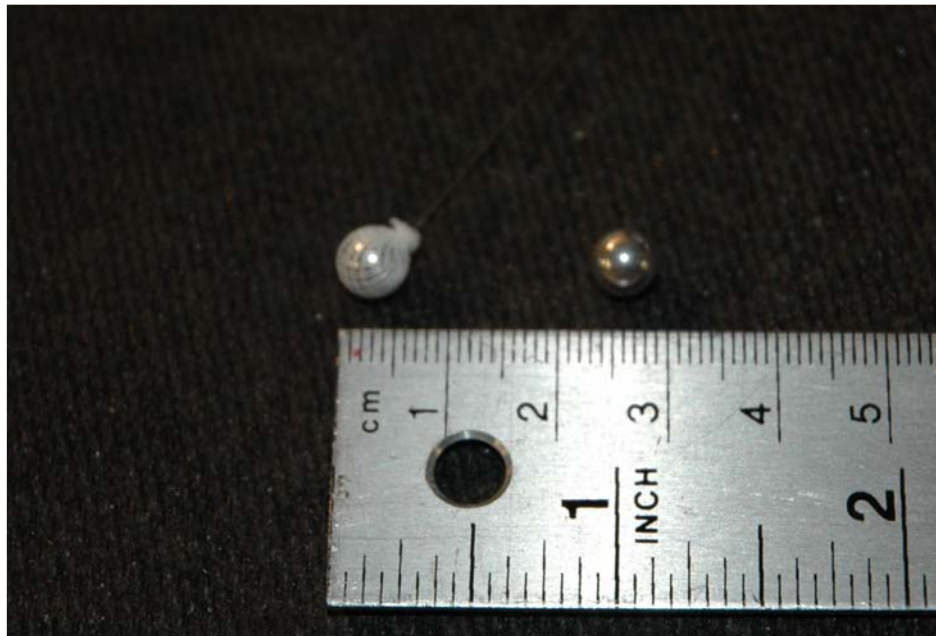


Figure 3.3: Picture of the standard aluminum spherical shell target free-standing (to the right) and wrapped in a thin layer of nylon netting that is secured using a piece of monofilament line.

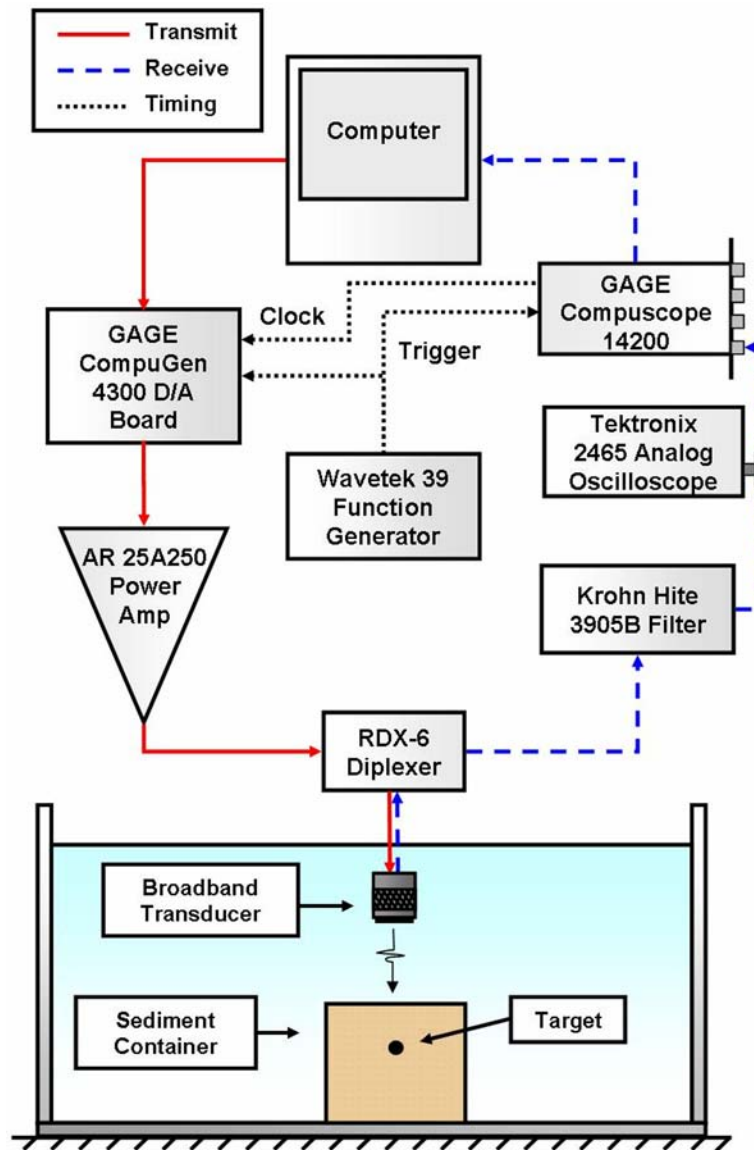


Figure 3.4: Diagram of experimental instrumentation used in time reversal experiments. Experiments are performed both with targets suspended in the free field beneath a layer of transparent tape and buried in a container filled with a sediment phantom. This illustration depicts the configuration used for buried target experiments.

3.2 System Calibration

For the iterative time reversal process to be free to converge without bias to any target resonance within the bandwidth of the transducer, the response of the transmit-receive system must be flat within this bandwidth. Since no real transducer possesses this specification, a digital filter is designed to flatten the combined transmit-receive response. The filter design procedure is similar to the ones employed in Refs.[96, 97]. A system diagram that summarizes the design of this filter is given in Figure 3.5. Under the assumption that scattering experiments are linear and time invariant, the measured return from a scattering target in the frequency domain is of the form

$$R(\omega) = K_t(\omega) K_r(\omega) G(\omega) E(\omega), \quad (3.70)$$

where $K_t(\omega)$ [Pascal/volt] and $K_r(\omega)$ [volt/Pascal] are the frequency responses of the transducer upon acoustic transmission and reception, respectively, $G(\omega)$ is the backscattering response of the target, and $E(\omega)$ is the driving signal sent to the transducer. To determine the combined transmit-receive response, $K_t(f) K_r(f)$, the transducer is pointed vertically up at the free-water surface, which is taken to be a flat pressure-release surface. A pulse, $e_0(t)$, is then transmitted and a pulse, $r_0(t)$, reflected from the surface is received. The Fourier transforms of the transmitted pulse and surface return are $E_0(\omega)$ and $R_0(\omega)$, respectively.

The transmitted waveform, shown in Figure 3.6a in the time domain and Figure 3.6b in the frequency domain, is a 100 μs duration linear frequency modulated chirp

sweeping frequencies 10–2200 kHz. This frequency range encompasses the full bandwidth of the transducer used. The waveform is designed such that its magnitude spectrum is flat over the $\sim 400\text{--}1600$ kHz band. Returns from the free-water surface are coherently averaged 2000 times. The resulting averaged waveform is shown in the time and frequency domains in Figures 3.6c and 3.6d, respectively. This waveform is characteristic of the frequency response of the V-303 transducer, with a center frequency of 1 MHz, and a quality factor of ~ 2 . The reader should note that it is especially important to allow the tank water to sit undisturbed for an extended period of time, such that oscillations of its surface reach a low amplitude steady state. In these experiments the tank is not perfectly isolated from vibrations of the laboratory floor and very low frequency oscillations of the water surface pervade the measurements. However, with averaging, the free-surface reflections are found to be sufficiently coherent for application of the calibration technique. An inverse filter $H(\omega)$ can then be generated using the transmitted and received waveforms by taking their reciprocal,

$$H(\omega) = -\frac{E_0(\omega)}{R_0(\omega)}, \quad (3.71)$$

where the negative sign accounts for the 180° phase shift at the pressure release surface.

However, in order to avoid singularities in the inverse filter's response due to small values of $R_0(\omega)$ at certain frequencies, it is constructed using a Weiner filter [98] such that

$$H(\omega) = \frac{-E_0(\omega)R_0^*(\omega)}{|R_0(\omega)|^2 + \varepsilon}, \quad (3.72)$$

where $\varepsilon \ll |R_0(\omega)|^2$ within the frequency of range of interest. For the calibration procedure described here, a value of $\varepsilon = 1 \times 10^{-6}$ is used. The magnitude response of the filter generated by equation (3.72) is shown as a dashed line in Figure 3.7a. This type of filter is typically sufficient to equalize transducer resonances. However, the time reversal procedure is extremely sensitive to the system response and a number of experiments show that the large peaks on either side of the transducer's bandwidth (see Figure 3.7a) have the effect of introducing false resonances into the system. That is, without a target in place, the time reversal procedure spuriously converges to one of these peaks.

In order to mitigate this effect, a polynomial fit of the Weiner filter response is performed over the 0.4-1.6 MHz frequency band shown by the shaded grey regions in Figure 3.7. The 'windowed' fit is then exponentially extrapolated outside this frequency range with a function proportional to $(1 - e^{-\eta\omega})$. The exponent, $\eta = 1 \times 10^{-6}$, is specified manually so that the extrapolated response is smoothly varying over the entire frequency range. A Yule-Walker recursive digital filter design function [99, 100] then operates on the polynomial fit to generate the coefficients of an infinite impulse response filter of order 50. The filter is then applied to return waveforms via a direct form II transposed implementation. The magnitude response and phase responses of this filter are presented as a thick solid lines in Figures 3.7a and 3.7b, respectively. These are both smoothly varying over the entire frequency range shown. The filter's phase delay and group delay are shown in Figure 3.7c. The group delay of a filter approximately represents the amount of time the envelope of a signal will shift upon application of the filter. Although

the calibration filter possesses nonlinear phase, the maximum group delay is less than 1 μs over the useable bandwidth. This is a fraction of the smallest window size studied in the current work and observations show that application of the filter does not significantly distort return signals. Finally, an additional low pass filter (not shown in Figure 3.7) is applied to help improve the fit between the ‘Yule Walker’ response and the Wiener filter response toward the high frequency end of the useable system bandwidth (see the right side of the shaded gray box in Figure 3.7a).

The resonances of the transducer are then removed from measured echoes through application of the inverse filter, where now calibrated returns are of the form

$$R(\omega) = K_t(\omega) K_r(\omega) H(\omega) G(\omega) E(\omega). \quad (3.73)$$

Since $H(\omega)$ and $K_t(\omega) K_r(\omega)$ are inverses within the frequency range of interest, the calibrated return is simply a product of the responses of the outgoing pulse and the scattering response of the target. This allows the iterative time reversal technique to be free to converge without bias to the dominant backscatter mode(s) of the target.

The inverse filter is tested by pointing the transducer at the free-water surface and transmitting the linear frequency modulated chirp depicted in Figure 3.6a in the time domain and in Figure 3.6b in the frequency domain (this is the same waveform used to generate the filter). Again, the backscattered return from the free-water surface, depicted in Figures 3.6c and 3.6d as a solid line, is characteristic of the transducer’s resonant response. The magnitude response of the generated calibration filter is presented as a dashed line in Figure 3.6d. When applied to the free surface return, the inverse filter normalizes the transducer’s response, resulting in the waveform presented in Figures 3.6e

and 3.6f. As observed in these figures, this calibrated waveform is a relatively accurate replica of the initial outgoing pulse. Therefore, it is now safe to assume that the system response has been successfully normalized and that the transducer's resonances will not interfere with convergence of the time reversal procedure to a resonance in the scattering response of a target. As evident in Figure 3.6f, the usable bandwidth of the system is between approximately 0.4-1.6 MHz. The magnitude of the calibrated system response varies by less than 10% from its mean value over this frequency range. As a final note, to be discussed in further detail in the next section, the reader should be aware that, if a flat system response is desired, any subsequent scattering experiments should be carried out at the same standing distance and angle of incidence at which the calibration is performed.

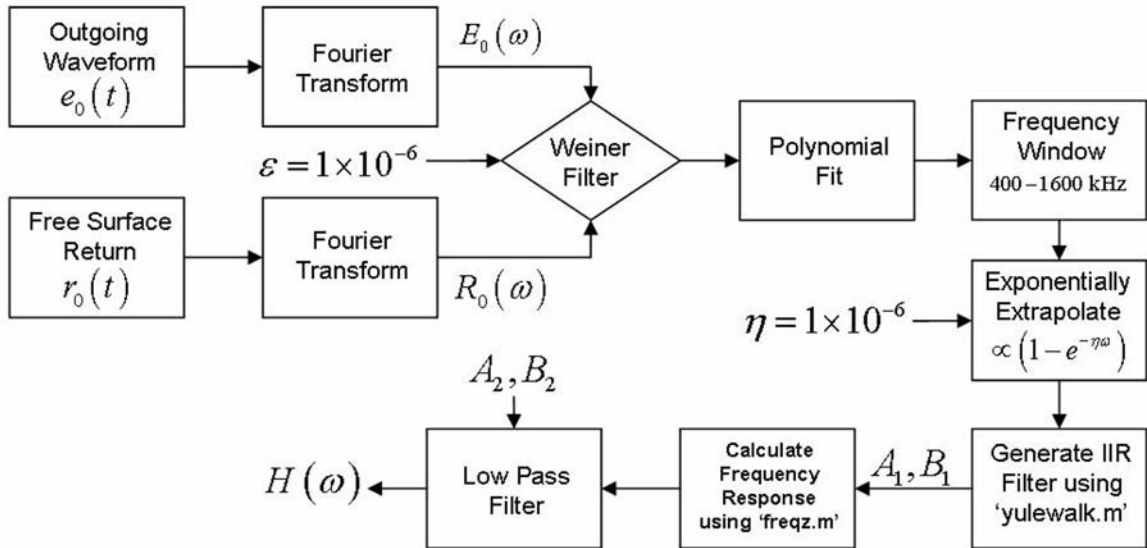


Figure 3.5: System diagram for generation of the calibration filter used in scattering and time reversal experiments.

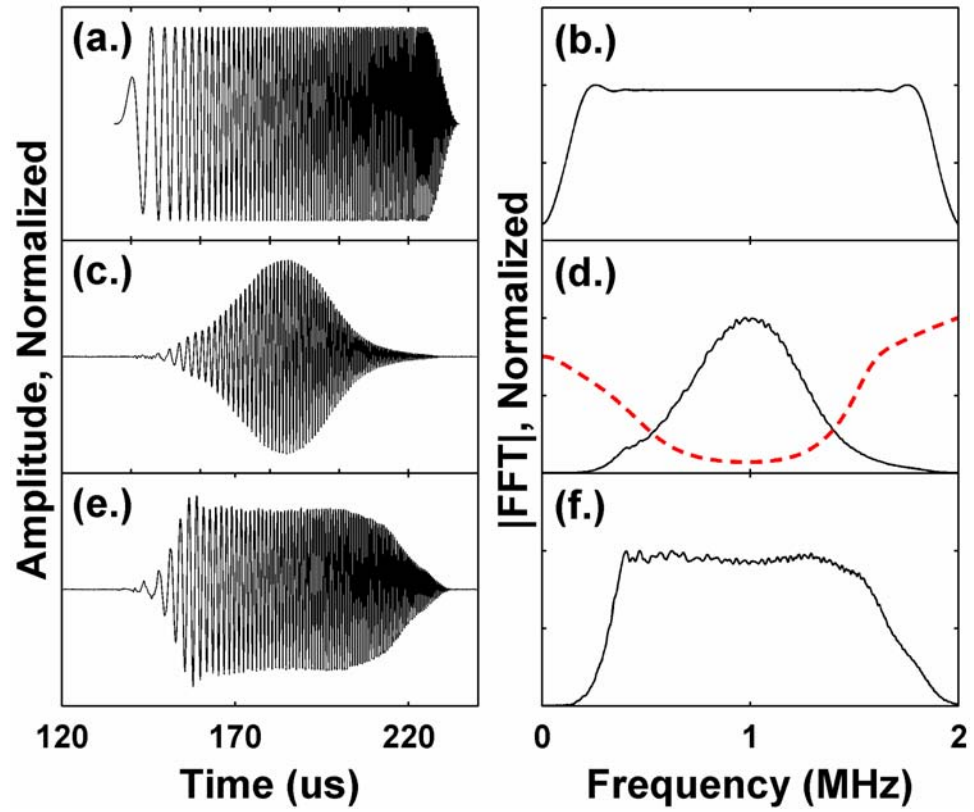


Figure 3.6: Waveforms and associated spectra from tests of the normalization procedure for the Panametrics V-303 unfocussed broadband, $Q \sim 2$, piston transducer nominally centered at 1 MHz. (a.) Linear chirp driving voltage sent to the transducer in which the transmitted pulse is directed normally at the pressure release water surface. (b.) Magnitude spectrum of (a). (c.) Transducer voltage for the first reflection from the pressure release tank surface. (d.) Solid line is the magnitude spectrum of (c) and the dashed line is the magnitude response of the inverse filter used in the transducer calibration procedure. (e.) Waveform (c) after application of the inverse filter. (f.) Magnitude spectrum of (e). The amplitude in all subplots is normalized to the maximum value and plotted on a linear scale.

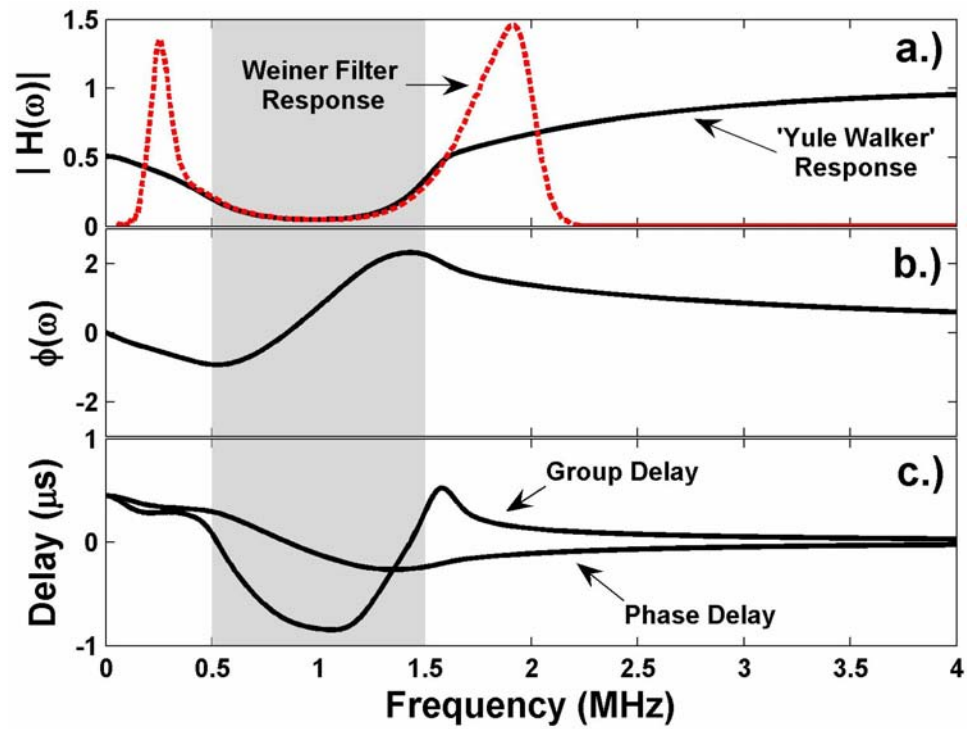


Figure 3.7: Response of the system calibration filter used in time reversal experiments plotted versus frequency. (a.) The thin dashed line is the magnitude response of the Weiner filter. The thick solid line is the magnitude response of the final calibration filter designed using the Yule Walker method. (b.) Same as (a) but the phase response of the Yule Walker filter is plotted over the same frequency range. (c.) The phase delay and group delay of the Yule Walker filter. The solid gray box in both subplots shows the full bandwidth of interest.

3.3 Transducer Characteristics

Ultrasonic piston transducers are known to generate pressure fields that exhibit complicated spatial variability. In this section, the sensitivity of the calibrated system is investigated with respect to range and angle of incidence. A model of sound radiation from a baffled piston is used to verify experimental observations and to determine constraints that must be imposed on the operational configurations of the system. An understanding of these effects will be important subsequently in guiding the interpretation of results from time reversal experiments.

3.3.1 Range Dependence

An analytical prediction of the pressure field radiated by a baffled circular piston provides a reasonable model for the field generated by the Panametrics V-303 transducer used in time reversal experiments. This field is classically modeled by the Rayleigh integral [78],

$$p(x, y, z, t) = \frac{-ik\rho_0 c_0 u_0 e^{-i\omega t}}{2\pi} \int_S \frac{e^{ikR}}{R} dS, \quad (3.74)$$

where ρ_0 is the density of propagation medium, c_0 is the sound speed, k is the wave number, $u_p = u_0 e^{-i\omega t}$ is the velocity of the piston face, and R is the distance from a point on the piston's face to a point in the field. Equation (3.74) is analytically tractable for only a small number of special cases. One such case is for the pressure distribution along the axis of a piston, which reduces to

$$p(r) = -i2P_0 \sin \left[(k/2) \left(\sqrt{r^2 + a^2} \right) - r \right] e^{i(kr + \xi - \omega t)}. \quad (3.75)$$

P_0 is the driving pressure amplitude, r is the axial distance from the face of the piston, a is the piston radius, and $2\xi = k\left(\sqrt{r^2 + a^2} - r\right)$ is a phase term. In cases where equation (3.74) is not analytically tractable it is solved numerically as, for example, in Refs. [101, 102].

Using the formulation in Ref. [102], the pressure field radiated by a 12.7 mm diameter piston driven at 1.6 MHz is calculated. This is the highest operational frequency of the calibrated transducer and is thus the frequency at which diffraction is most likely to impact the transmit/receive beam pattern at ranges of interest. The magnitude of the calculated pressure field, normalized to the maximum value, is presented in Figure 3.8a up to an axial distance of 150 mm and a radial distance of 12.5 mm. The magnitude of the *on-axis* pressure distribution, calculated from equation (3.75), is plotted in Figure 3.8b. Superimposed on Figure 3.8a are vertical lines at axial positions of 43 mm, 100 mm, and 137 mm. These lines intersect the on-axis location of the piston's nearfield distance, the standing distance used in time reversal experiments, and the Rayleigh distance of the piston, respectively. The Rayleigh distance of a baffled flat piston transducer, defined as [78]

$$R_0 = \frac{ka^2}{2} \quad (3.76)$$

specifies the approximate distance to the “farfield”. Beyond this distance, the pressure field can be considered to be spherically spreading, that is, its amplitude decays with a dependence of $1/r$. In addition, the pressure field in this region is, in general, smoothly varying spatially, as observed in Figure 3.8.

The nearfield distance is defined here as the location of the last peak in the on-axis pressure distribution. As evident in both subplots in Figure 3.8, the spatial pressure distribution within the nearfield is characterized by a complicated interference pattern, possessing a large number of peaks and nulls. Experiments conducted within this region are extremely sensitive to spatial misalignment and would be ill-suited for the current work. As observed in Figure 3.8, the spatial pressure distribution between the Rayleigh distance and the nearfield distance is relatively smoothly varying. As such, a nominal standing distance of 10 cm between the face of the transducer and the closest target of interest is selected for all experiments performed in this work. This distance is selected because the amplitude of measured target echoes is found to be sufficiently high. The 6-dB beamwidth of the transducer at a driving frequency 1 MHz is 7° . This results in insonification of a circular area that is approximately 1.2 cm in diameter at the 10 cm standing distance.

A study of the sensitivity of the system response to variations in range is conducted for standing distances near 10 cm. The same linear chirp shown in Figure 3.6a is transmitted at the free-water surface of the tank with the transducer aligned at normal incidence. A bubble level temporarily placed on the face of the transducer is used to confirm the angle of incidence, as the free-water surface is always level. For standing distances ranging from 8 cm to 12 cm in steps of 0.5 cm, Figure 3.9 shows the magnitude of the Fourier transform of scattered returns after calibration. As evident from this figure, the shape of the system response does not vary appreciably as the standing distance is varied over this range. This indicates that small errors in aligning the standing distance

of the transducer should not introduce an undesired bias in the frequency response of the system.

The circles superimposed on Figure 3.8b indicate the spectral magnitude taken from each trace in Figure 3.9 at a frequency of 1.6 MHz. The axial location of each data point in Figure 3.8b is twice the value of the range value stated in Figure 3.9. This is because the total distance traveled by received waveforms is equal to twice the range value. The values of the measured data are normalized so that the mean value over all measurements is equal to the mean value of the predicted response over the same axial range. The trend of both the measured and predicted pressure magnitudes shows cursory agreement, decreasing as the standing distance is increased. However, there are significant discrepancies between the measured and predicted values. To determine whether these are associated with error in the range setting, error bounds for the measured data (not shown in Figure 3.8) are generated by predicting the possible variation in pressure magnitude due to uncertainty in the range. Error bounds generated from uncertainties as high as ± 1 cm, an overly conservative estimate, do not fully account for the discrepancies between the predicted and measured axial pressure distribution. Therefore, variations in this data are likely due to angular misalignment of the transducer, a parameter to which the system response is especially sensitive, as will be seen in the next section. This is also confirmed upon examination of Figure 3.9 in which the pressure magnitude observed fluctuates more noticeably at higher frequencies, where the beam is narrower and thus the pressure scattered from the flat surface is more sensitive to angular misalignment.

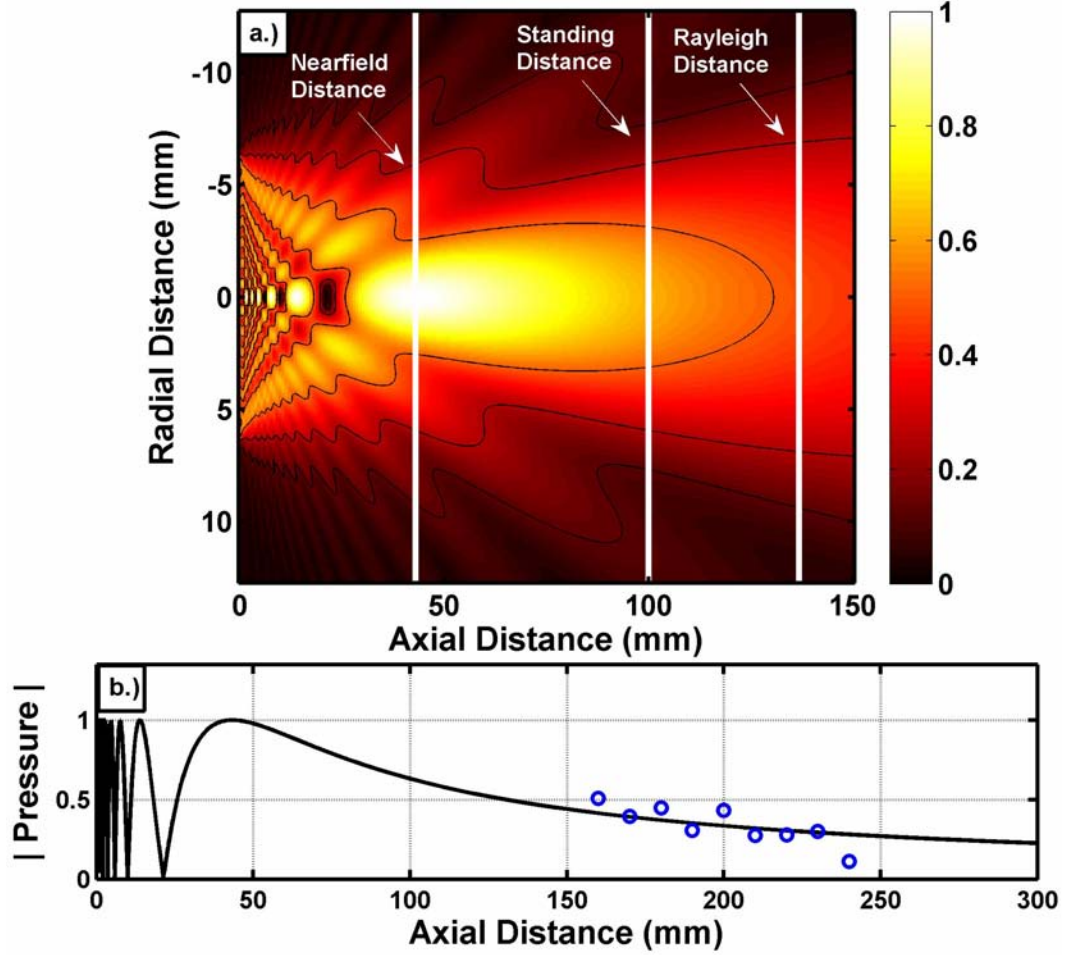


Figure 3.8: Magnitude of the pressure field radiated from a circular baffled piston for a driving frequency of 1.6 MHz. The piston is 6.35 mm in radius, the same radius as the Panametrics V-303 transducer used in time reversal experiments. (a.) Magnitude of the pressure field as a function of axial and radial distance from the center of the piston. Thin black lines represent contours of constant pressure magnitude, marking relative values of 0.5, 0.25, and 0.125. Vertical white lines intersect the on-axis location of the nearfield distance, the standing distance used in experiments, and the Rayleigh distance of the piston; the positions of these lines all scale linearly with frequency (see equation (3.76)). (b.) The solid black line represents the magnitude of the pressure distribution along the central axis of the piston. Circles represent measured values, normalized to the mean value of the predicted pressure at the same axial standing distance. The piston is positioned at the left side of each figure. Predicted values in both plots are normalized to their respective maximum value.

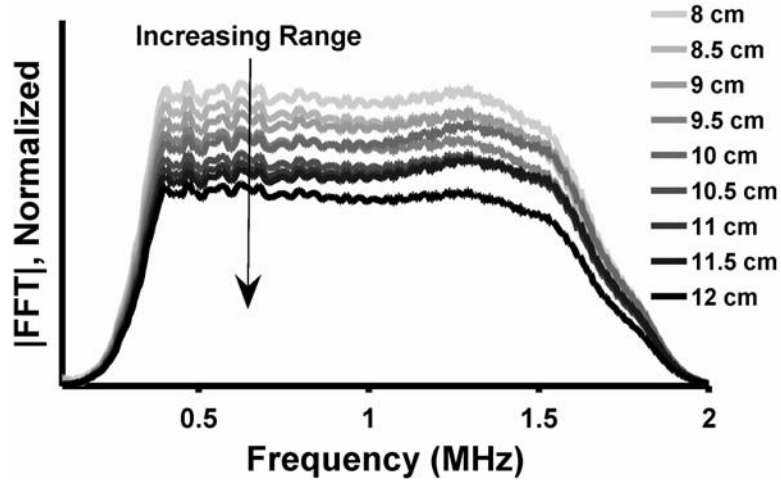


Figure 3.9: Magnitude spectra of waveforms backscattered from the free water surface given a linear chirp spanning 0.4-1.6 MHz, the useable bandwidth of the calibrated transducer. The standing distance between the transducer's face and the free water surface is varied in steps of 0.5 cm between 8 cm and 12 cm.

3.3.2 Angle Dependence

In order to examine the dependence of the system's frequency response on the angle of incidence, the transducer is initially positioned normally incident to the tank's free water surface at a distance of 10 cm. A linear chirp spanning 0.4-1.6 MHz, the useable bandwidth of the calibrated transducer, is transmitted and a backscattered waveform is received. This process is repeated at incident angles of 1-5 degrees, in steps of 1 degree, as well as at 10, 15, and 20 degrees. A 10 cm standing distance between the center of the transducer's face and the free water surface is maintained at all angles of incidence.

In Figure 3.10, the magnitude spectrum of the waveform backscattered from the free water surface is presented for each angle of incidence, after application of the calibration filter. Each result is normalized to the maximum amplitude recorded among all angles. At an incident angle of 0 degrees, the response is flat over the entire system

bandwidth. However, as the transducer is rotated to larger angles of incidence, a bias towards lower frequencies appears in the system response. This is because the calibration filter does not take into account the frequency dependence of the transducer's beam pattern.

The angular dependence of the transducer's beam can be modeled by an analytical prediction of the farfield directivity factor for a baffled vibrating piston,

$$D(\theta) = \frac{2J_1(ka \sin \theta)}{ka \sin \theta}. \quad (77)$$

Here, J_1 is a Bessel function of the first kind and order 1, k is the acoustic wavenumber in water, a is the radius of the piston, and θ is the angle from an axis extending from the center of the transducer's face. The directivity is plotted in Figure 3.11 for driving frequencies of 0.4, 1, and 1.5 MHz. For a driving frequency of 1.5 MHz, at incident angles greater than 5 degrees, the directivity of the transducer's main lobe is less than 10% of its maximum value. A similar decrease is observed for a 1 MHz driving frequency at angles greater than 7 degrees and for a 0.4 MHz driving frequency at angles greater than 18 degrees. These predictions show qualitative agreement with the results presented in Figure 3.10. The effect is especially apparent for an incident angle of 10 degrees. At this angle, the system's response consists of a peak centered at 0.4 MHz. At 1 and 1.5 MHz the response from the free water surface is negligible. At an incident angle of 20 degrees, the backscattering response from the surface is negligible at all frequencies. In these experiments, the directivity of the transducer acts as an additional filter that modifies the total response of the system.

The angular dependence of the system response is then examined with the transducer positioned at a standing distance of 10 cm over the surface of the glass bead sediment phantom. The results, presented in Figure 3.12, are qualitatively similar to those in Figure 3.10 but with a slightly larger bias toward lower frequency occurring at all angles of incidence. Whereas the free water surface acts as a perfect specular reflector, returns from the sediment include contributions from volume scattering and surface roughness. Because the calibration procedure is performed with the transducer facing the free water surface, it does not take into account these additional effects, and thus the system response is further shifted towards lower frequency, where these surface features are less influential. As will be seen in subsequent experiments, due to the sensitivity of the time reversal procedure to the system response, an understanding of the effects of angular alignment is especially important when operating at non-normal angles of incidence.

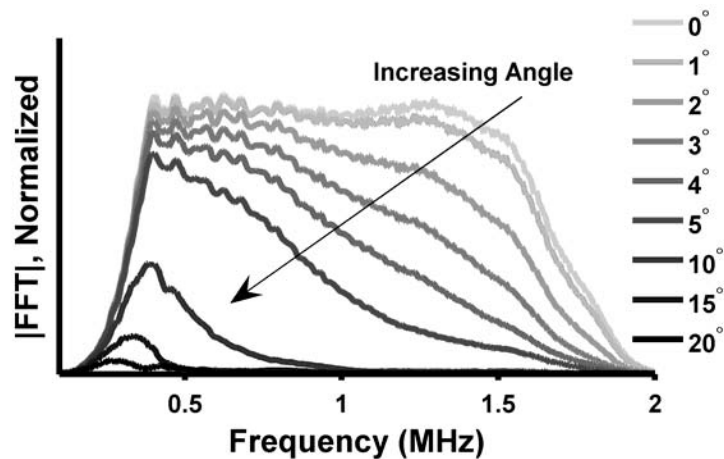


Figure 3.10: Magnitude spectra of waveforms backscattered from the free water surface given a linear chirp spanning 0.4-1.6 MHz, the useable bandwidth of the calibrated transducer. The transducer is positioned at a standing distance of 10 cm and angles of incidence range from 0-20 degrees.

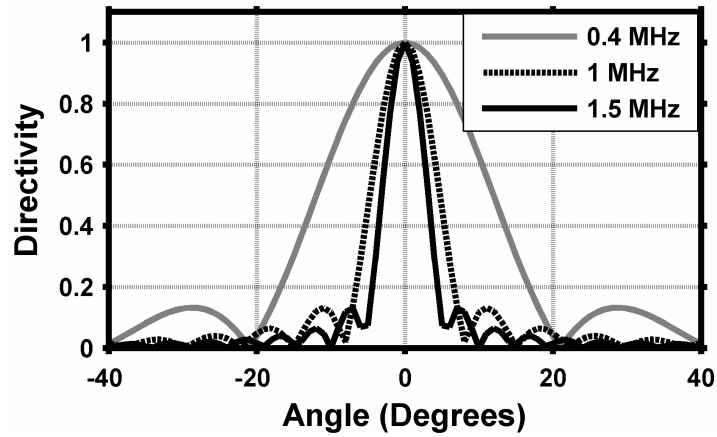


Figure 3.11: Transducer directivity factor as a function of angle for frequencies of 0.4, 1, and 1.5 MHz.

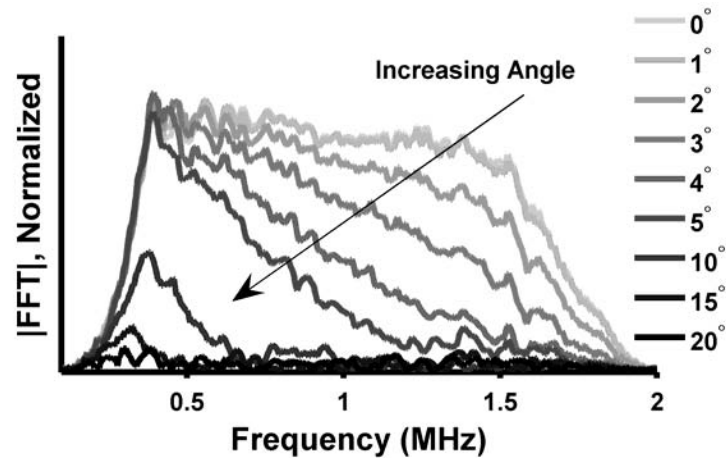


Figure 3.12: Magnitude spectra of waveforms backscattered from the glass bead simulated sediment surface given a linear chirp spanning 0.4-1.6 MHz, the useable bandwidth of the calibrated transducer. The transducer is positioned at a standing distance of 10 cm and angles of incidence range from 0-20 degrees.

3.4 Target Characterization

To test further the system calibration and to find the free-field resonances of the standard spherical shell target, an experimental measurement of the backscatter response of the target is compared with an analytical model. To measure the response of the target experimentally, it is suspended in the free field and interrogated with a $100\ \mu\text{s}$ linear chirp spanning 0.4 to 1.6 MHz. The backscattered return is then calibrated. The result is presented as a dashed line in Figure 3.13b in the frequency domain, normalized to its value at 800 kHz, and in Figure 3.13c in the time domain, normalized to its maximum amplitude. The response in Figure 3.13b is proportional to the magnitude of the monostatic far-field form function of the target band limited by the frequency response of the measurement system.

The form function of the target is computed using the formulation presented in Chapter 2. Form function calculations are sensitive to the geometric and material properties of a target as well as the ambient medium properties. As such, several of these properties are carefully measured. The procedures for estimation of the target parameters are presented first. A Fowler model A193 micrometer with 0.001 mm resolution is used to measure the outer diameter (radius) of the target. Fifty measurements, performed by manually rotating the sphere within the micrometer between measurements, reveal an outer radius of 3.182 mm (3.179-3.184; 95%).

A nominal density of $2740\ \text{kg/m}^3$ for aluminum 3003 is reported by the purveyor of the target spheres. The density of the target material is measured with a Mettler AT200 scale that allows one to take advantage of Archimede's principle. That is, by

measuring the mass of a sample material in air, m_{dry} , and also when submerged in water, m_{wet} , the density can be determined as,

$$\rho = \frac{m_{dry}}{V} = \frac{m_{dry}\rho_{H_2O}}{(m_{dry} - m_{wet})}. \quad (3.78)$$

Here, ρ_{H_2O} is the density of water and V is the volume of the material sample. Four targets, shipped in the same package as the target used in the acoustic response measurement, are cut open so that the inner cavity is exposed. The dry mass of each sample is then measured on the scale 30 times. A sample of water that is allowed to degas for several hours is then poured into a container within which the scale is suspended. From a measurement of the water temperature, 24.4°C, the water density is calculated to be 997.2 kg/m³ [103]. Repeated measurements show that the temperature does not shift significantly over the period of time in which mass measurements are performed. Samples of the target material are then submerged in the water and placed on the scale. Observations show that the material wets readily. Any bubbles persisting on the surface of the material are removed physically by scraping. Thirty mass measurements are performed on each of the four samples when submerged. Applying equation (3.78) to the measured data, the density of the shell material is determined to be 2725.1 kg/m³ (2586.0-2857.0; 95%).

The wall thickness of the shell target used in the acoustic response measurement is then determined by assuming that the inner and outer surfaces of the shell are perfectly spherical. The narrow range of uncertainty in outer diameter measurements (5 μ m)

shows that this is a valid assumption for the outer surface. Examining the four targets cut open for density measurements reveals that this should be a reasonable assumption for the inner surface as well. The dry mass of the target is measured to be 90.2 mg (89.6-90.8; 95%). The wall thickness is then calculated as

$$t = a - \left(a^3 - \frac{3m}{4\pi\rho^2} \right)^{1/3} \quad (3.79)$$

where a is the outer radius of the target, m is the mass of the target and ρ is the measured material density. The inner radius of the target is then determined by subtracting the wall thickness value from the outer radius, $b = a - t$.

The value of the elastic modulus of aluminum 3003 is taken as that reported by the manufacturer of the target, $E = 68.9$ GPa. The value of Poisson's ratio is taken as $\sigma = 0.33$ [78]. These two values are used to calculate the dilatational wave speed and shear wave speed of the material, along with both Lamè coefficients. For quick reference, the material properties of aluminum used in form function calculations are summarized in Table 3.1.

Table 3.1: Material properties used in the analytical prediction of the monostatic farfield form function of the aluminium spherical shell target.

	ρ (kg/m ³)	c_d (m/s)	c_s (m/s)	E (GPa)	σ	λ (GPa)	μ (GPa)
Al 3003	2680.0	6171.8	3108.9	68.9	0.33	50.3	25.9
Water	998.1	1483.8	-----	-----	-----	-----	-----
Air	1.0	340	-----	-----	-----	-----	-----

Also provided in this table are the density and sound speed of air, the interior fluid of the target, taken from tabulation [104]. The density and sound speed of the tank water are determined from calculations making use of a temperature measurement of 20.5 °C [103, 105].

The form function prediction is found to be convergent in the frequency range of interest upon summation over 44 modes, following the convention in Ref. [106]; partial wave series models typically converge through summation over $\sim 1.6(ka)_{\max}$ modes. A frequency spacing of 3052 Hz in the calculation provided adequate resolution. Decreasing the spacing does not reveal additional structure in the calculated form function up to 2 MHz. To generate a waveform for comparison with the experimentally measured target response, the analytically predicted form function, f_{∞} , is substituted in equation (3.73) for the target's backscattering response, $G(\omega)$, along with the transducer's measured transmit-receive response, $K_t(\omega)K_r(\omega)$ shown in Figure 3.6d. The magnitude of the Fourier transform of the simulated return after calibration is presented as a solid line in Figure 3.13b. It is normalized to its value at 800 kHz for comparison with the experimental result. The time domain response, shown as a solid line in Figure 3.13c, is calculated through an inverse Fourier transform and is normalized to its maximum amplitude. A cross-correlation between the simulated and measured target responses is used to determine the appropriate delay for the simulation and align the waveforms for comparison.

Agreement between the experimentally measured and simulated responses in both Figures 3.13b and 3.13c indicates that the inverse filter used for calibration does effectively account for the transducer's response. Additional time traces shown in Figure 3.14 demonstrate further agreement between predicted and measured returns. A numerical routine that calculates the error between the measured and simulated responses reveals that through variation of the shell density within its measured uncertainty to a value of 2680.0 kg/m^3 , a minimum normalized mean squared error (NMSE) of 4.54% is obtained. The grey shaded region in Figure 3.13b shows the 650-1650 kHz frequency range over which the error is computed. The NMSE is presented in Figure 3.15 as a function of density with a vertical dashed line marking the density value reported by the supplier of the target. Subsequent error minimization is performed by varying the elastic modulus of the target material $\pm 5\%$ from its nominal value while fixing the density at 2680.0 kg/m^3 . This reveals that the reported value is sufficiently accurate; variation yields a less than 1% improvement in NMSE as observed in Figure 3.16. Subsequent references to numerical scattering simulations in this work make use of the technique used to generate the simulated returns shown in this section.

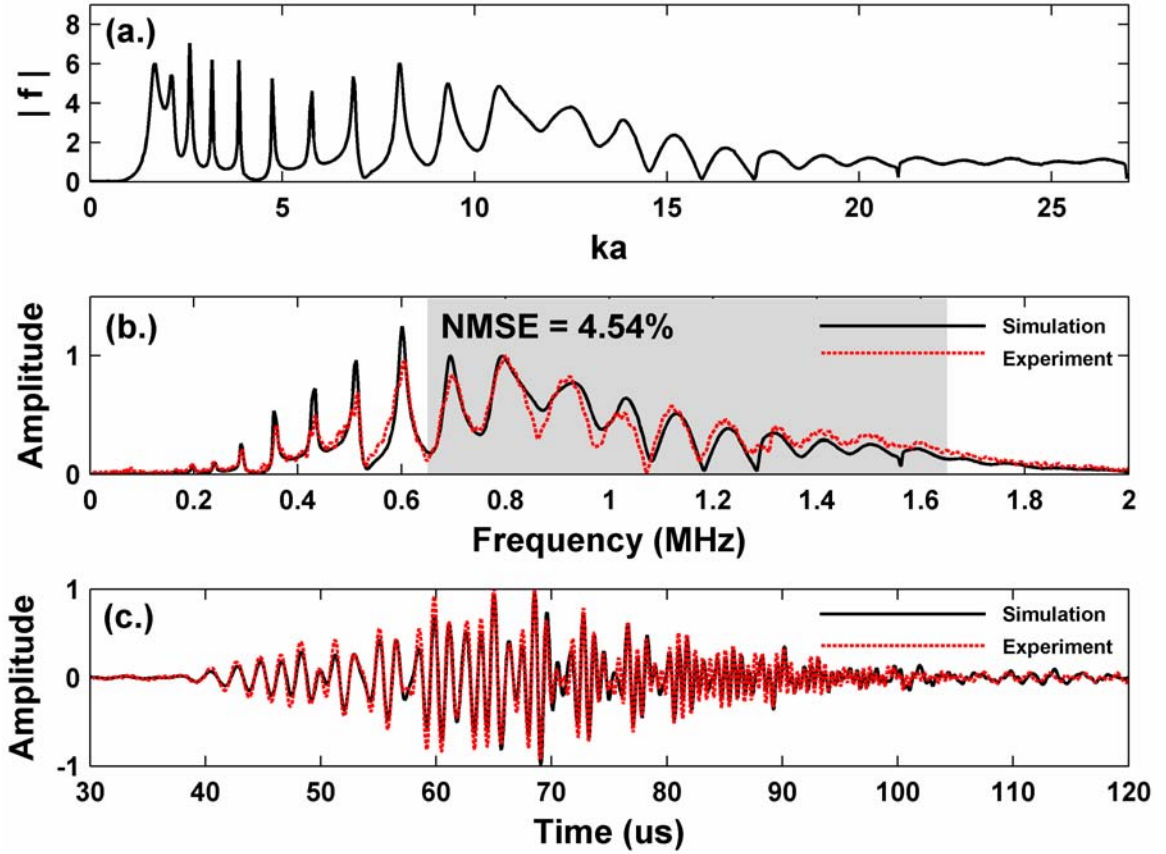


Figure 3.13: Waveforms and associated spectra from the target characterization experiment. (a.) Magnitude of the calculated monostatic far-field form function for the aluminum spherical shell target used in time reversal experiments versus ka . (b.) The dashed line is the magnitude spectrum of the return from the target in which a linear chirp spanning 0.5 to 2 MHz is used for interrogation. The solid line is the magnitude spectrum of the response of the target generated from a numerical simulation. Both spectra are normalized to their respective values at 800 kHz. (c.) The dashed and solid lines are the time domain waveforms associated with the spectra in (b) of experiment and simulation, respectively. Both waveforms are normalized to their maximum value.

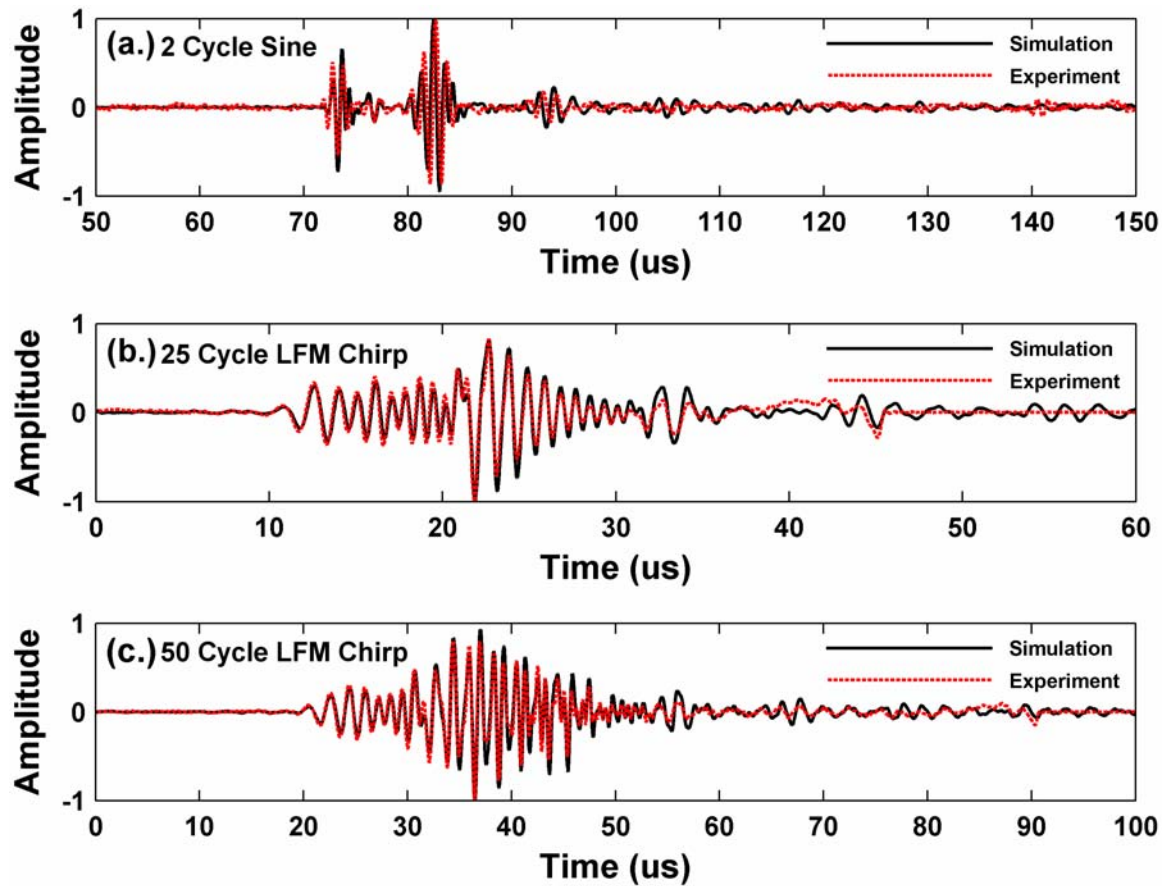


Figure 3.14: Additional time traces from the target characterization experiment. Measured results are shown as dashed lines while those generated from numerical simulation are presented as a solid line. (a.) Return from the standard spherical shell target given a 2 cycle, 1 MHz sine wave incident waveform. (b.) Return from the target given a 23 μs duration linear frequency modulated (LFM) chirp spanning 0.4-1.6 MHz used as an incident waveform. (c.) Return from the target given a 45 μs duration LFM chirp spanning 0.4-1.6 MHz used as an incident waveform.

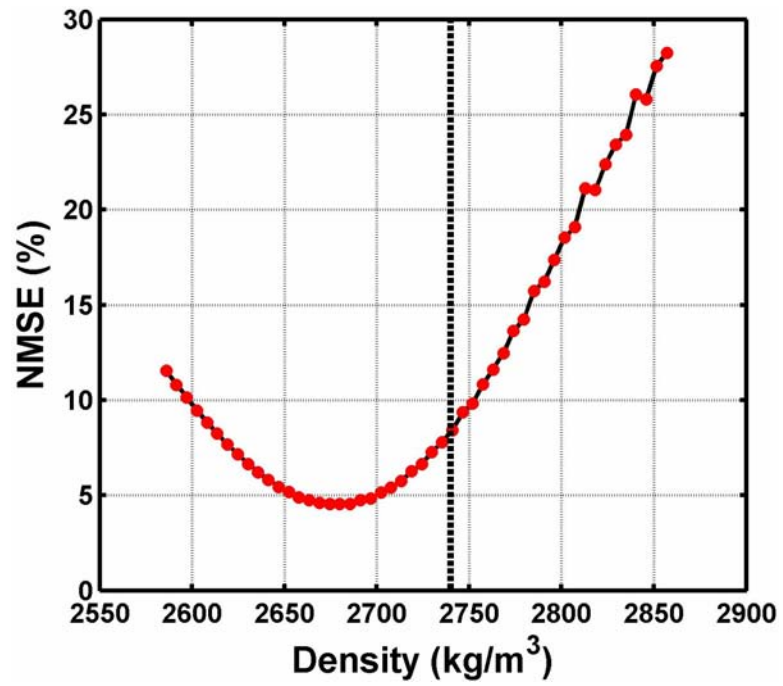


Figure 3.15: Normalized mean squared error between a measurement and simulation of the target response over the 650-1650 kHz frequency range. The density of aluminum 3003 used in the simulation is varied within its measured uncertainty. The vertical dashed line marks the density value reported by the supplier of the target.

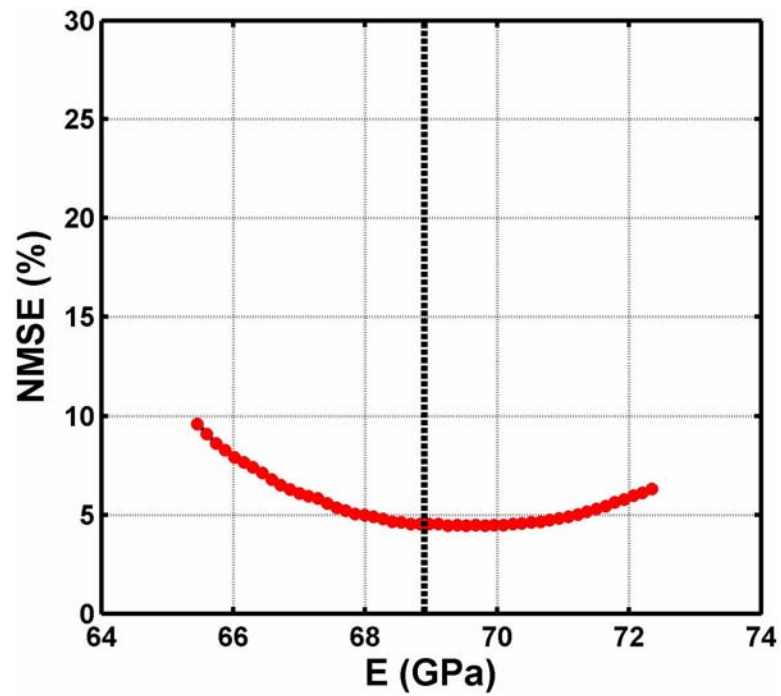


Figure 3.16: Normalized mean squared error between a measurement and simulation of the target response over the 650-1650 kHz frequency range. The elastic modulus of aluminum 3003 used in the simulation is varied $\pm 5\%$ from its nominal value, which is marked by the vertical dashed line.

3.5 Sediment Phantom Characterization

The speed and attenuation of dilatational waves that propagate in the sediment phantom are characterized by through-transmission experiments. A photograph of the physical setup is presented in Figure 3.17. Two Panametrics V-305 unfocussed piston transducers are press-fit into steel baffles. The transducers are 19.05 mm in diameter and possess a nominal center frequency of 2.5 MHz. They are aligned axially at normal incidence on either side of a sample of the glass bead sediment described in Section 3.1. The separation distance between the two baffles can be varied precisely, for one is mounted with sleeve bearings to rods that run the length of the test rig. This apparatus was designed for and employed in previous attenuation measurements conducted in Ref. [107]. The setup of electronic instrumentation is depicted in Figure 3.18. It is qualitatively similar to the setup used in time reversal experiments, except here separate transducers are used to transmit and receive.

The speed of sound of dilatational waves is determined by transmitting a signal from one transducer and digitizing the waveform received at the other. By cross-correlating the transmitted and received waveforms and searching for the location of the maximum value, a time of flight is determined. From the time of flight, the sound speed can be calculated, assuming that the propagation distance is known.

The following analysis details how values of the attenuation are determined. If a voltage $E(\omega)$ is sent to the transmitter, the waveform measured at the receiver will be of the form

$$R_d(\omega) = K_t(\omega) K_r(\omega) G(\omega, d) E(\omega) e^{-\alpha(\omega)d}. \quad (3.80)$$

Here, $K_t(\omega)$ and $K_r(\omega)$ represent the electroacoustic responses of the transmitter and receiver, respectively, $\alpha(\omega)$ is the attenuation of the sample, and d is the separation distance between the transducers. $G(\omega, d)$ is a term that accounts for diffractive effects, *i.e.* the spatial variability in the beam pattern of the transmitter. By measuring received waveforms at two separation distances, d_1 and d_2 , the absolute value of the attenuation can be determined as

$$\alpha(\omega) = \frac{\ln\left(\frac{R_{d_2}(\omega) G(\omega, d_1)}{R_{d_1}(\omega) G(\omega, d_2)}\right)}{d_1 - d_2}. \quad (3.81)$$

Here, the ratio of the $G(\omega, d)$ terms is referred to as a diffraction correction. It is especially important to take into account when performing measurements of attenuation at short standing distances in the ultrasonic regime [108]. In the current work, each term in the ratio is determined by a theoretical approximation similar to that described in Ref. [109]. With knowledge of the sound speed of the medium of interest, the pressure field radiated by the transmitter is calculated over two dimensions using the Rayleigh integral computation described in section 3.3.1. The predicted pressure magnitude is then numerically integrated over an aperture of the same size and position as the receiving transducer. The face of the aperture is divided into N concentric annuli and the pressure is assumed to be constant over each. An average pressure is then calculated from

$$\begin{aligned}
P_{avg}(\omega, d) &= \frac{1}{\pi a^2} \sum_{i=1}^N P_i(\omega, d) \pi \left[\left(r_i + \frac{dr}{2} \right)^2 - \left(r_i - \frac{dr}{2} \right)^2 \right] \\
&= \frac{2}{a^2} \sum_{i=1}^{32} P_i(\omega, d) r_i dr
\end{aligned} \tag{3.82}$$

where $P_i(\omega, d)$ is the pressure at the center of the i^{th} annulus, a is the radius of the aperture, r_i is the radial location of each annulus, and dr is the width of each annulus. In the current work, the average pressure is found to converge upon summation over 32 annuli. The theoretically predicted diffraction correction,

$$\frac{G(\omega, d_1)}{G(\omega, d_2)} = \frac{P_{avg}(\omega, d_1)}{P_{avg}(\omega, d_2)} \tag{3.83}$$

is then substituted in equation (3.81). The reader should note that the attenuation values reported include losses due to intrinsic absorption, volume scattering, and the conversion of dilatational waves to shear waves.

Measurements are first conducted in water to verify the experimental procedure. The plastic tank, within which the transducer rig is placed, is completely filled with distilled water that is allowed to degas overnight. Transducers at separation distances of 8 cm and 10 cm are utilized throughout the following experiments. Monotonic signals 20 cycles in duration are transmitted with frequencies ranging from 0.3-2 MHz in steps of 0.025 MHz. A pulse repetition frequency of 100 Hz allows enough time for the signals to decay between bursts. One hundred coherent averages of received waveforms are performed at each measurement frequency. The temperature of the tank water is measured as 20.5 °C, yielding a predicted sound speed of 1483.8 m/s [105] for the water. The temperature is found not to vary significantly over the time in which acoustic

measurements are conducted. Sound speeds determined from the cross-correlation procedure are shown as small dots in Figure 3.19. The measured and predicted sound speeds show agreement over the entire frequency range with a normalized root mean square error (NRMSE) of 0.28%.

For measurements performed in water, if the attenuation is assumed to be negligible over the frequency range of interest, equation (3.81) reduces to

$$\frac{G(\omega, d_1)}{G(\omega, d_2)} = \frac{R_{d2}(\omega)}{R_{d1}(\omega)}. \quad (3.84)$$

The ratio of waveform amplitudes measured at the two receiver standing distances should agree directly with an analytical prediction of the pressure field at those locations. Predicted pressure distributions for driving frequencies of 0.5, 1, 1.5, and 2 MHz are shown in Figure 3.20. The vertical solid lines in each figure panel represent the receiving aperture positioned at the two standing distances used in the experiment. It is clear, especially from Figure 3.20d, that the receiver is located within the nearfield of the transmitter for some operational frequencies. Thus, accounting for the spatial dependence of the pressure field in equation (3.81) is of paramount importance. The theoretically predicted pressure ratio is presented as a solid line in Figure 3.21. The results of the experiment are, presented as small dots in the same figure, are generated by computing the ratio of the received signal spectral magnitude measured at each separation distance. Agreement between the experimental measurements and the theoretical predictions, to a NRMSE of 2.55%, indicates that this technique provides a reasonable correction for diffractive effects.

Dry soda lime glass beads are then slowly poured into the degassed water, making an effort to not entrain air. The sample is then allowed to sit submerged overnight. Observations show that the sample is sufficiently gas free. The same experimental procedure employed for measurements in water is then repeated with the sediment phantom in place. Twenty independent measurements are conducted at each separation distance. In between measurements, the sample is mixed with a large spoon and allowed to settle for at least 30 seconds. The results of sound speed measurements are shown in Figure 3.22. Between frequencies of 0.3-0.925 MHz, the sound speed is approximately constant at 1730 m/s. Above 0.925 MHz, the sound speed exhibits negative dispersion, decreasing to a value of 1600 m/s at 2 MHz. As observed in Figure 3.23, the attenuation increases nonlinearly with frequency, ranging from 4 Nepers/m at 0.3 MHz to 59 Nepers/m at 2 MHz. The solid lines in Figure 3.23 represent error bounds generated from the uncertainty over multiple measurements, in the estimation of the diffraction correction, and in the separation distance. The results show qualitative agreement with those presented in Ref. [110] for medium grained sand at similar frequencies. Subsequently, they will be used as an input to numerical scattering simulations to help draw conclusions about buried target scattering experiments.

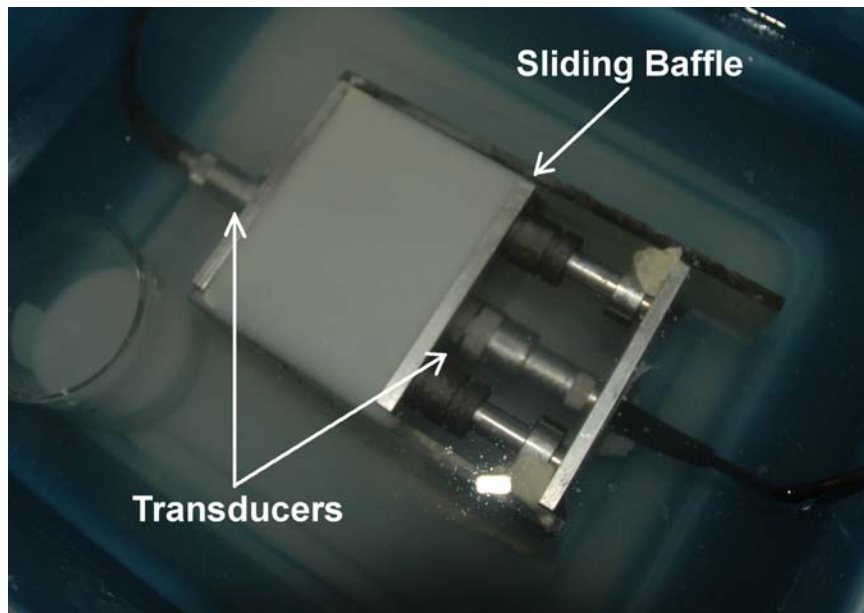


Figure 3.17: Picture of the setup used in sediment phantom characterization experiments. Two Panametrics V-305 unfocussed piston transducers are press-fit into steel baffles. They are aligned axially at normal incidence on either side of a sample of the sediment phantom described in section 3.1. The separation distance between the two baffles can be varied precisely, for one is mounted with sleeve bearings to rods that run the length of the rig.

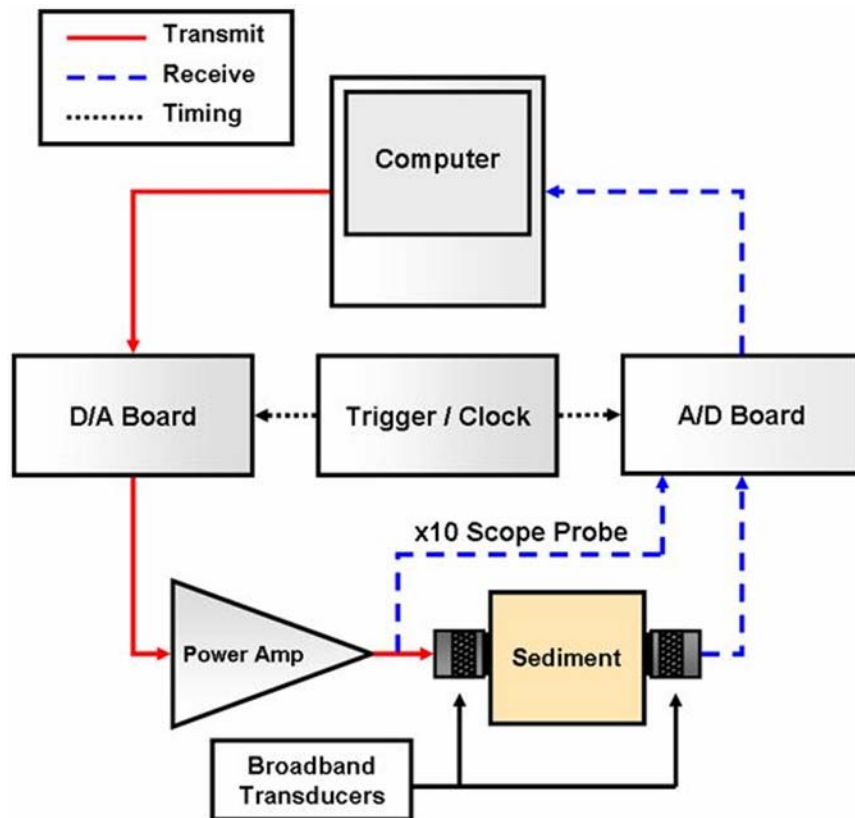


Figure 3.18: Diagram of experimental instrumentation used to characterize the acoustic properties of the sediment phantom used in time reversal experiments.

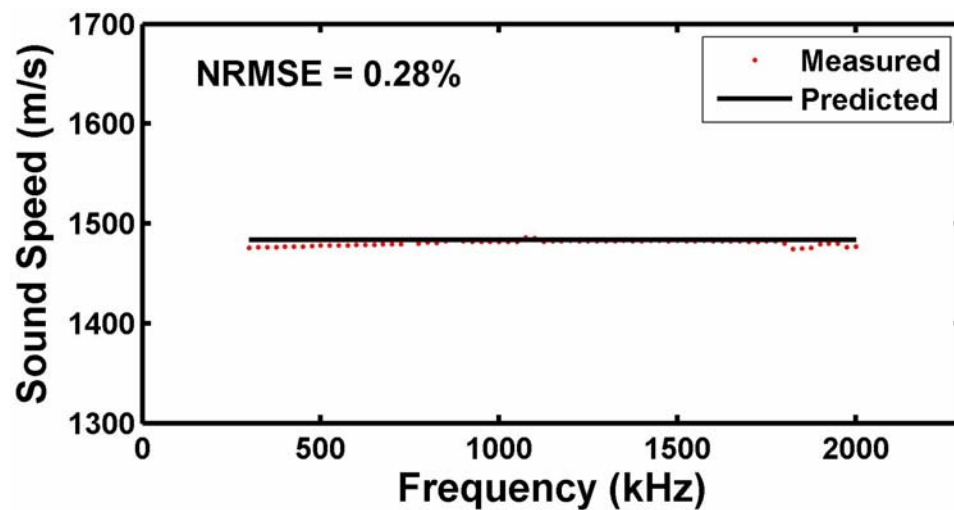


Figure 3.19: Sound speed in distilled water as a function of frequency. The solid line is the speed predicted from a measurement of the water temperature. Small dots depict values estimated through time of flight measurements. The normalized root mean square error between the predicted and measured results is reported on the figure.

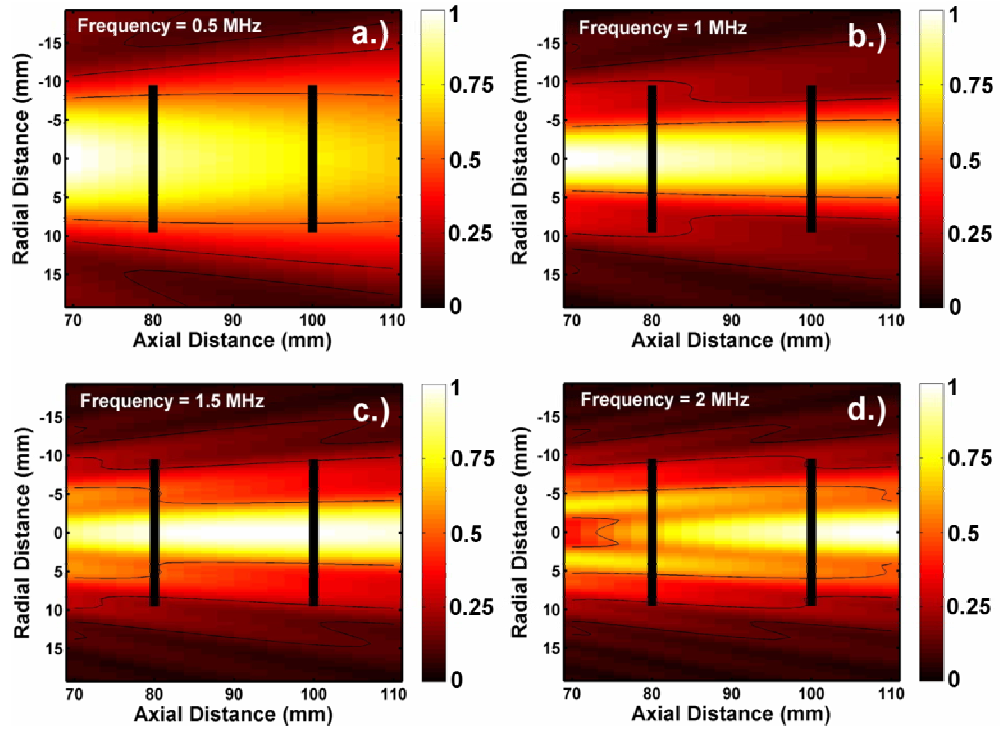


Figure 3.20: Magnitude of the pressure field radiated from a circular baffled piston submerged in water as a function of axial and radial position. The piston is 19.05 mm in diameter, the same diameter as the Panametrics V-305 transducers used in sediment characterization experiments. Thin black lines represent contours of constant pressure magnitude and mark relative values of 0.5, 0.25, and 0.125. The thick vertical black lines in each figure represent the aperture over which pressure is numerically integrated to generate the correction factor used in attenuation measurements. The piston is positioned at the left side of each figure. Predicted values in both plots are normalized to their respective maximum value.

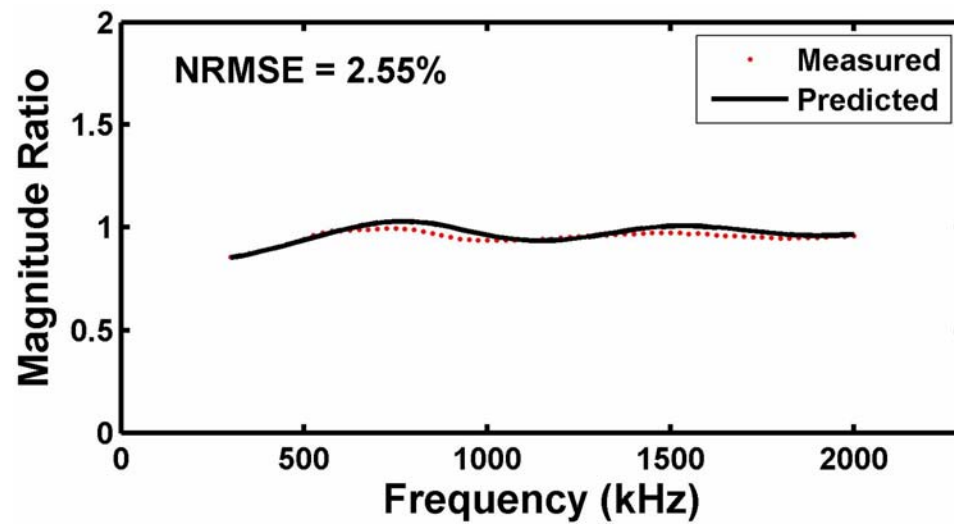


Figure 3.21: Magnitude ratio of pressure averaged over a receiving aperture placed 10 cm away from a radiating piston, divided by the pressure magnitude at 8 cm. The solid line represents the result predicted from numerical simulations. The small dots represent measured values. The normalized root mean square error between the predicted and measured results is reported on the figure.

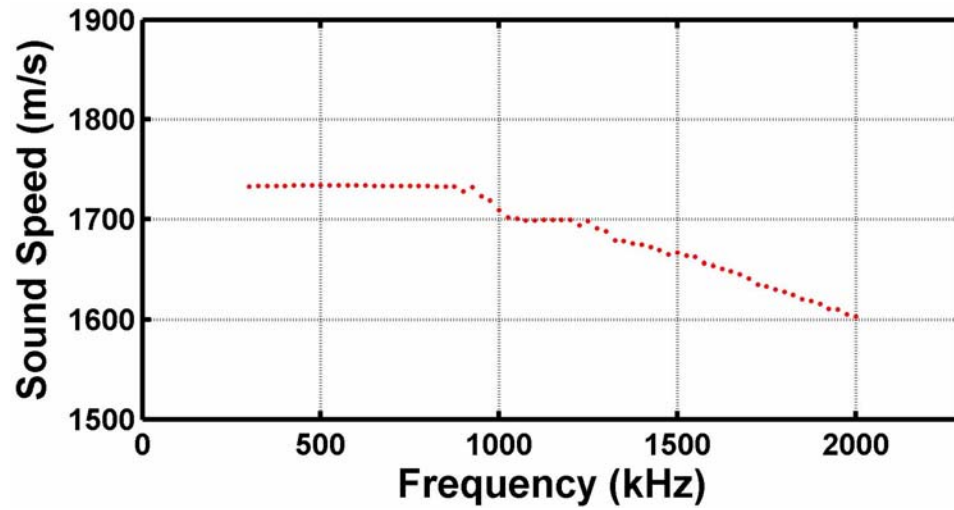


Figure 3.22: Dilatational wave speed in the sediment phantom as a function of frequency. Small dots depict values estimated through time of flight measurements.

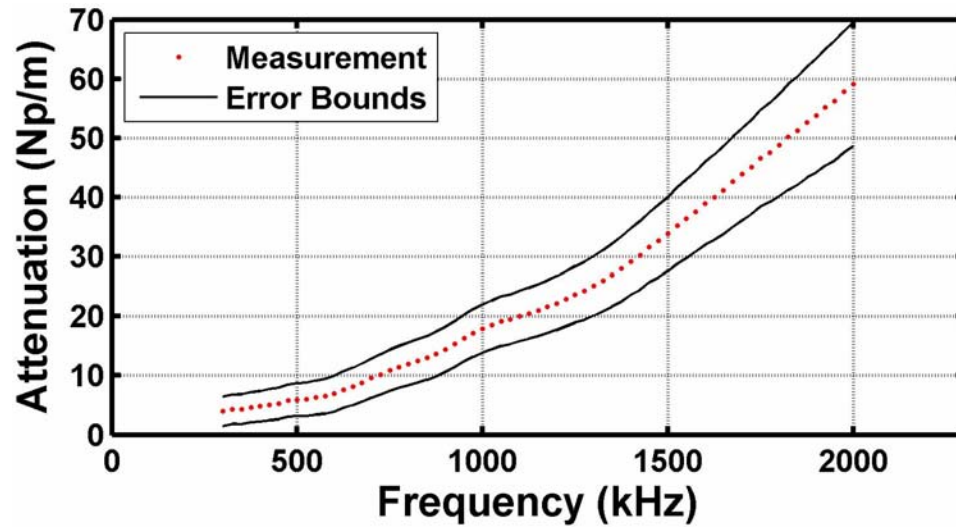


Figure 3.23: Attenuation of dilatational waves in the sediment phantom as a function of frequency. Small dots depict values estimated via through-transmission measurements. The solid lines represent error bounds generated from uncertainty over multiple measurements, in the estimation of the diffraction correction, and in the separation distance.

Chapter 4

Free Field Results

“The only source of knowledge is experience.”

Albert Einstein

This Chapter presents results from experiments conducted with targets positioned in the free field. In the first Section, the single-channel time reversal technique is used to isolate the dominant resonance in the scattering response of an elastic target. The effects of stochastic noise are studied in Section 4.2. The time reversal technique is then shown, in Section 4.3, to isolate surface elastic waves that propagate around the target and also multiple resonances in the target’s scattering response. Finally, the ability of the technique to distinguish between targets of differing type is investigated in Section 4.4.

4.1 Resonant Target Echo Enhancement

The Panametrics V-303 transducer is aligned to face the standard spherical shell target suspended in the free field at the center of the test tank. In Figure 4.1 are shown the results of an experiment where 50 iterations of the time reversal procedure are performed with the time reversal window centered on returns from the target. Time domain waveforms for iteration 0, iteration 10, and iteration 35 are shown in Figures 4.1a, 4.1b, and 4.1c, respectively. The two vertical dashed lines in each time trace specify the position of a $20\mu s$ long time reversal window. Figure 4.1d presents the magnitude spectrum of the signal within the time reversal window for successive iterations. Results in the frequency domain are normalized to the peak spectral magnitude at the final iteration.

To initiate the time reversal procedure, the target is insonified with a 2-cycle 1 MHz sine wave with temporal center located $10\mu s$ following the trigger event, which defines time zero. The echo for iteration 0, shown in Figure 4.1a, consists of a specular return located at $153\mu s$, which is a reflection from the surface of the target closest to the face of the transducer. Within the time reversal window, the specular return is followed by two surface elastic wave returns, one centered at $157\mu s$ and the other at $163\mu s$. Referring to the resonance scattering analysis performed in Section 2.2.2, it is determined that these returns correspond to s_0 symmetric and a_{0-} antisymmetric Lamb waves, respectively. In the frequency domain, as seen in Figure 4.1d, at iteration 0 there are a number of peaks present in the spectrum of the echo. These correspond to combinations

of different wave modes in the scattering response of the target. As evidenced in Figure 4.1b and Figure 4.1d, after 10 iterations of time reversal an 800 kHz monotonic signal begins to fill the time reversal window. After 35 iterations, the return from the target completely fills the time reversal window, as in Figure 4.1c, and has fully converged to the 800 kHz frequency. The resonance centered at this frequency is the dominant mode in the experimentally measured target response shown in Figure 3.13. It corresponds to an a_{0-} antisymmetric Lamb wave. The fluctuations observed in the frequency domain magnitude between even and odd iterations are due to changes in phase of the backscattered returns through iteration of the time reversal procedure as in equations (2.6) and (2.7).

The time reversal technique automatically tunes in to the frequency characteristic of the dominant wave mode resonance in the backscattering response of the target. The spectral magnitude of the 800 kHz target return increases by a factor of 6.6, or 16.4 dB, from iteration 0 to iteration 50. Transmitting average power equivalent to that present within the window at the last iteration at an arbitrarily chosen frequency would not lead to the same results unless one by chance guessed the proper frequency *a priori*.

In this experiment, and in many of the other experiments discussed in this work, 50 iterations of the time reversal procedure are conducted in order to ensure that the process fully converges. This is very likely a prohibitively large number of transmissions for practical applications. However, as evident from Figure 4.1, only a few iterations are necessary to obtain a significant enhancement in the spectral response. As a final note, in this example the signal-to-noise ratio of target returns is high enough to select the

optimum driving frequency after only a single transmission. This will not necessarily be true, however, in the presence of noise.

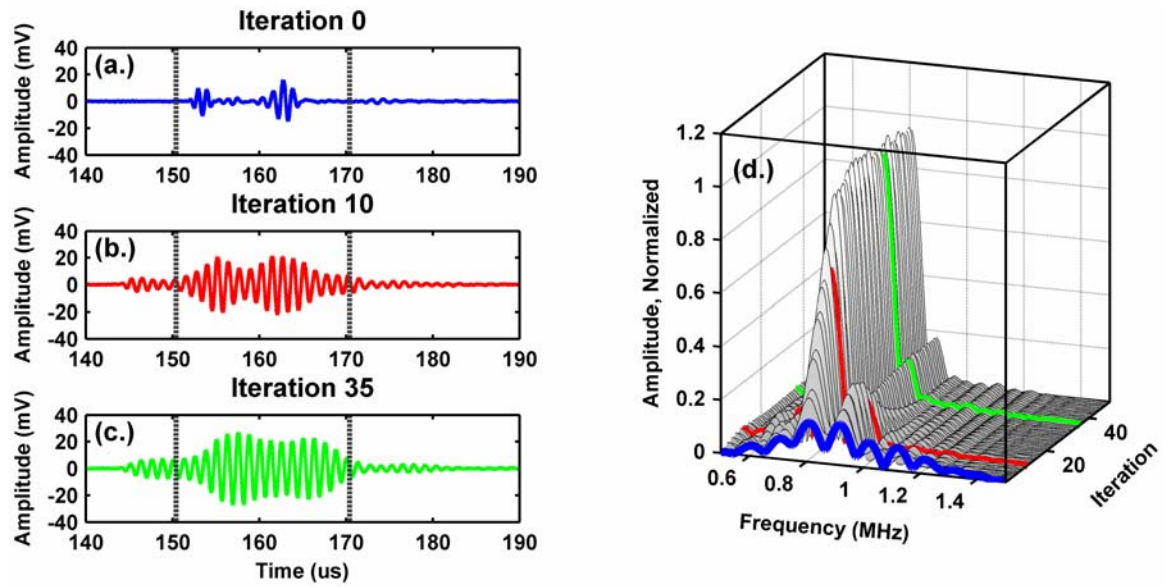


Figure 4.1: Backscattered returns from the spherical shell target suspended in the free field through multiple iterations of the time reversal procedure. Vertical lines in (a)-(c) depict the position of a $20\mu s$ long time reversal window. (a.) The first backscattered return, iteration 0, where a 2 cycle 1 MHz sine waveform is used for interrogation. (b.) Backscattered return at iteration 10 of the time reversal procedure. (c.) Backscattered return at iteration 35 of the time reversal procedure. (d.) Waterfall plot of magnitude spectra of signals within the time reversal window for iterations 0 through 50 normalized to the maximum spectral magnitude at the final iteration. The spectra from (a)-(c) are highlighted with solid black lines.

4.2 Time Reversal in the Presence of Stochastic Noise

The detection and identification of targets by acoustic scattering is often complicated by the presence of noise. For the purposes of the following discussion, the noise is divided into two categories. The first type is deterministic, that is, noise from other real scatterers which interferes with the backscattering response in a coherent way throughout successive receptions. This type of noise can arise from sources such as volume scattering, reverberation, or the presence of false targets. The second type of noise is stochastic in nature; its phase and amplitude varies non-deterministically throughout successive receptions. This type of noise can arise from the electronic instrumentation employed and often sets the threshold for the smallest signal detectable. Also, transient events can arise which are not coherent from throughout successive receptions, such as an object moving past the transducer or drift in waveforms due to the motion the transducer itself. For the purposes of this study, these noise sources are considered to be stochastic as well.

In this Section, the simulation of target scattering introduced in Section 3.4 is used to investigate the performance of the time reversal technique in the presence of stochastic noise, using numerics. Deterministic noise sources, which are not as straightforward to simulate numerically, will be considered experimentally in subsequent Sections. The performance of the time reversal technique is judged through quantitative comparison with the results of a simple autocorrelation operation performed on the first return signal. For these simulations, successful performance is defined as having successfully identified the dominant resonance in the response of the standard spherical

shell target. The first transmission consists of a standard interrogation waveform, specifically a linear frequency modulated (LFM) chirp that sweeps through the entire frequency bandwidth of the system. The energy in this waveform is evenly distributed among all frequencies.

As depicted in Figure 4.2a, a 20- μ s long receive window is centered on returns from the target, at approximately 8 μ s following the specular return. A window with these parameters encompasses a strong resonant portion in the response of the target. Because the strength of resonances in received waveforms is dependent upon the size and location of the window, the resonance to which the system converges under noise free conditions is defined as the dominant resonance. Under the selected operating conditions, this is the resonance centered at 800 kHz in the steady state response of the target. The half-power bandwidth of this resonance spans from 773.1 kHz to 836.2 kHz. If the maximum value in the spectral magnitude of a windowed received waveform lies within this bandwidth, the interrogation is considered to be a ‘correct call’.

Figure 4.2a and 4.2e present, in the time and frequency domains respectively, the waveform received after interrogating the target with a 20- μ s duration LFM chirp that spans the full system bandwidth. Figures 4.3a and 4.3e show the waveform that results after performing 50 iterations of the time reversal procedure. The vertical dashed lines in Figures 4.2a-4.2d and 4.3a-4.3d indicate the location of the receive window, while those in Figures 4.2e-4.2h and 4.3e-4.3h indicate the half-power bandwidth of the 800 kHz dominant resonance. In both Figures 4.2e and 4.3e, the maximum value in the spectral

magnitude of returns lies within the frequency window of the dominant resonance. Thus, the result in both cases is considered as a ‘correct call’.

Noise is then added to the scattering simulation as follows. A signal-to-noise ratio (SNR) is defined as,

$$\text{SNR} = 20\log_{10}\left(\frac{S_{max}}{\sigma_{noise}}\right) \quad (4.1)$$

where S_{max} is the maximum amplitude of the first backscattered return and σ_{noise} is the standard deviation (root mean square amplitude) of the noise. A pseudorandom number generating function is used to create a set of double precision floating point (16 decimal digit) numbers ranging from zero to one and possessing an amplitude distribution that is Gaussian. The Fourier transform of this signal is then computed and the spectrum is filtered using the magnitude response of the calibrated system. Figure 4.4 shows the magnitude spectrum of the noise after filtering. The spectral density is flat over the entire system bandwidth, and thus the noise is approximately white. Computing the inverse Fourier transform of the filtered noise signal yields a waveform that can then be added to a simulated target return. The rms-amplitude of this noise waveform is scaled to achieve a desired SNR value.

In noise-free conditions, depicted in Figure 4.2e, the dominant spectral peak in the response of the target is identified through only a single transmission. If this is always the case, there is no need to perform the time reversal procedure. Noise is then added to the system and new target returns are generated. The bottom three rows in Figures 4.2 and 4.3 show representative examples of noisy target returns for varying SNR’s. The

LFM chirp achieves a correct call for a SNR of 15 dB, while the time reversal technique is successful at a SNR of 15 dB and 12 dB. Both methods fail for a SNR of 6 dB. These specific examples show that in some cases, waveforms generated via the time reversal technique outperform the LFM chirp.

In order to quantitatively estimate performance, a numerical experiment is conducted where the number of correct calls is recorded over 300 trials. This numerical experiment is conducted both with and without a target in place for SNR's ranging from 0-36 dB in steps of 1 dB. Selected performance curves resulting from this experiment are presented in Figure 4.5. The solid black circles correspond to results generated from using a single LFM chirp interrogation. This waveform is also used to initiate the time reversal procedure. The data shown by white circles are generated from 10 iterations of the time reversal procedure. The solid black lines towards the bottom of the figure are generated by running the same numerical experiments without the target in place. These lines, with an average value of ~5%, indicate the percentage of times a dominant spectral peak falls within the frequency window randomly, by chance. As observed in this figure, for SNR's greater than approximately 10 dB, the time reversal technique outperforms the LFM chirp. The maximum improvement occurs at a SNR of 17 dB, where time reversal accurately identifies the dominant resonance of the target 60% more frequently than an autocorrelation of the first return. However, as shown by the gray data in Figure 4.5, coherent averaging of returns improves the performance of the LFM chirp. Here, performing the same number of averages as time reversal iterations reduces the maximal difference in performance to only 18.5% at an SNR of 15 dB.

In Figures 4.6 and 4.7, performance curves for both techniques are presented for a variety of iterations/averages up to a maximum of 19. It is clear from these figures that the performance of both techniques depends on both the SNR and the number of transmissions employed. As expected, because the same LFM chirp is used for the initial interrogation in both cases, the statistical properties at iteration/average 0 are approximately identical. In general, the time reversal technique possesses better performance for SNR's between ~15-35 dB, while the averaging technique performs better for SNR's less than 15 dB. For SNR's greater than 35 dB, both techniques identify the dominant resonance approximately 100% of the time. To summarize the comparison, a performance surface is generated. For each SNR and number of iterations/averages, the percentage of correct calls obtained via averaging is subtracted from the percentage correct calls observed through time reversal. The results of this subtraction are presented in Figure 4.8. Contours are drawn along values of -10%, 1%, 10% and 20%. The light shaded region (positive percentages), indicates the parameters for which the time reversal technique outperforms averaging returns from LFM chirp interrogation. In contrast, the dark shaded region indicates the parameters for which the averaging technique is more effective.

The results presented in this Section show that for some operational conditions, single-channel iterative time reversal yields an improvement over a more standard method in the identification of a dominant target response frequency. However, in order for the time reversal technique to outperform coherent averaging of returns given a LFM chirp interrogation, received signals must possess a minimum SNR. For the simulation

conditions studied, this is approximately 15 dB. The time reversal technique does not reduce the level of incoherent noise, as averaging does, it simply enhances the dominant spectral component present in a return signal. A decision to utilize the technique will depend upon a number of factors that may vary depending upon the system in use and the operating conditions. While the experiments conducted here only apply directly to the specific set of instrumentation, target, and window parameters employed, it is expected that the general properties observed should extrapolate to other operational scenarios.

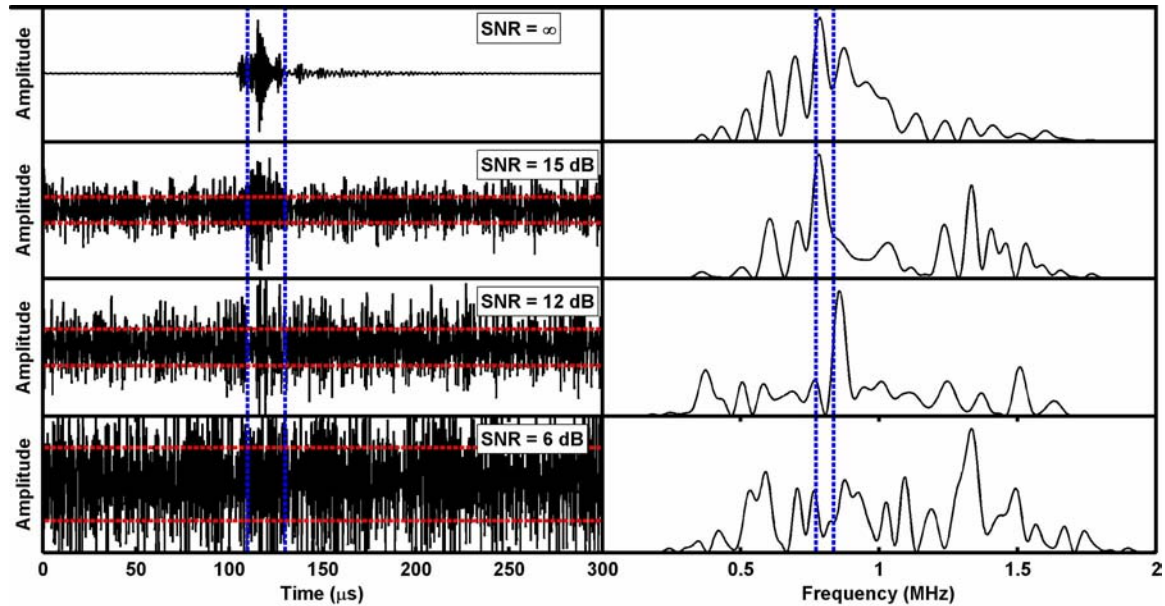


Figure 4.2: Target returns given a 20- μ s duration linear frequency modulated chirp interrogation waveform. Returns are generated in the presence of varying levels of additive Gaussian white noise. Panels (a.)-(d.) are time domain returns for signal to noise ratios of infinity, 15 dB, 12 dB, and 6 dB, respectively. The vertical dashed lines in each figure panel denote the position of a 20 μ s receive window. The horizontal dashed lines indicate the root-mean-square amplitude of the noise. Panels (e.)-(h.) present the magnitude spectrum of signals within the receive window in (a)-(d). The vertical dashed lines in these figure panels indicate the half-power bandwidth of the dominant target resonance present.

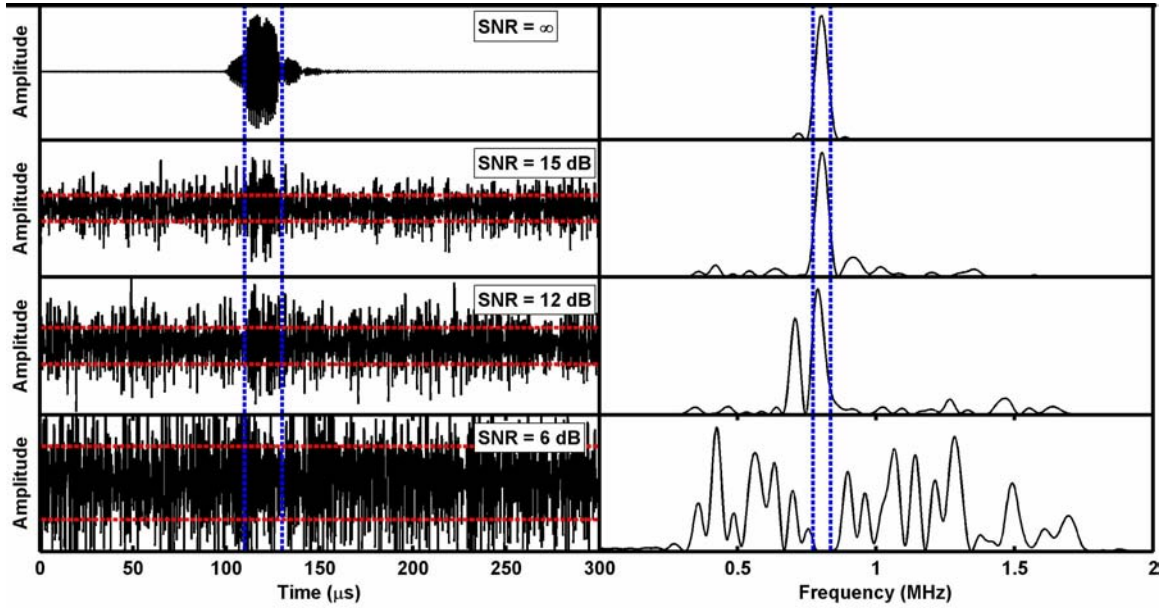


Figure 4.3: Target returns after 50 iterations of time reversal given a $20\text{-}\mu\text{s}$ duration linear frequency modulated chirp interrogation waveform used for the initial interrogation. Returns are generated in the presence of varying levels of additive Gaussian white noise. Panels (a.)-(d.) are time domain returns for signal to noise ratios of infinity, 15 dB, 12 dB, and 6 dB, respectively. The vertical dashed lines in each figure panel denote the position of a $20\text{ }\mu\text{s}$ receive window. The horizontal white dashed lines indicate the root-mean-square amplitude of the noise. Panels (e.)-(h.) present the magnitude spectrum of signals within the receive window in (a)-(d). The vertical dashed lines in these figure panels indicate the half-power bandwidth of the dominant target resonance present.

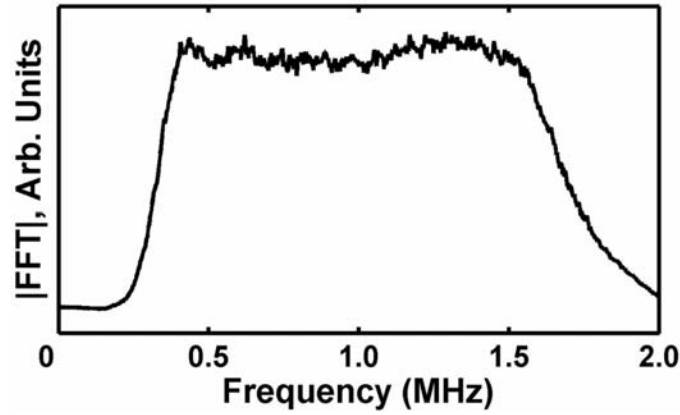


Figure 4.4: Magnitude spectrum of the numerically generated noise used in simulations of target scattering.

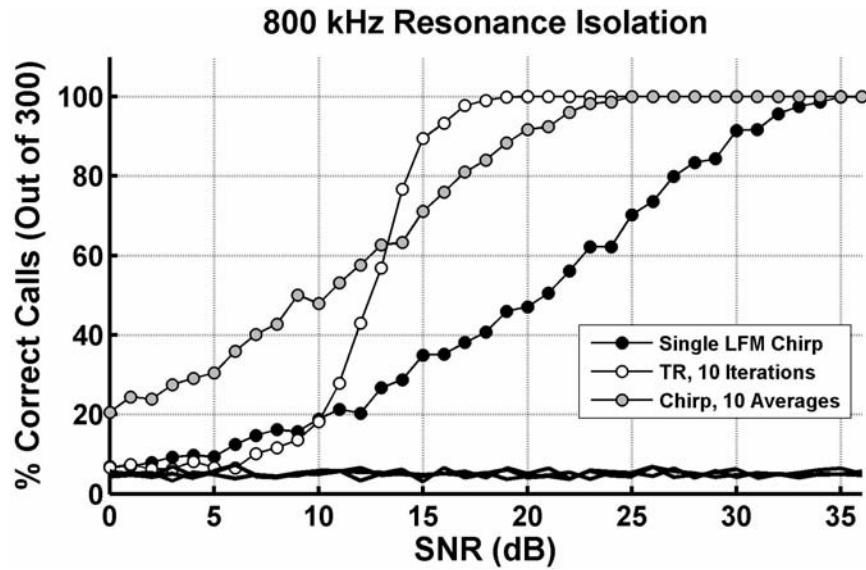


Figure 4.5: Selected performance curves comparing the efficacy of a single linear frequency modulated (LFM) chirp waveform, 10 iterations of time reversal, and 10 averages of returns from using a LFM chirp interrogation. The percentage of correct dominant target resonance identifications out of 300 trials is presented for signal-to-noise ratios ranging from 0-36 dB. The thick solid black lines near the bottom of the figure indicate the number of correct calls without a target in place.

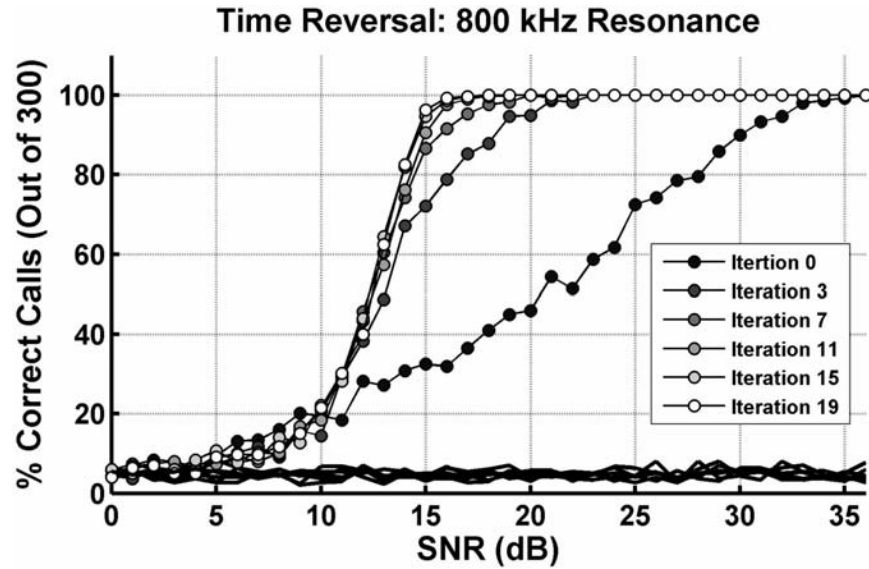


Figure 4.6: Performance curves for the single-channel time reversal technique utilizing 0-19 iterations. The percentage of correct dominant target resonance identifications out of 300 trials is presented for signal-to-noise ratios ranging from 0-36 dB. The thick solid black lines near the bottom of the figure indicate the number of correct calls without a target in place.

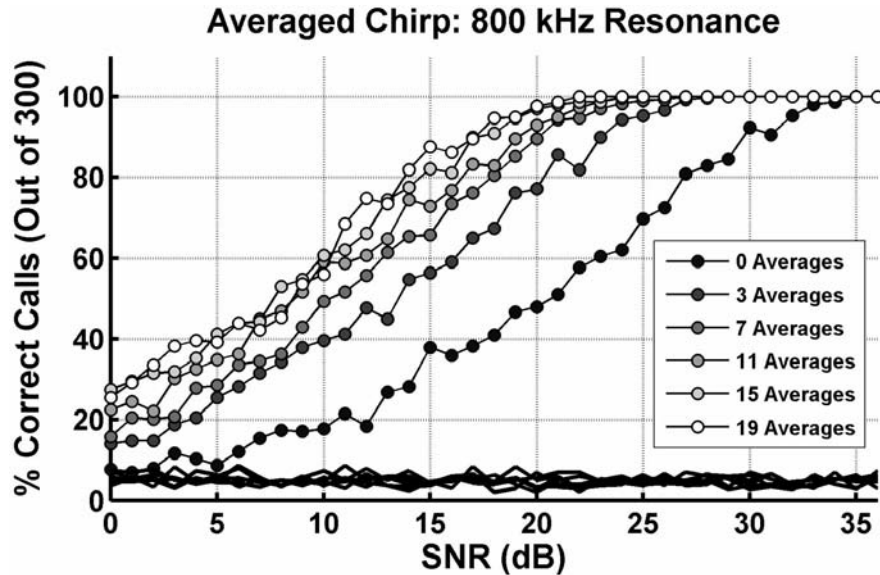


Figure 4.7: Performance curves for the technique where 0-19 coherent averages are performed on target returns given a 20- μ s duration linear frequency modulated chirp. The percentage of correct dominant target resonance identifications out of 300 trials is presented for signal-to-noise ratios ranging from 0-36 dB. The thick solid black lines near the bottom of the figure indicate the number of correct calls without a target in place.

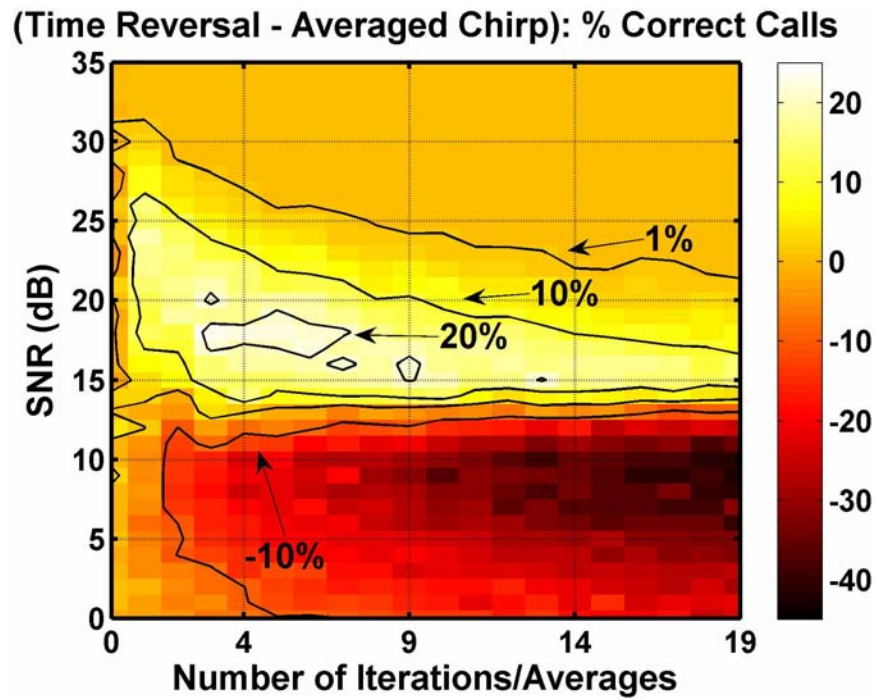


Figure 4.8: Performance surface generated by subtracting the percentage of correct calls via the averaging technique from the percent correct calls observed through time reversal. Contours are drawn along values of -10%, 1%, 10% and 20%.

4.3 Isolation of Surface Elastic Waves and Scattering Resonances

Results presented in the previous Sections of this Chapter demonstrate that the iterative single-channel time reversal technique yields an enhancement of the dominant resonance in the scattering response of a target. However, in practical applications, the isolation of only a single resonance is typically not enough to confirm positive identification. As such, the remainder of this Chapter investigates whether the technique can be used to isolate both surface elastic wave returns and multiple resonances in the scattering response of the target.

4.3.1 Window Timing Definition

In order to isolate and identify resonance features present in the extended echo return from a target, precise knowledge of the location of the time reversal window is crucial. To track the position of the time reversal window with respect to returns from a target, a reference time is defined as shown schematically in Figure 4.9. Before time reversal experiments are conducted, a 3 cycle, 1 MHz sine wave is transmitted with a delay such that its center lies at a time equal to one half of the duration of the time reversal window, $0.5\tau_{window}$. The transmitted pulse interacts with the scattering target at a time equal to τ_{target} , as depicted in Figure 4.9a. Because these experiments are monostatic, the center of the specular echo from the target will then arrive at the transducer at a time equal to $2\tau_{target}$. The time of flight of the center of the received wave packet is then manually recorded and defined as a relative window time of $t_r = 0$. For free field experiments, this

reference time is set as the center of the specular return from the front face of the target. In buried target experiments, because it is difficult to accurately isolate the specular return from a target, the reference time is set as the center of the return from the surface of the sediment phantom. As depicted in Figure 4.9b, when the center of the time reversal window is located at time $t_r = 0$, specular returns generated by transmitting arbitrarily shaped pulses at the target appear to be centered within the window. Because the reference time is specified manually, there is some variability throughout successive experiments. In this work it is estimated that the central position of the window is known to within approximately $\pm 1\mu s$.

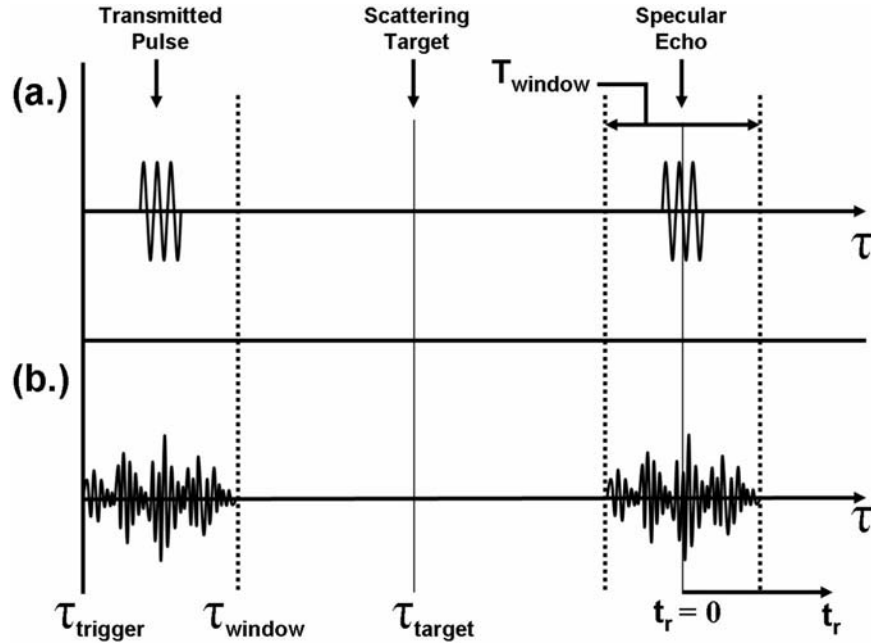


Figure 4.9: Schematic of how the relative window time, t_r , is defined in time reversal experiments. $\tau_{trigger}$ is the time at which a trigger event occurs. τ_{window} is the duration of the time reversal window. τ_{target} is the time at which a transmitted wave will interact with the target. (a.) A 3 cycle sine wave is transmitted at a scattering target and the echo is received. (b.) Returns from arbitrarily shaped transmissions appear to be centered within the time reversal window.

4.3.2 Isolation of Surface Elastic Wave (Lamb Wave) Returns

In order to determine whether surface elastic wave returns from the standard spherical shell target can be isolated in both time and frequency, a $5\mu\text{s}$ long time reversal window is shifted from relative window times of $-30\mu\text{s}$ to $60\mu\text{s}$ in steps of $0.5\mu\text{s}$. Here, the numerical target scattering simulation is employed to generate results. At each relative window time, 50 iterations of the time reversal procedure are performed. White noise $5\mu\text{s}$ in duration is used for the first interrogation at each window location. Figure 4.10 presents the results from this simulation in a format similar to a spectrogram. The horizontal axis in each figure panel indicates the relative window time. At each relative window time, the magnitude spectrum of the signal within the time reversal window is computed and plotted along the vertical axis. Before a spectrum is computed, a cosine squared envelope is applied to 20% of either side of the window. The intensity in both figure panels of Figure 4.10 is normalized to the maximum value in Figure 4.10b.

At iteration 0, the target is barely visible, as evident in Figure 4.10a. However, after 50 iterations of the time reversal technique, multiple discrete returns in time are present. The reader should note that the word “returns” is used loosely here. While Figure 4.10b is indeed reminiscent of a spectrogram, it is not generated from a single waveform. It is generated from 181 separate waveforms (one for each $0.5\mu\text{s}$ time step from $-30\mu\text{s}$ to $60\mu\text{s}$), the spectra of which form the intensities recorded along each vertical axis. In order to determine the relative time spacing between each packet of energy in Figure 4.10b, a profile of the figure is created. In Figure 4.11, the maximum spectral magnitude recorded at each relative window time is plotted. The reader should

note that again, as in Figure 4.10a, it is difficult to discern discrete returns at iteration 0. At iteration 50, however, there are a total of six broad local maxima, each of which is highlighted at its center with a vertical dashed line. The relative spacing between each peak is indicated.

In this simulation, the specular return is centered at $t_r = -1\mu s$, due to a slight error in defining the reference time. The time reversal window first interacts with the target at a window location approximately $5\mu s$ prior to the center of the specular return, a relative time equal to the width of the window. This phenomenon is consistent throughout all free field simulations and experiments and is expected based upon how the window reference time is defined (see Figure 4.9). The 5 returns following the specular return are then identified. The relative time between each wave packet correlates approximately to the echo delay predicted in Chapter 2 (see Figure 2.18 in that Chapter) for circumnavigations around the shell target of a_{0-} antisymmetric Lamb waves.

Plotted in Figure 4.12 are the waveforms and spectra at iteration 50 for relative window times marked in Figure 4.11. In Figures 4.12a-4.12f, vertical dashed lines highlight the location of the time reversal window. For each relative window time shown, the reader should note that a wave packet appears to be centered within the window. Figures 4.12g-4.12l present the spectra of these windowed signals. The center frequency and relative window time from each figure panel are recorded in the second and third columns of Table 4.1, respectively. Using these values, the theoretically predicted echo delays of the first five a_{0-} antisymmetric Lamb wave circumnavigations are computed using equation (2.68). These predicted times are presented in the fourth

column of Table 4.1. The normalized root mean square error between the measured and predicted times is presented in the final column of Table 4.1. The measured and predicted echo delays show good agreement, with a maximum error of 3.4%. Therefore, identification of the a_{0-} antisymmetric Lamb wave is confirmed.

The downshift in the convergence frequency as the window passes the target is due to radiation damping; that is, high frequencies radiate more strongly into the ambient fluid and are thus attenuated more after each circumnavigation around the sphere. A 1.212 MHz convergence frequency is observed when the window is centered on the specular return. This is higher than the 1 MHz frequency that would be expected with a specular reflector. This occurs because the cross-section of the target is smaller than the spot size illuminated on the free-water surface during calibration. Therefore, less low frequency energy is backscattered and a bias toward higher frequencies is introduced in what is otherwise a nominally flat response. Also, a s_0 symmetric Lamb wave, with a circumnavigation time of $\sim 4\mu s$, is mixed with the specular return.

To verify the numerical results, a laboratory tank experiment is conducted. Figure 4.13 presents the results, which are qualitatively similar to those in Figure 4.10. However, the fifth Lamb wave circumnavigation is not detected and the other returns are more damped than in the numerical results. In the numerical simulation, the returns could be stronger because the surface elastic waves are assumed to propagate along the surface of the shell unimpeded. In the physical experiment, the polypropylene tape beneath which the target is suspended may extract energy from the surface waves, damping their response.

Although an inverse problem is not explicitly solved here, it is expected that time and frequency information obtained using this methodology could possibly be useful for the purpose of target identification. Previous studies have shown that multiple surface elastic waves can be isolated in time and frequency using array based time reversal [20, 111]. The single-channel time reversal technique presented here could provide a simple and inexpensive alternative to these array based techniques.

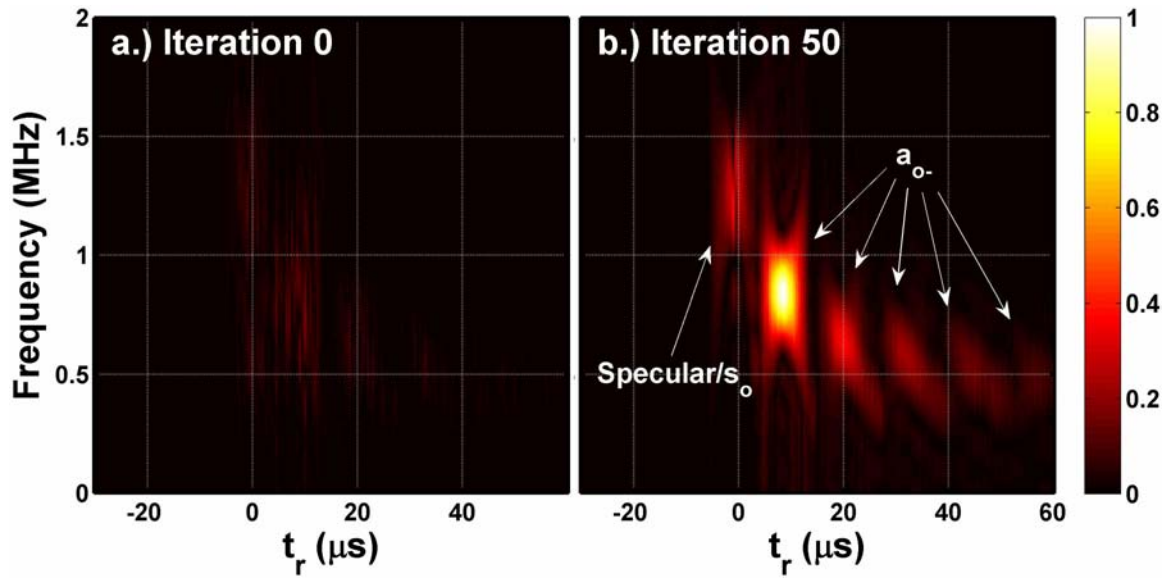


Figure 4.10: Echo spectral magnitude versus frequency and time from a numerical experiment where the center of a $5\mu\text{s}$ duration time reversal window is shifted in steps of $0.5\mu\text{s}$ from relative window times, t_r , of $-30\mu\text{s}$ to $60\mu\text{s}$. Spectra from iteration 0 and iteration 50 are shown in (a) and (b), respectively. The intensities in each are normalized to the maximum value in (b). Wave packets are labeled according to their type. Incident waves approach the target from the left side of the figure.

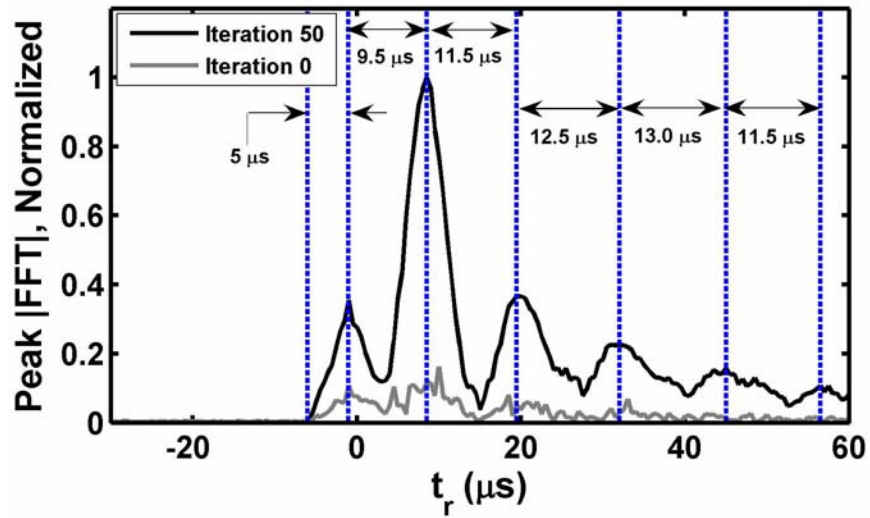


Figure 4.11: The black solid line represents the maximum spectral magnitude recorded at each relative window time in Figure 4.10b, iteration 50. The solid gray line presents the same results for Figure 4.10a, iteration 0. Both results are normalized to the maximum value at iteration 50. Vertical dashed lines highlight the time locations of local maxima. The relative time between maxima is also presented.

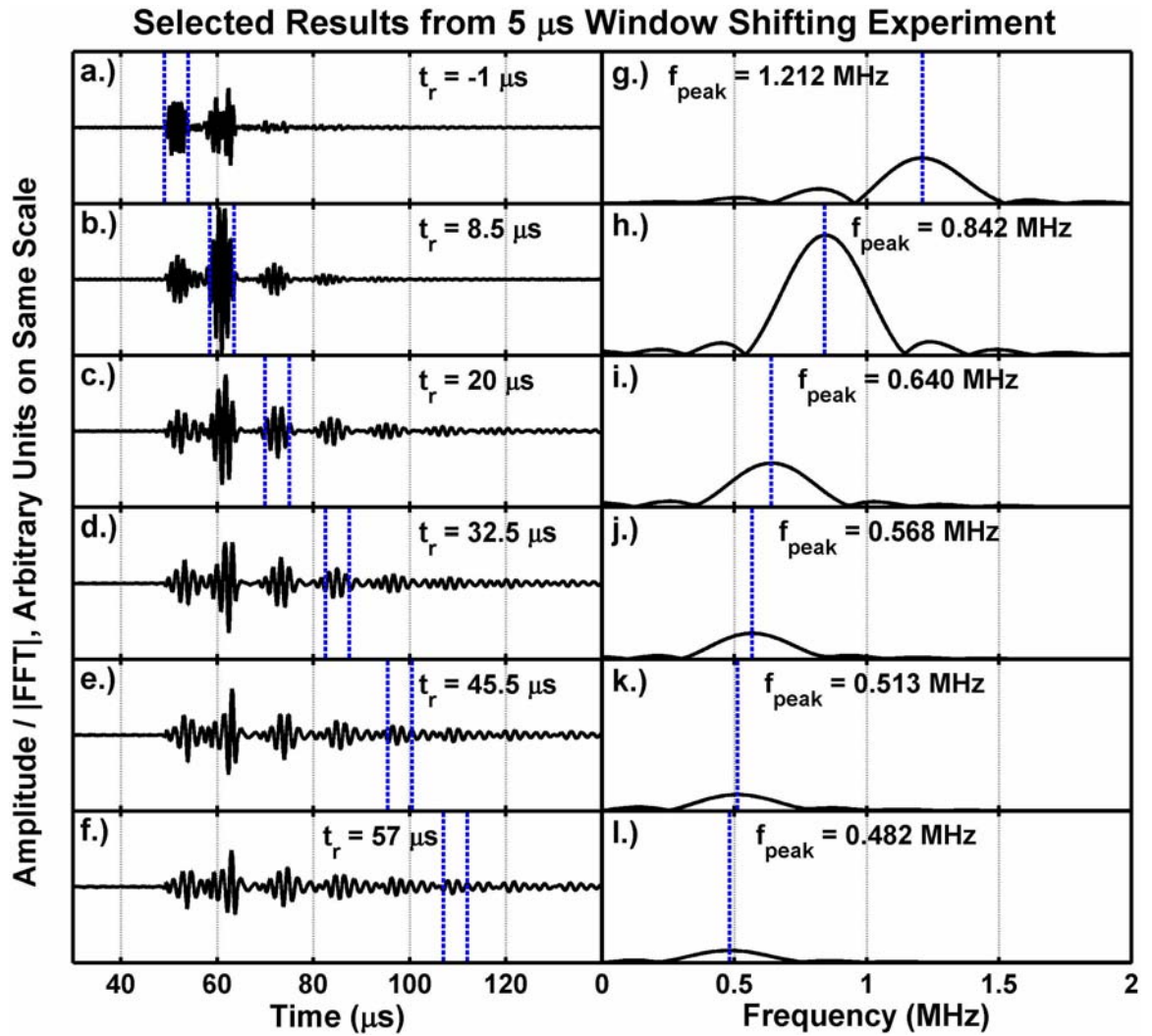


Figure 4.12: Waveforms from iteration 50 of time reversal appearing at relative window times, t_r , marked by vertical dashed lines in Figure 4.11. The vertical dashed lines in (a)-(f) outline the location of a 5 μs duration time reversal window. Panels (g)-(l) present the magnitude spectra of signals within the time reversal window in (a)-(f). Vertical dashed lines in these figure panels mark the location of the peak spectral magnitude. The vertical axes in time and frequency domain waveforms are presented in arbitrary units on the same scale.

Table 4.1: Wave types and their center frequencies, measured arrival times, and predicted arrival times for the $5\mu\text{s}$ duration time reversal window shifting experiment.

Wave Type	Frequency (MHz)	$t_{r,measured}$ (μs)	$t_{r,predicted}$ (μs)	NRMSE (%)
Specular / s_0	1.212	-1	-----	-----
a_{0-} , 1 st Circ	0.842	8.5	8.3	1.9
a_{0-} , 2 nd Circ	0.640	20	19.8	0.9
a_{0-} , 3 rd Circ	0.568	32.5	32.2	1.0
a_{0-} , 4 rd Circ	0.513	45.5	45.5	0.1
a_{0-} , 5 th Circ	0.482	57.0	59.0	3.4

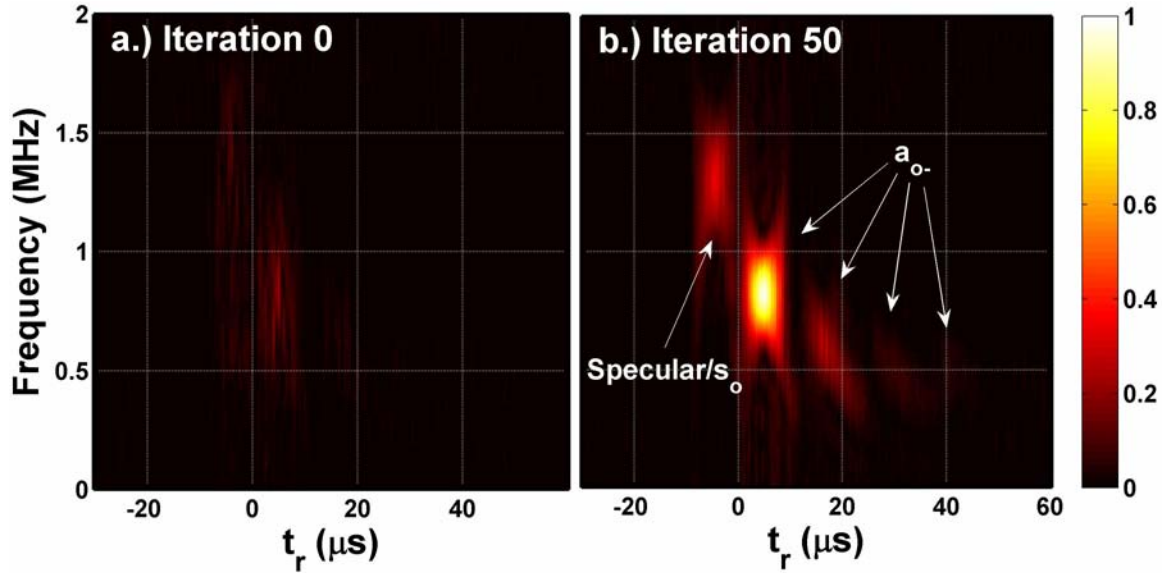


Figure 4.13: Echo spectral magnitude versus frequency and time from a laboratory tank experiment where the center of a $5\mu\text{s}$ duration time reversal window is shifted in steps of $0.5\mu\text{s}$ from relative window times, t_r , of $-30\mu\text{s}$ to $60\mu\text{s}$. Spectra from iteration 0 and iteration 50 are shown in (a) and (b), respectively. Wave packets are labeled according to their type. Incident waves approach the target from the left side of the figure.

4.3.3 Window Size Study (Multiple Resonance Isolation)

The $5\mu\text{s}$ window size employed in the previous Section is small enough to isolate individual surface elastic waves in time. However, there is a tradeoff between time resolution and frequency resolution. The frequency resolution of a square window is inversely proportional to the window length. Thus, a $5\mu\text{s}$ long window possesses a frequency resolution of approximately 0.2 MHz. That is, the center frequencies of resonances appearing within a spectrum must be separated by greater than 0.2 MHz to be resolved from one another. The spacing of resonances in the steady state form function of the standard spherical shell target is approximately 0.1 MHz. Therefore, with a $5\mu\text{s}$ window size it is not possible to confidently resolve individual resonances in the frequency domain. In order to do so, the duration of the time window must be expanded.

As such, the numerical window shifting simulation conducted in the previous Section is repeated using larger time windows. “Spectrograms” resulting from this analysis are presented in Figure 4.14 for window sizes ranging from $5-40\mu\text{s}$. It is evident from this figure that as the window size is increased, the bandwidth encompassed by any individual resonance is decreased. For example, in Figure 4.14a where a $5\mu\text{s}$ long window is employed, the energy packet centered at 0.800 MHz possesses a half-power bandwidth of approximately 0.250 MHz. The bandwidth of this energy packet decreases to 0.110 MHz in Figure 4.14b, where a $10\mu\text{s}$ time window is employed. Energy packets that are smeared across frequencies in Figure 4.14a, appear to become more distinct and narrow in Figure 4.14b. However, for some wave packets, the energy

is still distributed over a frequency band that encompasses two or more resonances in the scattering response of the target. When the window size is expanded to $15\mu s$, as in Figure 4.14c, the bandwidth of the 0.800 MHz energy packet decreases to 0.065 MHz. This is less than the 0.1 MHz spacing of resonances in the scattering response of the target. Therefore, individual resonances can now be confidently identified; this is also true for larger time windows. The improvement in frequency resolution is achieved, however, at the expense of temporal resolution.

It is apparent from Figure 4.14, that for window sizes larger than $10\mu s$ it is not possible to isolate individual surface elastic waves in time. However, although individual returns are not separated, evidence of them is still apparent in the data. For example, consider Figure 4.15. In this figure, for the corresponding window sizes shown in Figure 4.14, the peak spectral magnitude recorded at each relative window time is plotted. In Figure 4.15, for window sizes greater than or equal to $15\mu s$, there is a broad peak upon which are superimposed a number of sharp local maxima. Select local maxima are marked with vertical dashed lines.

To investigate the origin of these maxima, the waveforms recorded at the relative window times highlighted in Figure 4.15d (corresponding to a $20\mu s$ window size) are examined. These waveforms are presented in Figure 4.16. For this window size, the global maximum spectral amplitude is observed at a relative window time of $8\mu s$. The convergence frequency at this window location (see the second row of Figure 4.16) matches that of the a_{0-} antisymmetric Lamb wave resonance centered at 0.800 MHz in the steady state form function of the target. The convergence frequencies observed for

the smaller peaks on either side of the main peak in Figure 4.15d are also due to this a_{0-} wave resonance (see the first and third rows of Figures 4.16). The remaining peaks in Figure 4.15d display a downshift in convergence frequency (see the bottom 3 rows of Figures 4.16) due to radiation damping, as discussed previously in Section 4.3.2. Results generated using larger window sizes exhibit similar characteristics.

The time spacing between the local maxima highlighted in Figures 4.15c to 4.15h is then investigated to determine whether further information about the target response can be extracted. At the relative window times highlighted in each figure panel, the dominant frequency of the measured waveform is recorded. This frequency is then used to estimate the group velocity and echo delay for a single circumnavigation around the target of an a_{0-} Lamb wave, following the methodology presented in Chapter 2. The results of this analysis are reported in Table 4.2. The first column of the table presents the relative window times of local maxima highlighted in Figure 4.15. The dominant frequency component in waveforms recorded at these locations is then given in the second column. The third column of the table presents the relative time delay measured between each local maximum while the fourth column presents the theoretically predicted delay. Finally, the normalized root mean square error between the measured and predicted delays is presented in the last column of the table.

The numerical results indicate that using the single-channel time reversal technique with a shifting time window and searching for the frequency location of dominant spectral peaks, it is possible to isolate, in frequency, up to 4 resonances in the scattering response of the target for the window sizes employed in this investigation. It is

also possible to roughly extract propagation times for a_0 - surface elastic waves even when the window size is larger than the characteristic circumnavigation time. This is evident from column 5 of Table 4.2 where the error between predicted and measured circumnavigation times is less than approximately 10%. The reader should be cautioned that the larger windows employed here encompass multiple surface elastic wave circumnavigations and thus the computed delay times will only be approximate.

The efficacy of the technique will vary depending upon the target of interest and the operating conditions. It will be especially difficult to characterize targets possessing aspect dependence. However, the methodology reported here provides a unique means with which to extract both time and frequency information for surface waves that propagate on an elastic target. With a large enough time window, it is possible to identify in the frequency domain a number of resonances in the scattering response of the target while at the same time retaining temporal information.

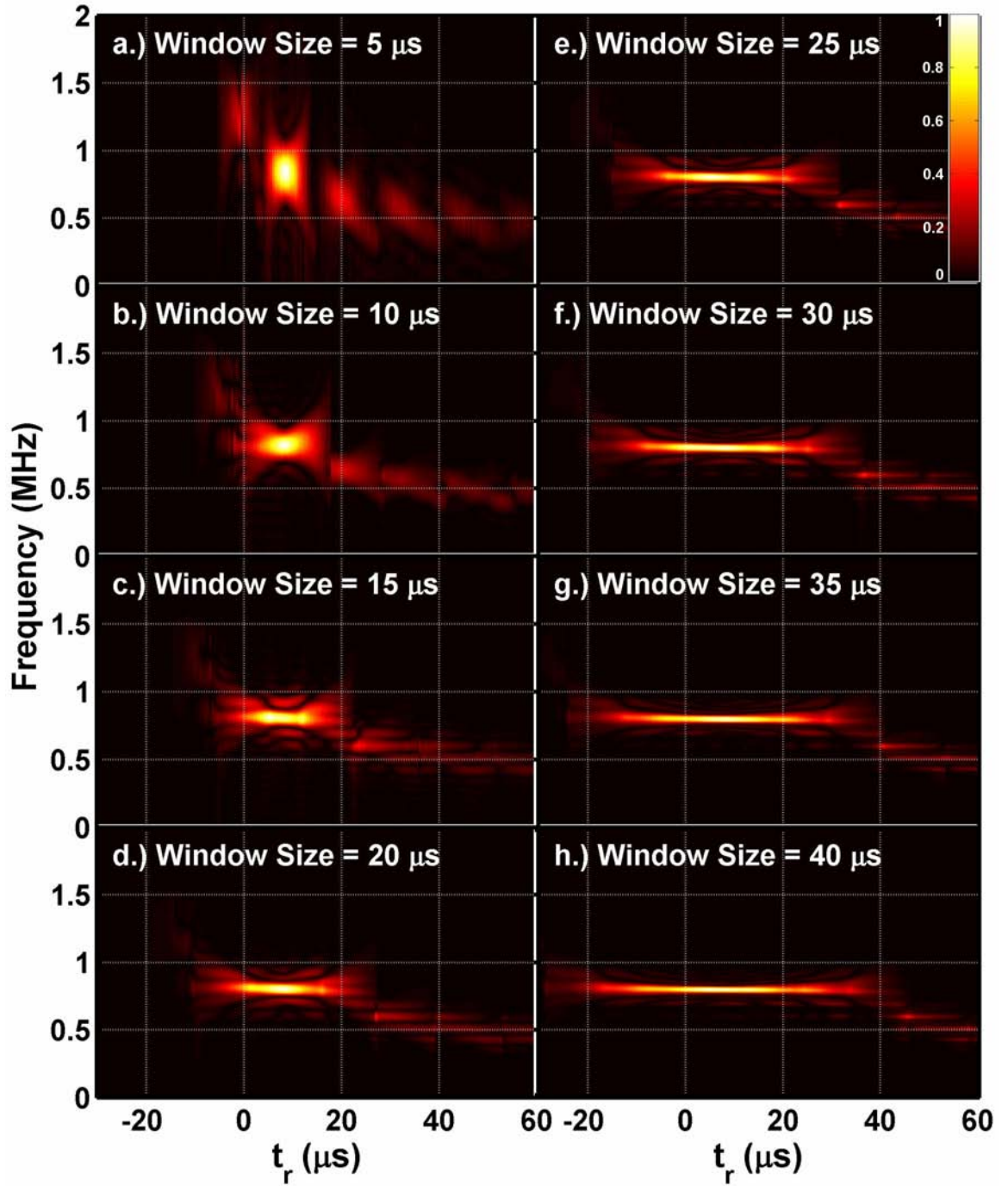


Figure 4.14: Echo spectral magnitude versus frequency and time where the center of the time reversal window is shifted in steps of $0.5\mu\text{s}$ from relative window times, t_r , of $-30\mu\text{s}$ to $60\mu\text{s}$. Panels (a)-(h) present results for window sizes ranging from $5-40\mu\text{s}$. Data is normalized to the maximum value within each figure panel. Incident waves approach the target from the left side of the figure.

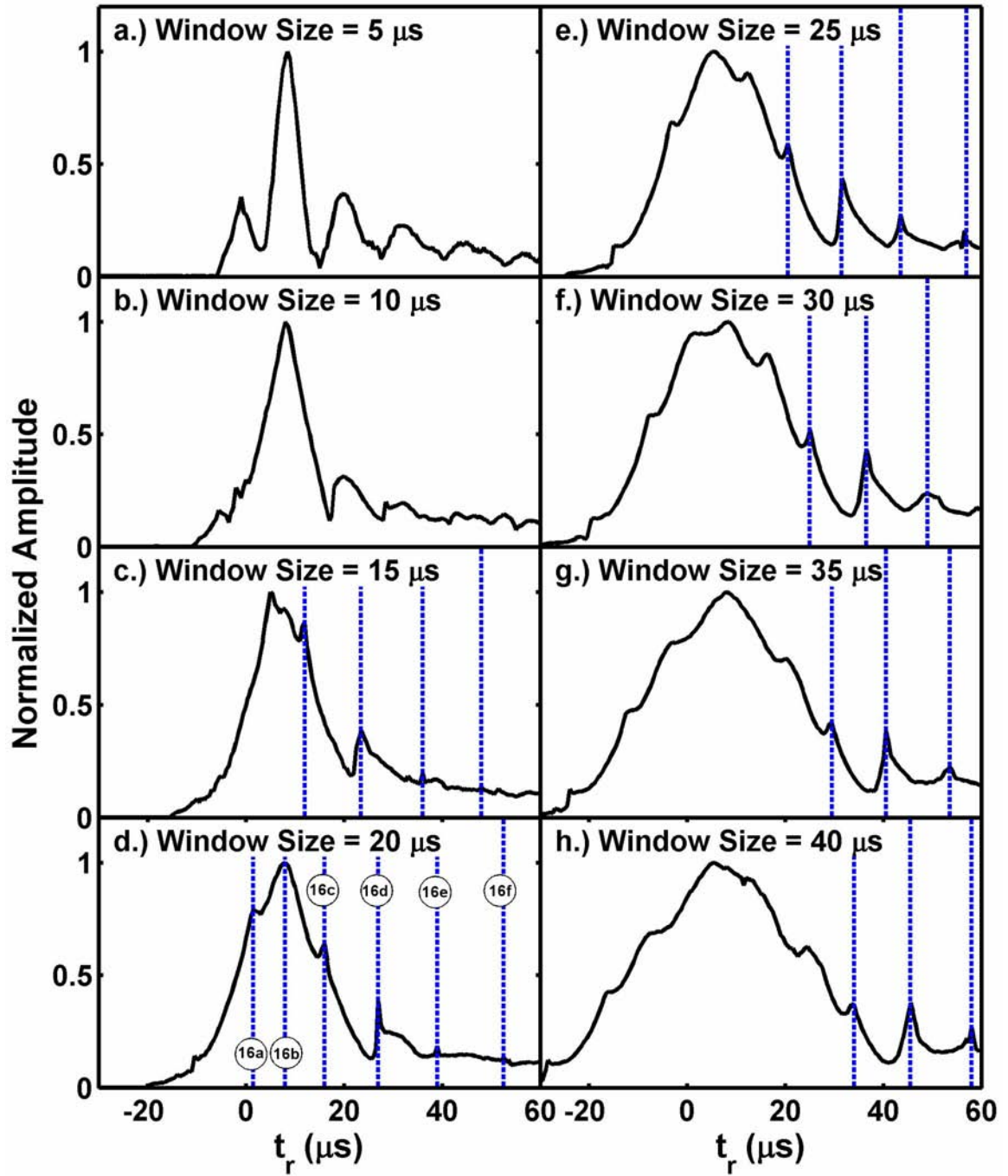


Figure 4.15: The maximum spectral magnitudes recorded at each relative window time in corresponding panels from Figure 4.14. Vertical dashed lines highlight the time locations of local maxima of interest. Results are normalized to the maximum value within each figure panel. The letters superimposed on the dashed lines in (d) are associated with the corresponding panels in Figure 4.16.

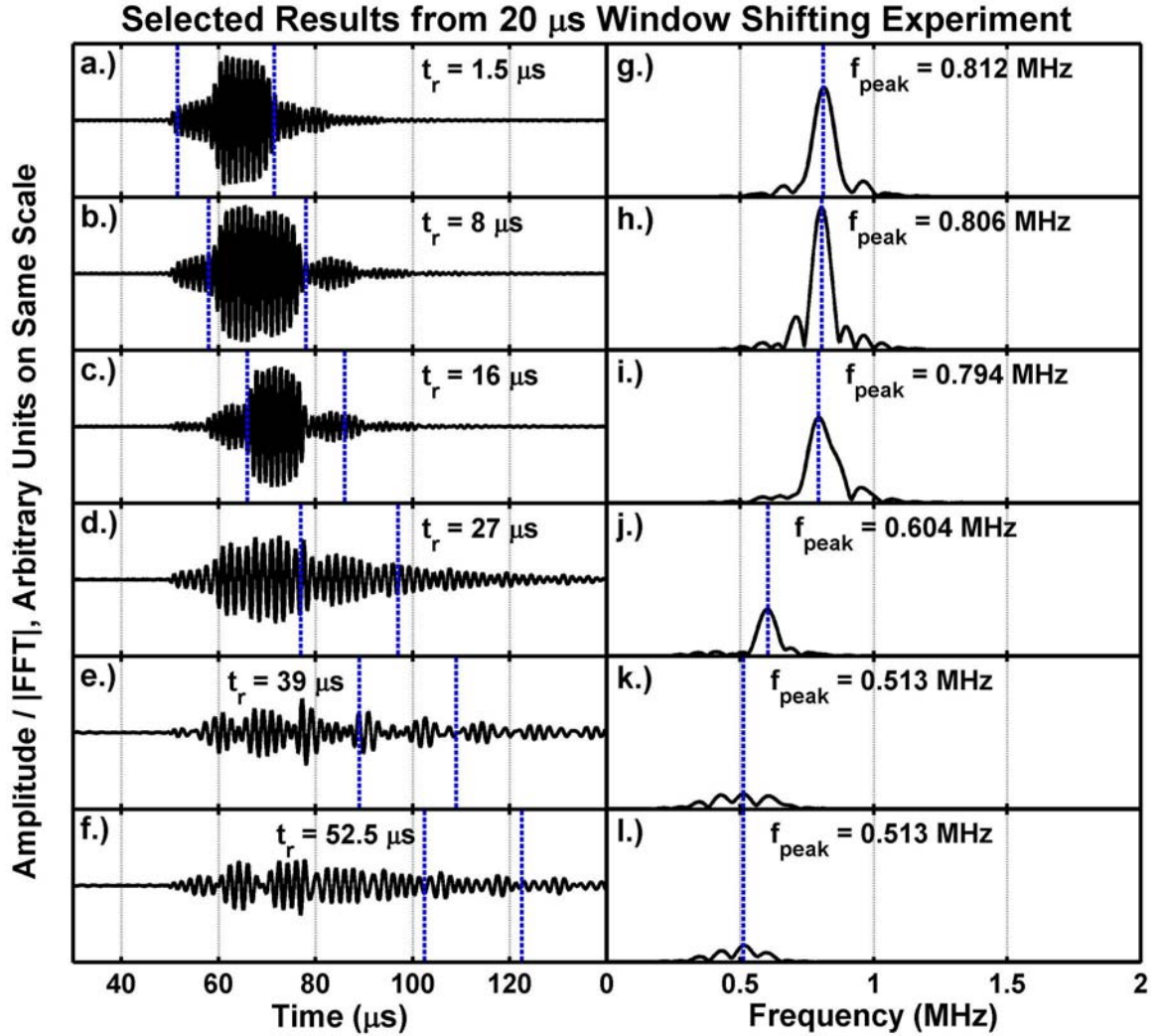


Figure 4.16: Waveforms from iteration 50 of time reversal appearing at relative window times, t_r , marked by vertical dashed lines in Figure 4.15d. The vertical dashed lines in (a)-(f) outline the location of a $5 \mu\text{s}$ duration time reversal window. Panels (g)-(l) present the magnitude spectra of signals within the time reversal window in (a)-(f). Vertical dashed lines in these figure panels mark the location of the peak spectral magnitude. The vertical axes in the time and frequency domain waveforms are presented in arbitrary units on the same scale.

Table 4.2: Comparison of echo delays of a_{0-} antisymmetric Lamb waves measured using the single-channel time reversal technique to those predicted by resonance scattering theory. The values in this table are determined from waveforms at the relative window times highlighted in Figures 4.15c to 4.15h. The normalized root mean square error between the measured and predicted echo delay is presented in the last column of the table.

		t_r (μs)	Frequency (MHz)	$\Delta t_{measured}$ (μs)	$\Delta t_{predicted}$ (μs)	NRMSE (%)
Window Size (μs)	15 μs	12	812	-----	-----	-----
		23.5	607	11.5	11.3	1.7
		36	613	12.5	11.2	10.4
		48	528	12	11.9	0.8
	20 μs	16.0	794	-----	-----	-----
		27.0	604	11.0	11.3	2.7
		39.0	513	12.0	12.1	0.8
		52.5	513	13.5	12.1	10.4
	25 μs	20.5	790	-----	-----	-----
		31.5	601	11.0	11.3	2.7
		43.5	513	12.0	12.1	0.8
		57.0	513	13.5	12.1	10.4
	30 μs	16.5	797	-----	-----	-----
		25.0	790	9.5	10.4	9.5
		36.5	601	11.5	11.3	1.7
	35 μs	29.5	787	-----	-----	-----
		40.5	601	11	11.3	2.7
		53.5	513	13	12.1	6.9
	40 μs	34	812	-----	-----	-----
		45.5	607	11.5	11.3	1.7
		58	613	12.5	11.2	10.4

4.4 Time Reversal with Multiple Targets Present

Previously, Pautet *et al.* [46] conducted an experiment where three targets possessing different scattering responses were aligned along the axis of a single-channel transducer. A time reversal experiment was conducted with the targets well separated so that the time reversal window encompassed returns from only a single target at any given time. They demonstrated that single-channel time reversal can automatically select the proper interrogation frequency for a given target, even though other targets were proximal to the face of the transducer and interfered with the incident sound waves. In this Section, the time reversal technique is applied to two targets positioned in proximity to one another on the axis of the transducer employed. The window shifting procedure employed in Section 4.3 is used to search for and isolate returns from both targets.

A solid stainless steel sphere is placed closest to the transducer front of the standard aluminum shell target. The steel sphere possesses the same outer diameter as the aluminum target. To position both targets at the center of the test tank, a layer of the polypropylene packing tape is positioned so that the sticky side is facing upwards. The targets are then gently adhered to the upper surface of the tape. The tape is stretched taught so that it deforms only minimally when the targets are resting upon it. The targets are positioned on the axis of the V-303 transducer as depicted in Figure 4.17, not to scale. The center of the stainless steel target is 9.5 cm from the face of the transducer. The center of the standard aluminum shell target is positioned 1.5 cm behind the stainless steel target.

The backscattering form functions of both targets are presented in Figure 4.18. Results of resonance scattering analysis performed on the steel sphere are presented in Appendix A.2. A few notes are made here regarding the types of waves that propagate on the steel target. Below 0.4 MHz, the response of the steel target is close to that of a rigid sphere. In the frequency bandwidth of the system, shown as a gray patch in Figure 4.18, Rayleigh waves (a type of surface elastic wave) circumnavigate the target. Higher order Rayleigh waves, commonly referred to as whispering gallery waves [88], also contribute to the backscatter, but are not observed in experimental results reported here. These surface elastic waves are indicated by sharp dips in the form function of the target because at steady state they interfere with the specular portion of the return. As observed in Figure 4.18, the resonant response of the standard aluminum shell target is stronger than that of the solid stainless steel target.

The window shifting experiment is first conducted with both targets in place for a range of window sizes. A relative window time of $t_r = 0\mu s$ is defined as the center of the specular return from the solid stainless steel sphere target. Fifty iterations of the time reversal procedure are performed at each relative window time where a single cycle 1 MHz sine wave is used as an initial interrogation. The results of this experiment for iteration 0 and iteration 50 are shown in the first and second columns of Figure 4.19, respectively. Window sizes of 2, 5, 10, and $20\mu s$ are employed. The aluminum shell target is then removed from the tank and the experiments are repeated with only the solid steel target in place. These results are presented in the third column of Figure 4.19. In Figure 4.19i, three discrete returns in time are observed. These energy packets

correspond to the specular return followed by two Rayleigh wave circumnavigations whose predicted echo delays are approximately $7\mu\text{s}$. These same returns are observed in Figures 4.19a and 4.19e but are followed by returns from the aluminum shell target. Qualitatively similar results are observed in the remaining sets of figures. The quality factors of resonances in the response of the steel target are not high enough to obscure resonances of the aluminum shell target. Thus the shell target is revealed even though it is partially shielded from incident waves by the solid steel target. In the second column of Figure 4.19, the frequencies of returns associated with the aluminum target at iteration 50 match those observed in Section 4.3.3. These frequencies are not readily identified in the first column of Figure 4.19 where only a single transmission is employed.

It is curious to note that for window sizes of $10\mu\text{s}$ and $20\mu\text{s}$, when the window encompasses returns from the solid steel sphere, a number of spectral peaks are present. This is because with 50 iterations, the time reversal procedure has not yet fully converged. Numerical simulations show that for a window size of $20\mu\text{s}$ convergence to the resonance centered at 1.535 MHz is observed after a greater number of iterations.

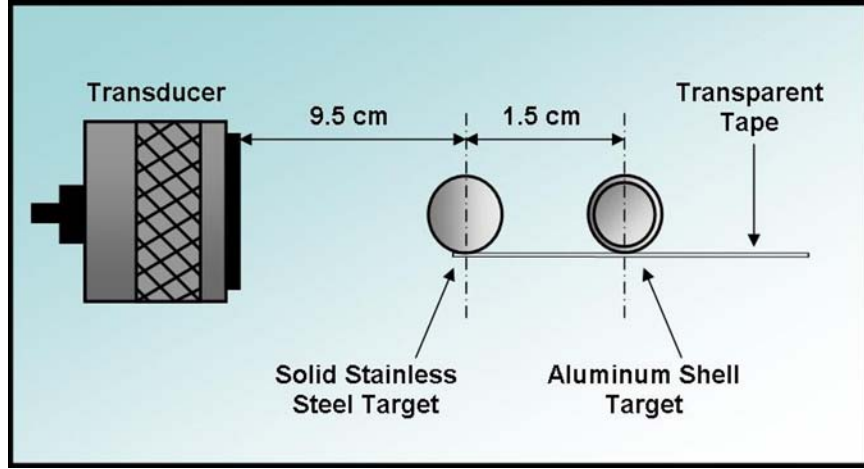


Figure 4.17: Schematic of the physical setup for time reversal experiments with multiple targets present. The schematic is not drawn to scale.

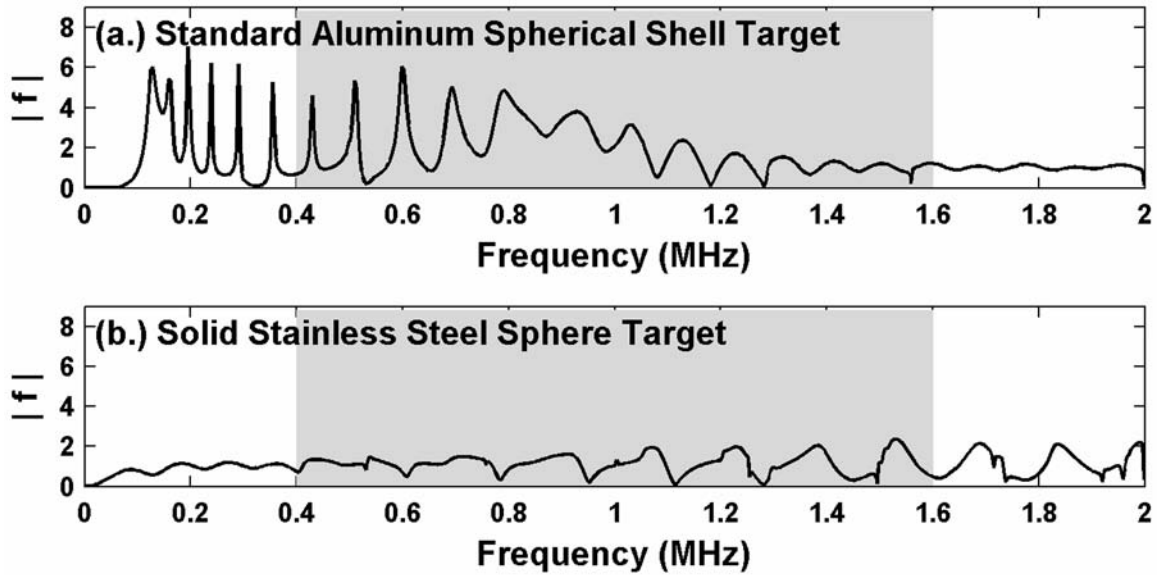


Figure 4.18: (a) Magnitude of the calculated monostatic far-field form function for the aluminum spherical shell target used in time reversal experiments versus frequency. (b) Magnitude of form function of the solid stainless steel sphere plotted versus frequency.

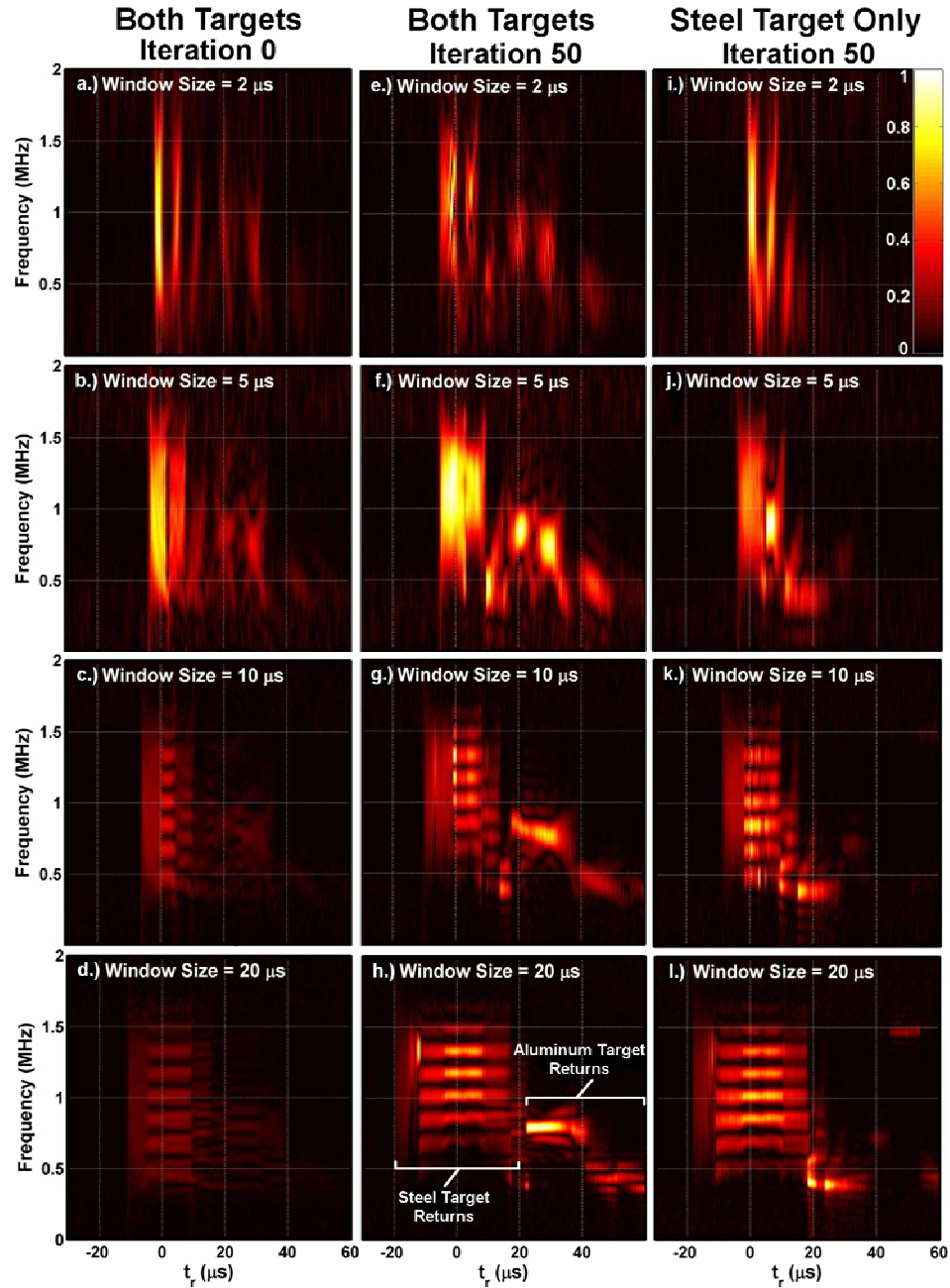


Figure 4.19: Echo spectral magnitude versus frequency and time, where the center of the time reversal window is shifted in steps of $0.5\mu\text{s}$ from relative window times, t_r , of $-30\mu\text{s}$ to $60\mu\text{s}$. Panels (a)-(d) present results at iteration 0 for window sizes ranging from 5–20 μs with both the aluminum shell target and solid sphere targets both in place. Panels (e)-(h) are the same as (a)-(d) but show iteration 50. Panels (i)-(l) present results at iteration 50 with only the solid stainless steel target in place. Data is normalized to the maximum value within each panel except (a)-(d) which are normalized to the maximum values in (e)-(h), respectively.

Chapter 5

Buried Target Results

“When beholding the tranquil beauty and brilliancy of the ocean’s skin,
one forgets the tiger heart that pants beneath it; and would not willingly
remember that this velvet paw but conceals a remorseless fang.”

Herman Melville, Moby Dick, The Gilder

Difficulties often arise in the detection and identification of buried targets due to noise, attenuation, and the presence of returns from false targets. This Chapter presents results from experiments where the time reversal technique is employed to help mitigate these difficulties. The first section of the Chapter provides a discussion of how the scattering response of the standard shell target changes when it is loaded with a fluid possessing the same properties as the sediment phantom employed. It is then demonstrated, in Section 5.2, that the time reversal technique can be used to enhance echoes from the target when it is buried in the sediment phantom. A sliding window study, the results of which are presented in Section 5.3, investigates the sensitivity of the time reversal technique to window position and is used to localize the depth of the target. The convergence

properties of time reversal are then examined in Section 5.4 as a function of target burial depth. The ability of the technique to isolate multiple resonances in the response of the buried target is demonstrated in Section 5.5. This property is examined in further detail in Section 5.6, which provides results from a comprehensive investigation of the effects of window size, window position, and angle of incidence. Finally, results presented in Section 5.7 demonstrate the ability of the technique to distinguish between two buried targets of the same size that possess different scattering responses.

5.1 Sediment Loaded Target Response

In order to confidently identify a target object acoustically, its scattering response must first be well understood. The analysis presented in Chapter 2 demonstrates that the response of a target submerged in water can be accurately modeled. However, predicting the response of a target buried in sediment is a much more difficult endeavor. Over the past two decades, significant efforts have been made towards this end [5, 6, 112-116]. There are two main complications in these modeling efforts. The first is in accounting for multiple scattering interactions between the target object and the sediment-water interface; targets that are only partially buried are especially difficult to characterize analytically. In the current work, targets are assumed to be deeply buried and so any interaction with the water-sediment interface is ignored.

The other complication inherent in modeling arises in determining the appropriate acoustic properties and propagation models for the sediment medium, that is, whether to assume the sediment is a fluid, an elastic/viscoelastic medium, or a poroelastic medium.

In this study, the sediment phantom employed is treated as a fluid. Its acoustic properties are determined through carefully conducted laboratory experiments; see Section 3.5.

Measured values of the frequency dependent speed and attenuation of dilatational waves in the sediment phantom (see Figure 3.22 and Figure 3.23 in Section 3.5) are fit with second order polynomials. This results in a dependence of

$$c_{sed}(f) = -480f^2 + 276f + 1733.8 \quad (5.2)$$

for the dilatational wave speed and

$$\alpha_{sed}(f) = 14.6160f^2 - 3.4825f + 5.1242 \quad (5.3)$$

for the attenuation, where f is in units of MHz. The density of water and the sediment phantom are assumed to be $\rho_{H_2O} = 998 \text{ kg/m}^3$ and $\rho_{sed} = 1830 \text{ kg/m}^3$, respectively. A value of $c_{H_2O} = 1483.8 \text{ m/s}$ is assumed for the sound speed of water. These properties are used to compute the scattering response of the standard aluminum shell target when it is buried in the sediment phantom. For convenience, in the remainder of this Chapter, the sediment phantom will be referred to simply as ‘sediment.’

For reference, the backscattering form function of the water-loaded standard shell target is presented in Figure 5.1a. The form function is then recalculated using an effective fluid possessing the same acoustic properties as the the sediment for the medium external to the sphere. Figure 5.1b presents this result. From this figure, it is apparent that the a_{0-} Lamb wave resonances in the target response take on a higher quality factor when the target is loaded with a fluid the sediment properties. This is because propagating surface waves do not radiate as efficiently into the external medium,

i.e. radiation damping of these waves is not at prominent. This observation is consistent with trends observed in another investigation that studied the response of silt-loaded and sand-loaded targets; see Figure 6 of Ref. [116].

An effort is then made to predict waveforms transiently scattered from the buried target by modifying the free field scattering simulation described previously, in Section 3.4. Figure 5.2 shows a schematic of the configuration assumed in buried target scattering simulations. The transducer is positioned at a distance of 10 cm from the surface of the sediment and is assumed to be in the farfield. The center of the shell target is buried on the central axis of the transducer at a depth D beneath the surface of the sediment. Plane acoustic waves propagate towards the target from the direction of the transducer.

Waveforms scattered by the surface of the sediment and the buried target are calculated individually. These two waveforms are then superimposed upon one another to form a final scattered return. The inherent assumption in this is that there is no multiple scattering between the target and the interface. Reflection and transmission coefficients computed at the interface are used to determine the amplitude of waves scattered from, entering, and leaving the sediment. Volume scattering from individual glass beads in the sediment is ignored.

The computation of scattered returns from the target is performed as follows. Equation (2.41) is used to compute the steady state scattering response of the buried target at a radial distance D in the monostatic direction. The location of this field point is highlighted in Figure 5.2. The calculation accounts for the dispersion and attenuation

of scattered waves in the sediment as they propagate from the location of the sphere to the field point. Transiently scattered waveforms are predicted in the frequency domain by computing the product of an incident waveform with the steady state response of the target. The incident waveform is weighted with a low pass filter possessing a frequency dependence of

$$\exp\{-\alpha_{sed}(f) \times D\}. \quad (5.4)$$

Here, D is the burial depth and $\alpha_{sed}(f)$ is the frequency dependent attenuation of the sediment in Nepers/m. This filter accounts for attenuation of the incident wave in the sediment before it interacts with the target. Finally, the amplitude of the returns from the buried target is scaled to account for transmission from the sediment into the water. Geometrically spherical spreading of waves scattered from the target location is assumed.

The simulation of buried target scattering is employed primarily to gain insight into the effects of attenuation on convergence of the time reversal procedure and to help confirm the types of waves that propagate on the buried target. Shown in Figure 5.3 is an experimentally measured scattered return from the target when its center is buried at a depth of 2 cm below the surface of the sediment. A 2 cycle 1 MHz sine wave is used as the waveform for interrogation. Figure 5.4 shows a return generated from the numerical scattering simulation, given the same parameters as in Figure 5.3. In both figures, a strong return from the surface of the sediment arrives earliest in time. This surface return is clipped in the figures so that returns from the target are clearly visible. A specular return from the target arrives after the surface return and is followed by both s_0 and a_0 Lamb wave returns. These are highlighted with arrows and labeled according to their

type in both figures. The arrival times of these surface elastic waves are comparable in both the experiment and simulation, although in the experiment the second a_{0-} Lamb wave circumnavigation arrives earlier than predicted. Also, although the shape and amplitude of the first a_{0-} Lamb wave returns are comparable in both figures, subsequent circumnavigations are more damped in the experimental measurement. This is likely because the nylon netting, within which the target is wrapped in the physical experiment, extracts energy from this wave type, damping its response. From these results, it is apparent that the numerical scattering simulation should provide a means with which to estimate returns from the standard shell target when it is buried.

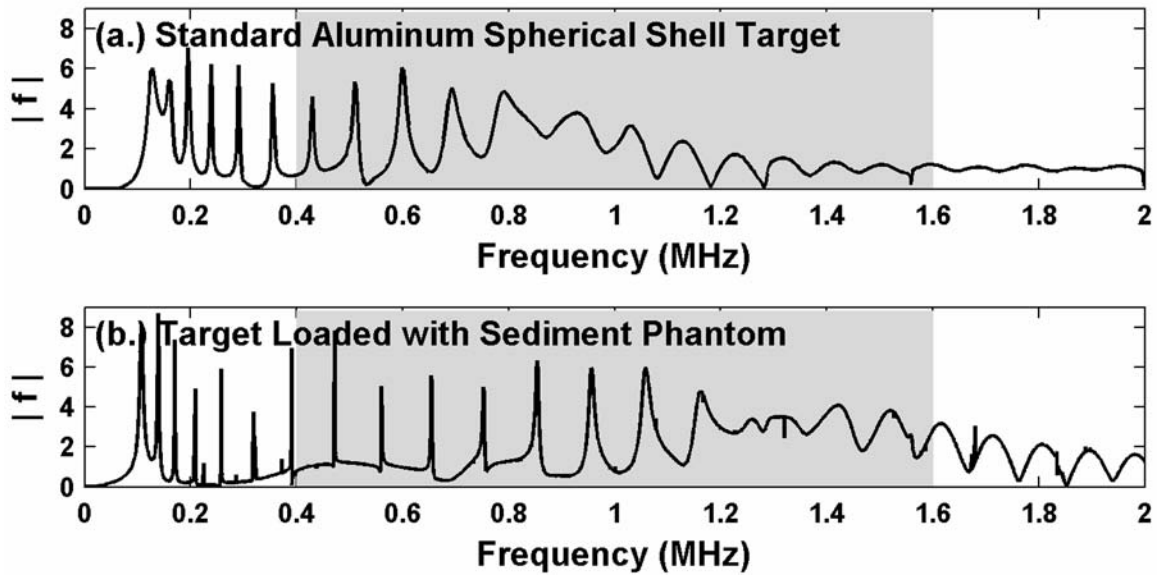


Figure 5.1: (a.) Magnitude of the calculated monostatic far-field form function for the aluminum spherical shell target used in time reversal experiments versus frequency. (b.) Magnitude of calculated form function of the aluminum shell target when loaded with the an effective fluid possessing the same acoustic properties as the glass bead sediment. The shaded gray region highlights the frequency bandwidth of the time reversal system.

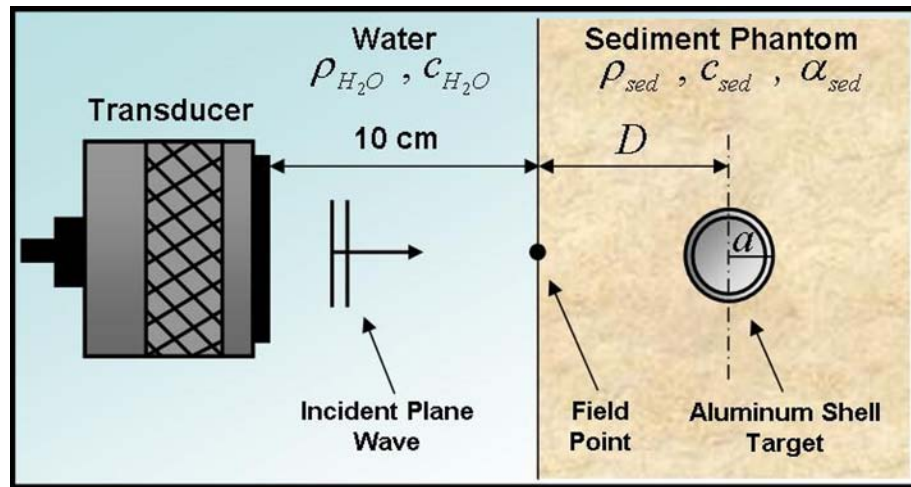


Figure 5.2: Schematic of the assumed configuration of for buried target transient scattering simulations. The schematic is not drawn to scale.

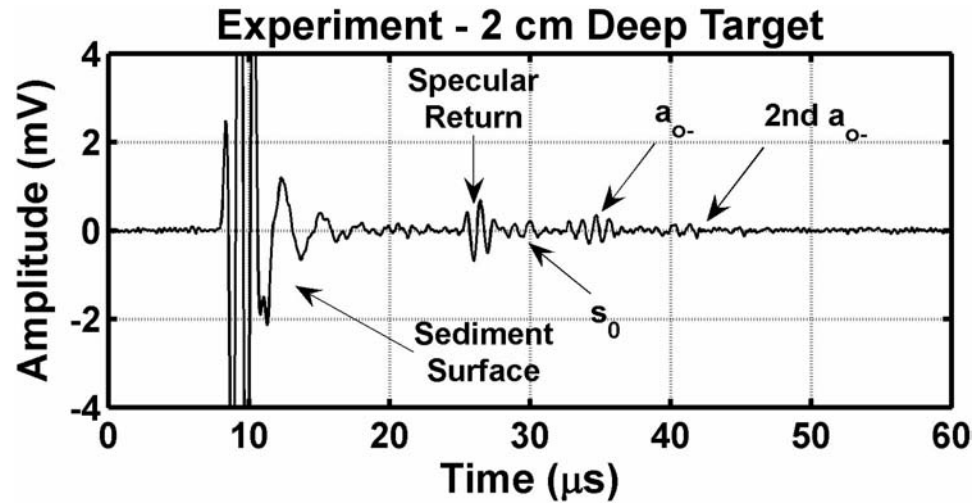


Figure 5.3: Experimentally generated waveform received after interrogating the 2 cm deep buried aluminum shell target with a 2 cycle 1 MHz sine wave. Arrows highlight various types of returns. The return from the sediment surface appears clipped on this display scale so that target returns are clearly visible.

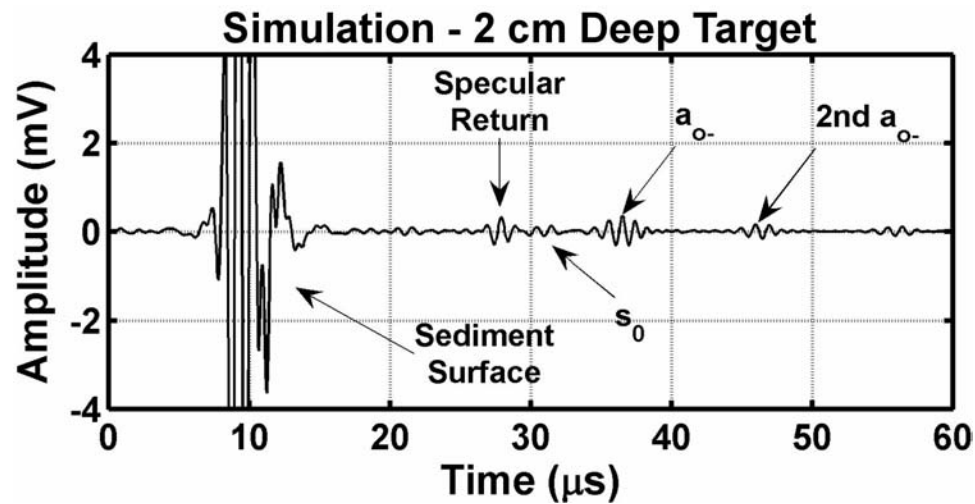


Figure 5.4: Waveform generated from the buried target numerical scattering simulation by interrogating the 2 cm deep buried aluminum shell target with a 2 cycle 1 MHz sine wave. Arrows highlight various types of returns. The return from the sediment surface appears clipped on this display scale so that target returns are clearly visible.

5.2 Buried Target Echo Enhancement

Armed with an understanding of the types of waves that propagate on the buried target, the time reversal technique is tested to determine whether echoes due to these waves can be enhanced. Depicted in Figures 5.5a to 5.5c in the time domain and in Figure 5.5d in the frequency domain with iteration number are results from an experiment where the time reversal window is centered on the location of returns from the target when buried at a depth of 2 cm. The two dashed vertical lines in each time trace illustrate the position of a $20\ \mu\text{s}$ long time reversal window, at a delay of approximately $25\ \mu\text{s}$ following the specular return from the surface of the sediment. Fifty time reversal iterations are performed in order to ensure that the procedure fully converges. This type of plot will be referred to subsequently as a “convergence plot.”

Figure 5.5a depicts the first backscattered return, iteration 0, where white noise $20\ \mu\text{s}$ in duration is used for interrogation. The pulse arriving earliest in time, at $135\ \mu\text{s}$, is a strong specular reflection from the surface of the sediment. Following the return due to the sediment surface, there is no obvious return from the target visible and in Figure 5d none of the peaks can be clearly identified as a target response. After ten iterations of the time reversal procedure, the return from the target is enhanced, as seen in Figure 5.5b, where a narrowband 1100 kHz pulse following the specular return from the sand surface is visible, centered near $170\ \mu\text{s}$. As evident in Figure 5.5c and 5.5d, respectively, by iteration 35 the location of the target is identified and application of the time reversal procedure results in convergence to an 1100 kHz waveform. Examination of Figure 5.1

indicates that this resonance likely corresponds to an a_{0-} antisymmetric Lamb wave. In the frequency domain, a factor of 37.6, or 31.5 dB, improvement in the magnitude of the target response is observed relative to the first backscattered return. The time reversal procedure picks out the dominant target response frequency, even though the signal is not distinguishable from background noise on the first return. This highlights the ability of the active time reversal technique to enhance returns from a target regardless of the waveform used for initial interrogation.

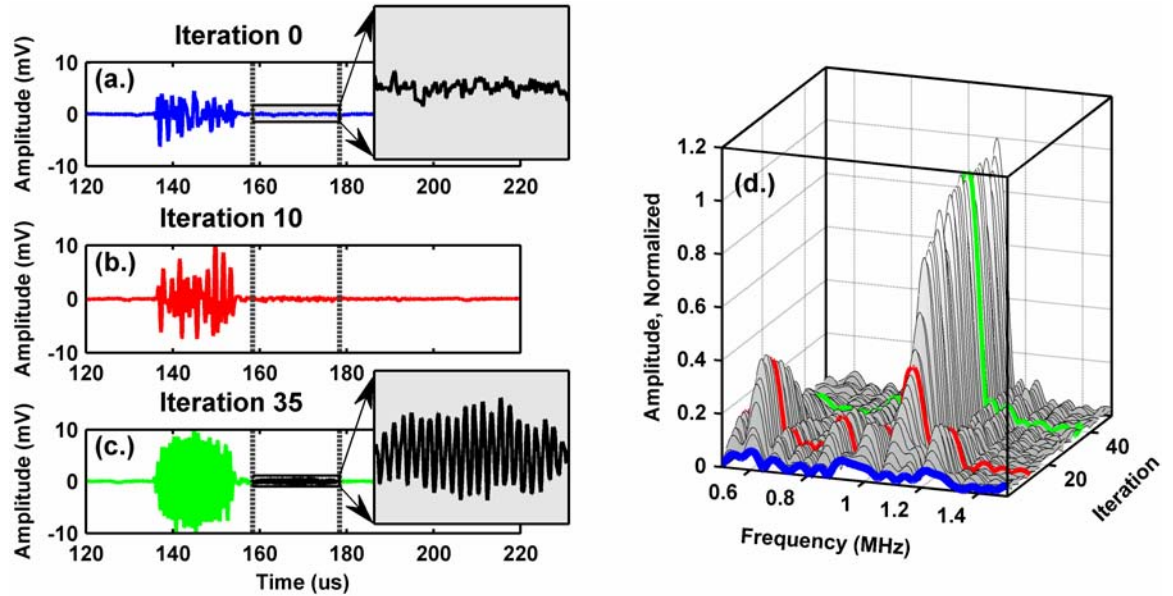


Figure 5.5: Convergence plot for the standard shell target buried 2 cm beneath the surface of the sediment through successive iterations of the time reversal procedure. The transducer is at normal incidence to the surface of the sediment. Vertical lines in (a)-(c) depict the position of a $20\mu s$ long time reversal window. (a.) The first backscattered return, iteration 0, where white noise $20\mu s$ in duration is used for interrogation. (b.) Backscattered return at iteration 10 of the time reversal procedure. (c.) Backscattered return at iteration 35 of the time reversal procedure. (d.) Waterfall plot of magnitude spectra of signals within the time reversal window for iterations 0 through 50 normalized to the maximum spectral magnitude at the final iteration. The spectra from (a)-(c) are highlighted with solid black lines.

5.3 Sliding Window Study

In order to understand the sensitivity of single-channel time reversal to window position and to localize the depth of the target, experiments are performed to quantify the signal-to-noise ratio of target returns after application of the technique. For each experiment, the center of the time reversal window is shifted, in steps of $1 \mu\text{s}$, from relative window times of $-30 \mu\text{s}$ to $60 \mu\text{s}$. A relative window time of $t_r = 0 \mu\text{s}$ corresponds to when the time reversal window is centered over reflections from the surface of the sediment. The experiment is performed once over the location of the target buried at a depth of 2 cm and then again with the transducer shifted to a position over the sediment without a target in place. A signal-to-noise ratio (SNR) is defined by:

$$SNR = 10 \log_{10} \left(\frac{\int_{f_0}^{f_1} |S(f)|^2 df}{\int_{f_0}^{f_1} |N(f)|^2 df} \right), \quad (5.5)$$

where $S(f)$ and $N(f)$ are the Fourier transforms of signals within the time reversal window in experiments with and without the target in place, respectively. For the computation of a particular SNR value, the windows in both experiments are positioned at the same relative window time. The calculated energy is integrated over a manually defined frequency bandwidth, where f_0 and f_1 define the respective lower and upper limits of this frequency band.

Results are presented in Figure 5.6, where a $20 \mu\text{s}$ long time reversal window is used and a 50 iteration time reversal sequence is obtained at each window position. A waveform, consisting of white noise $20 \mu\text{s}$ in duration, is used to initiate the time reversal

process at each window location. White noise is used in order to demonstrate the efficacy of the technique even when a sub-optimal waveform is used for the initial interrogation. The black solid and dashed lines, generated from iteration 0 and iteration 50, respectively, are computed from 0 to 2 MHz, a frequency band encompassing the entire bandwidth of the transducer used. In Figure 5.6, the SNR appears to fluctuate randomly for relative window times earlier than $-20 \mu s$. These window locations are earlier than the sediment return and thus no coherent returns are present within the time reversal window. Therefore, the time reversal procedure acts on incoherent noise. As the relative window time gets larger, between $-20 \mu s$ to $20 \mu s$, coherent returns from the surface of the sediment dominate the measured spectral response for both iteration 0 and 50 with and without the target in place. This results in a SNR of 0 dB. Finally, when the time reversal window is delayed such that it encompasses returns from the target and no longer includes returns from the sediment surface, an increase in the SNR is observed. At iteration 0, the SNR between relative window times of 20 to $40 \mu s$ has a maximum of approximately 4 dB. Fifty iterations of the time reversal procedure result in an improvement in the signal to noise ratio of 16 dB when the window is centered at a depth of $30 \mu s$. As the window is advanced beyond the location of the target to depths greater than $40 \mu s$, the time reversal window no longer encompasses returns from the target and the technique does not converge.

A further improvement in the SNR is achieved by limiting the bandwidth used in its calculation to a range of frequencies encompassing only the dominant wave mode resonance of the target. The solid gray line in Figure 7 depicts the signal to noise ratio

calculated over a frequency band of 750 kHz to 1200 kHz, within which the dominant wave mode in the scattering response of the target lies. An improvement in the signal to noise ratio of 30 dB is observed, relative to iteration 0 calculated over the full band. Thus, *a priori* knowledge of the scattering response of a particular target combined with additional signal processing can further improve detection and identification

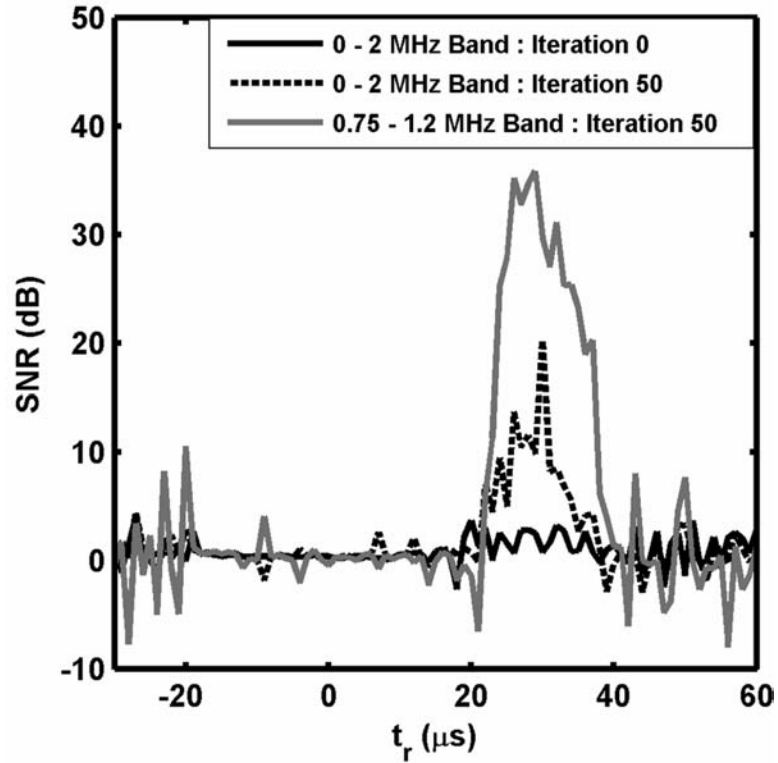


Figure 5.6: Signal to noise ratio of returns within a 20μ s long time reversal window as a function of relative window time, t_r , where white noise 20μ s in duration is used to initiate the process. The black solid and dashed lines, representing iteration 0 and iteration 50, respectively, are computed over a frequency band of 0 to 2 MHz, encompassing the full bandwidth of the transducer used. The solid gray line is computed from iteration 50 over a frequency band of 0.75 MHz to 1.2 MHz within which lies the dominant resonant wave mode of the buried target.

5.4 Convergence with Target Depth

In order to test the convergence properties of the time reversal technique, the experiment described in Section 5.1 is repeated with the center of the target buried at nominal depths of 1, 2, 3, and 4 cm. In Figures 5.7a to 5.7d, returns from iteration 50 of the time reversal procedure are shown for each target burial depth, where the dashed lines denote the position of the time reversal window. Figure 5.7e shows a similar result that is generated without a target in place. The peak amplitude of these waveforms is normalized to the maximum value in Figure 5.7c. The magnitude spectra of the signals within the time reversal window in Figures 5.7a to 5.7e are shown in Figures 5.7f to 5.7j, respectively. The frequency domain results are normalized to the peak spectral magnitude in Figure 5.7g and are all presented on the same scale. For each experiment, a 2 cycle 1 MHz sine wave is used as an interrogation pulse to initiate the time reversal process.

In the first three rows of Figure 5.7, the time reversal procedure converges to frequencies of 1220 kHz, 1100 kHz, 550 kHz, and 420 kHz for target depths of 1, 2, 3, and 4 cm, respectively. Thus, increasing the burial depth of the target leads to a downshift in the convergence frequency. This is due to the increase in attenuation of the sediment with frequency. That is, the layer of sediment above the target acts as a low-pass filter the strength of which increases with burial depth. When the target is buried at a depth of 4 cm, as in Figure 5.7d, the attenuation is too great for the system to overcome and returns from the target are indistinguishable from coherent background noise (volume scattering). This is evident in Figures 5.7e and 5.7j where the rms-amplitude of

the windowed return without a target in place is comparable to that of the target buried at 4 cm depth.

In order to confirm that attenuation in the sediment is indeed the cause of the observed downshift in convergence frequency, a set of numerical simulations are conducted using the buried target transient scattering simulation described in Section 5.1. The simulation is run for the same set of parameters used to generate the results presented in Figure 5.7. In Figures 5.8a to 5.8c, the time reversal procedure converges to frequencies of 1260 kHz, 1170 kHz, 480 kHz, and 500 kHz for target depths of 1, 2, 3, and 4 cm, respectively. Table 5.1 summarizes, for comparison, the convergence frequencies observed in experiment and simulation. Qualitative agreement is found between the experimental and numerical results, indicating that attenuation is indeed the primary reason for the observed downshift in convergence frequency with burial depth. The results of this section demonstrate the strength of iterative time reversal, to automatically redirect acoustic energy into the strongest available target resonance.

Table 5.1: Comparison of convergence frequencies observed for different target burial depths in experiments and through application of the buried target scattering simulation.

Target Burial Depth	Convergence Frequency from Experiment (kHz)	Convergence Frequency from Simulation (kHz)
1 cm	1220	1260
2 cm	1100	1170
3 cm	550	480
4 cm	420	500

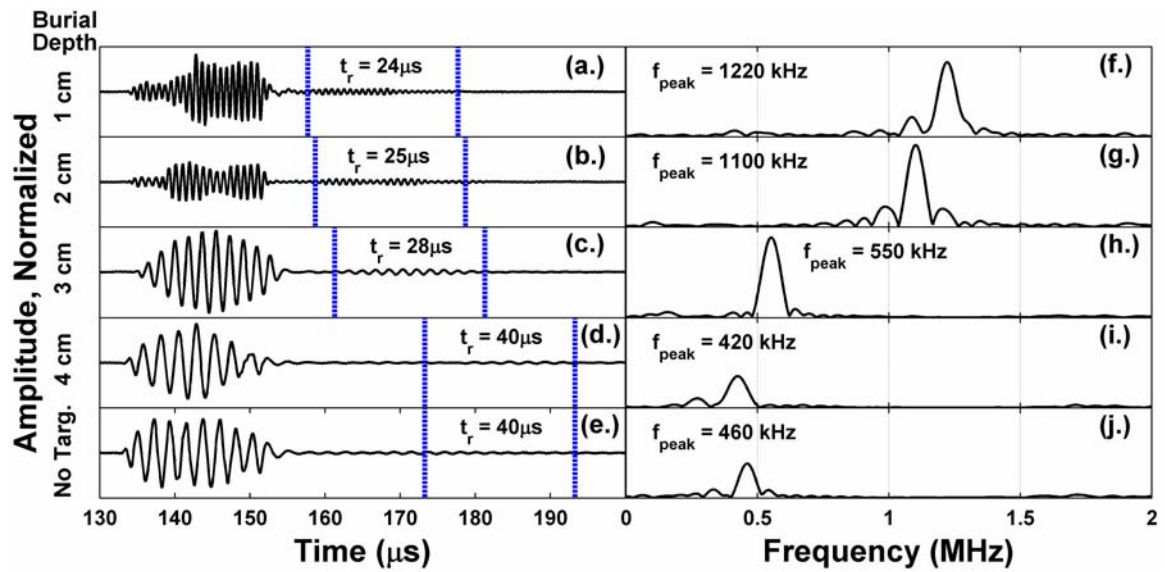


Figure 5.7: Experimental results from iteration 50 of the time reversal procedure with the target buried at different depths in the glass bead sediment. The vertical dashed lines depict the position of a $20\mu\text{s}$ long time reversal window. (a) – (d) Time domain returns with center of the target buried at 1.5 cm, 2 cm, 2.5 cm, and 4 cm depths, respectively. (e) Return at iteration 50 with no target in place. Time domain waveforms are normalized to the peak amplitude in (d) and are all presented on the same scale. (f) – (j) Fourier transforms of signals within the time reversal window from (a) – (e). Frequency domain results are normalized to the peak spectral magnitude in (f) and are all presented on the same scale.

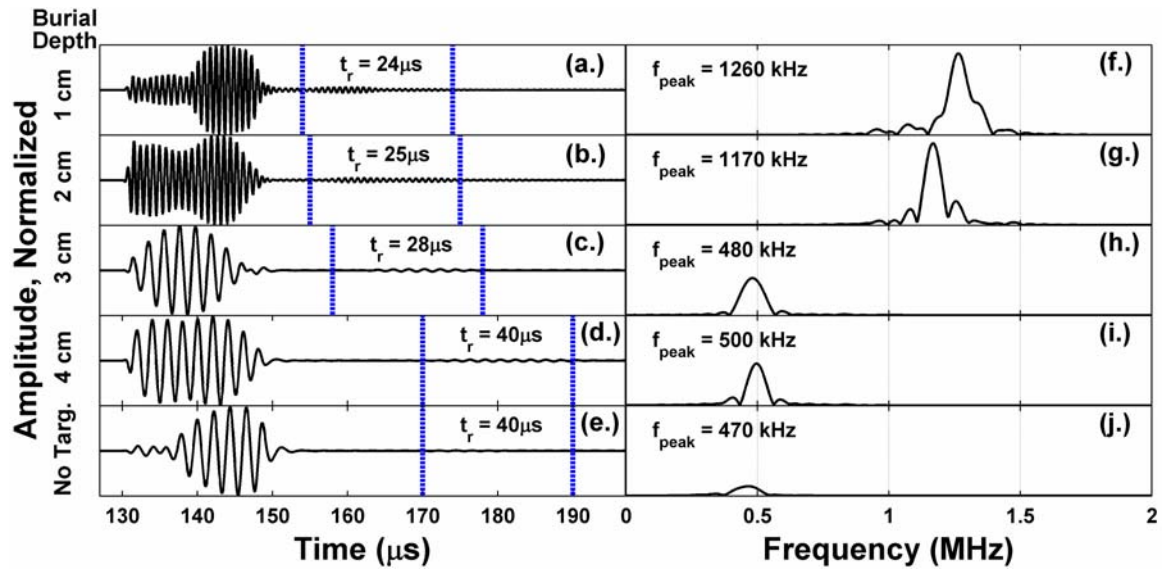


Figure 5.8: Numerical results from iteration 50 of the time reversal procedure with the target buried at different depths in the glass bead sediment. The vertical dashed lines depict the position of a $20\mu\text{s}$ long time reversal window. (a) – (d) Time domain returns with center of the target buried at 1.5 cm, 2 cm, 2.5 cm, and 4 cm depths, respectively. (e) Return at iteration 50 with no target in place. Time domain waveforms are normalized to the peak amplitude in (d) and are all presented on the same scale. (f) – (j) Fourier transforms of signals within the time reversal window from (a) – (e). Frequency domain results are normalized to the peak spectral magnitude in (f) and are all presented on the same scale.

5.5 Multiple Resonance Isolation

Previously, results in Section 4.3 demonstrated that when the standard shell target is suspended in the free field, multiple resonances in its scattering response are enhanced through application of single-channel time reversal. The studies made use of a sliding time window to search for scattered wave resonances. In this section, sliding window experiments are conducted with the transducer aligned at normal incidence to the surface of the sediment, beneath which the standard shell target is buried at a depth of 2 cm. Results from these experiments are presented in Figure 5.9 where window sizes of $8\mu s$, $14\mu s$, $20\mu s$, and $26\mu s$ are employed. The pixel intensity in each plot is given by the magnitude of the Fourier transform of the signal within the time reversal window. Cosine squared shading with a 20% envelope is applied to signals before Fourier transform computations are performed. The left and right columns of Figure 5.9 show results from iteration 0 and iteration 50, respectively. Plots are all presented on the same scale and have been normalized to the peak magnitude observed in returns from the target. Although this normalization has the effect of clipping returns from the surface of the sediment, it is performed so that returns attributed to the target are readily visible. In subsequent sections, a number of plots similar to those in Figure 5.9 are presented. They are hereafter referred to as “window shifting plots.”

In Figure 5.9, for all window sizes employed, a significant amount of broadband energy centered at $t_r = 0\mu s$ is observed. This is attributed to returns from the surface of the sediment which, when operating at normal incidence, are always much stronger than returns from the target. At iteration 0, returns from the buried target are detected

following returns from the surface of the sediment. The energy attributed to target returns is however smeared across a wide range of frequencies and it is difficult to isolate individual wave modes. In the second column of Figure 5.9, through 50 iterations of time reversal, an increase in the magnitude of target returns is obtained and the process is shown to selectively enhance specific target resonances. This is apparent, for example, in Figure 5.9e where a white circle outlines returns from the target. The highlighted energy packets are centered at frequencies of 1250 kHz, 850 kHz, and 450 kHz. These frequencies correlate approximately to the locations of a_0 - Lamb wave resonances in the response of the buried target; see Figure 5.1. In Figures 5.9f-5.9h, where larger window sizes are employed, these same returns are apparent. It is interesting to note, however, that in some cases all three frequency components appear concurrently. This is likely because the resonances are comparable in strength and the time reversal procedure has not yet fully converged.

In these experiments, it is not possible to isolate individual surface waves in time as it is when the target is suspended in the free field (see Section 4.3.2). When the target is positioned in the free field, the amplitude of a propagating surface elastic wave decays as the wave circumnavigates the target. This decay is attributed solely to radiation damping. When the target is buried, attenuation in the sediment accelerates this decay. This places a limit upon the maximum relative window time (window depth) at which returns from the target will be detected. The attenuation in the sediment also causes a more rapid downshift in the convergence frequency (relative to the free field results of Section 4.3) as the window passes the target. This is attributed to the low pass filtering

effect of the attenuation as described in Section 5.1. Examination of the data indicates that, at most, only two Lamb wave circumnavigations are visible in the experimental results reported here.

Finally, one notices that as the window size is increased, returns from the surface of the sediment have the effect of masking returns from the target. For example, in Figures 5.9f to 5.9h, when the window size is increased, the energy attributed to surface returns expands significantly in time while returns associated with the target do not. This is because, when operating at normal incidence, the surface of the sediment is always the dominant scatterer. Therefore, the window size should be optimized in order to maximize target returns, while still retaining the temporal resolution with which to isolate the target from the sediment surface. This will be explored in further detail in Section 5.6.2.

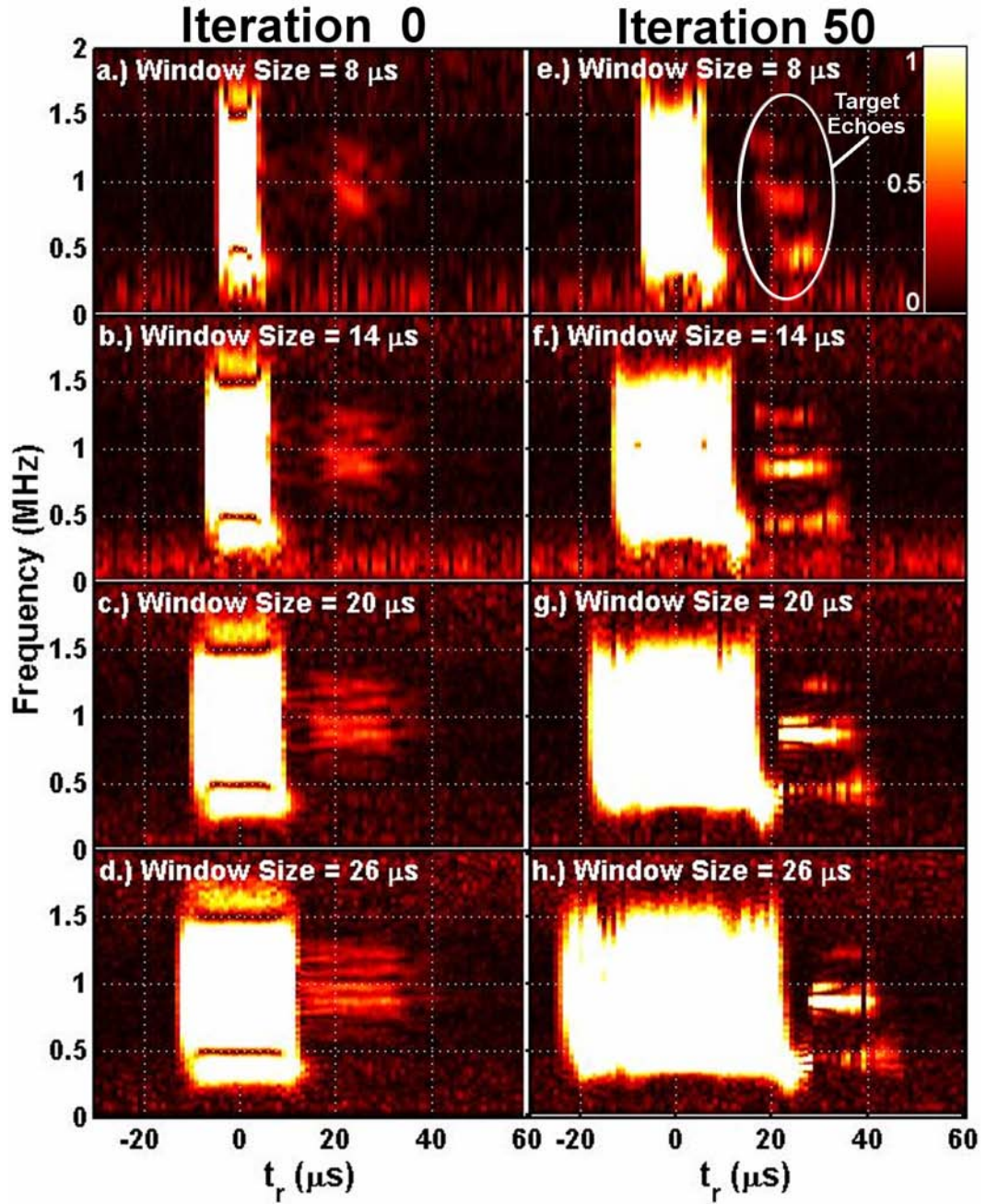


Figure 5.9: Results from an experiment where the center of the time reversal window is shifted in steps of $1\mu\text{s}$ from relative window times, t_r , of $-30\mu\text{s}$ to $60\mu\text{s}$ over the standard shell target buried at 2 cm depth. The pixel intensity represents the magnitude spectrum of the signal within the time reversal window. (a)-(d) present results at iteration 0 for window sizes of 8, 14, 20, and $26\mu\text{s}$. (e)-(h) present the same results but for iteration 50. Data is normalized to the maximum value for $t_r > 25\mu\text{s}$ within each row. The transducer is aligned at normal incidence to the surface of the sediment and incident waves approach the target from the left side of the Figure.

5.6 Comprehensive Parameter Investigations

In the previous section, using specific examples, it is demonstrated that multiple resonances in the response of a buried target are enhanced using single-channel time reversal. The current section provides an examination of this property for a wide-range of experimental parameters including window size, window position, and angle of incidence. First, an introduction summarizing the importance of incident angle is provided. The remaining sections detail results from parameter studies carried out at incident angles of 0, 10, and 20 degrees. A recapitulation of general conclusions is then provided in the final section.

5.6.1 Overview – Sensitivity to Incident Angle

In order to investigate the sensitivity of the technique to incident angle, the echo enhancement experiment described in Section 5.2 is repeated a number of times. The physical setup of experiments is depicted in Figure 5.10. Using an angle finding level, the transducer is rotated about an axis that passes through the center of the standard shell target buried at 2 cm depth. At incident angles of 0, 10, and 20 degrees, experiments are conducted with the time reversal window centered on returns from the target. The results from each experiment are summarized in Figure 5.11. At normal incidence, in Figure 5.11a, the technique converges to a resonance centered at a frequency of 850 kHz. Although this is a different resonance than the 1100 kHz frequency observed in Section 5.2, it corresponds to the same a_{0-} Lamb wave circumnavigation. Convergence to this

lower frequency arises because the transducer was likely not perfectly aligned over the target in the experiment. For justification of this, the reader is referred to Section 5.7.

When the transducer is rotated to an incident angle of 10 degrees, convergence to a frequency of 480 kHz is observed, as in Figure 5.11b. This is markedly different than the result at normal incidence. When the transducer is rotated, a bias towards low frequencies is induced in the system response. This results in convergence of the time reversal procedure to a lower frequency target resonance than expected. The bias arises in these experiments due to three effects. First, Snell's law dictates that because the sound speed in the sediment is higher than that of water, waves entering the sediment will be refracted. In setup shown in Figure 5.10b, this has the effect of shifting the beam of the transducer from the center of the target towards its left side (see the refracted ray path labeled in Figure 5.10b). Lower frequencies in the beam of the transducer spread more than higher frequencies. Therefore, the target will be preferentially excited by lower frequencies, while higher frequency components pass the target on its left and do not interact directly with it. Simple ray tracing calculations indicate, however, that the incident angle of the ray approaching the target shifts by less than ~2% at 10 degrees incidence. Therefore, it is likely that Snell's law effects cannot fully explain the observed downshift in convergence frequency in this experiment.

The second biasing effect arises as the incident angle is increased, because at larger angles, the sound passes through a greater effective thickness of sand which acts as a low pass filter as discussed in Section 5.4. The third biasing effect arises due to reflections from the surface of the sediment. In Section 3.3.2 a downward shift in

frequencies reflected from the sediment surface was observed for larger angles of incidence. This is because lower frequencies spread more and, when at non-normal incidence, these components are reflected off the sediment-water interface, directly back towards the transducer (see the low frequency path labeled in Figure 5.10b). Higher frequencies that are closer to the central axis of the transducer are reflected in the forward direction and do not return to the location of the transducer. For quick reference, the surface response of the sediment for 0, 10, and 20 degree incidence is shown in Figure 5.12. Clearly, as the incident angle is increased to 10 degrees a bias towards lower frequencies is observed.

Surface returns bias convergence of the time reversal procedure to resonances in the response of a target in the following way. Sometimes, the surface return is sufficiently long in time that it overlaps returns from the target. In such a case, frequency responses due to both the target and the surface are effectively added with one another. At normal incidence, for example in Figure 5.12, returns from the sediment surface are relatively flat in frequency. Therefore, when the surface response and target response are added, no significant bias is imposed upon the frequency response of the target. However, at an incident angle of 10 degrees, the surface response is biased towards low frequencies. In this case, the surface response effectively increases the spectral magnitude of lower frequency resonances in the response of the target. Therefore, these resonances will be preferentially excited in the frequency domain and, if the bias is strong enough, the time reversal procedure will select one of these lower frequency components. This occurs only if a portion of the surface return “leaks” into the time reversal window.

Observations of this phenomenon are confirmed, in Section 5.6.3, for experiments conducted at 10 degrees incidence.

At 20 degrees incidence, the majority of the transmitted energy is reflected in the forward direction (away from the transducer) and the surface response becomes negligible. This is evident in Figure 5.12, in the frequency domain, and also in the time domain plot of Figure 5.11c, where the surface return is barely visible. When time reversal is applied to target returns at this angle, it results in convergence to the same 850 kHz frequency resonance observed at normal incidence, the expected dominant frequency component in the response of the target. In this case, the surface response is of sufficiently low amplitude so as to not impose any significant bias upon the response of the target. Therefore, the incident angle can be optimized to minimize the sediment surface return while still converging to the expected target resonance frequency.

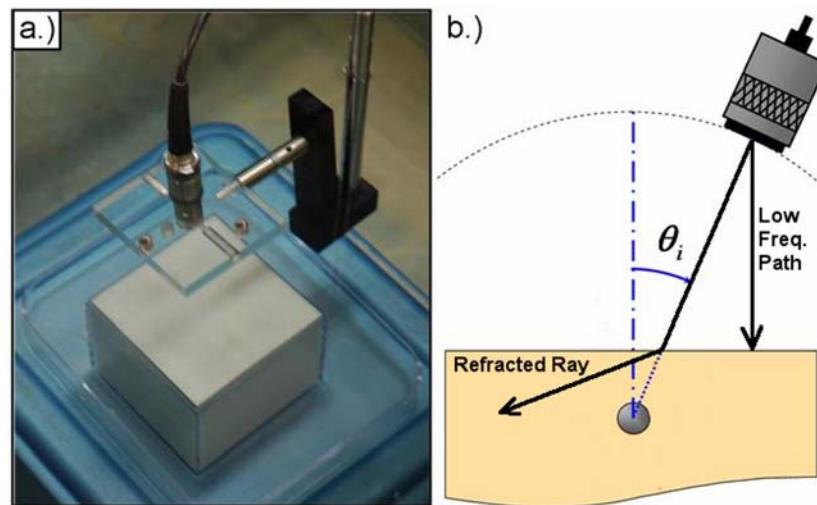


Figure 5.10: Physical setup for time reversal experiments where the angle of incidence is varied. (a.) Picture of the physical setup showing the transducer aligned over the sediment, within which the standard shell target is buried. (b.) Schematic showing the cross-section of the sediment and target. The schematic is not drawn to scale.

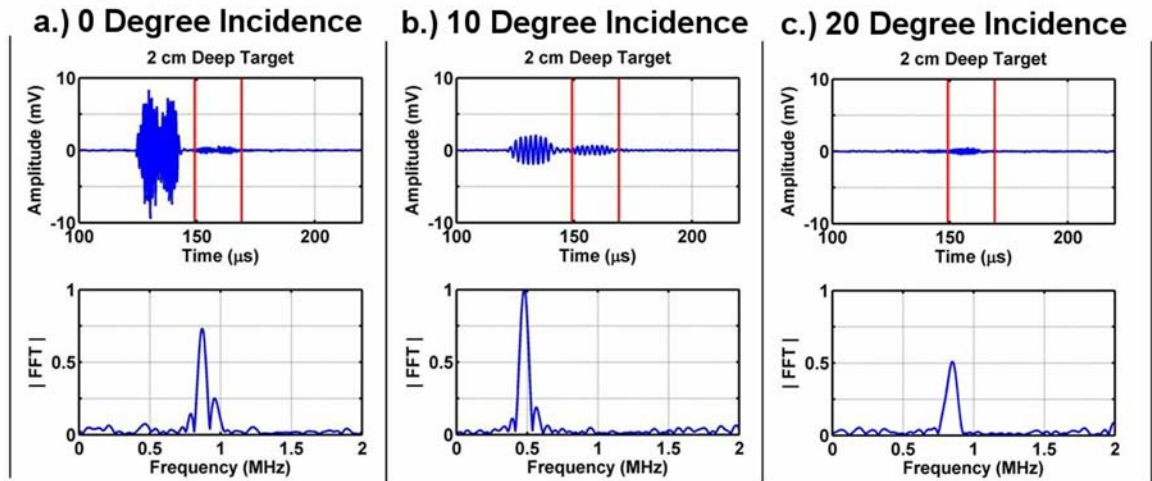


Figure 5.11: Time traces and spectra at iteration 50 of time reversal for incident angles of 0, 10, and 20 degrees. Vertical lines in the time traces highlight the location of the time reversal window. Spectra are computed from the signal within the window and are normalized to the maximum value in (b).

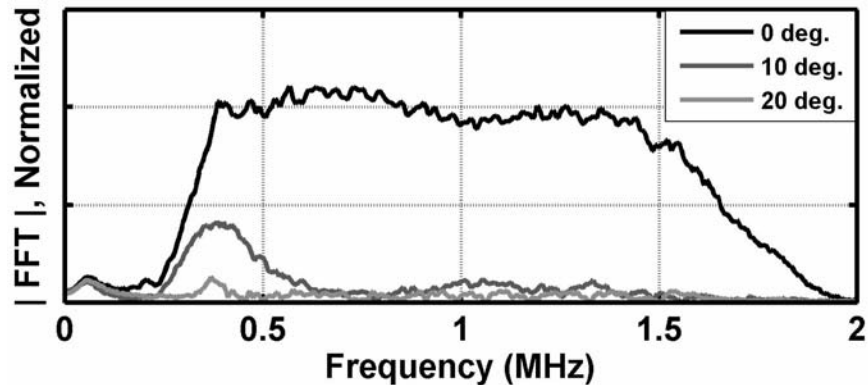


Figure 5.12: Magnitude spectra of reflections from the surface of the sediment for incident angles of 0, 10, and 20 degrees. A long linear chirp spanning the full system bandwidth is as the transmitted waveform in each case.

5.6.2 Normal Incidence Angle

In a comprehensive investigation of window parameters, the sliding window experiment described in Section 5.3 is repeated for window sizes ranging from $4\mu\text{s}$ to $60\mu\text{s}$ in length. In this investigation, waveforms are digitized at a sampling frequency of 25 MHz. The resulting data sets are too large to store on a personal computer and so all stored waveforms are downsampled to 5 MHz. Results of the study are summarized in Figure 5.13. The first and second rows of the figure present results from experiments without and with a target in place, respectively. The intensity of pixels in these plots is proportional to the square root of the energy within the time reversal window. Intensity values are normalized to the maximum value observed for target returns. This has the effect of clipping the energy associated with returns from the surface of the sediment. The bottom row presents the signal-to-noise ratio (SNR) calculated from equation (5.5) where data from the first two rows of Figure 5.13 is employed. A vertical dashed line in all the figure panels highlights a relative window time of $t_r = 0\mu\text{s}$. The first two columns of the figure present results over the entire bandwidth of the system for iteration 0 and iteration 50, respectively. The third and fourth columns only present energy contained within 750-950 kHz and 400-600 kHz frequency bands, respectively. These bands are selected because they are found to contain energy attributed to target resonances (see, for example, Figure 5.9). In subsequent sections, this type of figure will be referred to as a “SNR plot.”

In the first row of Figure 5.13, generated from experiments where there is no target in place, the energy is symmetrically distributed about $t_r = 0\mu\text{s}$. This energy is

attributed to reflections from the surface of the sediment. The distribution in time of these returns agrees with observations made in Section 5.5 (see Figure 5.9), i.e. as the window size increases, so too does the range of relative window times at which the returns are observed.

In the second row of the figure, generated from experiments with a target in place, a significant amount of energy appears at relative window times following those at which surface returns are observed. This energy is attributed to returns from the buried target. Using the data in the first two rows, signal-to-noise computations are then carried out. These results are presented in the bottom row of Figure 5.13. In this parameter study, the dominant target resonance is found to lie within the 750-950 kHz band most frequently, as evident in Figure 5.13k. At later relative window times, the resonance attributed to the 400-600 kHz band is observed. This agrees with observations made from Figure 5.9; lower frequency resonances are observed at later relative window times due to radiation damping and the frequency dependent attenuation of the sediment. A maximum SNR of 35 dB is observed in the 750-950 kHz band-limited data when a $22\mu\text{s}$ long window is used. Therefore, a window of approximately this size will be the most effective at identifying this target resonance at normal incidence. It is for this reason that a $20\mu\text{s}$ long time reversal window is most typically employed in this work. The results presented in this section provide a baseline to which results obtained at non-normal incidence can be compared.

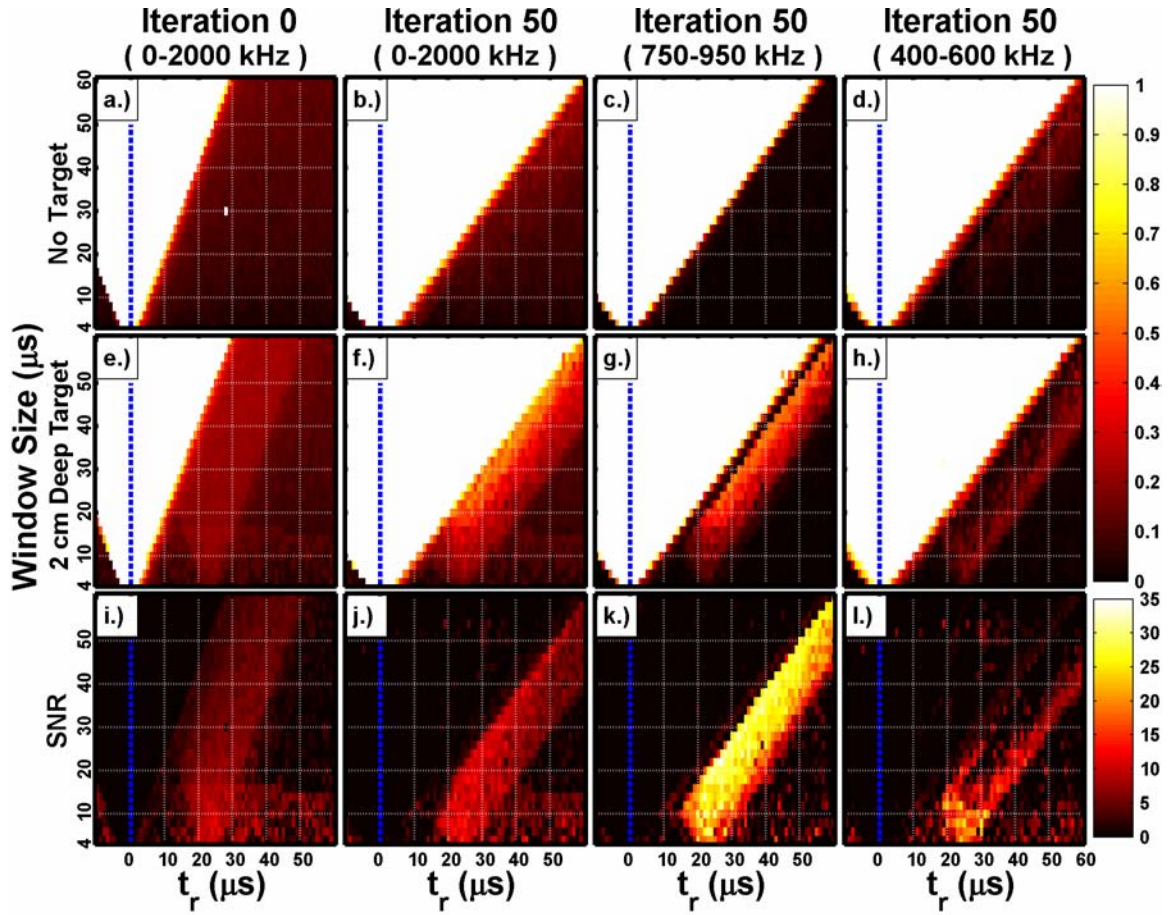


Figure 5.13: SNR plot summarizing the results of a window parameter study conducted with the transducer at normal incidence. In the first two rows, the intensity of pixels is proportional to the square root of the energy within the time reversal window over the specified frequency band specified at the top of each column. The bottom row the pixel intensity is proportional to the signal-to-noise ratio observed. The vertical axis in each figure panel corresponds to the window size. The horizontal axes correspond to the relative window time.

5.6.3 10-Degree Incidence Angle

The transducer is rotated to an incident angle of 10 degrees and the window parameter study described in the previous section is repeated. Figure 5.14 presents window-shifting plots for selected window sizes. The results are qualitatively similar to those observed at normal incidence (see Figure 5.9) but the convergence frequencies are located at the lower end of the system bandwidth. In Figure 5.14e, where a small $8\mu s$ window is used, the same three resonances that appear at normal incidence in Figure 5.9e are visible. However, for the larger window sizes employed to generate Figures 5.14f-5.14h, only the resonance centered at 480 kHz is readily identified. It is important to note from this figure that the convergence frequency observed for returns from the surface of the sediment is distinct and lower in frequency than that observed for returns from the target. This confirms that a wave resonance of the target is indeed being excited.

The SNR plot of Figure 5.15 exhibits a similar trend. The first two columns of the figure, generated using the full system bandwidth, are similar to those in Figure 5.13, the SNR plot for normal incidence. Energy attributed to target returns is readily visible following returns from the sediment surface. However, the third column of the figure indicates that there is very little energy in the 750-950 kHz band for all window sizes employed. The time reversal procedure most frequently converges to the resonance located in the low frequency 400-600 kHz band, as observed in the fourth column of the figure. Indeed, it is clear that a bias has been induced in the system response. Figure 5.15k helps to confirm that the source of the bias is likely attributed to returns from the surface of the sediment. From this figure, it is clear that the time reversal technique

detects energy attributed to the higher frequency target resonance when windows smaller than approximately $15\mu\text{s}$ are employed. However, this resonance appears to diminish as the window size is increased and is only observed at later relative window times. When small time windows are employed, target returns are isolated in time from the surface return and the biasing effect described in Section 5.6.1 does not take hold. As the window size is increased, the surface return expands in time and low frequency energy enters the time reversal window. This shifts convergence of the time reversal procedure towards a lower frequency target resonance located in the 400-600 kHz band.

Further evidence that the surface return partially imposes a low frequency bias is provided in Figure 5.16, which shows the convergence plot for a $20\mu\text{s}$ long window positioned at a relative window time of $t_r = 25\mu\text{s}$. Low frequency components are found to slowly enter the time window. This is apparent when one examines the time domain waveforms in Figure 5.16a-5.16c. In Figures 5.16a and 5.16b, although the sediment surface return (centered at approximately $132\mu\text{s}$ in each figure panel) is clearly of low frequency, it is easily distinguished from returns appearing within the time reversal window, which consist of a combination of higher frequencies. However, as successive iterations are carried out the low frequency surface return expands in time. Eventually, as in Figure 5.16c, the surface return enters the time reversal window and is not clearly separated in time from target returns. Convergence to a low frequency target resonance is then observed. This helps to confirm that the surface return can indeed enter the time reversal window and effectively induce a bias in the system response towards lower frequency. Examination of time domain returns from other experiments at 10 degree

incidence indicates that the surface return does indeed overlap target returns when convergence to a low frequency target resonance is observed.

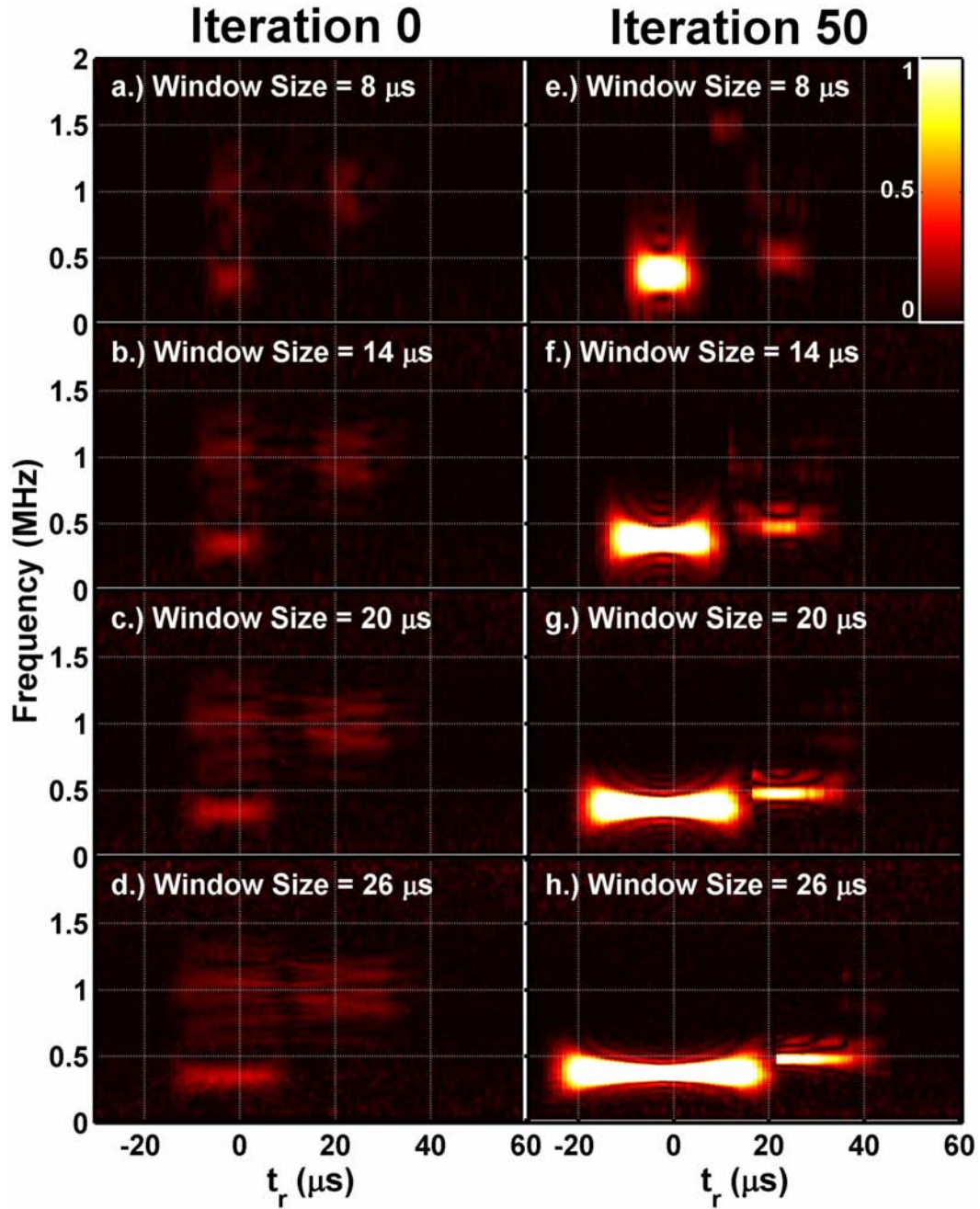


Figure 5.14: Experimental results where the center of the time reversal window is shifted in steps of $1\mu\text{s}$ from relative window times, t_r , of $-30\mu\text{s}$ to $60\mu\text{s}$ over the standard shell target buried at 2 cm depth. The pixel intensity represents the magnitude spectrum of the signal within the time reversal window. (a)-(d) present results at iteration 0 for window sizes of 8, 14, 20, and $26\mu\text{s}$. (e)-(h) present the same results but for iteration 50. Data is normalized to the maximum value for $t_r > 25\mu\text{s}$ within each row. The transducer is aligned at 10 degree incidence to the surface of the sediment and incident waves approach the target from the left side of the Figure.

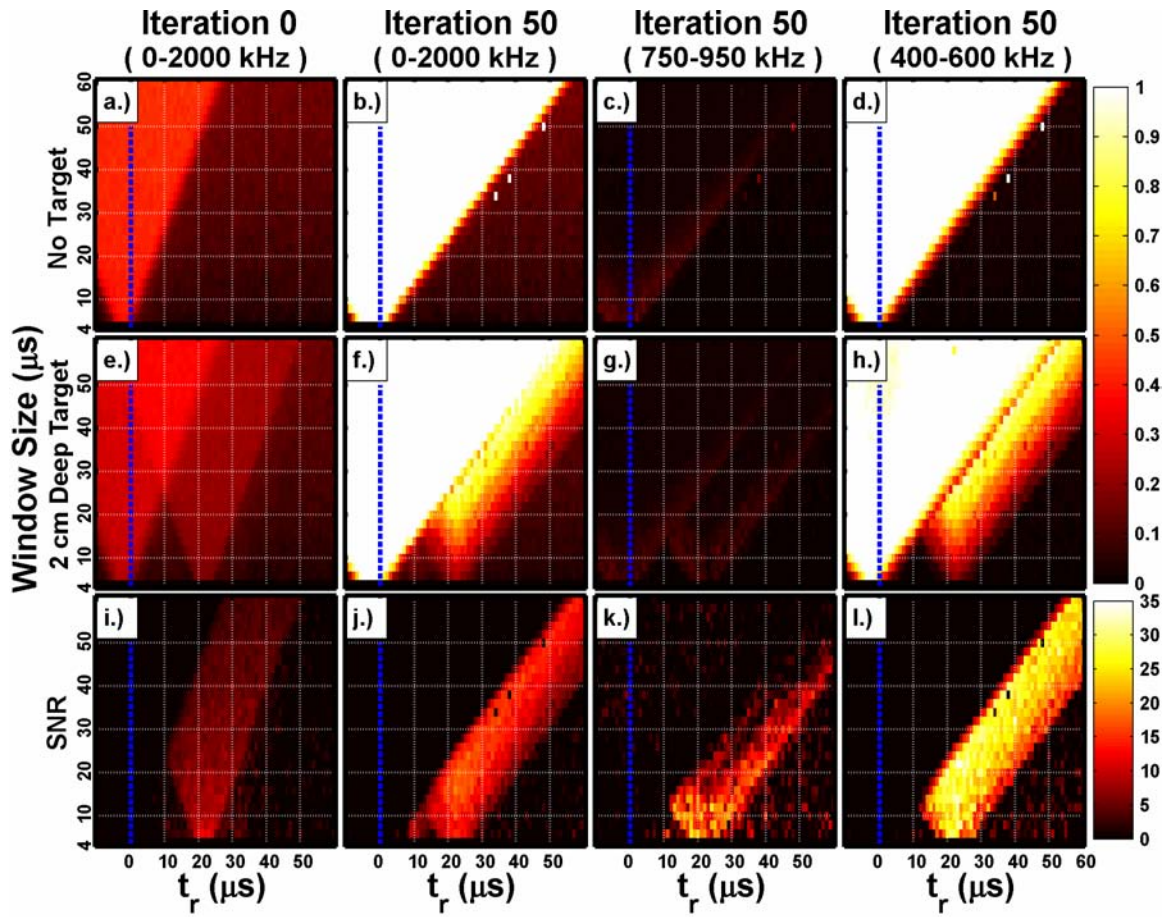


Figure 5.15: Results of a window parameter study conducted with the transducer at 10 degrees incidence. In the first two rows, the intensity of pixels is proportional to the square root of the energy within the time reversal window over the specified frequency band specified at the top of each column. The bottom row the pixel intensity is proportional to the signal-to-noise ratio observed. The vertical axis in each figure panel corresponds to the window size. The horizontal axes correspond to the relative window time.

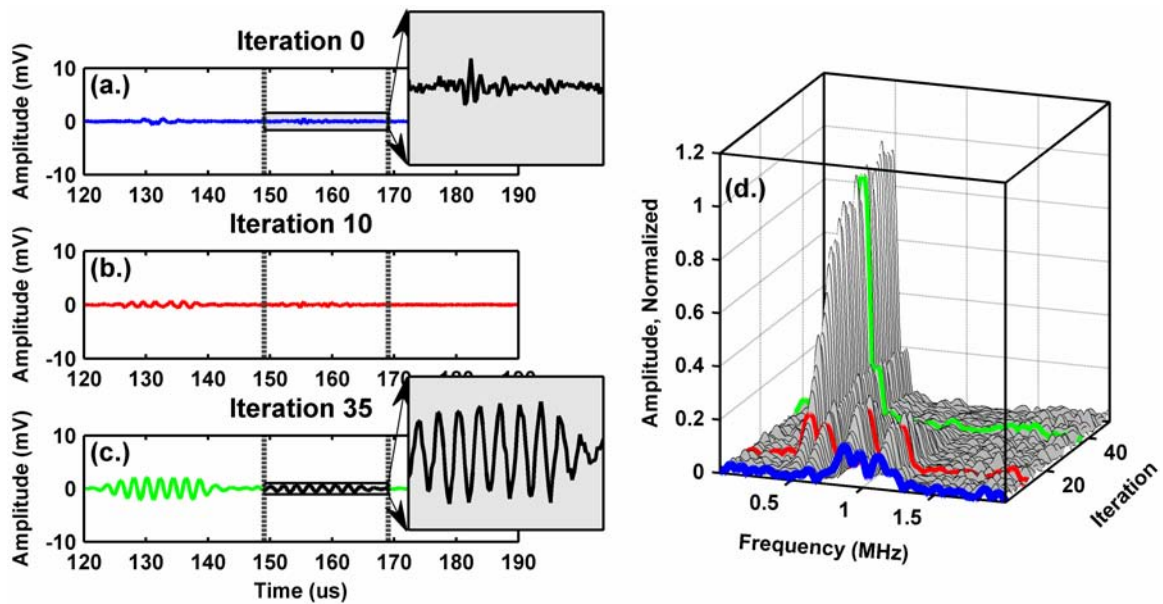


Figure 5.16: Convergence plot for the standard shell target buried 2 cm beneath the surface of the sediment through successive iterations of the time reversal procedure. The transducer is at 10 degree incidence to the surface of the sediment. Vertical lines in (a)-(c) depict the position of a $20\mu s$ long time reversal window. (a.) The first backscattered return, iteration 0, where white noise $20\mu s$ in duration is used for interrogation. (b.) Backscattered return at iteration 10 of the time reversal procedure. (c.) Backscattered return at iteration 35 of the time reversal procedure. (d.) Waterfall plot of magnitude spectra of signals within the time reversal window for iterations 0 through 50 normalized to the maximum spectral magnitude at the final iteration. The spectra from (a)-(c) are highlighted with solid black lines.

5.6.4 20-Degree Incidence Angle

A final window parameter study is conducted at an incident angle of 20 degrees. Window shifting plots are presented in Figure 5.17. The results are almost identical to those for 10 degree incidence (see Figure 5.14) but an 850 kHz convergence frequency is observed for target returns. This is the same target response frequency observed in normal incidence experiments. At 20 degree incidence, the influence of the surface return is less marked. This is confirmed in the convergence plot of Figure 5.18 where one notes, from time domain waveforms, that the amplitude of the sediment surface return is negligible compared to the amplitude of target returns. Therefore, the sediment surface return exerts less influence at this incident angle. One also notes that, for example in Figure 5.17h, returns from the target are much broader in time than the normal incident result in Figure 5.9h. The SNR plots in Figure 5.19 confirm these trends for all window sizes investigated. At 20 degree incidence, the time reversal procedure selects the expected target convergence frequency and does so for a wider range of relative window times than in the normal incidence study. Therefore, operating at such an angle would likely increase the probability of target detection and identification.

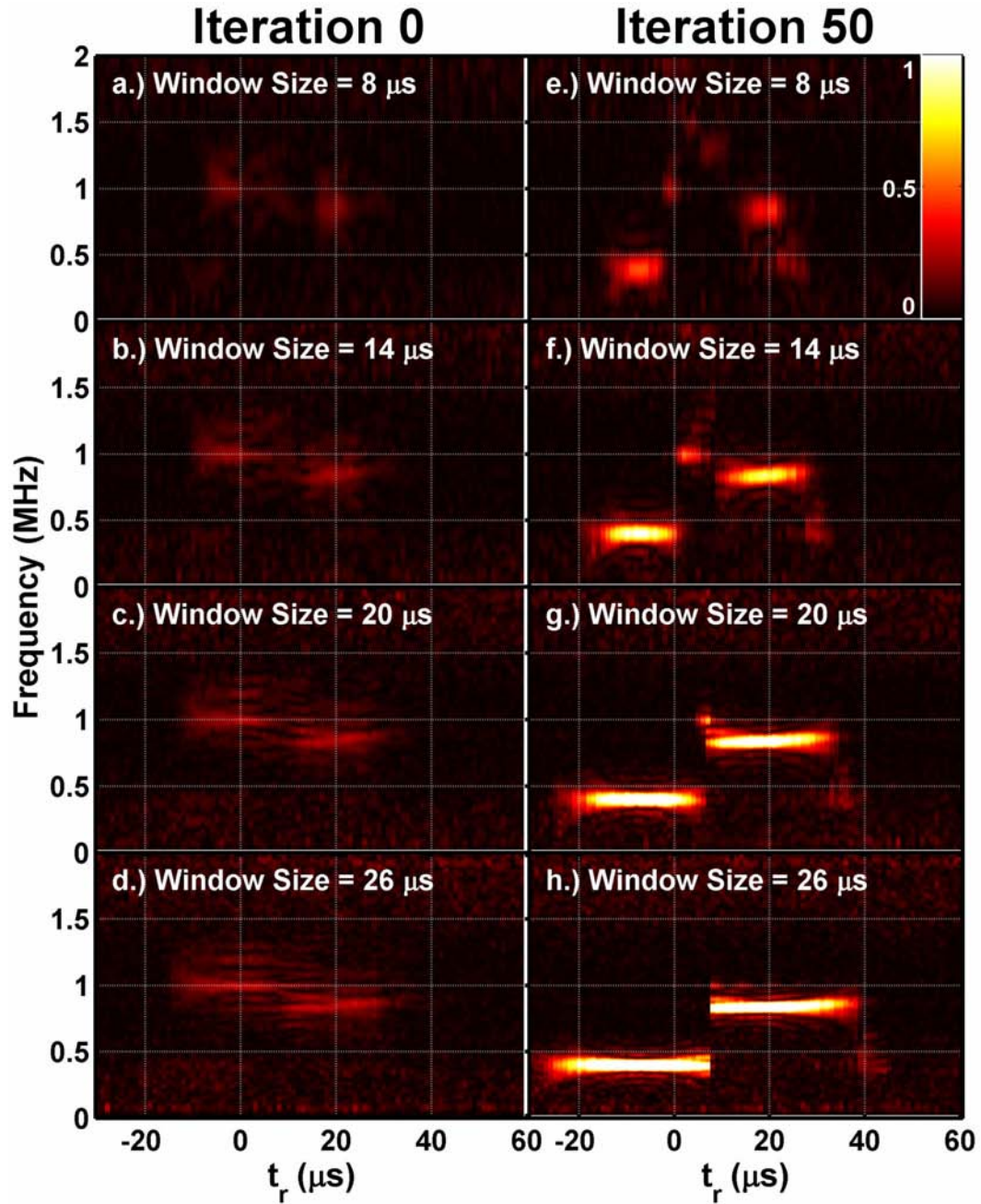


Figure 5.17: Experimental results where the center of the time reversal window is shifted in steps of $1\mu\text{s}$ from relative window times, t_r , of $-30\mu\text{s}$ to $60\mu\text{s}$ over the standard shell target buried at 2 cm depth. The pixel intensity represents the magnitude spectrum of the signal within the time reversal window. (a)-(d) present results at iteration 0 for window sizes of 8, 14, 20, and $26\mu\text{s}$. (e)-(h) present the same results but for iteration 50. Data is normalized to the maximum value for $t_r > 25\mu\text{s}$ within each row. The transducer is aligned at 20 degree incidence to the surface of the sediment and incident waves approach the target from the left side of the Figure.

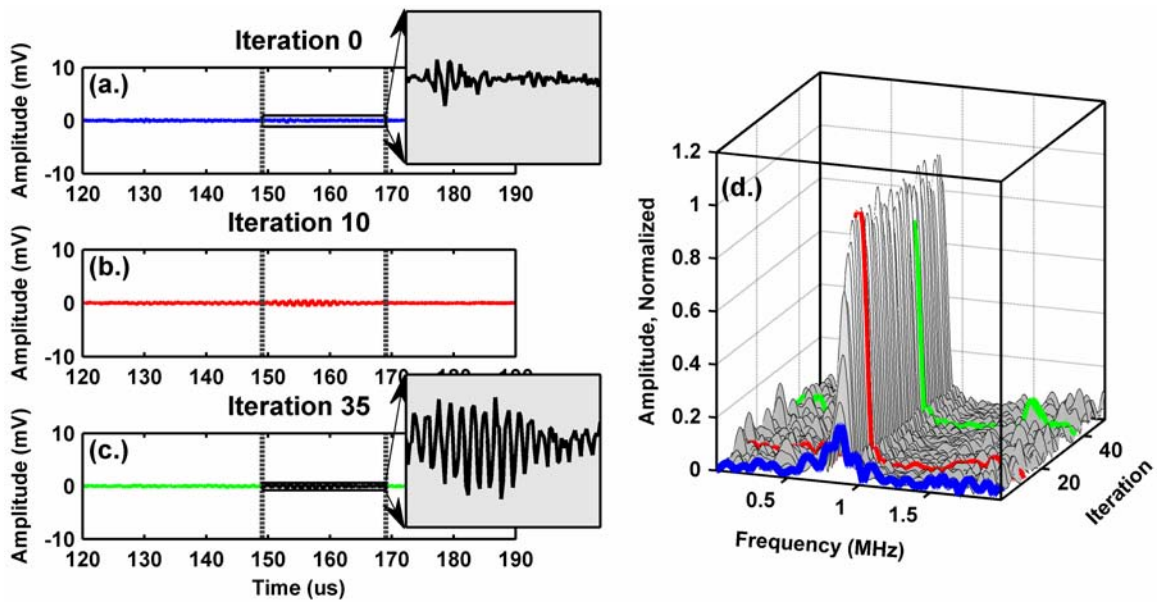


Figure 5.18: Convergence plot for the standard shell target buried 2 cm beneath the surface of the sediment through successive iterations of the time reversal procedure. The transducer is at 20 degree incidence to the surface of the sediment. Vertical lines in (a)-(c) depict the position of a $20\mu s$ long time reversal window. (a.) The first backscattered return, iteration 0, where white noise $20\mu s$ in duration is used for interrogation. (b.) Backscattered return at iteration 10 of the time reversal procedure. (c.) Backscattered return at iteration 35 of the time reversal procedure. (d.) Waterfall plot of magnitude spectra of signals within the time reversal window for iterations 0 through 50 normalized to the maximum spectral magnitude at the final iteration. The spectra from (a)-(c) are highlighted with solid black lines.

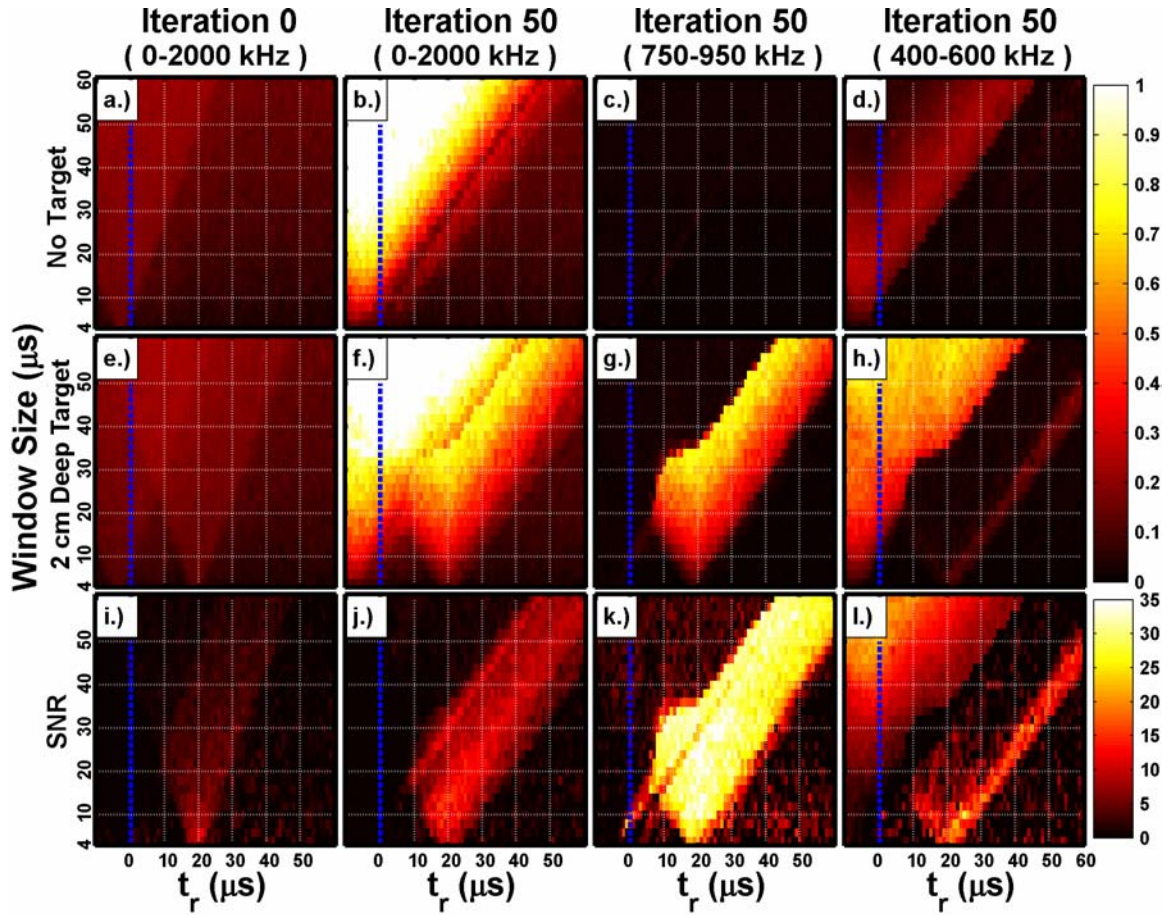


Figure 5.19: Results of a window parameter study conducted with the transducer at 20 degrees incidence. In the first two rows, the intensity of pixels is proportional to the square root of the energy within the time reversal window over the specified frequency band specified at the top of each column. The bottom row the pixel intensity is proportional to the signal-to-noise ratio observed. The vertical axis in each figure panel corresponds to the window size. The horizontal axes correspond to the relative window time.

5.6.5 Summary of Parameter Investigation

In this section, a brief recapitulation of the conclusions drawn from parameter studies is provided. Figure 5.20 presents the SNR observed for each set of window parameters given incident angles of 0, 10, and 20 degrees. The intensity of pixels in each plot is equal to the SNR of target returns, calculated from equation (5.5). Thus, the light shaded regions in this figure indicate the range of parameters for which returns from the target are identified. Results indicate that at 10 degree incidence, reflections from the surface of the sediment introduce a bias towards low frequencies in the system response when window sizes larger than approximately $15\mu s$ are employed. This results in convergence of the time reversal procedure to a lower frequency resonance in the response of the target than expected. Results from experiments conducted at 20 degree incidence indicate that there is no bias induced in the system response at this angle; the dominant resonance observed is the same as when operating at normal incidence. Also, comparing Figure 5.20k to Figure 5.20c, it is clear that target resonances are confidently identified for a wider range of relative window times when operating at 20 degree incidence and the SNR values observed at this angle are typically higher. The diminished amplitude of returns from the sediment surface and unbiased convergence indicate that operating under such a system configuration should increase the probability of positive target detection and identification.

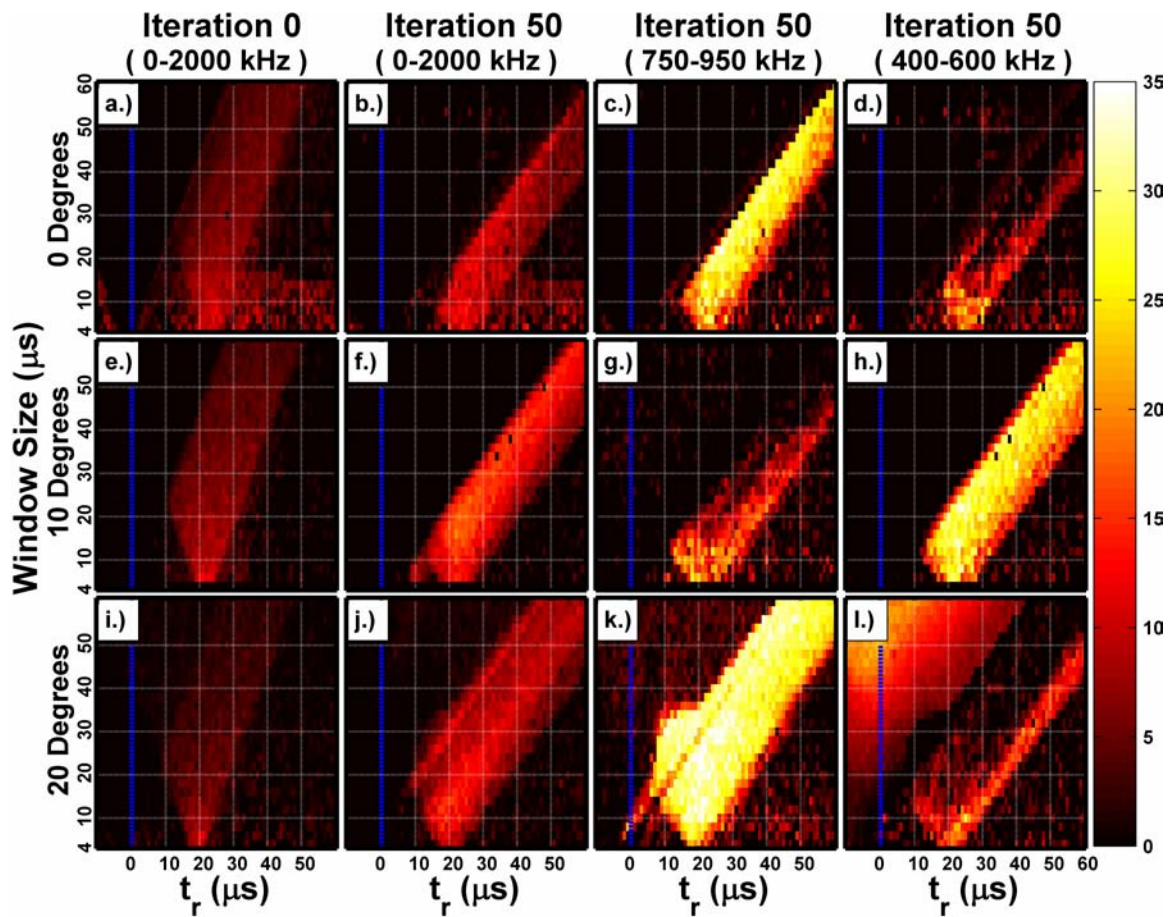


Figure 5.20: Results of a window parameter studies for all angles of incidence investigated. The pixel intensity in all figures is proportional to the signal-to-noise ratio observed.

5.7 Target Selectivity

The transducer is now mechanically scanned and the single-channel time reversal technique is utilized to create 2-D images in order to test the technique's ability to distinguish between buried targets possessing different physical characteristics. The transducer is mechanically raster scanned in steps of 1 mm over a 45 mm by 45 mm area of sediment containing the aluminum shell target buried at 2 cm depth. The scan plane is horizontal and parallel to the sediment surface; this axis of the transducer is normal to this plane. A solid stainless steel sphere, with the same outer diameter, is also buried at 2 cm depth, at a lateral distance of approximately 2 cm from the center of the shell target. A $20\ \mu\text{s}$ long time reversal window is shifted in $2\ \mu\text{s}$ steps between relative window times of $23\ \mu\text{s}$ to $29\ \mu\text{s}$. For each relative window time and transducer location, a 50 iteration time reversal sequence is obtained. Images are generated at each relative window time where pixels in the image represent the position of the transducer. The pixels are assigned intensity values based on the energy within the time reversal window summed over a band-limited frequency range.

Figure 5.21 depicts images generated from this experiment. In these images, the aluminum shell target is nominally centered at a (x,y) location of (15,30) mm. The solid stainless steel target is located at a (x,y) position of (30,15) mm. The images in the left column, Figures 8a to 8d, are generated from the energy within the time reversal window at iteration 0 over the full system bandwidth, where a 2 cycle 1 MHz sine wave is used for the initial interrogation. The images are presented on the same linear scale as those in the second column, Figure 5.21e to 5.21h, which are generated using the backscattered

return after 50 iterations of time reversal. At iteration 50, the backscattered energy is significantly greater than that at iteration 0, resulting in the blank appearance of Figures 5.21a-5.21d. This is due in part to the increased spectral response of the sediment and target through iteration of the time reversal procedure and also greater energy transmitted at iteration 50 than at iteration 0. The images are normalized to the peak intensity value in Figure 8n in order to highlight the improvement obtained through application of the time reversal procedure. The signal to noise ratio at iteration 0 is, however, high enough for the target to be visible when images 5.21a to 5.21d are normalized to a smaller scale.

In Figure 5.21e, returns from the target are not distinguishable from reflections off the surface of the sediment layer. However, when the center of the window is shifted to relative window times greater than or equal to $25\ \mu\text{s}$, the locations of both targets are revealed, as seen in Figures 5.21f and 5.21g. The decrease in target strength as the window progresses deeper into the sediment from $25\ \mu\text{s}$ to $29\ \mu\text{s}$ is attributed to the time reversal window shifting past returns from the target. Figures 5.21i-5.21l depict images generated from the same experiment, where now the processing bandwidth is narrowed to encompass only the 500 to 600 kHz frequency range. The results are similar to those in 5.21e-5.21h, but now only the solid stainless steel sphere is visible as in Figures 5.21j and 5.21k. Alternately, limiting the bandwidth of investigation to the 750-1200 kHz band results in isolation of the aluminum shell target, as evident in Figures 5.21m to 5.21p. Figures 5.21i and 5.21m show that, for this experiment, target returns are isolated from sediment surface returns through sub-band analysis. These results demonstrate that the time reversal technique automatically selects the proper interrogation frequency for an

arbitrary target and can be used to distinguish between targets possessing different resonant responses.

In addition, by further band-limiting the analysis, the technique is seen to isolate different resonances within the response of a single target. This is demonstrated in Figure 5.22, where images are presented from a different measurement with the same aluminum shell target employed in Figure 5.21, buried alone at 2 cm depth. Limiting the bandwidth to a frequency range of 750-950 kHz results in Figure 5.22a, in which an image corresponding to a portion of the target is visible. Expanding the bandwidth to 750-1200 kHz, reveals another portion of the target, (see Figure 5.22b). Figure 5.23 examines convergence to these resonances as a function of transducer position by presenting data obtained along slices taken from the horizontal axes of the image in Figure 5.22b at a transducer position of 22 mm. Figures 5.23a and 5.23b present spectra from iterations 0 and 50, respectively, where each image is scaled to its own maximum intensity value. In Figure 5.23b, between transducer positions of 0 to 17 mm and 27 to 40 mm, broadband energy centered at 425 kHz is observed. Convergence to this frequency was found to be characteristic of backscattered returns from the sediment and also occurred in experiments without the target in place.

In Figure 5.23a, at iteration 0, multiple wave mode resonances in the backscattering response of the target are visible between transducer positions of approximately 15 to 30 mm. Through resonance scattering theory, these are found to correspond to a_{0-} antisymmetric Lamb waves. The spatial distribution of frequencies (i.e. as a function of y-position) is due to the frequency dependent beam pattern of the

transducer [78], in which lower frequencies spread more than higher frequencies. In Figure 5.23b the spectral response of the target is apparent between transducer positions of 17 to 27 mm. Two discrete energy bands are present, one centered at 1100 kHz and the other at 825 kHz. As the transducer moves to positions away from the target (towards the edges of this figure), the time reversal procedure converges to the lower frequency band. This occurs because the system calibration filter does not take into account the off-axis spectral response of the transducer, which is biased towards lower frequencies. Thus, without using any additional signal processing techniques, two separate resonances of the target are revealed.

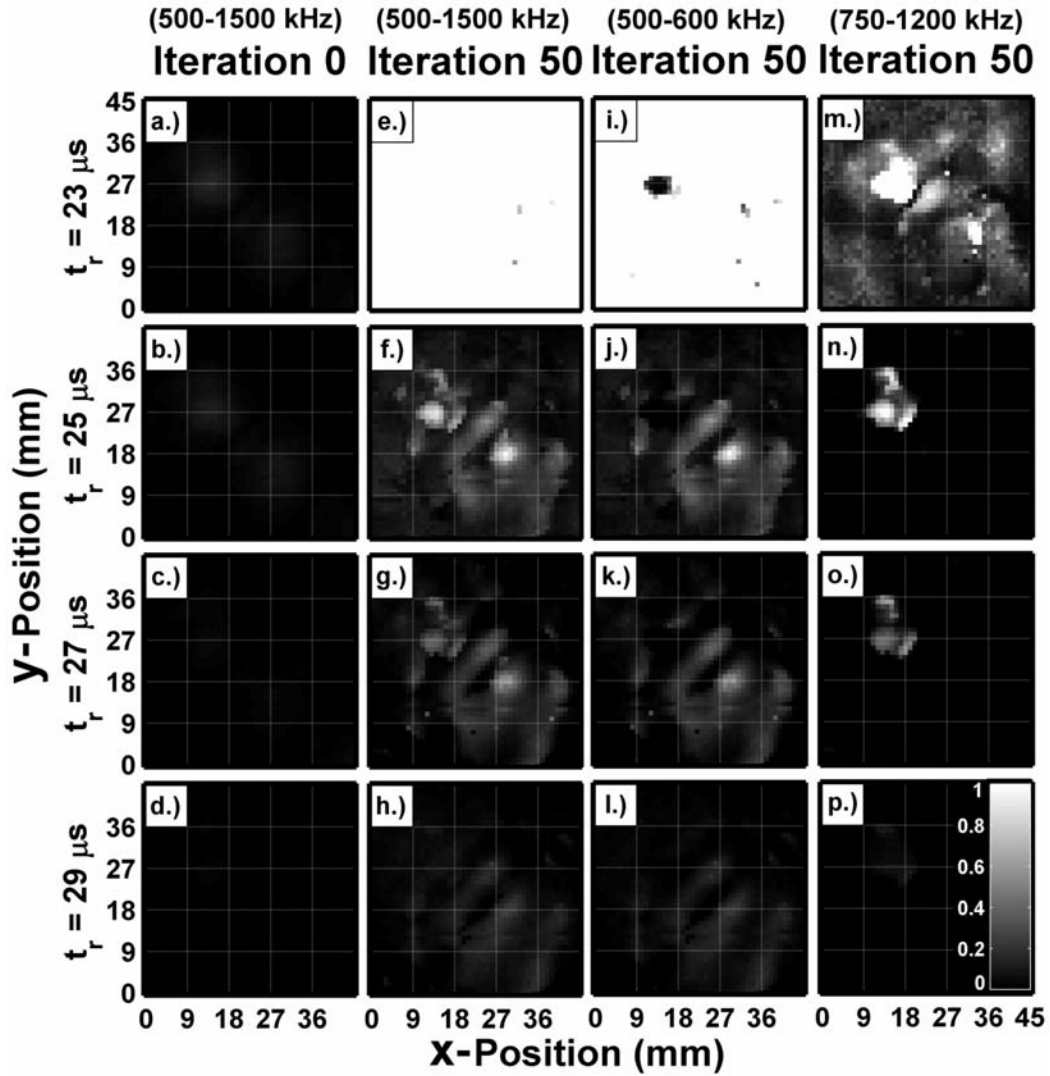


Figure 5.21: Wave mode images generated from raster scanning the transducer at normal incidence over an area of sediment containing an aluminum spherical shell (located at $[x, y] = [15, 30]$ mm) as well as a solid stainless steel sphere of the same diameter (located at $[x, y] = [30, 15]$ mm). Pixels in the images represent the energy within the time reversal window, at a specified transducer position, over a band-limited frequency range. Panels (a)-(d) are generated from the backscattered returns at iteration 0 over the full system bandwidth, shifting the time reversal window in $2 \mu\text{s}$ steps from $23 \mu\text{s}$ to $29 \mu\text{s}$ relative to the specular return from the sediment surface. Panels (e)-(h) are generated from backscattered returns after 50 iterations of the time reversal procedure, at the same relative window times as in Panels (a)-(d). Panels (i)-(l) and (m)-(p) are the same as in (e)-(h), but are defined over a band limited frequency range of 500-600 kHz and 750-1200 kHz, respectively. The energies displayed in all images are normalized to the maximum value in (n) and are presented on the same linear scale where white represents values greater than or equal to the maximum and black represents zero.

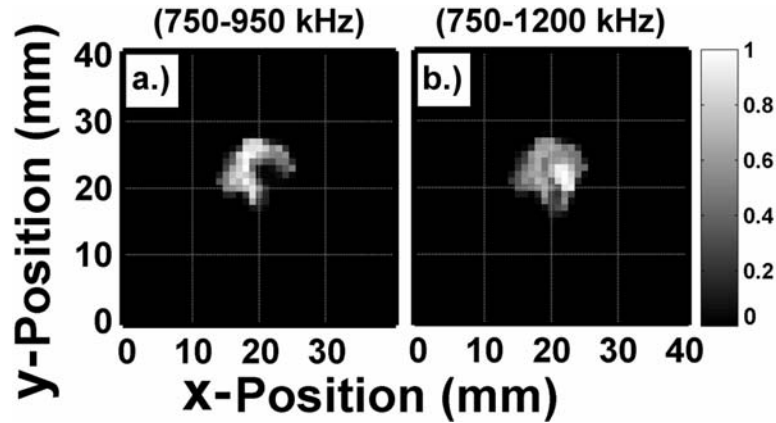


Figure 5.22: Wave mode images at iteration 50, generated from the same conditions as in Figure 5.21n, but with only the aluminum spherical shell target in place. The energy in (a) is band-limited to a frequency range of 750-950 kHz and (b) encompasses the 750-1200 kHz frequency range.

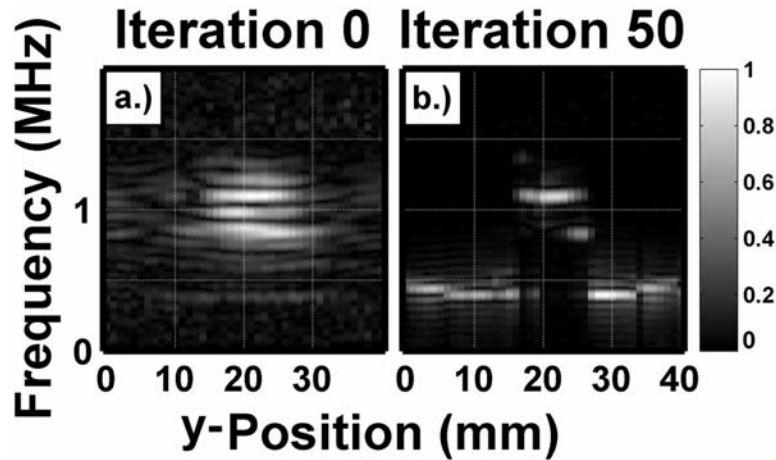


Figure 5.23: Magnitude spectra from data obtained along slices taken from the x-axis of Figure 5.22b at a transducer position of 22 mm for iteration 0 (Figure 5.23a) and iteration 50 (Figure 5.23b). The intensities in each image are normalized to their respective maximum values. In the images, white represents the maximum value and black represents the minimum value.

Chapter 6

Pond Experiments

In order to test the effectiveness of the single-channel time reversal technique in a more realistic setting, 5 field experiments are carried out in test facilities at the Naval Surface Warfare Center (NSWC) – Panama City Division. In this work, the insight gained in the laboratory is applied to detect and identify targets buried in medium grained sand. Table 6.1 summarizes the dates and objectives of each field experiment. The experiments were designed and conducted in collaboration with Dr. Benjamin Dzikowicz, a physicist at NSWC. In this Chapter, selected results from the field work carried out in January 2008 are presented; Dr. Dzikowicz generated the results shown in Figures 6.6-6.11. They are discussed here in order to demonstrate that the methodology applied in the laboratory is applicable at lower frequency operating conditions.

Table 6.1: Summary of field experiments conducted at the Naval Surface Warfare Center – Panama City Division. The date and a summary of each experiment are provided.

Experiment #	Date	Summary/Objectives
1	02/2007	System testing, Free field experiments
2	05/2007	System redesigned, Free field experiments
3	08/2007	Buried target experiment – Trial 1
4	11/2007	Buried target experiment – Trial 2
5	01/2008	Buried target experiment – Trial 3

6.1 Experimental Setup and Methodology

Field experiments are conducted in a fresh water test pond facility at NSWC, described in Ref. [117]. The test pond is 10.2 m deep and has a 1.5 m thick layer of medium grained sand at its bottom. The experimental apparatus employed is similar in nature to the system employed in the scaled laboratory work. Figure 6.1 presents a schematic of the electronic instrumentation and also a depiction of the configuration used in buried target studies. In this setup, a separate projector and receiver are employed. They are mounted to a wooden sawhorse shaped stand depicted in Figure 6.2a. The projector is affixed to the cross-beam of the sawhorse while a 0.635 mm diameter braided line holds the hydrophone in place half way between the projector and the sediment surface at a distance of 0.78 m from the face of the projector. The hydrophone is positioned on the central axis of the projector in the far field of the projector's beam.

The target employed is a 0.1524-m outer diameter air filled stainless steel spherical shell with a 0.95-mm wall thickness. When the target is submerged in water (or sediment) it is positively buoyant. Therefore, it was necessary to fix two solid steel weights to eyehooks located at opposite poles of the shell. One eyehook is welded to the shell while the other is threaded in place. The weights are oriented with respect to the projector as shown in Figure 6.1. A picture of the target with the weights attached is provided in Figure 6.2b. Divers manually bury the target in the sediment by hand and use a marked rod to gauge the burial depth. A plumb bob temporarily hung from the projector is used to align the target.

A computer controls the generation and acquisition of all waveforms via two digitizing boards. Waveforms generated by the computer are sent through a power amplifier and transmitted to an F-30 projector obtained from the Underwater Sound Reference Division at the Naval Undersea Warfare Center – Newport. The projector possesses a frequency bandwidth of approximately 30 kHz to 200 kHz. The active portion of the transducer is a 38.1 mm x 50.8 mm rectangle of lithium sulfate plates. An International Transducer Corporation model 1089 hydrophone with a 0.5 inch diameter spherical active element is used. Its response is omnidirectional. Waveforms received at the hydrophone are amplified 20 dB and band-pass filtered between 20-200 kHz before they are digitized. The hydrophone is nominally flat over the entire operational bandwidth of the projector and possesses a sensitivity of -215 dB re 1 μ V/Pa.

In order to normalize the combined frequency responses of the projector, receiver, and electronic instrumentation, the calibration procedure described in Section 3.2 is applied. The reader should refer to that section for details of how the calibration is carried out. In the field experiments, the waveform received along the direct path from the projector to the hydrophone is used whereas in the scaled work, free water surface reflections are employed. Results of the calibration are presented in Figure 6.3. Figures 6.3a and 6.3b show a linear frequency modulated chirp in both the time domain return and frequency domain, respectively. The chirp spans the full frequency bandwidth of the experimental system. It is sent to the projector which then transmits a signal in the direction of the hydrophone. The second row of Figure 6.3, presents the waveform received at the hydrophone along the direct path from the projector. This waveform is

characteristic of the frequency response of the system. Its shape is very complicated and the frequency domain response appears to possess three distinct modes.

A calibration filter is then generated from the transmitted voltage and the direct path received waveform by employing a Wiener filter. Yule-Walker estimation is not applied in the field work, due to the complicated nature of the system response. When the calibration filter is applied to the received signal, it results in the calibrated return shown in the third row of Figure 6.3. The spectrum of the resulting calibrated return is flat over the frequency bandwidth of interest. This result indicates that the calibration filter should effectively normalize resonances present in the response of the system. After the calibration filter is applied to received waveforms, these resonances should no longer interfere with convergence of time reversal to a resonance in the scattering response of the target. System calibration is performed at the beginning of each day field experiments are conducted.

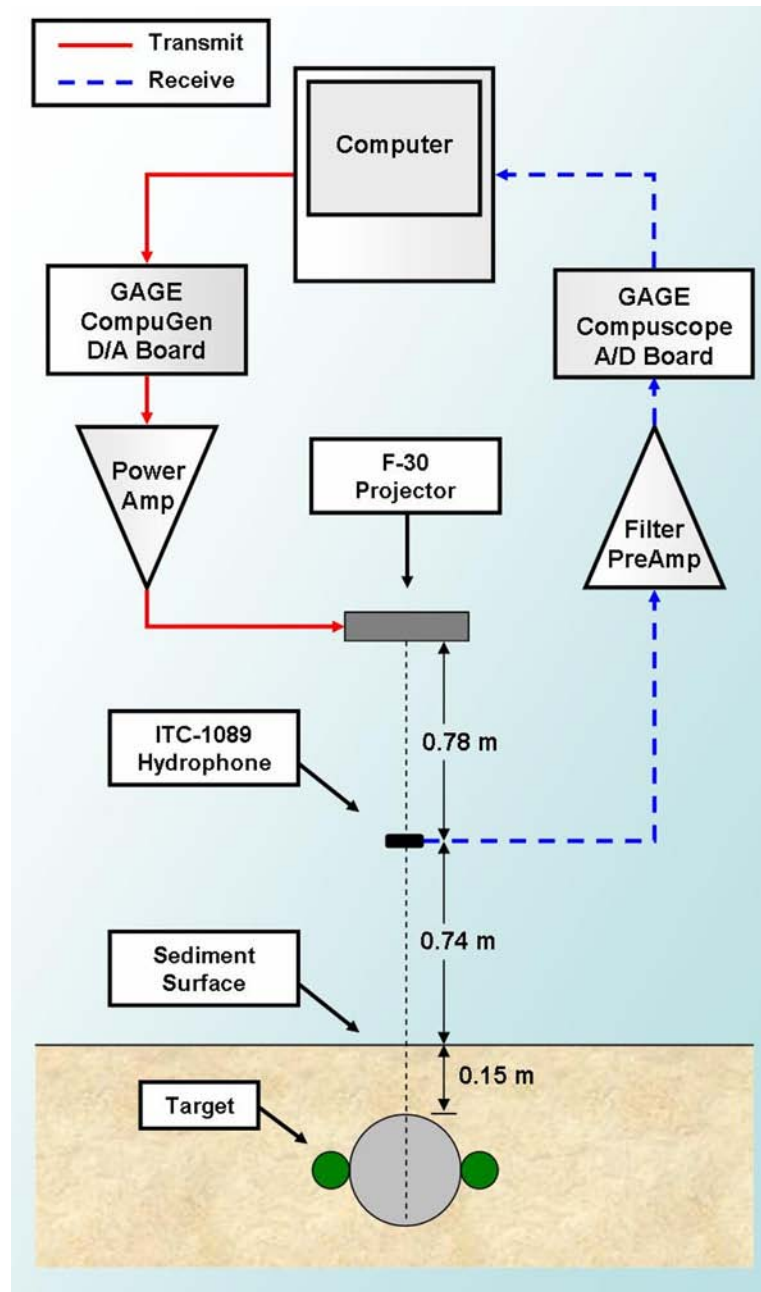


Figure 6.1: Schematic of the electronic instrumentation and configuration used in field experiments. The target is positioned on the axis of the projector and hydrophone with the weights on either side of the target as shown. Separate transmit and receive paths are shown with solid and dashed lines, respectively.

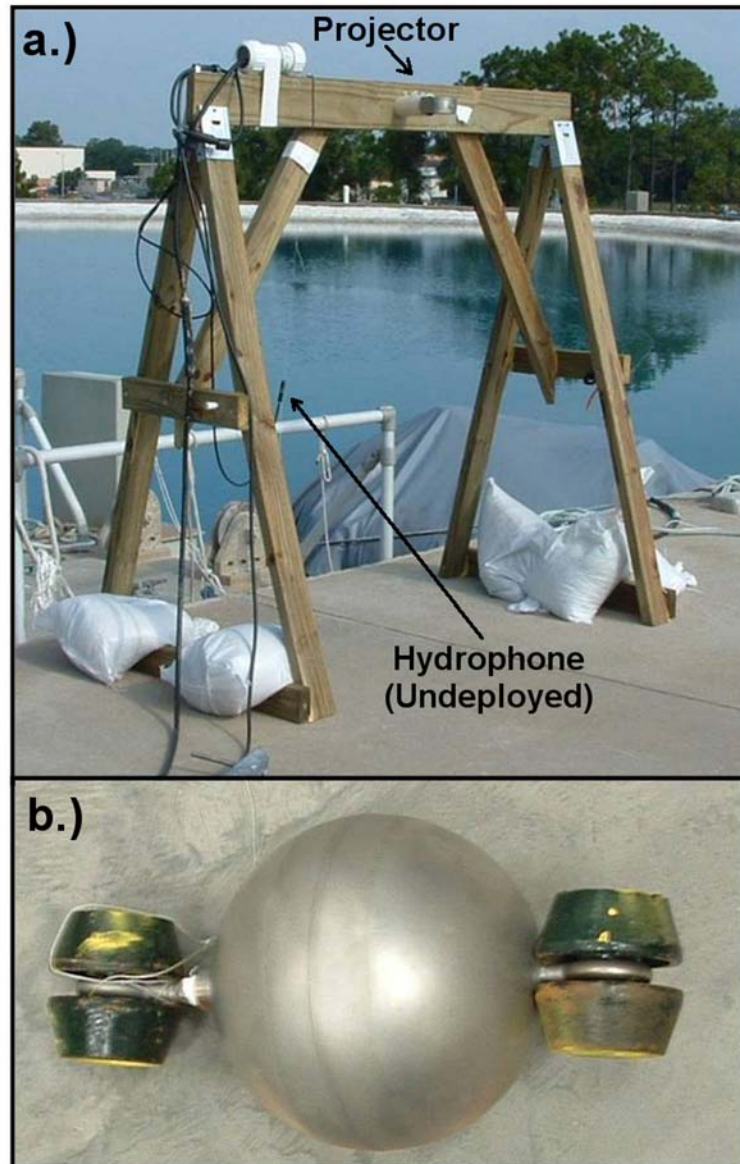


Figure 6.2: Picture of the experimental apparatus employed in field experiments. (a.) Sawhorse shaped stand on which the projector and hydrophone are mounted. The test pond is visible in the background. (b.) Stainless steel spherical shell target used in experiments. Weights are clamped to eyehooks located at the poles of the sphere.

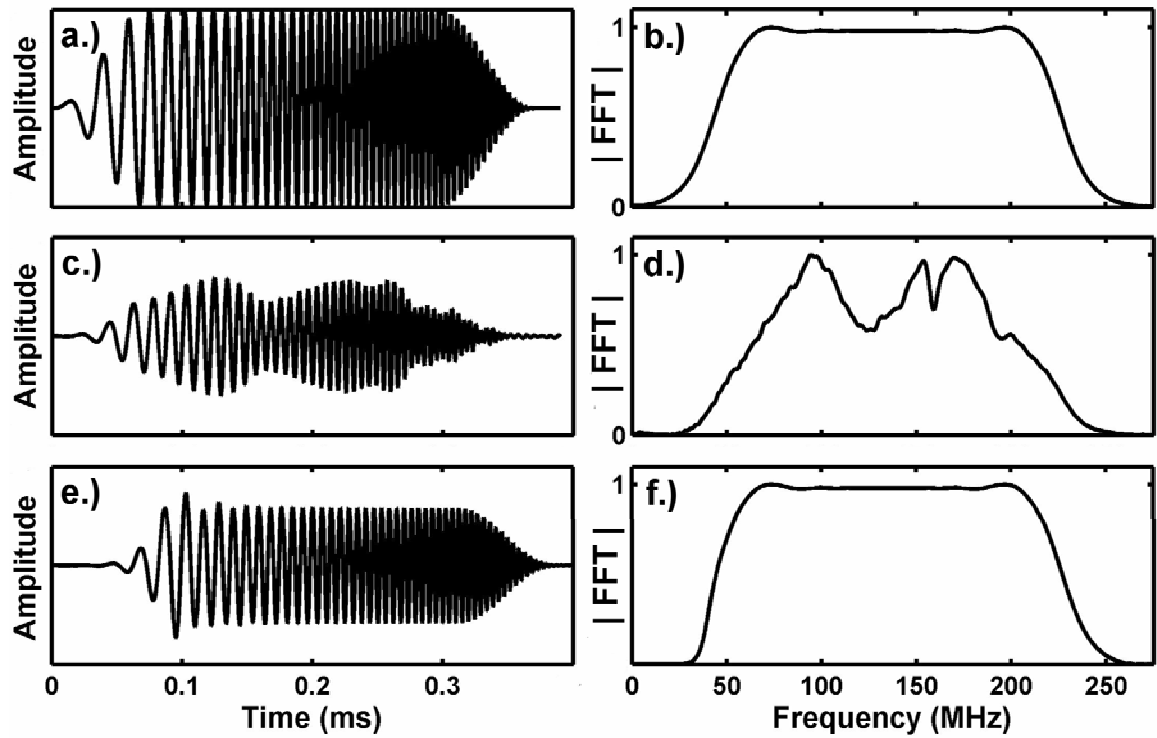


Figure 6.3: Waveforms and associated spectra from tests of the calibration procedure for the system employed in field experiments. (a.) Linear chirp driving voltage sent to the projector in which the transmitted pulse is directed normally at the sediment surface and is received at mid-path by the hydrophone. (b.) Magnitude spectrum of (a). (c.) Voltage of the received waveform (d.) Magnitude spectrum of (c). (e.) Waveform in (c) after application of the calibration filter. (f.) Magnitude spectrum of (e). The amplitude/magnitude in all subplots is in arbitrary units.

6.2 Target Response

The farfield form functions for an air-filled spherical shell loaded with water and water saturated medium grained sand (referred to here as sediment) are presented in Figure 6.4. The dimensions and composition of the shell are the same as those of the target. It is reasonable to assume that the eye-hooks attached at the target's poles do not interfere significantly with propagating surface elastic waves. Thus, treating the target as a spherical shell should provide a model for these effects. The predicted responses are given over 20-200 kHz, the approximate frequency bandwidth of the calibrated system. Material properties used in form function calculations are given in Table 6.2. The sediment is treated as a fluid with properties taken from Ref. [118].

In both form functions, several evenly spaced sharp dips appear at lower frequencies followed by a number of sharp peaks at higher frequencies. These peaks and nulls all correspond to resonances associated with symmetric, s_0 , Lamb waves. At low frequencies, these arise as sharp dips in the form function due to interference of the backscattered surface wave return with the specular portion of the target return. Through resonance scattering analysis, dispersion curves for this wave type are calculated for both the water-loaded and the sediment-loaded case. A rigid background is used to isolate purely elastic modes. The dispersion curves are used to determine the echo delay at which returns attributed to s_0 Lamb waves will arrive with respect to the specular return. These results are presented in Figure 6.5. For details of how the analysis is carried out, the reader is referred to Section 2.2.2.

One notes that the scattering response of the target does not vary significantly between the water-loaded and sediment-loaded cases. Most importantly, the frequency locations of s_0 Lamb wave resonances do not shift significantly in the form functions. These waves are relatively insensitive to the properties of the external medium because they are most strongly coupled into the shell material and not the external fluid. The antisymmetric Lamb waves observed in the laboratory work are more sensitive to the properties of the external medium. Predicted echo delays given in Figure 6.5 are used in the analysis of experimental data to isolate returns attributed to s_0 Lamb waves.

Table 6.2: Material properties used in form function calculations for the stainless steel shell target employed in field experiments.

Material	Density (kg/m³)	Dilatational Wave Speed (m/s)	Shear Wave Speed (m/s)
347 Stainless Steel	8000	5790	3100
Water	998	1483.8	-----
Sediment (Medium Grain Sand)	2000	1714	-----

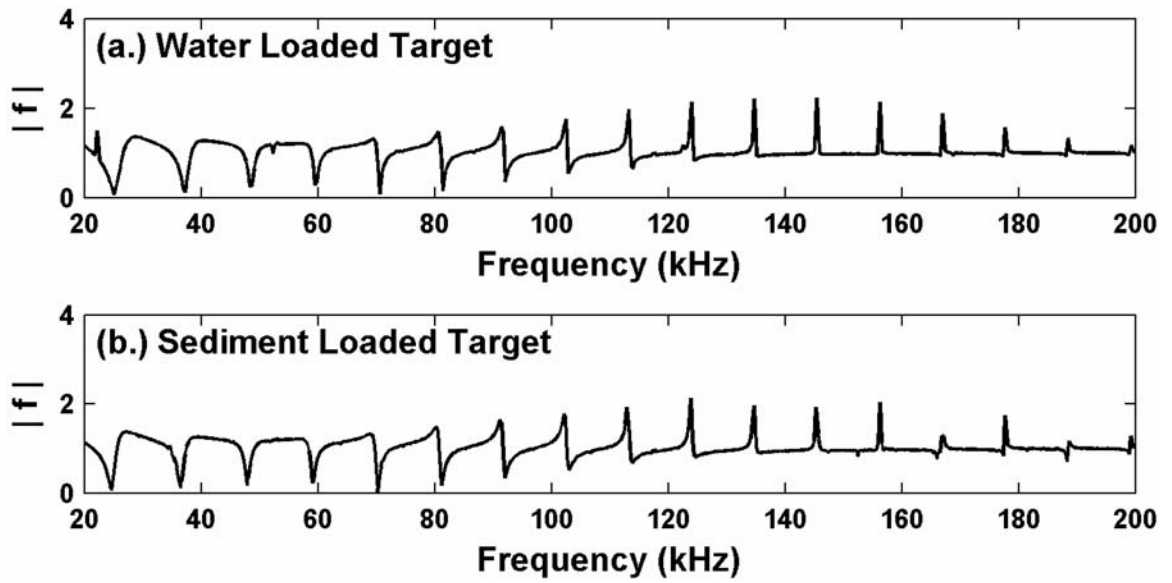


Figure 6.4: Scattering responses of the spherical shell of the same size and composition as the target used in field experiments (a.) Magnitude of the calculated monostatic far-field form function for the target loaded with water. (b.) Magnitude of calculated form function of the steel shell when loaded with the properties of water saturated medium grained sand, treated as a fluid. Both form functions are shown over the frequency bandwidth of the calibrated system used in experiments.

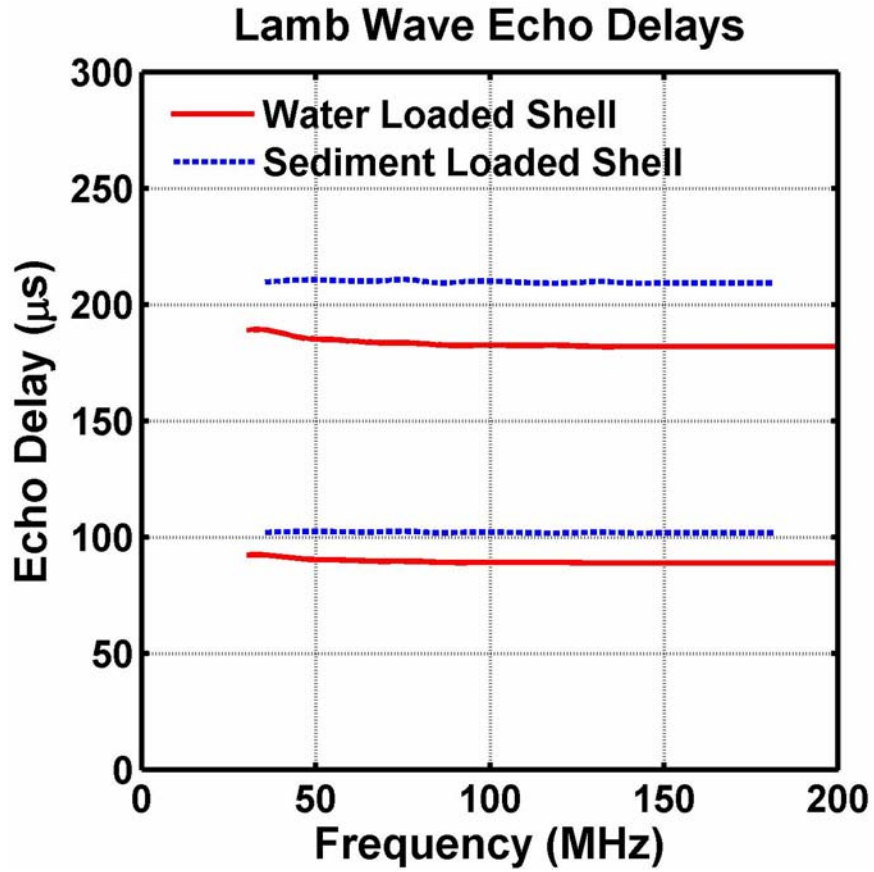


Figure 6.5: Echo delay with respect to the specular return versus frequency, of symmetric, s_0 , Lamb waves that circumnavigate the spherical shell. The delays for both the first and second circumnavigations of the waves are shown. The solid lines and dashed lines correspond to cases where the target is loaded with water and sediment, respectively.

6.3 Free Field Results

In order to verify that s_0 Lamb waves do indeed propagate on the target, time reversal experiments are conducted with the target positioned in the free field. In these experiments, the location of a $60\ \mu\text{s}$ long time reversal window is shifted with respect to returns from the target. Convergence plots with the window positioned over the first and second Lamb wave circumnavigations are shown in Figure 6.6 and Figure 6.7, respectively. In the time domain waveforms of Figures 6.6a-6.6c, the s_0 Lamb wave return is clearly identified as a discrete wave packet that follows the specular return. This Lamb wave arrives at a time delay of $80\ \mu\text{s}$ relative to the specular return. This is within approximately 10% of the predicted delay. Convergence to a resonance centered at 121 kHz is observed. This frequency is very close to the location of a resonance in the free field response of the shell at 124 kHz.

In Figures 6.7a-6.7c the return associated with the second s_0 Lamb wave circumnavigation appears. However, it is not clearly separated from the specular return. The appearance of this waveform at the final time reversal iteration (see Figure 6.7c) is consistent with observations made in the scaled laboratory experiments; for an example of this, the reader is referred to Figure 4.16d located in Section 4.3.3. The phase of the specular return and subsequent Lamb wave circumnavigations matches so that the returns appear as one. The second Lamb wave circumnavigation appears at an echo delay of $150\ \mu\text{s}$ relative to the specular return. This is approximately 20% sooner than predicted. In Figure 6.7, convergence to a resonance centered at 43 kHz is observed. These results

confirm that s_0 Lamb waves are indeed present in the scattering response of the target and that they can be isolated through the application of single-channel time reversal

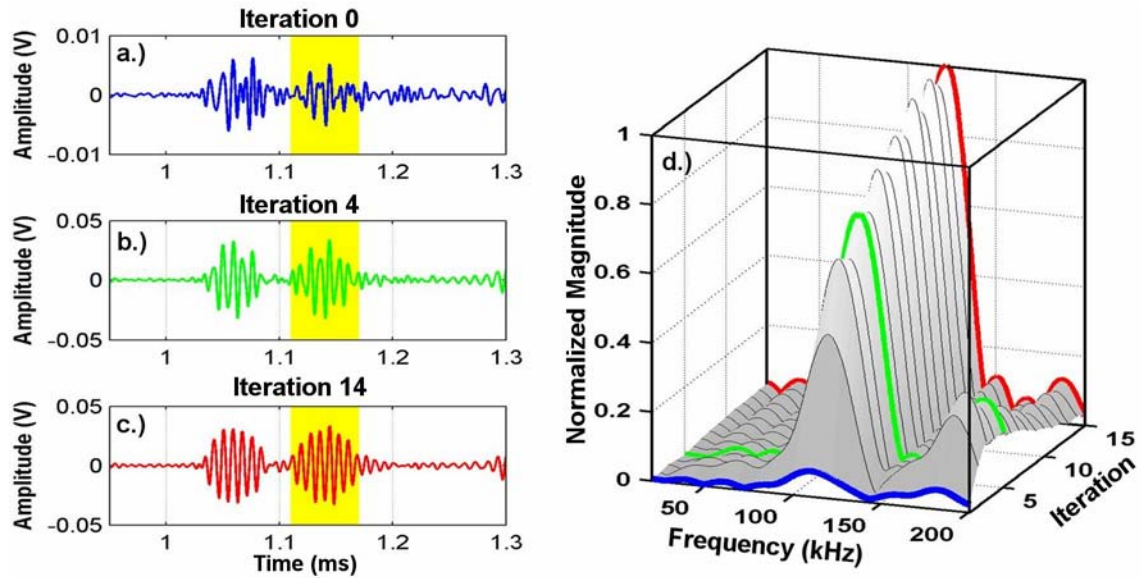


Figure 6.6: Convergence plot for the shell target in the free field through successive iterations of the time reversal procedure. The window is located at the expected position of the first s_0 Lamb wave circumnavigation. Vertical lines in (a)-(c) depict the position of a $60\mu s$ long time reversal window. (a.) The first backscattered return, iteration 0. (b.) Backscattered return at iteration 4 of time reversal. (c.) Backscattered return at iteration 14 of the time reversal procedure. (d.) Waterfall plot of magnitude spectra of signals within the time reversal window for iterations 0 through 14 normalized to the maximum spectral magnitude at the final iteration. The spectra from (a)-(c) are highlighted with lines of the same shading.

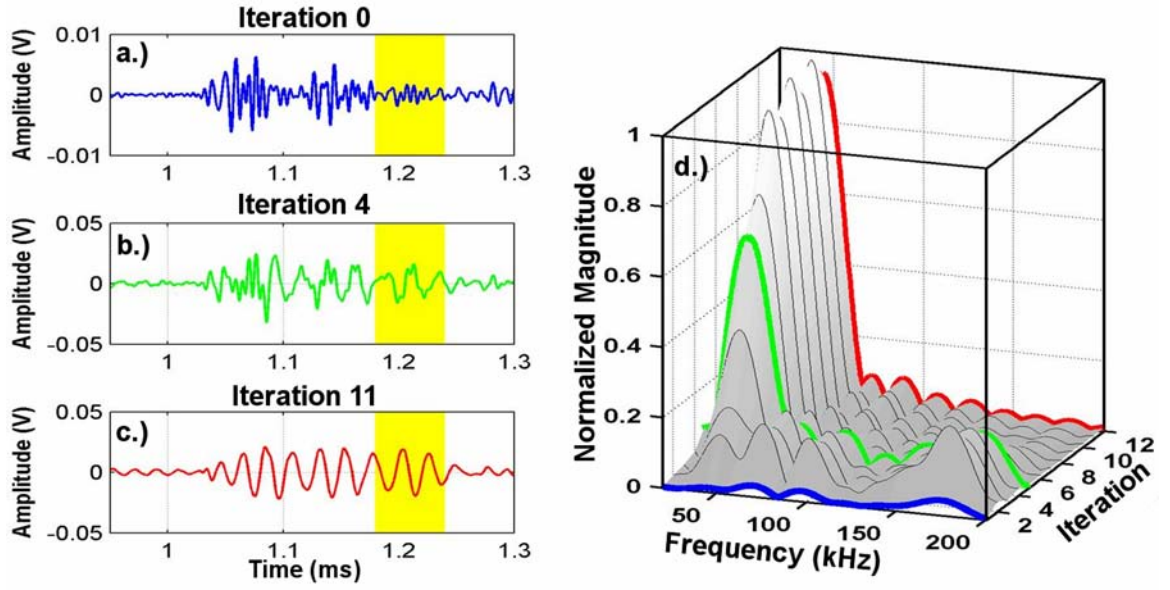


Figure 6.7: Convergence plot for the shell target in the free field through successive iterations of the time reversal procedure. The window is located at the expected position of the second s_0 Lamb wave circumnavigation. Vertical lines in (a)-(c) depict the position of a $60\mu s$ long time reversal window. (a.) The first backscattered return, iteration 0. (b.) Backscattered return at iteration 4 of time reversal. (c.) Backscattered return at iteration 11 of the time reversal procedure. (d.) Waterfall plot of magnitude spectra of signals within the time reversal window for iterations 0 through 11 normalized to the maximum spectral magnitude at the final iteration. The spectra from (a)-(c) are highlighted with lines of the same shading.

6.4 Buried Target Results

In this Section, results from buried target experiments are presented. The face of the target nearest the projector is buried at a depth of 6 inches beneath the surface of the sediment. Sliding window experiments are conducted where a $60\text{ }\mu\text{s}$ time reversal window is employed. A computer program automatically controls the number of iterations that are carried out, halting the procedure after convergence of received waveforms is achieved. Convergence of the time reversal procedure is determined by comparing the most recent backscattered signal to the backscattered signal two iterations prior. Formal convergence is defined when the mean absolute difference between the normalized signals is less than 2.5%.

The top half of Figure 6.8 shows the convergence plot for an experiment conducted without a target in place. The time reversal window is positioned on the expected location of returns from the target. Convergence to a frequency of 59 kHz is observed. In the experiment with a target in place convergence to a frequency of 45 kHz is observed. This is very close to the 43 kHz frequency observed in free field experiments and is different than the convergence frequency observed without a target in place. Although a coherent return is present within the window in both experiments, in the case where a target is present, the return is higher in amplitude.

A second set of experiments is then conducted where a high pass filter is applied to returns between time reversal iterations. The magnitude and phase response of this filter is shown in Figure 6.9. It is meant to reduce the magnitude of the low frequency resonance previously observed and to somewhat account for attenuation in the sediment.

The sliding window experiment is then repeated. Convergence plots depicting selected results are shown in Figure 6.10. They are much more striking than the results when no filter is used. In the experiment without a target in place, only a very low amplitude, low frequency, energy component is observed. In the experiment with a target in place, there is a high amplitude, relatively high quality factor, return visible within the time reversal window. A 105 kHz convergence frequency is observed. This is markedly different than the convergence frequency without a target in place. The frequency is also very close to the 102 kHz center frequency of a s_0 Lamb wave resonance in the sediment-loaded target response of Figure 6.4.

Figure 6.11 shows return signals at the final iteration for additional window locations from this experiment. Convergence frequencies are reported within each figure. The result from Figure 6.10 is repeated in the first row of Figure 6.11. The second and third rows of Figure 6.11 correspond to the expected locations of returns associated with s_0 Lamb waves. Convergence frequencies for the experiment with the target in place are different than those observed in the experiment without the target in place for all window locations. The frequencies observed in Figures 6.11e and 6.11f, 157 kHz and 187 kHz, correspond very closely to the center frequencies of resonances in the sediment-loaded target response of 156 kHz and 189 kHz. These results confirm that s_0 Lamb wave resonances are indeed being excited through application of the time reversal procedure and that techniques applied in the scaled laboratory work should extrapolate to experiments conducted at lower frequencies.

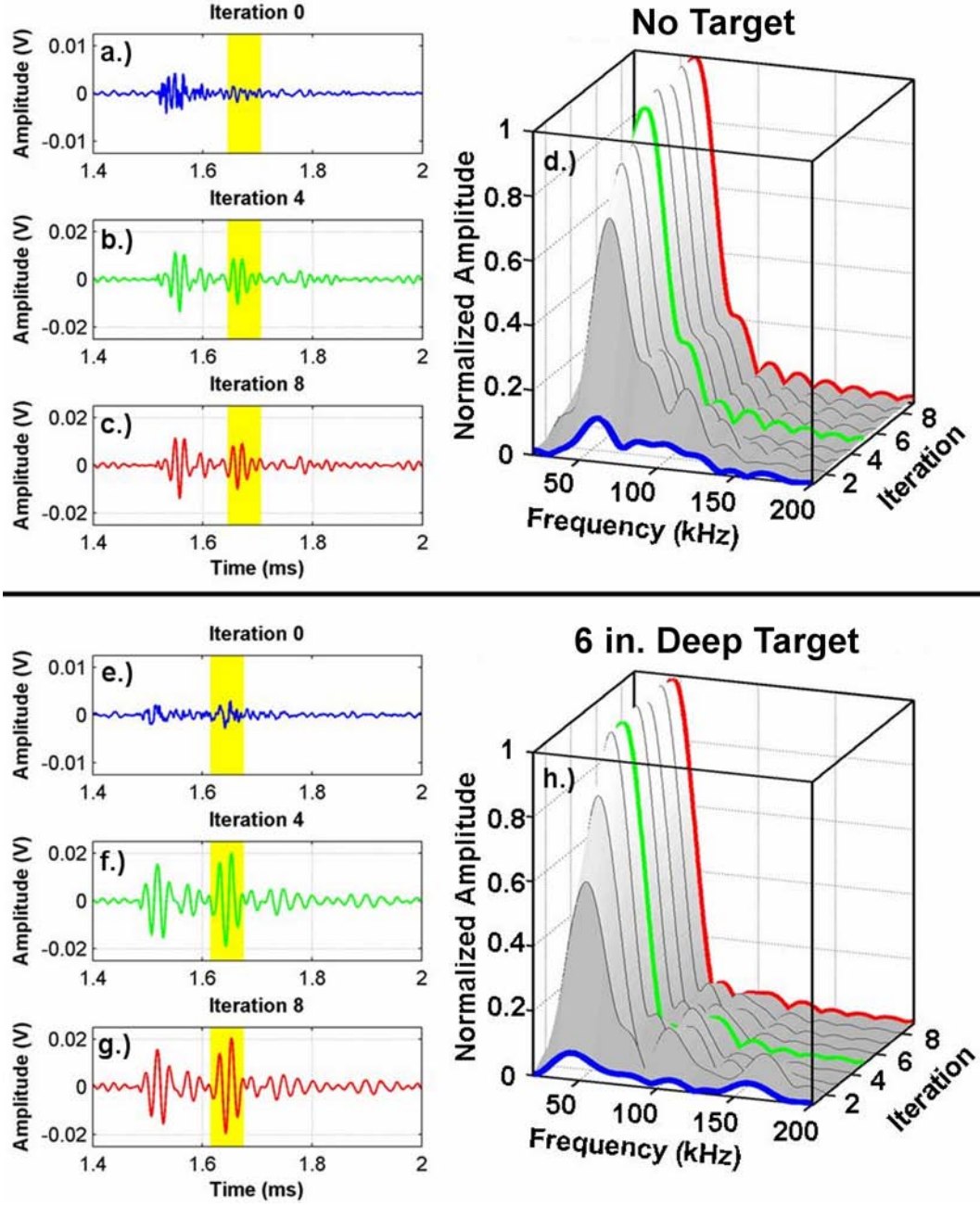


Figure 6.8: Convergence plots without and with the shell target buried at 6 inches. The window is located at the expected position of the first s_0 Lamb wave circumnavigation. Vertical lines in (a-c) & (e-g) depict the position of a $60\mu s$ long time reversal window. (a,e.) The first backscattered return, iteration 0. (b,f.) Backscattered return at iteration 4 of time reversal. (c,g.) Backscattered return at iteration 18 of the time reversal procedure. (d,h.) Waterfall plot of magnitude spectra of signals within the time reversal window for iterations 0 through 18 normalized to the maximum spectral magnitude at the final iteration. The spectra from (a-c) & (e-g) are highlighted with lines of the same shading.

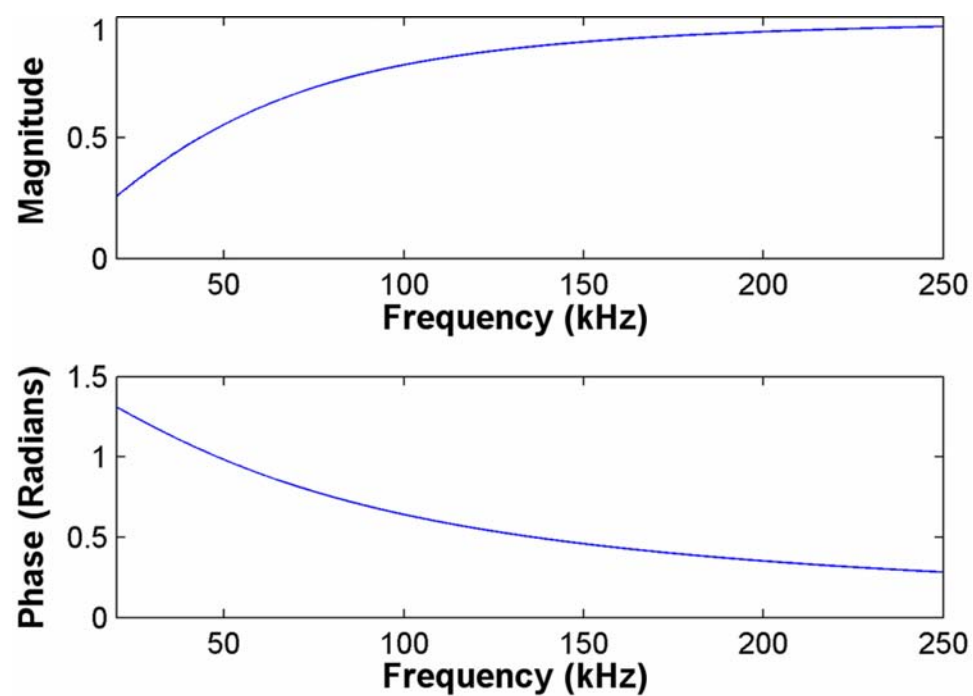


Figure 6.9: Magnitude and phase response of the high pass filter applied to returns in select buried target field experiments.

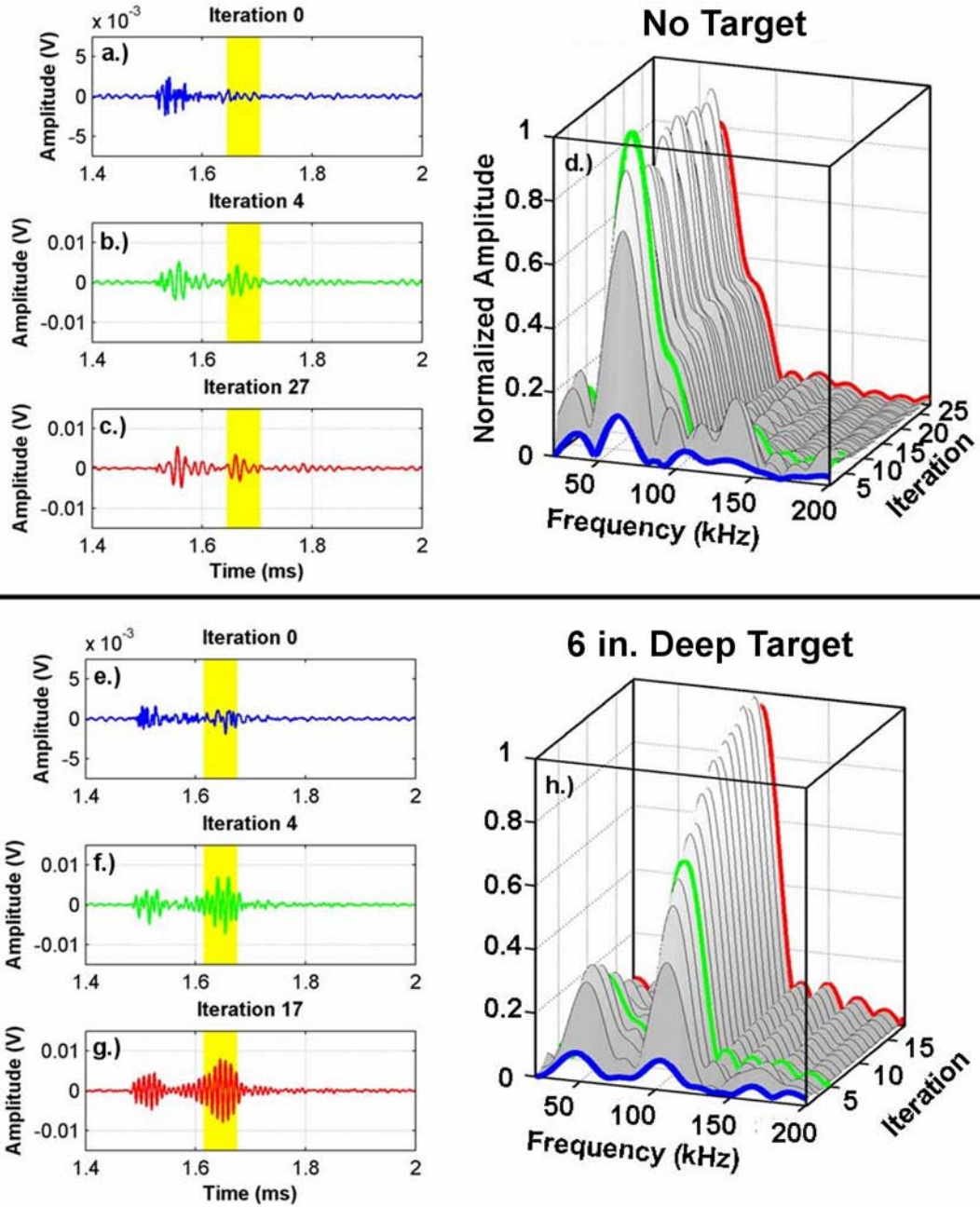


Figure 6.10: Convergence plots without and with the shell target buried at 6 inches with application of the high pass filter. The window is located at the expected position of the first s_0 Lamb wave circumnavigation. Vertical lines in (a-c) & (e-g) depict the position of a $60\mu s$ long time reversal window. (a,e.) The first backscattered return, iteration 0. (b,f.) Backscattered return at iteration 4 of time reversal. (c,g.) Backscattered return at iteration 18 of the time reversal procedure. (d,h.) Waterfall plot of magnitude spectra of signals within the time reversal window for iterations 0 through 18 normalized to the maximum spectral magnitude at the final iteration. The spectra from (a-c) & (e-g) are highlighted with lines of the same shading.

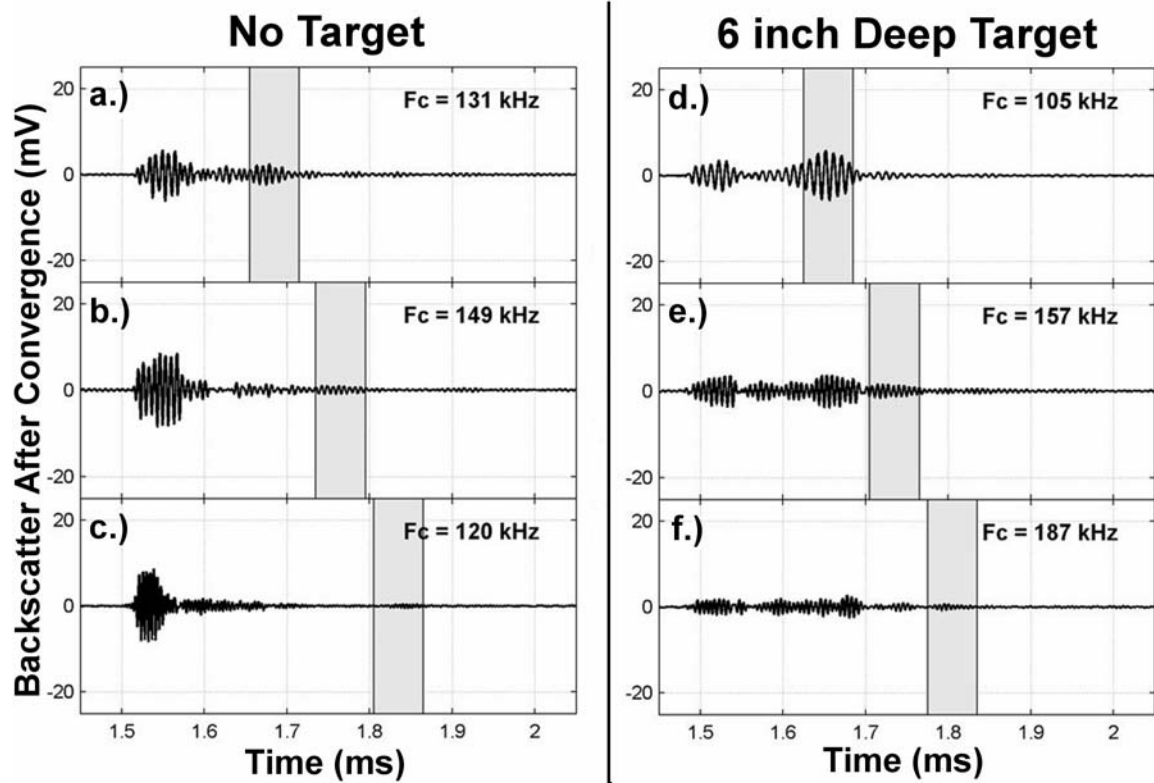


Figure 6.11: Time traces at the final iteration for buried target time reversal experiments where the high pass filter is employed. (a.)-(c.) Results generated without a target in place. (d.)-(f.) Results generated with the target buried at 6 inch depth. In each row, the position of the time reversal window is highlighted with a solid gray box. From the top row to the bottom row, window positions correspond to the expected time location of the specular return, the first s_0 Lamb wave circumnavigation, and the second s_0 Lamb wave circumnavigation. Convergence frequencies are given in each plot.

Chapter 7

Summary and Conclusions

In this work, an iterative, single-channel time reversal technique is applied to study scattered returns from resonant objects positioned both in the free field and fully buried in inhomogeneous media. The investigation consists of a three-pronged approach utilizing a combination of scaled laboratory experiments, numerical simulations, and field experiments. The current Chapter provides an overview of the work and draws conclusions based upon aforementioned results.

Theoretical calculations, presented in Section 2.1, illuminate a number of useful properties of iterative, single-channel time reversal. The technique consists of insonifying a scattering target with a broadband acoustic pulse, sampling the return using a finite time window, reversing the signal in time, and using this reversed signal as a source waveform for the next interrogation. Iteratively repeating the later three steps of this process has the effect of raising the spectral response of a target to a value proportional to the number of iterations carried out. In this way convergence to a narrowband waveform characteristic of the dominant resonance in the backscattering response of the target is achieved. Theoretical predictions indicate that application of the

technique should yield an improvement in the signal-to-noise ratio (SNR) of target returns in the presence of stochastic noise. For the technique to successfully isolate a target of interest, however, the dominant peak in its spectral response must be greater in amplitude than those from surrounding clutter or false targets in its vicinity. To investigate the properties of the technique, scaled laboratory experiments are designed and conducted.

A number of carefully controlled experiments are first carried out in order to characterize the experimental apparatus. The system employed in the laboratory is comprised primarily of an unfocused ultrasonic piston transducer operating in a monostatic pulse-echo configuration. It is well known that the frequency responses of acoustic transducers possess distinct resonance characteristics. In order to ensure that the time reversal procedure is free to converge without bias to a target resonance within the bandwidth of the transducer, the combined transmit-receive response of the measurement system must be flat within this bandwidth. For this reason, a digital filter is designed to equalize the frequency response of the system.

Application of the filter to returns backscattered from the free-water surface of the test tank (a good model of an ideal specular reflector) results in calibrated received waveforms that are accurate replicas of initial outgoing waveforms. This indicates that the digital filter does indeed account for any resonances present within the system. The application of such a filter is critical to ensure unbiased convergence of the time reversal procedure. Experiments conducted to probe the sensitivity of the calibrated system to various transducer orientations, indicate that the flatness of its frequency response is

relatively insensitive to the standing distance but strongly dependent upon the angle of incidence.

Broadband scattering measurements are then conducted in order to characterize the frequency response of the spherical shell target employed in the laboratory work. Interrogation of the target with linear frequency modulated (LFM) chirp waveforms, which sweep the full system bandwidth, indicates that a number of resonances are present within its scattering response. Verification of the geometric and material properties of the target is confirmed by comparing experimentally measured returns with theoretical predictions. By varying the density of the shell material within its measured uncertainty, a normalized mean squared error of less than 5% between the measured and predicted target response is observed. This provides further evidence that the system calibration is indeed reliable. Additional measurements confirm theoretical predictions that the observed target resonances are primarily attributed to symmetric, s_0 , and antisymmetric, a_{0-} , Lamb wave returns.

A final set of characterization experiments probes the acoustic properties of the sediment phantom employed, which consists of a consolidation of water saturated spherical glass beads. Through-transmission experiments are conducted in which the sound speed and attenuation of dilatation waves in the phantom are measured. Both properties are found to possess significant frequency dependence, with the sound speed decreasing, and the attenuation increasing, as a function of frequency. The trends observed in these measurements exhibit qualitative agreement with those reported in the literature. The measured values are used in a transient scattering simulation to predict the

response of the shell target when it is buried and to verify the effects of attenuation on convergence of the time reversal procedure.

With a well-characterized measurement system and an understanding of the types of waves that propagate on the scattering target of interest, it is possible to test the efficacy of the single-channel time reversal technique. Experiments are first conducted with the target suspended in the free-field. Results confirm that application of the technique results in convergence to the dominant resonance in the experimentally measured target response. For the target employed, this resonance is attributed to the propagation of an a_{0-} antisymmetric Lamb wave. The spectral magnitude at this resonance location increases by a factor of 6.6 or 16.4 dB by the final iteration. Convergence to this resonance is observed regardless of the waveform used for the initial interrogation. Although fifty iterations of the time reversal procedure are typically performed, results from a number of experiments indicate that only a few iterations are usually necessary to obtain a significant enhancement in a target's spectral response.

When applied to target returns in the presence of stochastic noise, the time reversal technique yields enhanced performance compared to a simple autocorrelation performed on the first return signal, given a LFM chirp interrogation. The time reversal technique successfully identifies the dominant resonance in the response of the target a maximum of 60% more frequently than the passive autocorrelation technique. Coherently averaging returns, however, improves the performance of the autocorrelation. In a parameter study, the performance of both techniques is evaluated over a range of SNRs where varying numbers of averages/iterations are employed. Results from the

study indicate that the time reversal technique outperforms averaging a maximum of 23% of the time, for SNRs greater than 15 dB. For lower SNR values, averaging outperforms time reversal. This study assumes the perfectly coherent averaging of returns, which is not likely possible in applications where the position of the transducer or scattering target may shift between transmissions. It is likely that this effect will reduce the efficacy of coherent averaging significantly more than that of single-channel time reversal. It is also possible that, for a given number of transmissions, combining averaging and time reversal could yield further enhancements in performance; this is recommended for future study.

A final set of experiments are conducted in the free field where the time reversal technique is employed to isolate multiple resonances in the scattering response of the target and to isolate surface elastic wave returns in time. When the window is smaller than the characteristic circumnavigation time of these surface waves, the averaged normalized root mean squared error (NMRSE) between predicted and measured return times is 1.5%. With small windows, however, it is not possible to isolate individual resonances in the frequency domain. In order to do so, the duration of the time window must be expanded. When larger window sizes are employed, up to four different resonances are identified in the frequency domain. Also, at the same time it is also possible to estimate the circumnavigation times of surface waves even though the window size is larger than the characteristic circumnavigation time. This is accomplished by tracking the peak spectral magnitude observed at each window location. When the window is centered over a surface wave return, a greater spectral magnitude is

typically observed. In this way, the circumnavigation times of a_{0-} Lamb waves are estimated with an average NMRSE of less than 5%. These surface waves are isolated on the shell target even when a solid stainless steel target of the same size is placed between it and the transducer, shielding scattered returns.

After having verified the fundamental properties of the technique in the free field, a number of experiments are conducted with the shell target buried at various depths in a sediment phantom. The sediment phantom introduces coherent noise to returns in the form of volume scattering from individual glass beads and also from returns attributed to its surface. With the target buried at 2 cm depth, convergence to a high Q resonance peak is observed through application of the time reversal technique. Predictions of the target response when loaded by a fluid with the same properties as the sediment phantom indicate that the resonance is likely attributed to an a_{0-} Lamb wave. An improvement of 16 dB in the SNR of target returns is obtained, relative to the first backscattered return, when the entire system bandwidth is employed in the calculation. Limiting the SNR computation to a band encompassing only the dominant resonance results in an improvement of 30 dB.

When the target is buried at various depths ranging from 1 cm to 4 cm, the convergence frequency is found to shift downwards as the target is buried deeper. Numerical simulations confirm that this is due to the frequency dependent attenuation of the sediment. That is, the layer of sediment above the target acts as a low pass filter, the strength of which increases with burial depth. When the target is buried at depths of 4 cm or greater, attenuation diminishes returns to an extent that they are indistinguishable from

coherent background noise. The shift in convergence frequency with increased burial depth demonstrates the strength of iterative time reversal to automatically redirect acoustic energy into the strongest available target resonance.

An investigation is then carried out with the target buried at 2 cm depth and the transducer oriented at incident angles of 0, 10, and 20 degrees. Window shifting experiments are conducted at each angle where window sizes ranging from 4 μ s to 60 μ s are utilized. Results indicate that multiple resonances in the response of the buried target are isolated. At normal incidence, the sediment surface is always the dominant scatterer, and for large window sizes it can mask returns from the buried target. Therefore, the window size should be optimized in order to maximize the energy attributed to target returns, while still retaining the temporal resolution with which to isolate the target from the sediment surface. For this study, a window size of approximately 20 μ s is found to yield the greatest SNR for target returns.

Operating at 10 degrees incidence results in biased convergence to a lower frequency resonance in the response of the target. A bias arises in the frequency response of the system due to mainly to three effects. The first effect is attributed to the spreading of the transducer's beam. Refraction of incident waves at the sediment-water interface results in the center of the transducer's beam being shifted to one side of the target. Lower frequencies spread more than higher frequencies. Therefore, the target will be preferentially excited by these lower frequencies. The second biasing effect arises as the incident angle is increased, because at larger angles, the sound passes through a greater effective thickness of sand which acts as a low pass filter as discussed in Section 5.4.

The third biasing effect is attributed to returns from the sediment surface, which can enter the time reversal window and interfere with target returns. If the dominant response frequency of the sediment surface is located at low frequencies (which it indeed is at 10 degrees incidence) application of the time reversal procedure can result in convergence to a lower frequency target resonance than expected. At 20 degree incidence, the majority of the energy reflected from the sediment surface propagates in the forward direction and does not return to the transducer. Application of the time reversal procedure at this angle results in convergence to the same frequency observed at normal incidence. Also, returns from the sediment surface are barely visible compared to target returns. Therefore, the angle of incidence can be optimized to minimize the sediment surface return while still converging to the expected target resonance frequency.

Wave mode images are generated by raster scanning the transducer over an area of sediment containing two targets of the same size, but possessing different resonance responses. In this way it is possible to isolate the locations of both targets by selectively plotting the energy present within different frequency bands. In addition, two distinct resonances in the response of the standard shell target are observed as a function of transducer position and processing bandwidth. This is due to lower frequency excitation of the target as the transducer is moved away from the target burial location. This result does not rely on any additional signal processing techniques.

Finally, a set of field experiments is conducted in a test pond at the Naval Surface Warfare Center – Panama City Division. In these experiments the insight gained in the laboratory work is applied in a lower frequency (20-200 kHz) regime to detect and

identify a stainless steel shell target buried in water saturated medium grained sand. Results of these experiments indicate that target resonances attributed to s_0 symmetric Lamb waves are identified both when the target is suspended in the free field and when it is buried in sand at 15.24 cm depth. The results confirm that s_0 symmetric Lamb waves survive burial and that the time reversal technique is indeed applicable at lower frequency operating conditions.

The single-channel technique provides a straightforward and inexpensive alternative to array based schemes for isolation of the dominant resonance in the response of a target-object. However, the reader should note that there is no spatial focusing and, as the technique requires the use of a time-gate window, it is unable to exploit multi-path propagation. Therefore, array based time reversal will afford an improvement in these respects. An obvious extension of the current work would be to apply the methodology presented here in an array-based scheme. Also, in this work, the location of the transducer is stationary as successive iterations of the time reversal technique are carried out. It would be interesting to determine whether an improvement in target detection or identification could be achieved by performing time reversal iteratively, while slowly translating the position of the transducer. This would have applications in ocean acoustics, where unmanned underwater vehicles autonomously search for scattering targets of interest. Although the work reported in this dissertation is specific to the detection of objects buried in sands and sediments, the techniques described can be used to isolate acoustic returns from any resonating object imbedded in media possessing high

levels of clutter and noise, including applications in biomedical sensing and imaging as well as flaw detection and material characterization.

Appendix A

Additional Scattering & Wave Propagation Theory

This section provides additional analysis regarding the scattering of acoustic waves from targets. Included is a derivation for the scattering response of a solid sphere, fluid sphere, elastic cylindrical shell that is filled with an elastic solid, and a solid cylinder. Resonance scattering theory is used to determine the properties of waves that propagate on a solid stainless steel spherical target used in some time reversal experiments. Finally, a review of analysis used to determine dispersion curves for Lamb waves on a flat plate *in vacuo* is provided.

A.1 Acoustic Scattering from an Elastic Sphere

A solid sphere, of outer radius a , is located at the origin of an infinite space consisting of a fluid medium of density ρ_1 and dilatational wave speed c_{d1} . A schematic is presented in Figure A.1. The sphere consists of an elastic solid with density ρ_2 , dilatation wave speed c_{d2} , and shear wave speed c_{s2} . An infinite plane acoustic wave is incident upon the sphere and approaches from the negative \hat{e}_z direction.

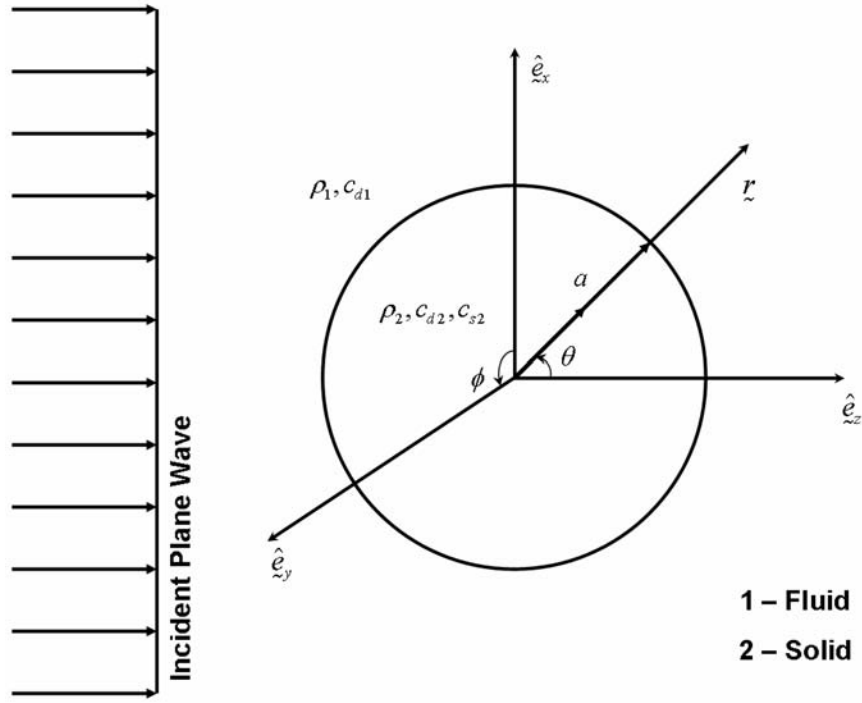


Figure A.1: Schematic of the geometry for the scattering of a plane acoustic wave by an elastic sphere submerged in an infinite fluid medium.

Solutions of the elastic wave equation in terms of displacement

$$\rho \left(\frac{\partial^2 \underline{u}}{\partial t^2} \right) = (\lambda + 2\mu) \nabla (\nabla \cdot \underline{u}) - \mu \nabla \times (\nabla \times \underline{u}) \quad (\text{A.1})$$

are expressed in terms of scalar and vector potential functions φ and Ψ , respectively, such that

$$\underline{u} = \nabla \varphi + \nabla \times \Psi. \quad (\text{A.2})$$

Assuming an $e^{-i\omega t}$ time harmonic convention (where ω is angular frequency and t is time), the scalar potential satisfies the Helmholtz equation,

$$\nabla^2 \varphi + k_d^2 \varphi = 0 \quad (\text{A.3})$$

where $k_d = \omega / c_d$ is the wave number for dilatational waves. This relationship will be useful subsequently, in resolving the relevant components of stress in the system.

In spherical coordinates, the gradient and curl operators are as follows:

$$\nabla \varphi = \frac{\partial \varphi}{\partial r} \hat{e}_r + \frac{1}{r} \frac{\partial \varphi}{\partial \theta} \hat{e}_\theta + \frac{1}{r \sin \theta} \frac{\partial \varphi}{\partial \phi} \hat{e}_\phi \quad (\text{A.4})$$

$$\begin{aligned} \nabla \times \Psi = & \frac{1}{r \sin \theta} \left\{ \frac{\partial}{\partial \theta} (\psi_\phi \sin \theta) - \frac{\partial \psi_\theta}{\partial \phi} \right\} \hat{e}_r + \dots \\ & \dots + \left\{ \frac{1}{r \sin \theta} \frac{\partial \psi_r}{\partial \phi} - \frac{1}{r} \frac{\partial}{\partial r} (r \psi_\phi) \right\} \hat{e}_\theta + \frac{1}{r} \left\{ \frac{\partial}{\partial r} (r \psi_\theta) - \frac{\partial \psi_r}{\partial \theta} \right\} \hat{e}_\phi \end{aligned} \quad (\text{A.5})$$

Here, one notes that for scattering from a sphere there will be no dependence on ϕ and only one of the shear potential's components contributes, $\Psi = (0, 0, \psi_\phi)$. Substituting equations (2.26) and (2.27) into equation (2.24) yields the components of displacement in spherical coordinates,

$$u_r = \frac{\partial \varphi}{\partial r} + \frac{\cot \theta}{r} \psi_\phi + \frac{1}{r} \frac{\partial \psi_\phi}{\partial r} \quad (\text{A.6})$$

$$u_\theta = \frac{1}{r} \frac{\partial \varphi}{\partial \theta} - \frac{\psi_\phi}{r} - \frac{\partial \psi_\phi}{\partial r} \quad (\text{A.7})$$

$$u_\phi = 0. \quad (\text{A.8})$$

The constitutive relation, between the component of radial stress and displacement, can be expanded as

$$\begin{aligned} \tau_{rr} = & \lambda (\nabla \cdot \underline{u}) + 2\mu \left\{ \frac{\partial u_r}{\partial r} \right\} \\ = & -\lambda k_d^2 \varphi + 2\mu \left\{ \frac{\partial^2 \varphi}{\partial r^2} + \frac{\cot \theta}{r} \frac{\partial \psi_\phi}{\partial r} - \frac{\cot \theta}{r^2} \psi_\phi + \frac{1}{r} \frac{\partial^2 \psi_\phi}{\partial r \partial \theta} - \frac{1}{r^2} \frac{\partial \psi_\phi}{\partial \theta} \right\}. \end{aligned} \quad (\text{A.9})$$

where, making use of the identity $\nabla \cdot \underline{u} = \nabla \cdot \nabla \varphi = \nabla^2 \varphi$, equation (2.25) is substituted for the divergence term. The component of stress tangential to the sphere's surface in the \hat{e}_θ direction is

$$\begin{aligned}\tau_{r\theta} &= \mu \left\{ \frac{\partial u_\theta}{\partial r} - \frac{u_\theta}{r} + \frac{1}{r} \frac{\partial u_r}{\partial \theta} \right\} \\ &= \mu \left\{ 2 \frac{\partial}{\partial r} \left[\frac{1}{r} \frac{\partial}{\partial \theta} \left(\varphi + \frac{\partial}{\partial r} (r\psi) \right) \right] + k_s^2 \frac{\partial^2 \psi}{\partial \theta^2} \right\}\end{aligned}\quad (\text{A.10})$$

where $k_s = \omega / c_s$ is the wave number for shear waves. With the displacements and constitutive relations defined, it is now possible to proceed with solution of the boundary value problem of interest.

Assuming an $e^{-i\omega t}$ time harmonic convention, where t is time, the pressure of the incident wave, p_i , expanded in terms of spherical harmonics is

$$p_i = p_0 e^{-i\omega t} \sum_{n=0}^{\infty} i^n (2n+1) j_n(k_1 r) P_n(\cos \theta). \quad (\text{A.11})$$

where p_0 is the pressure amplitude, $k_1 = \omega / c_{d1}$ is the dimensionless Helmholtz number in the medium external to the sphere, $j_n(k_1 r)$ is a spherical Bessel function, and $P_n(\cos \theta)$ is a Legendre polynomial. The pressure scattered from the sphere, p_s , can be expressed as

$$p_s = p_0 e^{-i\omega t} \sum_{n=0}^{\infty} i^n (2n+1) a_n h_n^{(1)}(k_1 r) P_n(\cos \theta) \quad (\text{A.12})$$

where $h_n^{(1)}(k_1 r)$ is a spherical Hankel function of the first kind. The $p_0 i^n (2n+1)$ term is included for convenience and it is assumed that the a_n coefficients absorb the appropriate

factors to account for this substitution. The total pressure in the fluid external to the sphere is equal to the sum of the incident and scattered pressures,

$$p_1 = p_i + p_s = p_0 e^{-i\omega t} \sum_{n=0}^{\infty} i^n (2n+1) \left[j_n(k_1 r) + a_n h_n^{(1)}(k_1 r) \right] P_n(\cos \theta). \quad (\text{A.13})$$

It is also necessary to determine the radial displacement, $u_{r,1}$, in the fluid external to the sphere. This is accomplished through use of the linearized momentum equation [78] where

$$u_{r,1} = \frac{1}{\rho_1 \omega^2} \frac{\partial p_1}{\partial r} = \frac{p_0}{\rho_1 \omega^2} e^{-i\omega t} \sum_{n=0}^{\infty} i^n (2n+1) \left[k_1 j_n'(k_1 r) + a_n k_1 h_n^{(1)'}(k_1 r) \right] P_n(\cos \theta). \quad (\text{A.14})$$

Expressions for the potential functions in the sphere's interior are

$$\varphi_2(r, \theta, t) = p_0 e^{-i\omega t} \sum_{n=0}^{\infty} i^n (2n+1) \left[b_n j_n(k_{d2} r) \right] P_n(\cos \theta), \quad (\text{A.15})$$

$$\psi_2(r, \theta, t) = p_0 e^{-i\omega t} \sum_{n=0}^{\infty} i^n (2n+1) \left[c_n j_n(k_{s2} r) \right] \frac{d}{d\theta} [P_n(\cos \theta)]. \quad (\text{A.16})$$

where a Neumann function is excluded in equations (A.15) and (A.16) to ensure that the solution remains bounded at the origin of the coordinate system, located at the sphere's interior.

The three unknown coefficients, a_n , b_n , and c_n are determined by matching the boundary conditions for displacement, normal stress, and transverse stress at the external surface of the sphere. On the sphere's external surface, at $r = a$,

$$p_1 = -\tau_{rr,2} \quad (\text{A.17})$$

$$u_{r,1} = u_{r,2} \quad (\text{A.18})$$

$$\tau_{r\theta,2} = 0 \quad (\text{A.19})$$

Application of the boundary conditions results in a set of linear equations that are presented here in matrix form as,

$$\begin{bmatrix} d_{11} & d_{12} & d_{13} \\ d_{21} & d_{22} & d_{23} \\ d_{31} & d_{32} & d_{33} \end{bmatrix} \begin{Bmatrix} a_n \\ b_n \\ c_n \end{Bmatrix} = \begin{bmatrix} A_1 \\ A_2 \\ A_3 \end{bmatrix} \quad (\text{A.20})$$

where,

$$d_{11} = a^2 h_n^{(1)}(k_1 a)$$

$$d_{12} = \left[-(\lambda_2 + 2\mu_2)(k_{d2}a)^2 + 2\mu_2 n(n+1) \right] j_n(k_{d2}a) - 4\mu_2 [k_{d2}a] j_n'(k_{d2}a)$$

$$d_{13} = 2\mu_2 [n(n+1)] j_n(k_{s2}a) - 2\mu_2 [n(n+1)k_{s2}a] j_n'(k_{s2}a)$$

$$A_1 = -a^2 j_n(k_1 a)$$

$$d_{21} = \frac{k_1 a}{\rho_1 \omega^2} h_n^{(1)'}(k_1 a)$$

$$d_{22} = [-k_{d2}a] j_n'(k_{d2}a)$$

$$d_{23} = n(n+1) j_n(k_{s2}a)$$

$$A_2 = -\frac{k_1 a}{\rho_1 \omega^2} j_n'(k_1 a)$$

$$d_{31} = 0$$

$$d_{32} = -2j_n(k_{d2}a) + 2[k_{d2}a] j_n'(k_{d2}a)$$

$$d_{33} = \left[2 - 2n(n+1) + (k_{s2}a)^2 \right] j_n(k_{s2}a) + 2k_{s2}a j_n'(k_{s2}a)$$

$$A_3 = 0$$

The system of equations (2.54) is solved for the coefficients a_n in order to determine the frequency dependence of the scattered field. The computer program used for this calculation is written in MATLAB® [119]. If the sphere target of interest consists of a fluid instead of an elastic solid, the same system of equations can be used by setting the second Lamé coefficient in the target medium to $\mu_2 = 0$.

A.2 Resonance Scattering Theory - Solid Stainless Steel Sphere

In this section, results of resonance scattering analysis are provided for the 6.35 mm outer diameter stainless steel sphere target used in some time reversal experiments. The reader should refer to the section on resonance scattering theory in Chapter 2 for details of how the analysis is carried out. The parameters used to calculate the stainless steel target's form function, shown in Figure A.2a, are presented in Table A.1. The individual partial waves of the target's scattering response are presented in Figure A.2b-l. Over the depicted frequency range, the response consists of a Rayleigh wave and several whispering gallery waves.

Table A.2 presents the location in ka of the center frequency of each of the resonances for partial wave numbers up to $n = 34$. The phase and group velocities of the Rayleigh wave ($l = 1$) and the first whispering gallery wave ($l = 2$) are plotted in Figure A.3. The values of the phase velocity are interpolated with a solid line. Finally, the echo

delay between the specular return and the arrival of each surface elastic wave is plotted in Figure A.4.

Table A.1: Material properties used in the analytical prediction of the solid stainless steel target's monostatic farfield form function.

Sphere outer radius	3.182 mm
External fluid density, water	998 kg/m ³
External fluid sound speed, water	1476 m/s
Density, SS-316 stainless steel	2680 kg/m ³
Dilatational wave speed, SS-316 stainless steel	5380.5 m/s
Shear wave speed, SS-316 stainless steel	3106.4 m/s

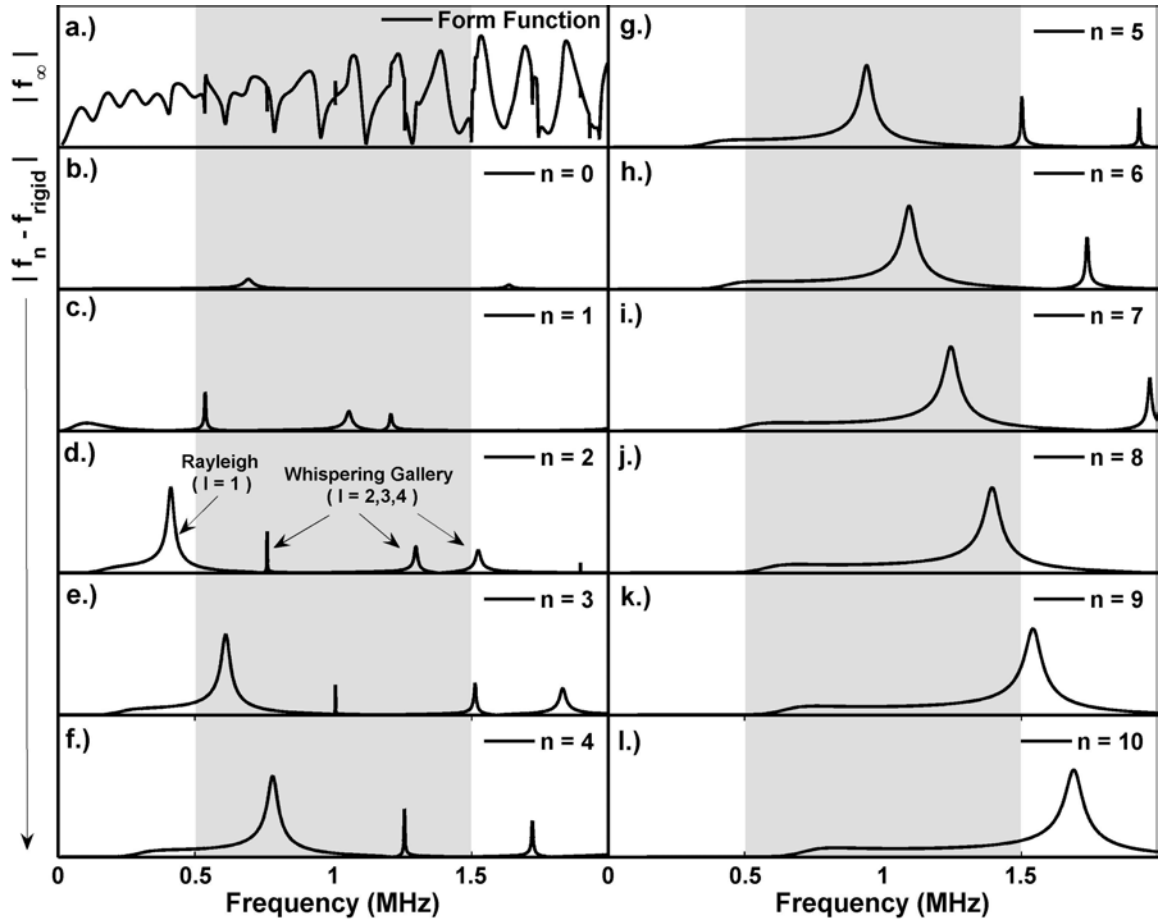


Figure A.2: Far-field acoustic form function of the solid stainless steel target decomposed into the individual components of its partial wave series solution after subtraction of the partial waves from a rigid sphere. (a.) Magnitude of the far-field acoustic form function versus frequency. (b.)-(l.) Partial waves $n = 0$ to $n = 10$, magnitude versus frequency, after background subtraction. The vertical axis is normalized and presented on the same scale for all subfigures. The gray shaded region depicts the frequency range of interest for the current work. Within subfigures b.-l. is plotted the angular dependence of each partial wave. In (d.) resonance types are identified with arrows.

Table A.2: List of resonance ka locations (center frequency of resonance) for each partial wave of the Rayleigh ($l = 1$), and first three whispering gallery ($l = 2, 3, 4$) type wave resonances in the purely elastic response of a 6.35mm diameter solid stainless sphere target used in time reversal experiments.

	Resonance ka Location			
n	$l = 1$	$l = 2$	$l = 3$	$l = 4$
1	-----	7.2007	14.2414	16.2976
2	5.5206	10.2410	17.5298	20.5781
3	8.2088	13.5854	20.4260	24.7185
4	10.5091	16.9617	23.2343	28.5229
5	12.6733	20.2740	26.0266	31.9392
6	14.7495	23.4743	28.8509	35.0675
7	16.7977	26.5467	31.7232	38.0118
8	18.8179	29.4749	34.6435	40.8601
9	20.8261	32.2792	37.6038	43.6684
10	22.8183	34.9715	40.5801	46.4686
11	24.8025	37.5798	43.5484	49.2689
12	26.7827	40.1160	46.4766	52.0932
13	28.7509	42.6043	49.3649	54.9335
14	30.7231	45.0525	52.1892	57.7978
15	32.6873	47.4687	54.9415	60.6781
16	34.6515	49.8530	57.6378	63.5584
17	36.6117	52.2292	60.2860	66.4306
18	38.5639	54.5815	62.8783	69.2789
19	40.5241	56.9177	65.4305	72.0952
20	42.4762	59.2459	67.9548	74.8635
21	44.4284	61.5622	70.4470	77.5998
22	46.3846	63.8704	72.9153	-----
23	48.3328	66.1666	75.3595	-----
24	50.2850	68.4588	77.7918	-----
25	52.2332	70.7431	-----	-----
26	54.1814	73.0233	-----	-----
27	56.1296	75.2955	-----	-----
28	58.0738	77.5598	-----	-----
29	60.0220	-----	-----	-----
30	61.9662	-----	-----	-----
31	63.9104	-----	-----	-----
32	65.8586	-----	-----	-----
33	67.7988	-----	-----	-----
34	69.7430	-----	-----	-----

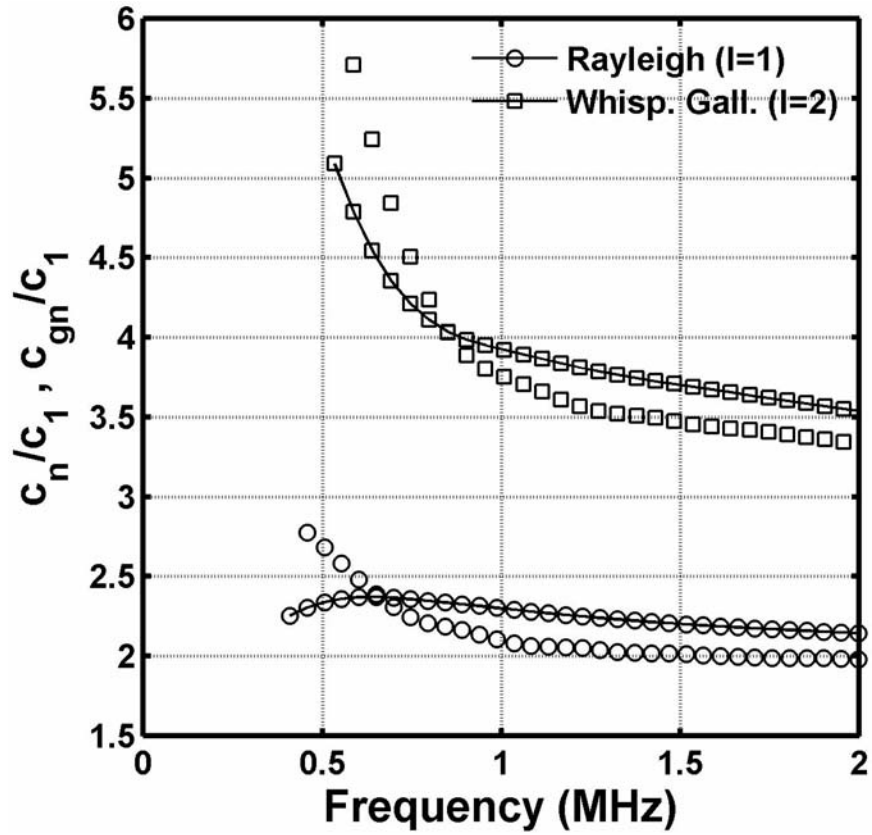


Figure A.3: Phase and group velocities of Rayleigh ($l=1$) and whispering gallery ($l=2$) waves that propagate on a solid stainless steel target. The wave velocities are normalized by the sound speed of water, $c=1476$ m/s, and plotted versus frequency over a range relevant to the current work. Phase velocities of the Rayleigh wave and the first whispering gallery wave are shown as circles and squares, respectively. The phase velocity results are interpolated with a solid line.

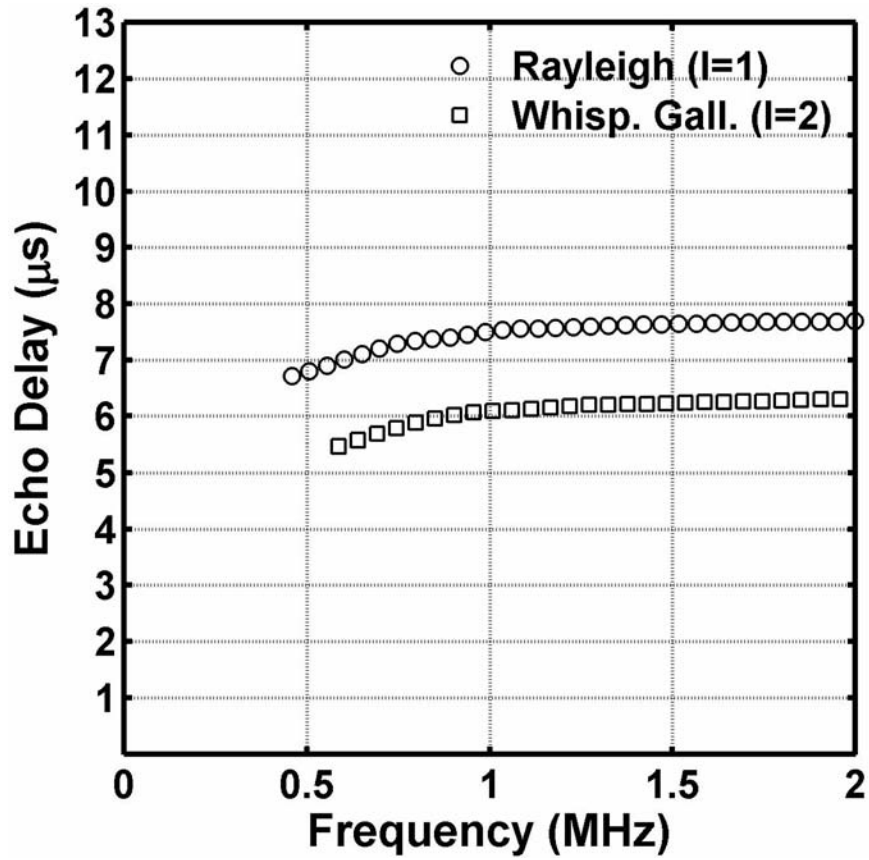


Figure A.4: Echo delay with respect to the specular return versus frequency, of the first circumnavigation of Rayleigh ($l=1$) and whispering gallery ($l=2$) waves that circumnavigate the solid stainless steel target.

A.3 Acoustic Scattering from an Elastic Cylindrical Shell Filled with an Elastic Medium

An infinite cylindrical shell, of outer radius a and inner radius b , is located at the origin of an infinite space consisting of a fluid medium of density ρ_1 and dilatational wave speed c_{d1} . A schematic is presented in Figure A.5. The shell, filled with a solid of density ρ_3 , dilatational wave speed c_{d3} , and shear wave speed c_{s3} consists of an elastic solid with density ρ_2 , dilatation wave speed c_{d2} , and shear wave speed c_{s2} . An infinite plane acoustic wave is incident upon the shell and approaches from the negative \hat{x} direction, as in.

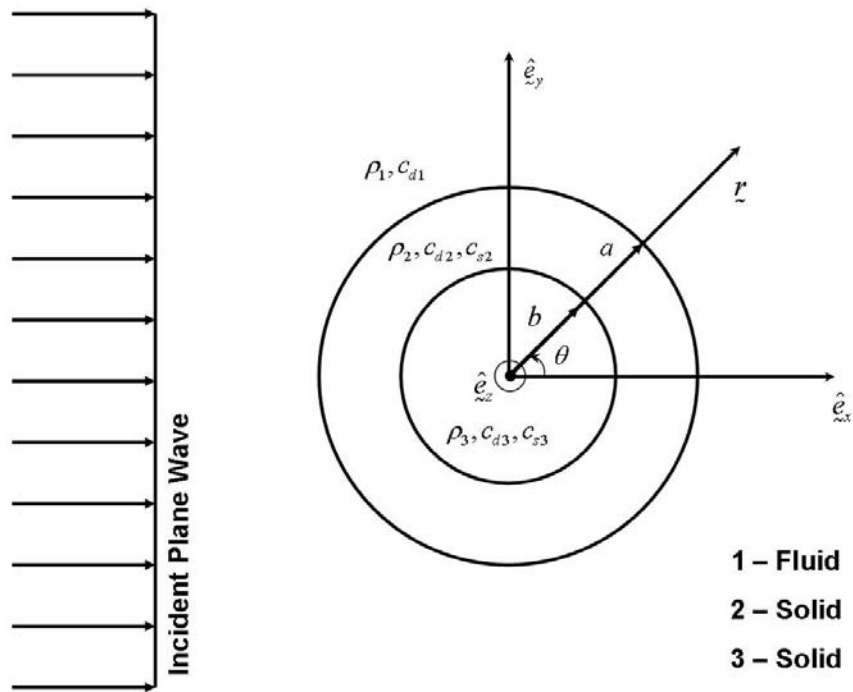


Figure A.5: Schematic of the geometry for the scattering of a plane acoustic wave by an elastic sphere submerged in an infinite fluid medium.

Solutions of the elastic wave equation in terms of displacement

$$\rho \left(\frac{\partial^2 \underline{u}}{\partial t^2} \right) = (\lambda + 2\mu) \underline{\nabla} (\underline{\nabla} \cdot \underline{u}) - \mu \underline{\nabla} \times (\underline{\nabla} \times \underline{u}) \quad (\text{A.21})$$

are expressed in terms of scalar and vector potential functions φ and $\underline{\Psi}$, respectively, such that

$$\underline{u} = \underline{\nabla} \varphi + \underline{\nabla} \times \underline{\Psi}. \quad (\text{A.22})$$

Assuming an $e^{-i\omega t}$ time harmonic convention (where ω is angular frequency and t is time), the scalar potential satisfies the Helmholtz equation,

$$\nabla^2 \varphi + k_d^2 \varphi = 0 \quad (\text{A.23})$$

where $k_d = \omega / c_d$ is the wave number for dilatational waves. This relationship will be useful subsequently, in resolving the relevant components of stress in the system.

In cylindrical coordinates, the gradient and curl operators are as follows:

$$\underline{\nabla} \varphi = \frac{\partial \varphi}{\partial r} \hat{e}_r + \frac{1}{r} \frac{\partial \varphi}{\partial \theta} \hat{e}_\theta + \frac{\partial \varphi}{\partial z} \hat{e}_z \quad (\text{A.24})$$

$$\underline{\nabla} \times \underline{\Psi} = \left\{ \frac{1}{r} \frac{\partial \psi_z}{\partial \theta} - \frac{\partial \psi_\theta}{\partial z} \right\} \hat{e}_r + \left\{ \frac{\partial \psi_r}{\partial z} - \frac{\partial \psi_z}{\partial r} \right\} \hat{e}_\theta + \frac{1}{r} \left\{ \frac{\partial}{\partial r} (r \psi_\theta) - \frac{\partial \psi_r}{\partial \theta} \right\} \hat{e}_z \quad (\text{A.25})$$

Here, one notes that for scattering from an infinite cylinder under broadside insonification there will be no dependence on z and only one of the shear potential's components contributes, $\underline{\Psi} = (0, 0, \psi_z)$. Substituting equations (2.26) and (2.27) into equation (2.24) yields the components of displacement in spherical coordinates,

$$u_r = \frac{\partial \varphi}{\partial r} + \frac{1}{r} \frac{\partial \psi_z}{\partial \theta} \quad (\text{A.26})$$

$$u_\theta = \frac{1}{r} \frac{\partial \varphi}{\partial \theta} - \frac{\partial \psi_z}{\partial r} \quad (\text{A.27})$$

$$u_z = 0. \quad (\text{A.28})$$

The constitutive relation, between the component of radial stress and displacement, can be expanded as

$$\begin{aligned} \tau_{rr} &= \lambda (\nabla \cdot \underline{u}) + 2\mu \left\{ \frac{\partial u_r}{\partial r} \right\} \\ &= -\lambda k_d^2 \phi + 2\mu \left\{ \frac{\partial^2 \phi}{\partial r^2} - \frac{1}{r^2} \frac{\partial \psi_z}{\partial \theta} + \frac{1}{r} \frac{\partial^2 \psi_z}{\partial r \partial \theta} \right\}. \end{aligned} \quad (\text{A.29})$$

where, making use of the identity $\nabla \cdot \underline{u} = \nabla \cdot \nabla \phi = \nabla^2 \phi$, equation (2.25) is substituted for the divergence term. The component of stress tangential to the sphere's surface is

$$\begin{aligned} \tau_{r\theta} &= \mu \left\{ \frac{\partial u_\theta}{\partial r} - \frac{u_\theta}{r} + \frac{1}{r} \frac{\partial u_r}{\partial \theta} \right\} \\ &= \mu \left\{ 2 \frac{\partial^2}{\partial r \partial \theta} \left(\frac{\phi}{r} \right) + \left[-\frac{\partial^2 \psi_z}{\partial r^2} + \frac{1}{r} \frac{\partial \psi_z}{\partial r} + \frac{1}{r^2} \frac{\partial \psi_z}{\partial \theta^2} \right] \right\}. \end{aligned} \quad (\text{A.30})$$

With the displacements and constitutive relations defined, it is now possible to proceed with solution of the boundary value problem of interest.

It is necessary to express the pressure of the incident plane wave as a sum of spherical harmonic functions [120]. Assuming an $e^{-i\omega t}$ time harmonic convention, where t is time, the pressure of the incident wave, p_i , expanded in terms of spherical harmonics is

$$p_i = p_0 e^{-i\omega t} \sum_{n=0}^{\infty} i^n \varepsilon_n J_n(k_1 r) \cos(n\theta). \quad (\text{A.31})$$

where p_0 is the pressure amplitude, $k_1 = \omega / c_{d1}$ is the wave number in the medium external to the sphere, $J_n(k_1 r)$ is an ordinary Bessel function, and $\varepsilon_n = 2 - \delta_{n0}$ where

$$\delta_{n0} = \begin{cases} 1, & \text{if } n = 0 \\ 0, & \text{if } n \neq 0 \end{cases} \quad (\text{A.32})$$

is the Kronecker delta function.

The scattered pressure, p_s , can be expressed as

$$p_s = p_0 e^{-i\omega t} \sum_{n=0}^{\infty} i^n \varepsilon_n a_n H_n^{(1)}(k_1 r) \cos(n\theta) \quad (\text{A.33})$$

where $H_n^{(1)}(k_1 r)$ is a Hankel function of the first kind. The $p_0 i^n \varepsilon_n$ term is included for convenience and it is assumed that the a_n coefficients absorb the appropriate factors to account for this substitution. The total pressure in the fluid external to the cylinder is equal to the sum of the incident and scattered pressures,

$$p_1 = p_i + p_s = p_0 e^{-i\omega t} \sum_{n=0}^{\infty} i^n \varepsilon_n \left[J_n(k_1 r) + a_n H_n^{(1)}(k_1 r) \right] \cos(n\theta). \quad (\text{A.34})$$

It is also necessary to determine the radial displacement, u_{r1} , in the fluid external to the sphere. This is accomplished through use of the linearized momentum equation [78] where

$$u_{r1} = \frac{1}{\rho_1 \omega^2} \frac{\partial p_1}{\partial r} = \frac{p_0}{\rho_1 \omega^2} e^{-i\omega t} \sum_{n=0}^{\infty} i^n \varepsilon_n \left[k_1 J_n'(k_1 r) + a_n k_1 H_n^{(1)'}(k_1 r) \right] \cos(n\theta). \quad (\text{A.35})$$

Expressions for the potential functions in the shell material are

$$\varphi_2(r, \theta, t) = p_0 e^{-i\omega t} \sum_{n=0}^{\infty} i^n \varepsilon_n \left[b_n J_n(k_{d2} r) + c_n N_n(k_{d2} r) \right] \cos(n\theta), \quad (\text{A.36})$$

$$\psi_2(r, \theta, t) = p_0 e^{-i\omega t} \sum_{n=0}^{\infty} i^n \varepsilon_n \left[d_n J_n(k_{s2} r) + e_n N_n(k_{s2} r) \right] \sin(n\theta). \quad (\text{A.37})$$

The potential functions in the filler fluid are

$$\varphi_3(r, \theta, t) = p_0 e^{-i\omega t} \sum_{n=0}^{\infty} i^n \varepsilon_n \left[f_n J_n(k_{d3} r) \right] \cos(n\theta) \quad (\text{A.38})$$

$$\psi_3(r, \theta, t) = p_0 e^{-i\omega t} \sum_{n=0}^{\infty} i^n \varepsilon_n \left[g_n J_n(k_{s3} r) \right] \sin(n\theta) \quad (\text{A.39})$$

where the Neumann function typically found in equations (2.46) and (A.39) is excluded to ensure that the solution remains bounded at the origin of the coordinate system.

The seven unknown coefficients, a_n , b_n , c_n , d_n , e_n , f_n , and g_n are determined by matching the boundary conditions for displacement, normal stress, and transverse stress at the internal and external surfaces of the sphere. On the sphere's external surface, at $r = a$,

$$p_1 = -\tau_{rr,2} \quad (\text{A.40})$$

$$u_{r,1} = u_{r,2} \quad (\text{A.41})$$

$$\tau_{r\theta,2} = 0 \quad (\text{A.42})$$

and on the internal surface, at $r = b$,

$$\tau_{rr,2} = \tau_{rr,3} \quad (\text{A.43})$$

$$u_{r,2} = u_{r,3} \quad (\text{A.44})$$

$$u_{\theta,2} = u_{\theta,3} \quad (\text{A.45})$$

$$\tau_{r\theta,2} = 0. \quad (\text{A.46})$$

Application of the boundary conditions results in a set of linear equations that are presented here in matrix form as,

$$\begin{bmatrix} d_{11} & d_{12} & d_{13} & d_{14} & d_{15} & d_{16} & d_{17} \\ d_{21} & d_{22} & d_{23} & d_{24} & d_{25} & d_{26} & d_{27} \\ d_{31} & d_{32} & d_{33} & d_{34} & d_{35} & d_{36} & d_{37} \\ d_{41} & d_{42} & d_{43} & d_{44} & d_{45} & d_{46} & d_{47} \\ d_{51} & d_{52} & d_{53} & d_{54} & d_{55} & d_{56} & d_{57} \\ d_{61} & d_{62} & d_{63} & d_{64} & d_{65} & d_{66} & d_{67} \\ d_{71} & d_{72} & d_{73} & d_{74} & d_{75} & d_{76} & d_{77} \end{bmatrix} \begin{pmatrix} a_n \\ b_n \\ c_n \\ d_n \\ e_n \\ f_n \\ g_n \end{pmatrix} = \begin{bmatrix} A_1 \\ A_2 \\ A_3 \\ A_4 \\ A_5 \\ A_6 \\ A_7 \end{bmatrix} \quad (\text{A.47})$$

where,

$$d_{11} = \frac{a^2}{\mu_2} H_n^{(1)}(k_1 a)$$

$$d_{12} = \left[-(k_{s2} a)^2 + 2n^2 \right] J_n(k_{d2} a) - 2[k_{d2} a] J_n'(k_{d2} a)$$

$$d_{13} = \left[-(k_{s2} a)^2 + 2n^2 \right] N_n(k_{d2} a) - 2[k_{d2} a] N_n'(k_{d2} a)$$

$$d_{14} = -2n J_n(k_{s2} a) + 2n[k_{s2} a] J_n'(k_{s2} a)$$

$$d_{15} = -2n N_n(k_{s2} a) + 2n[k_{s2} a] N_n'(k_{s2} a)$$

$$d_{16} = 0$$

$$d_{17} = 0$$

$$A_1 = -\frac{a^2}{\mu_2} J_n(k_1 a)$$

$$d_{21} = -\frac{k_1 a}{\rho_1 \omega^2} H_n^{(1)'}(k_1 a)$$

$$d_{22} = [k_{d2} a] J_n'(k_{d2} a)$$

$$d_{23} = [k_{d2} a] N_n'(k_{d2} a)$$

$$d_{24} = nJ_n(k_{s_2}a)$$

$$d_{25} = nJ_n(k_{s_2}a)$$

$$d_{16} = 0$$

$$d_{17} = 0$$

$$A_2 = -\frac{k_1 a}{\rho_1 \omega^2} J_n'(k_1 a)$$

$$d_{31} = 0$$

$$d_{32} = 2nJ_n(k_{d_2}a) - [k_{d_2}a]J_n'(k_{d_2}a)$$

$$d_{33} = 2nN_n(k_{d_2}a) - [k_{d_2}a]N_n'(k_{d_2}a)$$

$$d_{34} = \left[-2n^2 + (k_{s_2}a)^2 \right] J_n(k_{s_2}a) + 2[k_{s_2}a]J_n'(k_{s_2}a)$$

$$d_{35} = \left[-2n^2 + (k_{s_2}a)^2 \right] N_n(k_{s_2}a) + 2[k_{s_2}a]N_n'(k_{s_2}a)$$

$$d_{36} = 0$$

$$d_{37} = 0$$

$$A_3 = 0$$

$$d_{41} = 0$$

$$d_{42} = [k_{d_2}b]J_n'(k_{d_2}b)$$

$$d_{43} = [k_{d_2}b]N_n'(k_{d_2}b)$$

$$d_{44} = nJ_n(k_{s_2}b)$$

$$d_{45} = nN_n(k_{s_2}b)$$

$$d_{46} = -[k_{d3}b]J_n'(k_{d3}b)$$

$$d_{47} = -nJ_n(k_{s3}b)$$

$$A_4 = 0$$

$$d_{51} = 0$$

$$d_{52} = nJ_n(k_{d2}b)$$

$$d_{53} = nN_n(k_{d2}b)$$

$$d_{54} = [k_{s2}b]J_n'(k_{s2}b)$$

$$d_{55} = [k_{s2}b]N_n'(k_{s2}b)$$

$$d_{56} = -nJ_n(k_{d3}b)$$

$$d_{57} = -[k_{s3}b]J_n'(k_{s3}b)$$

$$A_5 = 0$$

$$d_{61} = 0$$

$$d_{62} = \frac{\mu_2}{\mu_3} \left\{ \left[-(k_{s2}b)^2 + 2n^2 \right] J_n(k_{d2}b) - 2[k_{d2}b]J_n'(k_{d2}b) \right\}$$

$$d_{63} = \frac{\mu_2}{\mu_3} \left\{ \left[-(k_{s2}b)^2 + 2n^2 \right] N_n(k_{d2}b) - 2[k_{d2}b]N_n'(k_{d2}b) \right\}$$

$$d_{64} = 2n \frac{\mu_2}{\mu_3} \left\{ -J_n(k_{s2}b) + [k_{s2}b]J_n'(k_{s2}b) \right\}$$

$$d_{65} = 2n \frac{\mu_2}{\mu_3} \left\{ -N_n(k_{s2}b) + [k_{s2}b]N_n'(k_{s2}b) \right\}$$

$$d_{66} = \left[(k_{s3}b)^2 - 2n^2 \right] J_n(k_{d3}b) + 2[k_{d3}b] J_n'(k_{d3}b)$$

$$d_{67} = 2nJ_n(k_{s3}b) - 2n[k_{s3}b] J_n'(k_{s3}b)$$

$$A_6 = 0$$

$$d_{71} = 0$$

$$d_{72} = 2nJ_n(k_{d2}b) - 2n[k_{d2}b] J_n'(k_{d2}b)$$

$$d_{73} = 2nN_n(k_{d2}b) - 2n[k_{d2}b] N_n'(k_{d2}b)$$

$$d_{74} = \left[-2n^2 + (k_{s2}b)^2 \right] J_n(k_{s2}b) + 2[k_{s2}b] J_n'(k_{s2}b)$$

$$d_{75} = \left[-2n^2 + (k_{s2}b)^2 \right] N_n(k_{s2}b) + 2[k_{s2}b] N_n'(k_{s2}b)$$

$$d_{76} = 2n \frac{\mu_2}{\mu_3} \{ -J_n(k_{d3}b) + [k_{d3}b] J_n'(k_{d3}b) \}$$

$$d_{77} = \frac{\mu_2}{\mu_3} \left\{ \left[-(k_{s3}b)^2 + 2n^2 \right] J_n(k_{s3}b) - 2[k_{s3}b] J_n'(k_{s3}b) \right\}$$

$$A_7 = 0$$

Note that only first order derivatives of the Bessel functions are present in the above coefficients. Recursive relations relate ordinary Bessel functions and their first order derivatives [76],

$$J_n(z) = \frac{z}{2n} [J_{n-1}(z) + J_{n+1}(z)] \quad (\text{A.48})$$

$$\frac{d}{dz} J_n(z) = \frac{1}{2} [J_{n-1}(z) - J_{n+1}(z)]. \quad (\text{A.49})$$

Using the above expressions, a Bessel function's second order derivative can then be expanded as,

$$J_n''(z) = \left[\frac{n^2}{z^2} - 1 \right] J_n(z) - \frac{1}{z} J_n'(z). \quad (\text{A.50})$$

This expression is used to reduce the order of Bessel function second derivatives in equations (A.47), a procedure that significantly reduces the amount of time required for computation.

To determine the coefficients of the scattered field, the system of equations (A.47) is solved for a_n through the method of Gaussian elimination [79]. The computer program used for this calculation is written in MATLAB[®] [119]. Derivatives of ordinary Bessel functions are solved numerically.

For a solid cylinder, the system of equations that results from the boundary value problem can be written in terms of the coefficients listed in (A.47) as follows:

$$\begin{bmatrix} d_{11} & d_{12} & d_{14} \\ d_{21} & d_{22} & d_{24} \\ 0 & d_{32} & d_{34} \end{bmatrix} \begin{Bmatrix} a_n \\ b_n \\ d_n \end{Bmatrix} = \begin{bmatrix} A_1 \\ A_2 \\ 0 \end{bmatrix} \quad (\text{A.51})$$

This system of equations is solved in the same manner as (A.47).

A.4 Lamb Waves

The following analysis follows that of Grisby [121] and Lamb [91]. The geometry for this investigation is depicted in Figure A.6.

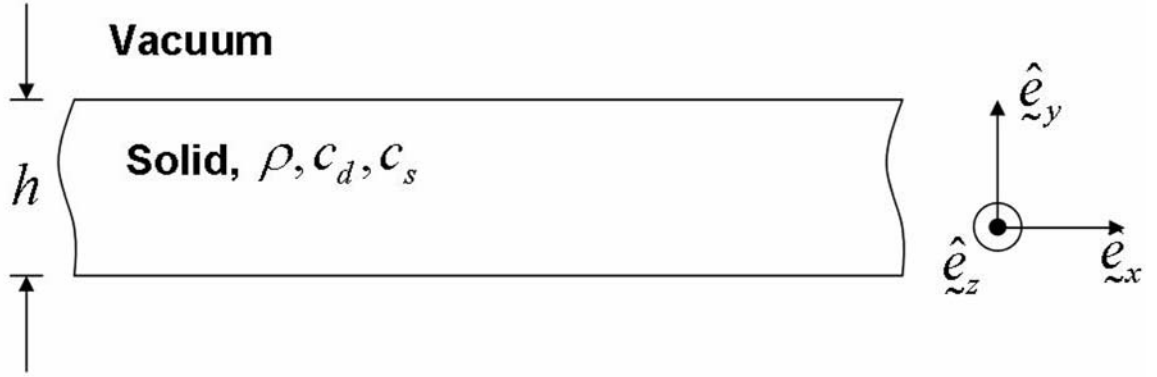


Figure A.6: Schematic depicting a flat plate *in vacuo* relevant to the calculation of Lamb wave dispersion curves.

A flat plate of thickness h extends infinitely in the x -direction and z -direction. The relevant displacements for this two-dimensional problem are written in terms of potential functions as

$$u = \frac{\partial \phi}{\partial x} + \frac{\partial \psi}{\partial y} \quad (\text{A.1})$$

and

$$v = \frac{\partial \phi}{\partial y} - \frac{\partial \psi}{\partial x} \quad (\text{A.2})$$

where u and v are displacements in the x -direction and y -direction, respectively. The relevant components of stress for this problem are in terms of displacement

$$\tau_{xy} = \mu \left(\frac{\partial v}{\partial x} + \frac{\partial u}{\partial y} \right) \quad (\text{A.3})$$

the stress in the x-direction on a plane parallel with the xz-plane (i.e. y-face) and

$$\tau_{yy} = \lambda \left(\frac{\partial u}{\partial x} + \frac{\partial v}{\partial y} \right) + 2\mu \frac{\partial v}{\partial y} \quad (\text{A.4})$$

the stress in the y-direction. The potential functions of (A.1) and (A.2) satisfy the equations

$$\begin{aligned} \frac{\partial^2 \phi}{\partial t^2} &= c_d^2 \nabla^2 \phi \\ \frac{\partial^2 \psi}{\partial t^2} &= c_s^2 \nabla^2 \psi \end{aligned} \quad (\text{A.5})$$

where c_d and c_s are the dilatational and shear wave speeds in the solid and are expressed in terms of Lamé coefficients as

$$c_d = \sqrt{\frac{\lambda + 2\mu}{\rho}} \quad (\text{A.6})$$

and

$$c_s = \sqrt{\frac{\mu}{\rho}}. \quad (\text{A.7})$$

Assuming that wave propagation is time harmonic and periodic in the x-direction, the solutions to (A.5) are

$$\begin{aligned} \phi &= F(y) e^{i(kx - \omega t)} \\ \psi &= G(y) e^{i(kx - \omega t)} \end{aligned} \quad (\text{A.8})$$

Equations (A.8) are then substituted in (A.5) and simplified, resulting in the following ordinary differential equations

$$\begin{aligned}\frac{\partial^2 \varphi}{\partial y^2} &= \alpha^2 \varphi \\ \frac{\partial^2 \psi}{\partial y^2} &= \beta^2 \psi\end{aligned}\tag{A.9}$$

where

$$\begin{aligned}\alpha &= \sqrt{k^2 - \frac{\omega^2}{c_d^2}} = k \sqrt{1 - \frac{c^2}{c_d^2}} \\ \beta &= \sqrt{k^2 - \frac{\omega^2}{c_s^2}} = k \sqrt{1 - \frac{c^2}{c_s^2}}.\end{aligned}\tag{A.10}$$

The solutions of (A.9) are, in terms of hyperbolic functions,

$$\begin{aligned}F(y) &= A \sinh(\alpha y) + B \cosh(\alpha y) \\ G(y) &= C \sinh(\beta y) + D \cosh(\beta y).\end{aligned}\tag{A.11}$$

The displacements, u and v , as well as the relevant components of stress, τ_{xy} and τ_{yy} are then expanded as follows:

$$u = \left\{ ik \left[A \sinh(\alpha y) + B \cosh(\alpha y) \right] + \beta \left[C \cosh(\beta y) + D \sinh(\beta y) \right] \right\} e^{i(kx - \omega t)} \tag{A.12}$$

$$v = \left\{ \alpha \left[A \cosh(\alpha y) + B \sinh(\alpha y) \right] - ik \left[C \sinh(\beta y) + D \cosh(\beta y) \right] \right\} e^{i(kx - \omega t)} \tag{A.13}$$

$$\tau_{xy} = \mu \left\{ \begin{aligned} &2ika \left[A \cosh(\alpha y) + B \sinh(\alpha y) \right] + \dots \\ &\dots + (k^2 + \beta^2) \left[C \sinh(\beta y) + D \cosh(\beta y) \right] \end{aligned} \right\} e^{i(kx - \omega t)} \tag{A.14}$$

$$\tau_{yy} = \mu \left\{ \begin{aligned} &(\beta^2 + k^2) \left[A \sinh(\alpha y) + B \cosh(\alpha y) \right] - \dots \\ &\dots - 2ik\beta \left[C \cosh(\beta y) + D \sinh(\beta y) \right] \end{aligned} \right\} e^{i(kx - \omega t)} \tag{A.15}$$

It is now important to note that there are generally two types of displacement characteristic of such a system. Displacement may be either symmetric or asymmetric about the $y = 0$ plane. Each type of motion gives rise to what are referred to as symmetric and asymmetric Lamb waves. Upon inspection of equation (A.13) for displacement of the plate in the y -direction, we note that if the motion is to be symmetric about the $y = 0$ plane, v must be an odd function, that is $v(y) = -v(-y)$, and thus, $A = D = 0$ because \cosh is an even function. For the case of asymmetric displacement, v must be an even function, that is $v(y) = v(-y)$, and thus, $B = C = 0$ because \sinh is an odd function. Applying these conditions to the expressions for stress results in two independent systems one for the symmetric and asymmetric Lamb waves, respectively. For the case of symmetric waves, equations (A.14) and (A.15) reduce to

$$\tau_{xy} = \{2\mu ik\alpha B \sinh(\alpha y) + \mu(k^2 + \beta^2)C \sinh(\beta y)\} e^{i(kx - \omega t)} \quad (\text{A.16})$$

$$\tau_{yy} = \{\mu(k^2 + \beta^2)B \cosh(\alpha y) - 2\mu ik\beta C \cosh(\beta y)\} e^{i(kx - \omega t)} \quad (\text{A.17})$$

At the boundaries of the plate, $y = \pm h/2$, the stress vanishes. The equations for stress can then be written in matrix form as

$$\begin{bmatrix} 2\mu ik\alpha \sinh(\alpha h) & \mu(k^2 + \beta^2) \sinh(\beta h) \\ \mu(k^2 + \beta^2) \cosh(\alpha h) & -2\mu ik\beta \cosh(\beta h) \end{bmatrix} \begin{Bmatrix} B \\ C \end{Bmatrix} = \begin{Bmatrix} 0 \\ 0 \end{Bmatrix} \quad (\text{A.18})$$

and are satisfied if the determinant of the matrix on the left hand side of (A.18) is equal to zero. After algebraic manipulation, solution of the determinant results in the following frequency equation

$$\frac{\tanh(\beta h / 2)}{\tanh(\alpha h / 2)} = \frac{4k^2 \alpha \beta}{(k^2 + \beta^2)} \quad (\text{A.19})$$

the real roots of which specify the phase velocity of the symmetric Lamb wave modes.

Similar analysis, performed for the asymmetric Lamb waves results in the frequency equation,

$$\frac{\tanh(\alpha h / 2)}{\tanh(\beta h / 2)} = \frac{4k^2 \alpha \beta}{(k^2 + \beta^2)}. \quad (\text{A.20})$$

Although the expressions described in this section are arrived at specifically through analysis of a plate *in vacuo*, the analysis provides the foundation for more complicated investigation. Dispersion curves of the phase velocity for the first three Lamb wave modes, calculated from equations (A.19) and (A.20), are presented in Figure A.7 versus the dimensionless parameter kh .

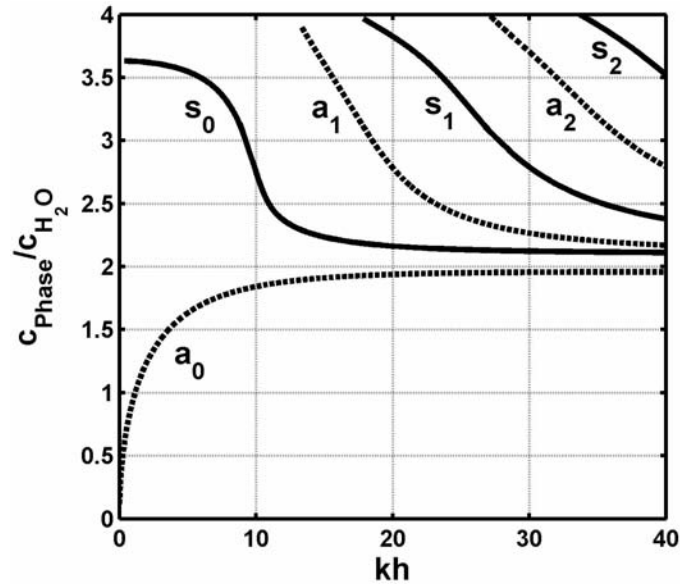


Figure A.7: Dispersion curves for the phase velocity of Lamb waves on a plate. Symmetric Lamb waves are presented as solid lines whereas asymmetric Lamb waves are presented as dashed line. The phase velocity is normalized to that of water with $c = 1479$ m/s and plotted versus the dimensionless parameter kh .

Appendix B

Why Time Reverse?

The single-channel time reversal technique presented in this work relies upon a time gate windowing operation to isolate signals of interest. Therefore, it is unable to exploit multi-path propagation. Also, there is no spatial focusing achieved as with array based time reversal techniques. The response of a target is enhanced because its spectrum is raised to a power proportional to the number of iterations. As such, one might argue that phase information is unimportant and that reversing the temporal order of signals is unnecessary. Comparable results could be obtained through iterative retransmission of received signals without applying the time reversal operation. In this section, the effects of the time reversal operation are investigated to ascertain whether it is necessary. The analysis presented implicitly draws upon techniques described in other chapters.

First, a simple thought experiment is presented schematically in Figure B.1. In Figure B.1a, a pulse is transmitted at a specularly reflecting target. The receive window is positioned such that the echo appears at its rightmost side. The windowed echo is then

retransmitted without performing a time reversal operation. The result of this transmission is presented in Figure B.1b. The additional time delay imposed on the transmitted signal results in the received signal “leaving” the time window. The receive window appears to be empty and successive retransmissions would not reveal the location of the scattering target. However, performing a time reversal operation on received signals, as in Figure B.1c, results in echoes remaining within the receive window throughout successive iterations. Therefore, in this case, employing the time reversal operation is of paramount importance if the target is to be detected.

A numerical scattering simulation is then conducted where the standard spherical shell is used as a target. For window sizes ranging from $4\mu\text{s}$ to $60\mu\text{s}$, the receive window is shifted from relative window times ranging from $-30\mu\text{s}$ to $60\mu\text{s}$ in steps of $0.5\mu\text{s}$. Fifty retransmissions (iterations) are performed at each window location with and without performing the time reversal operation. The average power within the receive window at a frequency of 800 kHz (the dominant target response frequency) is then calculated and recorded at each window location. A cosine squared shading with a 20% envelope is applied to the receive window before conducting Fourier analysis and computing the power.

The results of this simulation are presented in Figure B.2 where the intensity of each pixel represents the average power within the receive window. The vertical dashed line at a relative window time of $t_r = 0\mu\text{s}$ in each subfigure indicates the center of the specular return from the target. For window sizes less than $15\mu\text{s}$, the results are comparable. The 800 kHz resonance is centered at a relative window time of

approximately $t_r = 9.5\mu s$, the expected location based upon resonance scattering theory.

Without application of the time reversal operation the resonance is detected only for relative window times $\pm 5\mu s$ from its central location, as observed in Figure B.2b. The resonance is detected for a wider range of relative window times when the time reversal operation is employed, as in Figure B.2a.

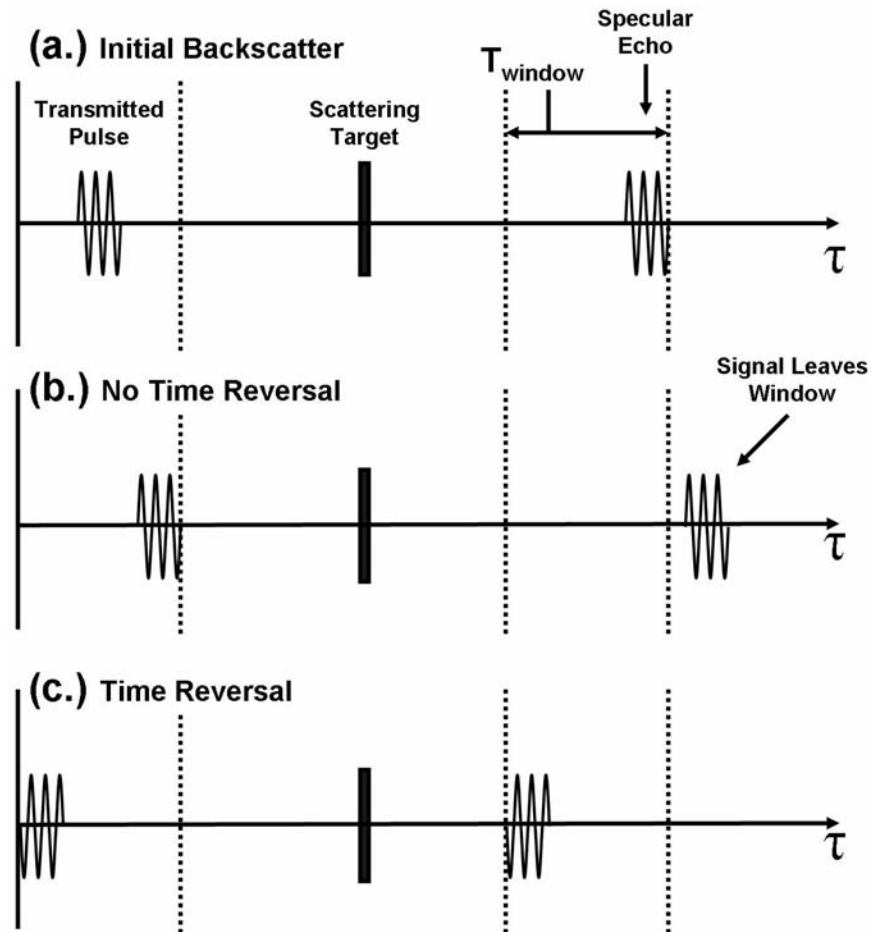


Figure B.1: Schematic of a thought experiment where a windowed target echo is retransmitted with and without performing a time reversal operation. (a.) A short pulse centered at a delay equal to one half the length of the receive window is transmitted. The receive window is positioned with the echo at the rightmost side of the window. (b.) Retransmission of the windowed echo without time reversal. (c.) Retransmission of the echo after a time reversal operation has been performed.

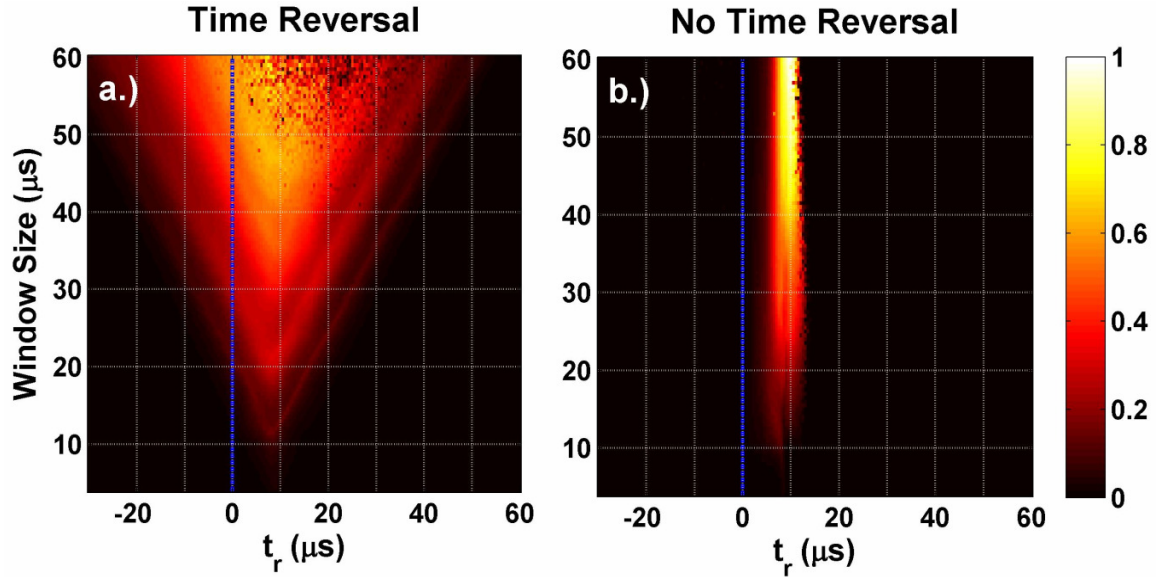


Figure B.2: Results of a window shifting simulation with and without performing a time reversal operation. The receive window is shifted from relative window times of $-30\mu s$ to $60\mu s$. The average power within the time reversal window is computed at iteration 50. The numerical experiment is repeated for receive window sizes ranging from $4\mu s$ to $60\mu s$. (a.) Results generated from application of a time reversal operation. (b.) Results generated without performing a time reversal operation. The intensity within each subfigure is scaled to the maximum value recorded in (b).

Bibliography

- [1] Favaro, A., ed. *Le opere di Galileo Galilei*. Vol. 10. 1890-1909, Barbera: Florence.
- [2] Goldberg, B.B., J.B. Liu, and F. Forsberg, *Ultrasound contrast agents: a review*. *Ultrasound in Medicine and Biology*, 1994. **20**(4): p. 319-327.
- [3] Korman, M.S. and J.M. Sabatier, *Nonlinear acoustic techniques for landmine detection*. *The Journal of the Acoustical Society of America*, 2004. **116**(6): p. 3354-3369.
- [4] Tesei, A., W.L.J. Fox, A. Maguer, and A. Løvik, *Target parameter estimation using resonance scattering analysis applied to air-filled, cylindrical shells in water*. *The Journal of the Acoustical Society of America*, 2000. **108**(6): p. 2891-2900.
- [5] Tesei, A., A. Maguer, W.L.J. Fox, R. Lim, and H. Schmidt, *Measurements and modeling of acoustic scattering from partially and completely buried spherical shells*. *The Journal of the Acoustical Society of America*, 2002. **112**(5): p. 1817-1830.
- [6] Lucifredi, I. and H. Schmidt, *Subcritical scattering from buried elastic shells*. *The Journal of the Acoustical Society of America*, 2006. **120**(6): p. 3566-3583.
- [7] Pinto, M.A., A. Bellettini, R. Hollett, and A. Tesei, *Real- and synthetic-array signal processing of buried targets*. *IEEE Journal of Oceanic Engineering*, 2002. **27**(3): p. 484-494.
- [8] Wilkens, R.H. and M.D. Richardson, *Mine burial prediction: A short history and introduction*. *IEEE Journal of Oceanic Engineering*, 2007. **32**(1): p. 3-9.
- [9] Strutt, J.W., *The Theory of Sound*. 1945, Dover Publications: New York. p. 145.
- [10] Parvulescu, A., *Matched-signal ("MESS") processing by the ocean*. *The Journal of the Acoustical Society of America*, 1995. **98**(2): p. 943-960.
- [11] Stitch, M.L. and M. Bass, *Laser Handbook: Volume 4*. 1985, North Holland Physics Publishing: Amsterdam. p. 333-485.
- [12] Fisher, R.A., ed. *Optical Phase Conjugation*. 1983, Academic Press: New York.

- [13] Jackson, D.R. and D.R. Dowling, *Phase conjugation in underwater acoustics*. The Journal of the Acoustical Society of America, 1991. **89**(1): p. 171-181.
- [14] Prada, C., F. Wu, and M. Fink, *The iterative time reversal mirror: A solution to self-focusing in the pulse echo mode*. The Journal of the Acoustical Society of America, 1991. **90**(2): p. 1119-1129.
- [15] Fink, M., *Time reversal of ultrasonic fields. I. Basic principles*. IEEE Transactions on Ultrasonics, Ferroelectrics and Frequency Control, 1992. **39**(5): p. 555-566.
- [16] Wu, F., J.-L. Thomas, and M. Fink, *Time reversal of ultrasonic fields. II. Experimental results*. IEEE Transactions on Ultrasonics, Ferroelectrics and Frequency Control, 1992. **39**(5): p. 567-578.
- [17] Fink, M., D. Cassereau, A. Derode, C. Prada, P. Roux, M. Tanter, J.-L. Thomas, and F. Wu, *Time-reversed acoustics*. Reports on Progress in Physics, 2000(12): p. 1933.
- [18] Prada, C., J.-L. Thomas, and M. Fink, *The iterative time reversal process: Analysis of the convergence*. The Journal of the Acoustical Society of America, 1995. **97**(1): p. 62-71.
- [19] Prada, C., S. Manneville, D. Spoliansky, and M. Fink, *Decomposition of the time reversal operator: Detection and selective focusing on two scatterers*. The Journal of the Acoustical Society of America, 1996. **99**(4): p. 2067-2076.
- [20] Prada, C. and M. Fink, *Separation of interfering acoustic scattered signals using the invariants of the time-reversal operator. Application to Lamb waves characterization*. The Journal of the Acoustical Society of America, 1998. **104**(2): p. 801-807.
- [21] Mordant, N., C. Prada, and M. Fink, *Highly resolved detection and selective focusing in a waveguide using the D.O.R.T. method*. The Journal of the Acoustical Society of America, 1999. **105**(5): p. 2634-2642.
- [22] Folegot, T., C. Prada, and M. Fink, *Resolution enhancement and separation of reverberation from target echo with the time reversal operator decomposition*. The Journal of the Acoustical Society of America, 2003. **113**(6): p. 3155-3160.
- [23] Prada, C. and J.-L. Thomas, *Experimental subwavelength localization of scatterers by decomposition of the time reversal operator interpreted as a covariance matrix*. The Journal of the Acoustical Society of America, 2003. **114**(1): p. 235-243.

- [24] Minonzio, J.-G., C. Prada, D. Chambers, D. Clorennec, and M. Fink, *Characterization of subwavelength elastic cylinders with the decomposition of the time-reversal operator: Theory and experiment*. The Journal of the Acoustical Society of America, 2005. **117**(2): p. 789-798.
- [25] Montaldo, G., M. Tanter, and M. Fink, *Real time inverse filter focusing through iterative time reversal*. The Journal of the Acoustical Society of America, 2004. **115**(2): p. 768-775.
- [26] Montaldo, G., M. Tanter, and M. Fink, *Revisiting iterative time reversal processing: Application to detection of multiple targets*. The Journal of the Acoustical Society of America, 2004. **115**(2): p. 776-784.
- [27] Kim, J.S., H.C. Song, and W.A. Kuperman, *Adaptive time-reversal mirror*. The Journal of the Acoustical Society of America, 2001. **109**(5): p. 1817-1825.
- [28] Oberai, A.A., G.R. Feijoo, and P.E. Barbone, *Lanczos iterated time-reversal*. The Journal of the Acoustical Society of America, 2009. **125**(2): p. EL70-EL76.
- [29] Fink, M., *Time-reversal mirrors*. Journal of Physics D: Applied Physics, 1993(9): p. 1333.
- [30] Tanter, M., J.-L. Thomas, and M. Fink, *Focusing and steering through absorbing and aberrating layers: Application to ultrasonic propagation through the skull*. The Journal of the Acoustical Society of America, 1998. **103**(5): p. 2403-2410.
- [31] Kuperman, W.A., W.S. Hodgkiss, H.C. Song, T. Akal, C. Ferla, and D.R. Jackson, *Phase conjugation in the ocean: Experimental demonstration of an acoustic time-reversal mirror*. The Journal of the Acoustical Society of America, 1998. **103**(1): p. 25-40.
- [32] Hodgkiss, W.S., H.C. Song, W.A. Kuperman, T. Akal, C. Ferla, and D.R. Jackson, *A long-range and variable focus phase-conjugation experiment in shallow water*. The Journal of the Acoustical Society of America, 1999. **105**(3): p. 1597-1604.
- [33] Smith, K.B., A.A.M. Abrantes, and A. Larraza, *Examination of time-reversal acoustics in shallow water and applications to noncoherent underwater communications*. The Journal of the Acoustical Society of America, 2003. **113**(6): p. 3095-3110.
- [34] Higley, W.J., P. Roux, W.A. Kuperman, W.S. Hodgkiss, H.C. Song, T. Akal, and M. Stevenson, *Synthetic aperture time-reversal communications in shallow water: Experimental demonstration at sea*. The Journal of the Acoustical Society of America, 2005. **118**(4): p. 2365-2372.

- [35] Hursky, P., M.B. Porter, M. Siderius, and V.K. McDonald, *Point-to-point underwater acoustic communications using spread-spectrum passive phase conjugation*. The Journal of the Acoustical Society of America, 2006. **120**(1): p. 247-257.
- [36] Song, H.C., W.A. Kuperman, and W.S. Hodgkiss, *Basin-scale time reversal communications*. The Journal of the Acoustical Society of America, 2009. **125**(1): p. 212-217.
- [37] Carin, L., H. Liu, T. Yoder, L. Couchman, B. Houston, and J. Bucaro, *Wideband time-reversal imaging of an elastic target in an acoustic waveguide*. The Journal of the Acoustical Society of America, 2004. **115**(1): p. 259-268.
- [38] Gaumond, C.F., D.M. Fromm, J.F. Lingeitch, R. Menis, G.F. Edelmann, D.C. Calvo, and E. Kim, *Demonstration at sea of the decomposition-of-the-time-reversal-operator technique*. The Journal of the Acoustical Society of America, 2006. **119**(2): p. 976-990.
- [39] Prada, C., J.d. Rosny, D. Clorennec, J.-G. Minonzio, A. Aubry, M. Fink, L. Berniere, P. Billand, S. Hibril, and T. Folegot, *Experimental detection and focusing in shallow water by decomposition of the time reversal operator*. The Journal of the Acoustical Society of America, 2007. **122**(2): p. 761-768.
- [40] Philippe, F.D., C. Prada, J.d. Rosny, D. Clorennec, J.-G. Minonzio, and M. Fink, *Characterization of an elastic target in a shallow water waveguide by decomposition of the time-reversal operator*. The Journal of the Acoustical Society of America, 2008. **124**(2): p. 779-787.
- [41] Sabra, K.G., P. Roux, H.C. Song, W.S. Hodgkiss, W.A. Kuperman, T. Akal, and J.M. Stevenson, *Experimental demonstration of iterative time-reversed reverberation focusing in a rough waveguide. Application to target detection*. The Journal of the Acoustical Society of America, 2006. **120**(3): p. 1305-1314.
- [42] Sutin, A.M., J.A. Tencate, and P.A. Johnson, *Single-channel time reversal in elastic solids*. The Journal of the Acoustical Society of America, 2004. **116**(5): p. 2779-2784.
- [43] Draeger, C., J.C. Aime, and M. Fink, *One-channel time-reversal in chaotic cavities: Experimental results*. The Journal of the Acoustical Society of America, 1999. **105**(2, Pt.1): p. 618-625.
- [44] Quieffen, N., S. Catheline, R.K. Ing, and M. Fink, *Real-time focusing using an ultrasonic one channel time-reversal mirror coupled to a solid cavity*. J. Acoust. Soc. Am., 2004. **115**(5, Pt.1): p. 1955-1960.

- [45] Heinemann, M.G., A. Larraza, and K.B. Smith, *Acoustic communications in an enclosure using single-channel time-reversal acoustics*. Applied Physics Letters, 2002. **80**(4): p. 694-696.
- [46] Pautet, L., A. Tesei, P. Guerrini, and E. Pouliquen, *Target echo enhancement using a single-element time reversal mirror*. IEEE Journal of Oceanic Engineering, 2005. **30**(4): p. 912-920.
- [47] Pierson, D.M., *Buried-Object Detection Using Time-Reversed Acoustics*. 2003, North Carolina State University.
- [48] Chambers, D.H., *Analysis of the time-reversal operator for scatterers of finite size*. The Journal of the Acoustical Society of America, 2002. **112**(2): p. 411-419.
- [49] Houston, B.H., J.A. Bucaro, T. Yoder, L. Kraus, J. Tressler, J. Fernandez, T. Montgomery, and T. Howarth. *Broadband low frequency sonar for non-imaging based identification*. in *Oceans '02 MTS/IEEE VO - 1*. 2002.
- [50] Urick, R.J., *Principles of Underwater Sound for Engineers*. 1967, New York: McGraw-Hill Book Company.
- [51] Logan, N.A., *Survey of some early studies of the scattering of plane waves by a sphere*. Proceedings of the IEEE, 1965. **53**(8): p. 773-785.
- [52] Rayleigh, J.W.S., *Investigation of the Disturbance Produced by a Spherical Obstacle on the Waves of Sound*. Proceedings of the London Mathematical Society, 1872. **4**: p. 253-283.
- [53] Anderson, V.C., *Sound Scattering from a Fluid Sphere*. The Journal of the Acoustical Society of America, 1950. **22**(4): p. 426-431.
- [54] Feuillade, C. and C.S. Clay, *Anderson (1950) revisited*. The Journal of the Acoustical Society of America, 1999. **106**(2): p. 553-564.
- [55] James J. Faran, J., *Sound Scattering by Solid Cylinders and Spheres*. The Journal of the Acoustical Society of America, 1951. **23**(4): p. 405-418.
- [56] Hickling, R., *Analysis of Echoes from a Solid Elastic Sphere in Water*. The Journal of the Acoustical Society of America, 1962. **34**(10): p. 1582-1592.
- [57] Brill, D. and G. Gaunard, *Resonance theory of elastic waves ultrasonically scattered from an elastic sphere*. The Journal of the Acoustical Society of America, 1987. **81**(1): p. 1-21.

- [58] Gaunaurd, G.C. and H. Uberall, *RST analysis of monostatic and bistatic acoustic echoes from an elastic sphere*. The Journal of the Acoustical Society of America, 1983. **73**(1): p. 1-12.
- [59] Williams, K.L. and P.L. Marston, *Synthesis of backscattering from an elastic sphere using the Sommerfeld--Watson transformation and giving a Fabry--Perot analysis of resonances*. The Journal of the Acoustical Society of America, 1986. **79**(6): p. 1702-1708.
- [60] Williams, K.L. and P.L. Marston, *Backscattering from an elastic sphere: Sommerfeld--Watson transformation and experimental confirmation*. The Journal of the Acoustical Society of America, 1985. **78**(3): p. 1093-1102.
- [61] Doolittle, R.D., H. Uberall, and P. Uginčius, *Sound Scattering by Elastic Cylinders*. The Journal of the Acoustical Society of America, 1968. **43**(1): p. 1-14.
- [62] Stanton, T.K., *Sound scattering by cylinders of finite length. III. Deformed cylinders*. The Journal of the Acoustical Society of America, 1989. **86**(2): p. 691-705.
- [63] Stanton, T.K., *Sound scattering by cylinders of finite length. II. Elastic cylinders*. The Journal of the Acoustical Society of America, 1988. **83**(1): p. 64-67.
- [64] Stanton, T.K., *Sound scattering by cylinders of finite length. I. Fluid cylinders*. The Journal of the Acoustical Society of America, 1988. **83**(1): p. 55-63.
- [65] Goodman, R.R. and R. Stern, *Reflection and Transmission of Sound by Elastic Spherical Shells*. The Journal of the Acoustical Society of America, 1962. **34**(3): p. 338-344.
- [66] Hickling, R., *Analysis of Echoes from a Hollow Metallic Sphere in Water*. The Journal of the Acoustical Society of America, 1964. **36**(6): p. 1124-1137.
- [67] Diercks, K.J. and R. Hickling, *Echoes from Hollow Aluminum Spheres in Water*. The Journal of the Acoustical Society of America, 1967. **41**(2): p. 380-393.
- [68] Flax, L. and W.G. Neubauer, *Acoustic reflection from layered elastic absorptive cylinders*. The Journal of the Acoustical Society of America, 1977. **61**(2): p. 307-312.
- [69] Gaunaurd, G.C., *Sonar cross section of a coated hollow cylinder in water*. The Journal of the Acoustical Society of America, 1977. **61**(2): p. 360-368.

- [70] Murphy, J.D., E.D. Breitenbach, and H. Uberall, *Resonance scattering of acoustic waves from cylindrical shells*. The Journal of the Acoustical Society of America, 1978. **64**(2): p. 677-683.
- [71] Anson, L.W. and R.C. Chivers, *Ultrasonic scattering from spherical shells including viscous and thermal effects*. The Journal of the Acoustical Society of America, 1993. **93**(4): p. 1687-1699.
- [72] Hay, A.E. and R.W. Burling, *On sound scattering and attenuation in suspensions, with marine applications*. The Journal of the Acoustical Society of America, 1982. **72**(3): p. 950-959.
- [73] Allegra, J.R. and S.A. Hawley, *Attenuation of Sound in Suspensions and Emulsions: Theory and Experiments*. The Journal of the Acoustical Society of America, 1972. **51**(5B): p. 1545-1564.
- [74] Officer, C.B., *Introduction to the Theory of Sound Transmission*. 1958, New York: McGraw-Hill Book Company.
- [75] Jackson, J.D., *Classical Electrodynamics*. 1999, New York: John Wiley & Sons, Inc.
- [76] Morse, P.M. and K.U. Ingard, *Theoretical Acoustics*. 1968, Princeton: Princeton University Press. p. 334.
- [77] Abramowitz, M. and I.A. Stegun, eds. *Handbook of Mathematical Functions*. 1964, Dover Publications, Inc.: New York.
- [78] Blackstock, D.T., *Fundamentals of Physical Acoustics*. 2000, New York: John Wiley & Sons, Inc. p. 92, p.342.
- [79] Kreysig, E., *Advanced Engineering Mathematics*. 8th ed. 1962, New York: John Wiley & Sons, Inc. p. 324.
- [80] Rayleigh, L., *On the Transmission of Light Through an Atmosphere Containing Small Particles in Suspension, and on the Origin of the Blue Sky*. Phil. Mag. Ser., 1899. **5**(47): p. 375-384.
- [81] Lilienfeld, P., *A Blue Sky History*, in *Optics and Photonics News*. 2004. p. 32-39.
- [82] Neubauer, W.G., ed. *Acoustic Reflection from Surfaces and Shapes*. 1986, Naval Research Laboratory: Washington, D.C. p. 35.
- [83] Kargl, S.G. and P.L. Marston, *Observations and modeling of the backscattering of short tone bursts from a spherical shell: Lamb wave echoes, glory, and axial reverberations*. J. Acoust. Soc. Am., 1989. **85**(3): p. 1014-1028.

- [84] Sammelmann, G.S., D.H. Trivett, and R.H. Hackman, *The acoustic scattering by a submerged, spherical shell. I: The bifurcation of the dispersion curve for the spherical antisymmetric Lamb wave*. The Journal of the Acoustical Society of America, 1989. **85**(1): p. 114-124.
- [85] Bethe, H.A. and G. Placzek, *Resonance Effects in Nuclear Processes*. Phys. Rev., 1937. **51**: p. 450.
- [86] Wigner, E.P., *Resonance Reactions and Anomalous Scattering*. Phys. Rev., 1946. **70**: p. 15.
- [87] Flax, L., L.R. Dragonette, and H. Uberall, *Theory of elastic resonance excitation by sound scattering*. The Journal of the Acoustical Society of America, 1978. **63**(3): p. 723-731.
- [88] Flax, L., G.C. Gaunaurd, and H. Uberall, *Theory of Resonance Scattering*, in *Physical Acoustics*, W.P. Mason and R.N. Thurston, Editors. 1981, Academic Press Inc. p. Chapter 3, p. 191-294.
- [89] Gaunaurd, G.C. and M.F. Werby, *Acoustic resonance scattering by submerged elastic shells*. Applied Mechanics Reviews, 1990. **43**(8): p. 171-208.
- [90] Murphy, J.D., J. George, A. Nagl, and H. Uberall, *Isolation of the resonant component in acoustic scattering from fluid-loaded elastic spherical shells*. The Journal of the Acoustical Society of America, 1979. **65**(2): p. 368-373.
- [91] Lamb, H., *On Waves in an Elastic Plate*. Proc. R. Soc. London Ser. A, 1917. **93**: p. 114-128.
- [92] Izbicki, J.-L., J.-L. Rousselot, A. Gerard, G. Maze, and J. Ripoche, *Analysis of resonances related to Scholte--Stoneley waves around circular cylindrical shells*. The Journal of the Acoustical Society of America, 1991. **90**(5): p. 2602-2608.
- [93] Maze, G., F. Leon, J. Ripoche, and H. Uberall, *Repulsion phenomena in the phase-velocity dispersion curves of circumferential waves on elastic cylindrical shells*. The Journal of the Acoustical Society of America, 1999. **105**(3): p. 1695-1701.
- [94] Talmant, M., H. Uberall, R.D. Miller, M.F. Werby, and J.W. Dickey, *Lamb waves and fluid-borne waves on water-loaded, air-filled thin spherical shells*. The Journal of the Acoustical Society of America, 1989. **86**(1): p. 278-289.
- [95] Kaiser, A.R., C.A. Cain, E.Y. Hwang, J.B. Fowlkes, and R.J. Jeffers, *A cost effective degassing system for use in ultrasonic measurements: The multiple*

- pinhole degassing system*. The Journal of the Acoustical Society of America, 1996. **99**(6): p. 3857-3859.
- [96] Thorne, P.D., T.J. Brudner, and K.R. Waters, *Time-domain and frequency-domain analysis of acoustic scattering by spheres*. The Journal of the Acoustical Society of America, 1994. **95**(5): p. 2478-2487.
 - [97] Feuillade, C., R.W. Meredith, N.P. Chotiros, and C.S. Clay, *Time domain investigation of transceiver functions using a known reference target*. The Journal of the Acoustical Society of America, 2002. **112**(6): p. 2702-2712.
 - [98] Oppenheim, A.V., ed. *Applications of Digital Signal Processing*. 1978, Prentice Hall Inc.: Englewood Cliffs. 206-210.
 - [99] *MATLAB® 2006a Version 7.2 Help Files*. "yulewalk." The Mathworks. Natick, MA.
 - [100] Friedlander, B. and B. Porat, *The Modified Yule-Walker Method of ARMA Spectral Estimation*. IEEE Transactions on Aerospace Electronic Systems, 1984. **AES-20**(2): p. 158-173.
 - [101] Zemanek, J., *Beam Behavior within the Nearfield of a Vibrating Piston*. The Journal of the Acoustical Society of America, 1971. **49**(1B): p. 181-191.
 - [102] Liauh, C.-T. and W.-L. Lin, *Fast numerical scheme of computing acoustic pressure fields for planar circular ultrasound transducers*. The Journal of the Acoustical Society of America, 1999. **105**(4): p. 2243-2247.
 - [103] Moran, M.J. and H.N. Shapiro, *Fundamentals of Engineering Thermodynamics*. 5th ed. 2004: John Wiley & Sons, Inc. 760.
 - [104] Kinsler, L.E., A.R. Frey, A.B. Coppens, and J.V. Sanders, *Fundamentals of Acoustics: 4th Ed.* 2000, New York: John Wiley & Sons Inc. pp. 121.
 - [105] Kinsler, L.E., A.R. Frey, A.B. Coppens, and J.V. Sanders, *Fundamentals of Acoustics: 4th Ed.* 2000, New York: John Wiley & Sons Inc. 121.
 - [106] Ihlenburg, F., *Finite Element Analysis of Acoustic Scattering*. 1998, Springer: New York. p. 35.
 - [107] Huang, J., *Heating in Vascular and Flow-Through Tissue Phantoms Induced by Focused Ultrasound*. 2002, Boston University.
 - [108] Seki, H., A. Granato, and R. Truell, *Diffraction Effects in the Ultrasonic Field of a Piston Source and Their Importance in the Accurate Measurement of*

- Attenuation*. The Journal of the Acoustical Society of America, 1956. **28**(2): p. 230-238.
- [109] Xu, W. and J.J. Kaufman, *Diffraction correction methods for insertion ultrasound attenuation estimation*. Biomedical Engineering, IEEE Transactions on, 1993. **40**(6): p. 563-570.
 - [110] Lee, K.I., V.F. Humphrey, B.-N. Kim, and S.W. Yoon, *Frequency dependencies of phase velocity and attenuation coefficient in a water-saturated sandy sediment from 0.3 to 1.0 MHz*. The Journal of the Acoustical Society of America, 2007. **121**(5): p. 2553-2558.
 - [111] Thomas, J.-L., P. Roux, and M. Fink, *Inverse scattering analysis with an acoustic time-reversal mirror*. Physical Review Letters, 1994. **72**(5): p. 637 LP - 640.
 - [112] Kargl, S.G. and R. Lim, *A transition-matrix formulation of scattering in homogeneous, saturated, porous media*. The Journal of the Acoustical Society of America, 1993. **94**(3): p. 1527-1550.
 - [113] Lim, R., *Scattering by an obstacle in a plane-stratified poroelastic medium: Application to an obstacle in ocean sediments*. The Journal of the Acoustical Society of America, 1994. **95**(3): p. 1223-1244.
 - [114] Lim, R., J.L. Lopes, R.H. Hackman, and D.G. Todoroff, *Scattering by objects buried in underwater sediments: Theory and experiment*. The Journal of the Acoustical Society of America, 1993. **93**(4): p. 1762-1783.
 - [115] Zampolli, M., A. Tesei, G. Canepa, and O.A. Godin, *Computing the far field scattered or radiated by objects inside layered fluid media using approximate Green's functions*. The Journal of the Acoustical Society of America, 2008. **123**(6): p. 4051-4058.
 - [116] Tesei, A., J.A. Fawcett, and R. Lim, *Physics-based detection of man-made elastic objects buried in high-density-clutter areas of saturated sediments*. Applied Acoustics
The detection of buried marine targets, 2008. **69**(5): p. 422-437.
 - [117] Lopes, J.L., C.L. Nesbitt, R. Lim, D. Tang, K.L. Williams, and E.I. Thorsos, *Shallow Grazing Angle Sonar Detection of Targets Buried Under a Rippled Sand Interface*. Oceans '02 MTS/IEEE, 2002. **1**: p. 461-467.
 - [118] Hamilton, E.L., *Compressional-Wave Attenuation in Marine Sediments*. Geophysics, 1972. **37**(4): p. 620-646.
 - [119] *MATLAB Version 7.2*. 2006a: Natick, MA. p. Help Files. "yulewalk".

- [120] Fitzpatrick, R., *Quantum Mechanics: A graduate level course*. 2006,
<http://farside.ph.utexas.edu/teaching/qm/lectures/lectures.html>.
- [121] Grisby, T.N. and E.J. Tajchman, *Properties of Lamb waves relevant to ultrasonic inspection of flat plates*. IRE Transactions on Ultrasonic Engineering, 1961. **UE-8**: p. 26-33.

REPORT DOCUMENTATION PAGE					Form Approved OMB No. 0704-0188	
<p>The public reporting burden for this collection of information is estimated to average 1 hour per response, including the time for reviewing instructions, searching existing data sources, gathering and maintaining the data needed, and completing and reviewing the collection of information. Send comments regarding this burden estimate or any other aspect of this collection of information, including suggestions for reducing the burden, to Department of Defense, Washington Headquarters Services, Directorate for Information Operations and Reports (0704-0188), 1215 Jefferson Davis Highway, Suite 1204, Arlington, VA 22202-4302. Respondents should be aware that notwithstanding any other provision of law, no person shall be subject to any penalty for failing to comply with a collection of information if it does not display a currently valid OMB control number.</p> <p>PLEASE DO NOT RETURN YOUR FORM TO THE ABOVE ADDRESS.</p>						
1. REPORT DATE (DD-MM-YYYY) 11/4/09		2. REPORT TYPE Final Report		3. DATES COVERED (From - To) 1/1/08 - 12/31/08		
4. TITLE AND SUBTITLE Supplemental Student Support: Detection and Identification of Buried Targets using Time Reversal Acoustics				5a. CONTRACT NUMBER		
				5b. GRANT NUMBER N00014-08-1-0148		
				5c. PROGRAM ELEMENT NUMBER		
6. AUTHOR(S) Roy, Ronald, A. Waters, Zachary, J.				5d. PROJECT NUMBER		
				5e. TASK NUMBER		
				5f. WORK UNIT NUMBER		
7. PERFORMING ORGANIZATION NAME(S) AND ADDRESS(ES) The Trustees of Boston University Office of Sponsored Programs 881 Commonwealth Avenue Boston, MA 02215-2303				8. PERFORMING ORGANIZATION REPORT NUMBER		
9. SPONSORING/MONITORING AGENCY NAME(S) AND ADDRESS(ES) Robert Manning, Code 32 Office of Naval Research 875 North Randolph Street Arlington, VA 22203-1995				10. SPONSOR/MONITOR'S ACRONYM(S) ONR-32		
				11. SPONSOR/MONITOR'S REPORT NUMBER(S)		
12. DISTRIBUTION/AVAILABILITY STATEMENT Approved for public release. Distribution unlimited.						
13. SUPPLEMENTARY NOTES This report addresses work done on a grant intended to provide supplemental student support for ONR Grant N00014-06-1-0044.						
14. ABSTRACT Noise and coherent returns from clutter often confounds efforts to acoustically detect and identify target objects buried in inhomogeneous media. Using iterative time reversal with a single channel transducer, returns from resonant targets are enhanced, yielding convergence to a narrowband waveform characteristic of the dominant mode in a target's elastic scattering response. We excite the target with a broadband acoustic pulse, sample the return using a finite time window, reverse the signal in time, and using the reversed signal as the source waveform for the next interrogation. Scaled laboratory experiments (0.4-2 MHz) are performed employing a piston transducer and spherical targets suspended in the free field and buried in a sediment phantom. Signal-to-noise enhancement of target echoes is demonstrated. The methodology reported provides a means to extract both time and frequency information for surface waves that propagate on an elastic target. Methods developed in the laboratory are then applied in medium scale (20-200 kHz) pond experiments for the detection of a steel shell buried in sandy sediment.						
15. SUBJECT TERMS sound propagation, sound scattering, time reversal, buried objects, detection and classification, signal processing						
16. SECURITY CLASSIFICATION OF:			17. LIMITATION OF ABSTRACT SAR	18. NUMBER OF PAGES	19a. NAME OF RESPONSIBLE PERSON ONR	
a. REPORT U	b. ABSTRACT U	c. THIS PAGE U			19b. TELEPHONE NUMBER (Include area code)	

Reset